Molecular approach towards the design and the preparation of supported and non-supported Pt- and Pd-based nanoparticles

Pierre Laurent

N° d'ordre
Année 2012

THESE DE L'UNIVERSITE DE LYON

Délivrée par

L'UNIVERSITE CLAUDE BERNARD LYON 1

ECOLE DOCTORALE

CHIMIE (ED 206)

DIPLOME DE DOCTORAT

(arrêté du 7 août 2006)

soutenue publiquement le 19 octobre 2012

par

M. Pierre LAURENT

TITRE :

Approche moléculaire du design et de la synthèse de nanoparticules supportées et non-supportées à base de Pt et Pd

Directeur de thèse :

M. Christophe Copéret

Jury:
M. Christophe COPERET
M. Stéphane BELLEMIN-LAPONNAZ
M. Stéphane DANIELE
M. Sébastien DONET
M. Nicolas MEZAILLES
Mme. Chloé THIEULEUX
M. François WEISS

Rapporteurs:
M. Stéphane BELLEMIN-LAPONNAZ
M. Nicolas MEZAILLES

N° d'ordre
Année 2012

THESE DE L'UNIVERSITE DE LYON

Délivrée par

L'UNIVERSITE CLAUDE BERNARD LYON 1

ECOLE DOCTORALE

CHIMIE (ED 206)

DIPLOME DE DOCTORAT

(arrêté du 7 août 2006)

soutenue publiquement le 19 octobre 2012

par

M Pierre LAURENT

TITRE :

Molecular approach towards the design and the preparation of supported and non-supported Pt- and Pd-based nanoparticles

Directeur de these :

M. Christophe Copéret

Jury:
M. Christophe COPERET
M. Stéphane BELLEMIN-LAPONNAZ
M. Stéphane DANIELE
M. Sébastien DONET
M. Nicolas MÉZAILLES
Mme. Chloé THIEULEUX
M. François WEISS

Rapporteurs:
M. Stéphane BELLEMIN-LAPONNAZ
M. Nicolas MÉZAILLES

UNIVERSITE CLAUDE BERNARD - LYON 1

Président de l'Université	**M. François-Noël GILLY**
Vice-président du Conseil d'Administration	M. le Professeur Hamda BEN HADID
Vice-président du Conseil des Etudes et de la Vie Universitaire	M. le Professeur Philippe LALLE
Vice-président du Conseil Scientifique	M. le Professeur Germain GILLET
Secrétaire Général	M. Alain HELLEU

COMPOSANTES SANTE

Faculté de Médecine Lyon Est – Claude Bernard	Directeur : M. le Professeur J. ETIENNE
Faculté de Médecine et de Maïeutique Lyon Sud – Charles Mérieux	Administrateur provisoire : M. le Professeur G. KIRKORIAN
UFR d'Odontologie	Directeur : M. le Professeur D. BOURGEOIS
Institut des Sciences Pharmaceutiques et Biologiques	Directeur : Mme la Professeure C. VINCIGUERRA.
Institut des Sciences et Techniques de la Réadaptation	Directeur : M. le Professeur Y. MATILLON
Département de formation et Centre de Recherche en Biologie Humaine	Directeur : M. le Professeur P. FARGE

COMPOSANTES ET DEPARTEMENTS DE SCIENCES ET TECHNOLOGIE

Faculté des Sciences et Technologies	Directeur : M. le Professeur F. De MARCHI
Département Biologie	Directeur : M. le Professeur F. FLEURY
Département Chimie Biochimie	Directeur : Mme le Professeur H. PARROT
Département GEP	Directeur : M. N. SIAUVE
Département Informatique	Directeur : M. le Professeur S. AKKOUCHE
Département Mathématiques	Directeur : M. le Professeur A. GOLDMAN
Département Mécanique	Directeur : M. le Professeur H. BEN HADID
Département Physique	Directeur : Mme S. FLECK
Département Sciences de la Terre	Directeur : Mme la Professeure I. DANIEL
UFR Sciences et Techniques des Activités Physiques et Sportives	Directeur : M. C. COLLIGNON
Observatoire de Lyon	Directeur : M. B. GUIDERDONI
Polytech Lyon	Directeur : M. P. FOURNIER
Ecole Supérieure de Chimie Physique Electronique	Directeur : M. G. PIGNAULT
Institut Universitaire de Technologie de Lyon 1	Directeur : M. C. VITON
Institut Universitaire de Formation des Maîtres	Directeur : M. R. BERNARD
Institut de Science Financière et d'Assurances	Directeur : Mme la Professeure V. MAUME-DESCHAMPS

Remerciements

Les travaux ayant abouti à la soutenance de cette thèse se sont déroulés de novembre 2009 à octobre 2012 suite à la mise en place d'une collaboration entre le CEA de Grenoble, CPE Lyon, le CNRS et l'Université Lyon 1 aboutissant à l'ouverture de la plateforme « Nanochimie » dans les locaux de CPE Lyon en janvier 2010. Ce laboratoire est rattaché à l'UMR 5265 C2P2, Chimie, Catalyse, Polymérisation et Procédés et est dirigé par le Pr. Bernadette Charleux. Il est lui-même divisé en 2 entités, l'équipe Chimie et Procédés de Polymérisation et l'équipe de Chimie Organométallique de Surface à laquelle j'étais rattaché.

Je tiens en premier lieu à remercier MM. Mézailles et Bellemin-Laponnaz qui ont accepté de juger ce travail en tant que rapporteurs. Merci aussi à MM. Weiss et Daniele d'avoir accepté de faire partie du jury témoignant ainsi de leur intérêt pour ces travaux.

Merci à mes encadrants, Sébastien Donet, « facilitateur » de projets en tous genres qui par sa confiance et ses conseils à su guider mon chemin dans l'immensité du CEA, Chloé Thieuleux, toujours prompte à débloquer une situation - en suggérant « quelques » manips supplémentaires et enfin last but not least, Christophe Copéret, dont la disponibilité, l'engagement et l'exigence n'ont pas faibli malgré son départ pour les montagnes suisses.

Merci à l'équipe du C2P2, et plus particulièrement à Laurent Veyre, dont l'efficacité lors de la mise en place et du « rodage » de la plateforme Nanochimie a été prépondérante. Merci aussi à Kai Szeto qui fut le soutien indéfectible d'une récente session au synchrotron de Grenoble. Merci à Aimery de Mallmann pour cette même session. Merci à Christine Lucas et François Bayard pour leurs appuis techniques.

Côté CEA, un grand merci à Michel Jouve, Thierry (Titi) Krebs, Aurélie Vandeneynde et Dominique Baguet du laboratoire des Composants pour la Conversion de l'Energie (LITEN/L2CE) pour leur accueil et aide précieuse. Merci à Marc Plissonnier, directeur de ce même laboratoire, de m'avoir accueilli au sein de son équipe. Merci à Eric de Vito pour les caractérisations XPS et son accueil enthousiaste, merci aussi à Nicolas Guillet pour sa disponibilité et son temps consacré à m'enseigner les rudiments d'électrochimie.

Merci à la joyeuse équipe étudiante du labo, la liste, trop longue, serait forcément incomplète, citons Popoff, PhD es BBQ et Philippe le montagnard.

Merci aux étudiants du « team Copéret » et particulièrement à David Gajan et Raphaël Wischert pour leur disponibilité et (très) nombreux conseils, particulièrement en début de thèse, il y avait beaucoup à apprendre. Un salut spécial à Arthur compagnon de labeur et Laurent, chanteur du vendredi après-midi et « ambianceur » du laboratoire.

Merci aux camarades d'études, de prépa et d'école, particulièrement à Clair et Bruno à l'origine de nombreuses péripéties mémorables.

Enfin, merci à ma famille pour son soutien durant ces études, mes beaux-parents pour leur sollicitude et mon père pour ses encouragements constants et sa confiance toujours renouvelée.

Je ne peux terminer sans remercier Diane, ma femme, tu es un soutien indéfectible et un moteur indispensable, ta patience infinie en cette fin de thèse un peu spéciale ne peut que me donner confiance en notre avenir !

Table of content

Abbreviations vii

1. Bibliography 1

1.1. Introduction 3

1.2. Platinum and palladium based nanoparticles for catalysis 3

1.2.1. Car exhaust depollution 3

1.2.2. Fuel-cell 5

1.2.2.1. Fuel-cell fundamentals 5

1.2.2.2. Fuel cell catalysts 7

1.3. Synthesis of supported nanoparticles 9

1.3.1. Metal Organic Chemical Vapor Deposition (MOCVD) 10

1.3.1.1. MOCVD principles 10

1.3.1.2. Platinum organometallic complexes for MOCVD 11

1.3.2. Surface Organometallic Chemistry (SOMC) 12

1.3.2.1. Principle 12

1.3.2.2. Supports 13

1.3.2.3. Nanoparticles synthesis 16

1.4. Colloidal route to the synthesis of nanoparticles 18

1.5. Research project 21

2. From well-defined Pt^{II} surface species to the controlled growth of oxide supported Pt nanoparticles 23

2.1. Introduction 25

2.2. Synthesis and characterization of Pt^{II} complexes 25

2.3. Grafting onto silica 27

2.3.1. Symmetrical complexes 27

2.3.2. Dissymmetrical complexes 29

2.3.2.1. (COD)Pt(Me)($OSi(OtBu)_3$) 29

2.3.2.2. (COD)Pt(Me)(Cl) 29

2.3.2.3. (COD)Pt(Me)($N(SiMe_3)_2$) 30
2.3.2.4. (COD)Pt(Cl)($N(SiMe_3)_2$) 30
2.3.2.5. (COD)Pt($OSi(OtBu)_3$)($N(SiMe_3)_2$) 31
2.3.3. Nanoparticles formation 34
2.3.4. Conclusion 39
2.4. Ceria surface organometallic chemistry 40
2.4.1. Ceria surface chemistry 40
2.4.1.1. Surface morphology 40
2.4.1.2. IR-Study 40
2.4.1.3. OH titration 41
2.4.2. Platinum complexes grafting 45
2.4.3. Nanoparticles formation 47
2.4.4. Conclusion 48
2.5. Chapter conclusion 48
2.6. Experimental 49
2.6.1. General procedures 49
2.6.2. Platinum complexes preparation 50
2.6.3. Grafting procedures 52
2.6.4. Nanoparticles formation 55
2.7. Appendix 56
3. Platinum Nanoparticles deposited from (COD)Pt($OSi(O\mathit{t}Bu)_3)_2$ on GDLs by DLI-MOCVD and application in fuel-cell catalysis 87
3.1. Introduction 89
3.2. Results and discussion 89
3.2.1. Precursor characterization 89
3.2.2. Nanoparticles characterization 90
3.2.2.1. Elemental analysis results 90
3.2.2.2. Transmission Electron Microscopy (TEM) 92

3.2.2.3. Scanning Electron Microscopy (SEM) 94
3.2.2.4. X-Ray Diffraction (XRD) 95
3.2.2.5. X-Ray Photoelectron spectroscopy (XPS) 95
3.2.3. Electrocatalysis 99
3.2.3.1. Electroactive surface area 99
3.2.3.2. Hydrogen Oxidation Reaction 102
3.2.3.3. Oxygen Reduction Reaction 103
3.3. Chapter conclusion 104
3.4. Experimental 106
3.4.1. General 106
3.4.2. MOCVD 106
3.4.3. Sample preparation for half-cell tests 108
3.4.4. Half-cell tests 109
3.4.4.1. Electroactive surface measurement 109
3.4.4.2. Oxygen Reduction Reaction 112
3.5. Appendix 113
4. Colloidal nanoparticles stabilized by octylsilane, from monometallic to bimetallic systems 117
4.1. Introduction 119
4.2. Platinum nanoparticles 119
4.2.1. From Pt^0 precursor 119
4.2.1.1. Synthesis using H_2 as an external reductant 119
4.2.1.2. Synthesis in the absence of H_2 120
4.2.1.3. In-situ NMR monitoring of platinum nanoparticles formation 121
4.2.2. From Pt^{II} precursors 123
4.2.2.1. $(COD)Pt(Me)_2$ 123
4.2.2.2. $(COD)Pt(OSi(OtBu)_3)_2$ 124
4.2.2.3. $(COD)Pt(Me)(OSi(OtBu)_3)$ and (COD)Pt(Cl)(Me) 135

4.2.3. Conclusion 139
4.3. Palladium nanoparticles 139
4.3.1. Synthesis using H_2 as an external reductant 139
4.3.2. Synthesis in the absence of H_2 140
4.3.3. Conclusion 141
4.4. Platinum/palladium bimetallic nanoparticles 141
4.4.1. Synthesis and characterization 141
4.4.1.1. UV-Vis spectroscopy 142
4.4.1.2. Transmission electron microscopy 142
4.4.1.3. Infrared spectroscopy 144
4.4.2. Determining the nature of the nanoparticles prepared from mixtures of Pt and Pd precursors 146
4.4.2.1. X-Ray photoelectron spectroscopy (XPS) 146
4.4.2.2. High-Resolution Transmission Electron Microscopy 149
4.4.2.3. Energy Dispersive X-Ray spectrometry 150
4.4.3. Conclusion 151
4.5. Electroanalysis and catalysis 152
4.5.1. Loading on high surface area carbon 152
4.5.2. Cyclic voltamperometry 152
4.5.3. Oxygen Reduction Reaction 155
4.5.4. Conclusion 156
4.6. Chapter conclusion 156
4.7. Experimental 157
4.7.1. Preparation of palladium nanoparticles 157
4.7.2. Preparation of monometallic nanoparticles 157
4.7.2.1. From $Pt(dba)_2$ 157
4.7.2.2. From $Pd(dba)_2$ 158
4.7.2.3. From $(COD)Pt(OSi(OtBu)_3)_2$ 158

4.7.2.4. From (COD)Pt(Me)(OSi(O_tBu)$_3$) 158
4.7.2.5. From (COD)Pt(Cl)(Me) 158
4.7.3. Preparation of Bimetallic nanoparticles 158
4.7.1. UV-Vis spectroscopy 159
4.7.2. NMR experiments 159
4.7.2.1. Kinetic 159
4.7.2.2. DOSY 160
4.7.3. IR 160
4.7.4. Impregnation on silica and alumina 160
4.7.5. H_2 chemisorption 161
4.7.6. X-Ray photoelectron spectroscopy (XPS) 161
4.7.7. Carbon supported nanoparticles preparation 162
4.7.7.1. Vulcan preparation 162
4.7.7.2. Nanoparticles loading 162
4.7.7.3. Preparation of the rotating electrodes 162
4.7.8. Electrocatalysis 162
4.8. Appendix 164
5. Conclusion and perspectives 173
6. References 179

Abbreviations

NMR	Nuclear Magnetic Resonance
SS-NMR	Solid-State NMR
δ	chemical shift in NMR downfield from TMS, Hz or ppm
TMS	tetramethylsilane, Si(CH3)4
CP	Cross-Polarisation
MAS	Magic Angle Spinning
DOSY	Diffusion Ordered Spectroscopy
Hz	Hertz, s^{-1}
$^{n}J_{A-B}$	scalar coupling constants between nuclei A B separated by n bonds, Hz
XRD	X-Ray Diffraction
IR	infrared
DRIFT	Direct Reflectance Infrared Fourrier Transform spectroscopy
δ(A-B)	deformation frequencies of A-B bond
ν(A-B)	stretching frequencies of A-B bond
TEM	Transmission Electron Microscopy
XPS	X-ray Photoelectron Spectroscopy
GC	Gas Chromatography
MS	Mass Spectroscopy
EXAFS	Extended X-ray Absorption Fine Structure
HR-TEM	High-Resolution Transmission Electron Microscopy
ESA	Electroactive Surface Area
nm	nanometer
Å	angström
°C	relative temperature in Celsius degree: T = °C + 273.15
MOCVD	Metal Organic Chemical Vapor Deposition
SOMC	Surface OrganoMetallic Chemistry
ORR	Oxygen Reduction Reaction
HOR	Hydrogen Oxidation Reaction
COD	1,5-cyclooctadiene
dba	dibenzylideneacetone
Me	methyl, CH_3
*t*Bu	tert-butyl
equiv.	molecular equivalent (mol / mol)
eV	electron-volts, 1 eV = 1.60217646 × 10^{-19} J
h	hour
min	minute
s	second
M	metal or molar concentration
NP	nanoparticles
RT	Room Temperature
1D, 2D, 3D	one dimensional, two dimensional and three dimensional

1. Bibliography

1.1. Introduction

The synthesis of nanoparticles for catalysis applications has now a long history of research at an academic as well as at an industrial level but new synthesis procedures and better understanding of parameters that control the growth and the composition of metal nanoparticles are still of major interest today. Pt and Pd nanoparticles are among the best catalysts for numerous reactions from refining in the petroleum industry[1] to fine chemistry[2] and biomedical applications.[3] In coherence with research programs currently pursued at the CEA Grenoble, we will mainly focus on two potential applications for such nanoparticles, car exhaust depollution and Polymer Electrolyte Membrane (PEM) fuel cells. The synthesis methods will then be described, emphasizing onto Metal Organic Chemical Vapor Deposition, Surface Organometallic chemistry (SOMC) and the colloidal approach.

1.2. Platinum and palladium based nanoparticles for catalysis

1.2.1. Car exhaust depollution

Pollution from car exhausts is a major concern and European programs (Euro 1 to Euro 6) are implemented every four years since 1993 with increase constraints concerning the nitrogen oxides (NO_x), carbon monoxide (CO) and hydrocarbons (HC) emissions thus pushing research and innovation towards more efficient catalysts.

Rhodium is the catalyst of choice for the NOx reduction[4] into N_2, whereas Pt and Pd are used for the catalytic oxidation of CO and HC into CO_2. This Rh/Pt/Pd system is referred as three-way catalyst (TWC) used in car's catalytic converters. Nanoparticles are supported onto a high surface area cordierite monolith with a honeycomb like structure and embedded into a washcoat with alumina as the principal component. Ceria is added to stabilize nanoparticles through the so-called Strong Metal Support Interaction (SMSI)[5] and to increase the thermal stability of the support.[6] It is moreover added to promote the low temperature water-gas shift reaction (WGSR) and to store oxygen under lean (fuel deficient) conditions.[7] The oxygen storage capacity comes from its unique property as it can be reversibly reduced from the Ce^{4+} stable form to Ce^{3+}, forming oxygen vacancies (bulk and surface – see Equation 1). Upon thermal treatment under reducing atmosphere ceria thus forms non-stoichiometric oxides often described as $CeO_{(2-x)}$ with $0 \leq x \leq 0.5$. This phenomenon and its influence over the catalytic properties of three-way catalysts has been widely studied.[8-10] This is of importance to keep an air to fuel ratio (λ) at a fixed value regardless the motor regime, rich ($\lambda < 14.6$) or lean

conditions ($\lambda > 14.6$), this ratio allowing the best catalytic performances for both reduction and oxidation reactions (Figure 1). Nanoparticles have sizes between two and more than 20 nm particles (Figure 2).

$$2\ CeO_2 = Ce_2O_3 + \tfrac{1}{2}O_2$$

Equation 1. Ceria reduction

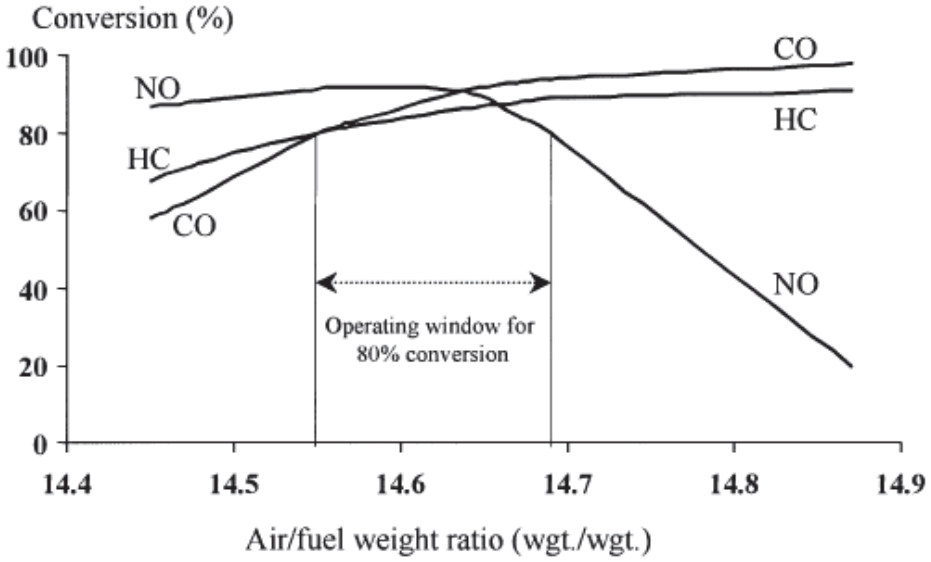

Figure 1. Three-way catalyst performance determined by engine air to fuel ratio, reproduced from ref[11]

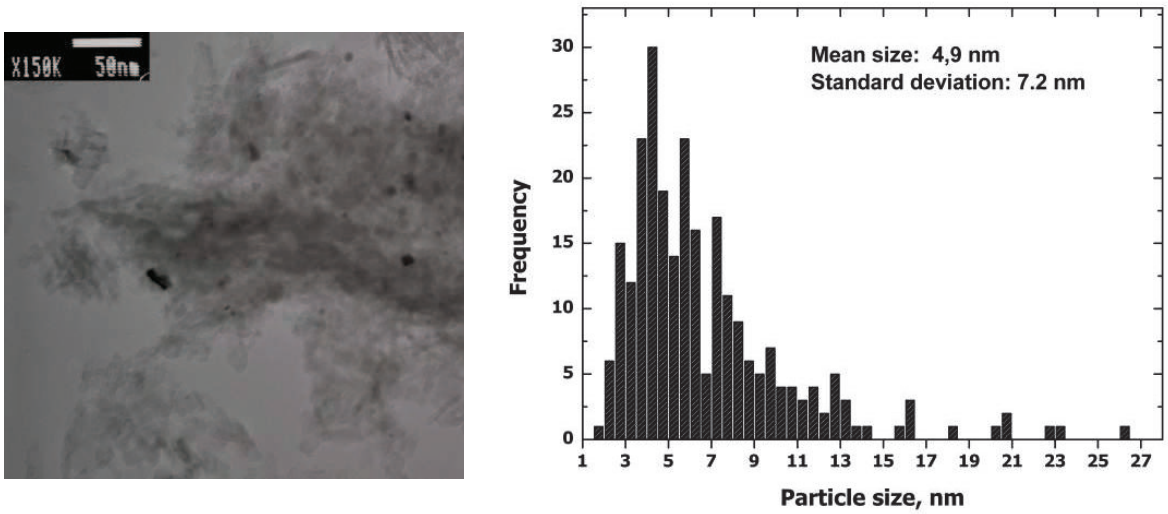

Figure 2. TEM, Diesel Oxidation Catalyst (DOC), Pt and Pd nanoparticles (in a 2:1 ratio), Renault reference catalyst, reproduced from CEA internal analysis report.

Moreover ceria was found to promote the redispersion of aggregated nanoparticles, this happened through atomic migration rather than particle coalescence/splitting.[12] Under oxidative conditions, oxygen absorb onto Pt particles, some mobile Pt oxide species migrates

and are trapped onto ceria through the strong metal support interaction. Under reducing conditions, the Pt-O-Ce bonds are broken and new small Pt particles are formed.
Finally note that industrially, the catalysts are prepared by impregnation of cordierite monolith by sol-gel containing metal salts. This allows the formation of both the washcoat and metallic nanoparticles under subsequent thermal treatments; a major drawback of this method is that embedded nanoparticles are not all accessible for catalysis, generating poor noble-metal utilization yields.

1.2.2. Fuel-cell

1.2.2.1. Fuel-cell fundamentals

Fuel-cells convert chemical energy into electricity through redox reactions. The oxidation of the fuel at the anode leads to the formation of cation (positively charge) and electrons. A specifically designed electrolyte allows for the transfer of the cation but not of the electrons, these are driven through an electrical circuit and produce electricity. These electrons are recombined at the cathode with the cation and following a reduction reaction (most often with O_2) forms the byproduct of the fuel cell. The most common work-up is using H_2 as a fuel and atmospheric O_2 as the oxidant, the only by-product being water. Protons are produced at the anode and conducted to the cathode through a Polymer Electrolyte Membrane (Figure 3). This polymer is very often Nafion (produced by DuPont), a proton conductive polymer grafted with sulfonic acid functions. A schematic representation is presented in Figure 3.The reactions involved are the following:

At the anode (Hydrogen Oxydation Reaction - HOR): $H_2 \rightarrow 2\ H^+ + 2\ e^-$
At the cathode (Oxygen Reduction Reaction - ORR): $½\ O_2 + 2\ H^+ + 2\ e^- \rightarrow H_2O$
Overall reaction: $H_2 + ½\ O_2 \rightarrow H_2O$

Note here that PEM fuel cell can use methanol too as a fuel (Direct Methanol Fuel Cell). This technology is actually under intense research[13,14] as methanol would be safer and easier to handle than H_2.

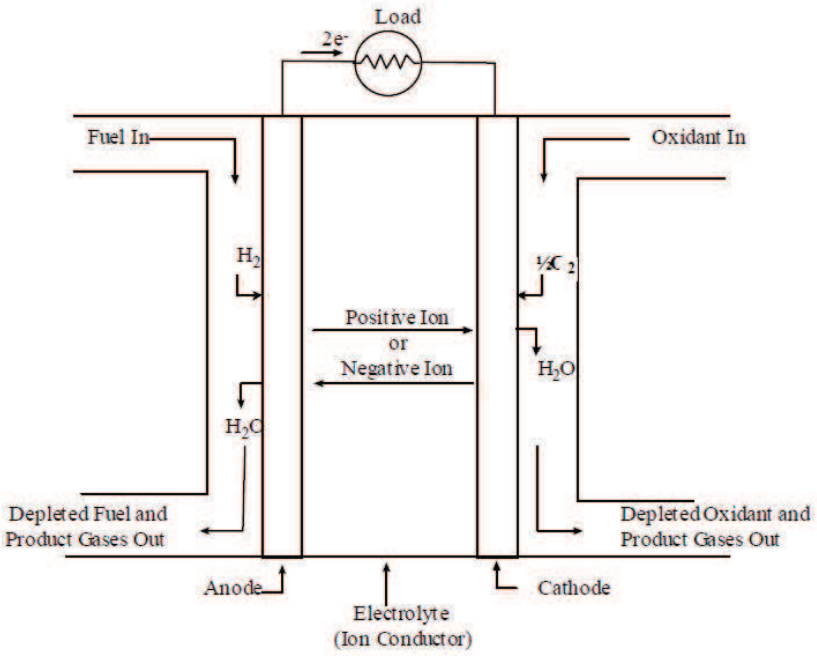

Figure 3. Schematic of a PEM fuel-cell H_2/O_2, reproduced from ref[15]

The theoretical potential of such system is 1.23 V *vs.* the Hydrogen Reference Electrode (HRE) but in practice this potential is limited by various factors such as gas diffusion, water transportation and electrical resistivity. The polarization curve (Figure 4) presents 3 main areas:

1) the kinetic is limited by the activation energy of the electrochemical reactions
2) the polarization curve is linear (U = R.I), this stems from the ohmic losses due the addition of various resistivity from the fuel cell set-up (electrolyte, interfaces)
3) diffusion limitations hinder the fuel cell efficiency

Fuel cells are thus operated in the area 2, most often around 0.7 V.

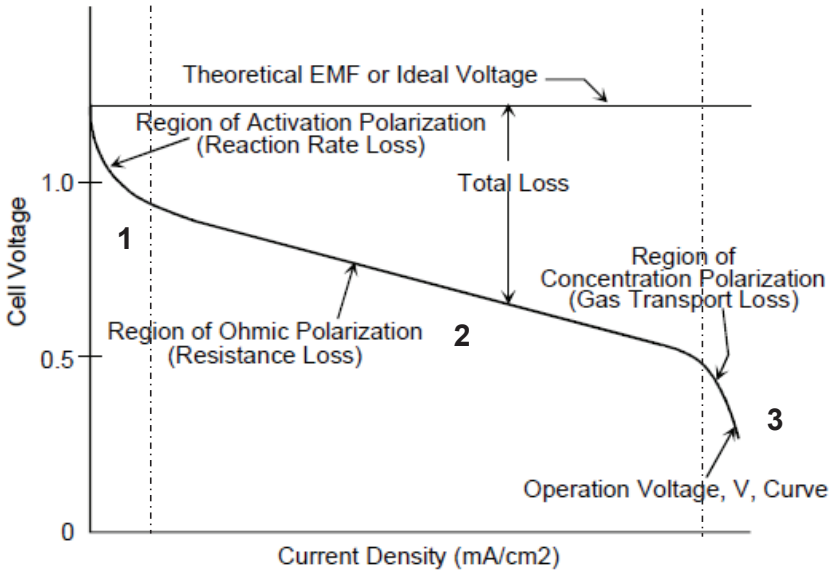

Figure 4. Polarization curve of a typical PEMFC, reproduced from[15]

1.2.2.2. Fuel cell catalysts

H_2 oxidation is fast while O_2 reduction is slow. The ORR is thus the limiting reaction of any fuel cell. Fuel cells are nowadays available for a wide range of stationary applications such emergency power systems to transportation application like public buses. The latter application suffers, among other issues, of the catalyst price. Indeed platinum is the best catalyst so far but its price tripled in the last 10 years from 13 to 38 €/g (with maximum up to 51 €/g); this is moreover a scarce resource.[16] Targets fixed by the American Department of Energy (DOE) are widely used for comparison purposes (Figure 5). Today the catalyst represents about 25% of the total price of the fuel-cell systems. The goal is thus to lower the content of platinum down to 0.15 $mg.cm^{-2}$ (today's best performance have been achieved down to 0.4 $mg.cm^{-2}$) with efficiency of 0.125 $g.kW^{-1}$ in order to meet those targets (100 kW for a car at a 30 $\$.kW^{-1}$ price to be competitive against internal combustion motors – 30 $\$.kW^{-1}$ as well).[17]

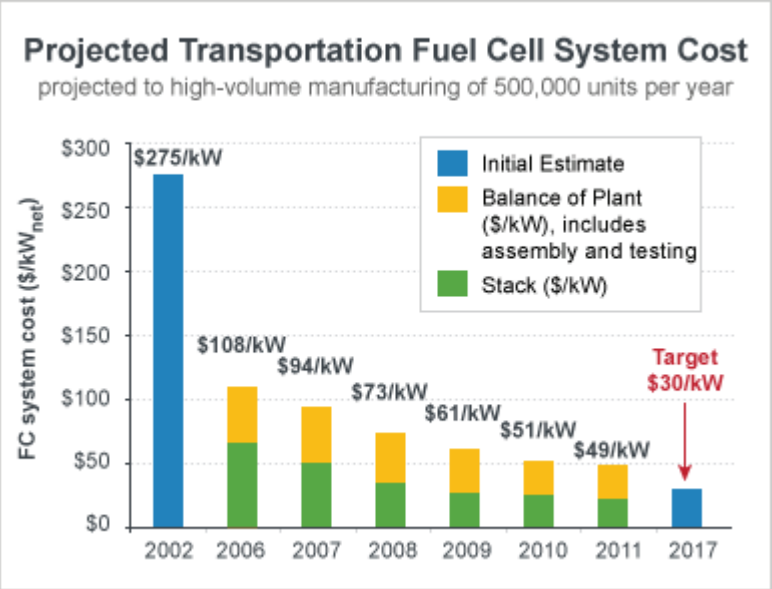

Figure 5. Price targets set by the DOE, reproduced from ref[17]

Lowering the Pt-loading for the anode (H_2 feeding) has been achieved[18] down to 0.05 mg_{Pt}/cm^{-2} due to the large activity of Pt toward the hydrogen oxidation reaction. Another issue at the anode is to avoid pollution of the catalyst, indeed CO is found in H_2 as a pollutant and is a strong poison for platinum catalyst. It strongly binds onto the Pt surface blocking the active sites access. Alloying Pt with other metals such as Ir gives satisfying results.[19]

For the cathode (O_2 feeding), two strategies are pursued: i) the optimization of the electrode structure in order to increase the platinum utilization yield and limit the voltage loss and ii) the synthesis of more active Pt based alloys to improve the Pt mass activity (expressed in $A.mg^{-1}_{Pt}$).[20] Pt has been alloyed with many other metals such as Fe, Ni, Co[21], Au[22] and Pd[23,24] for enhanced catalytic activities.

Moreover, the size of the nanoparticles is of importance as demonstrated by various studies, most agree on a size comprised between 2 and 3 nm for enhanced performances (Figure 6).[25,26] Finally, the shape is of prior interest as Pt facet do not all demonstrate the same catalytic properties towards the ORR.[27]

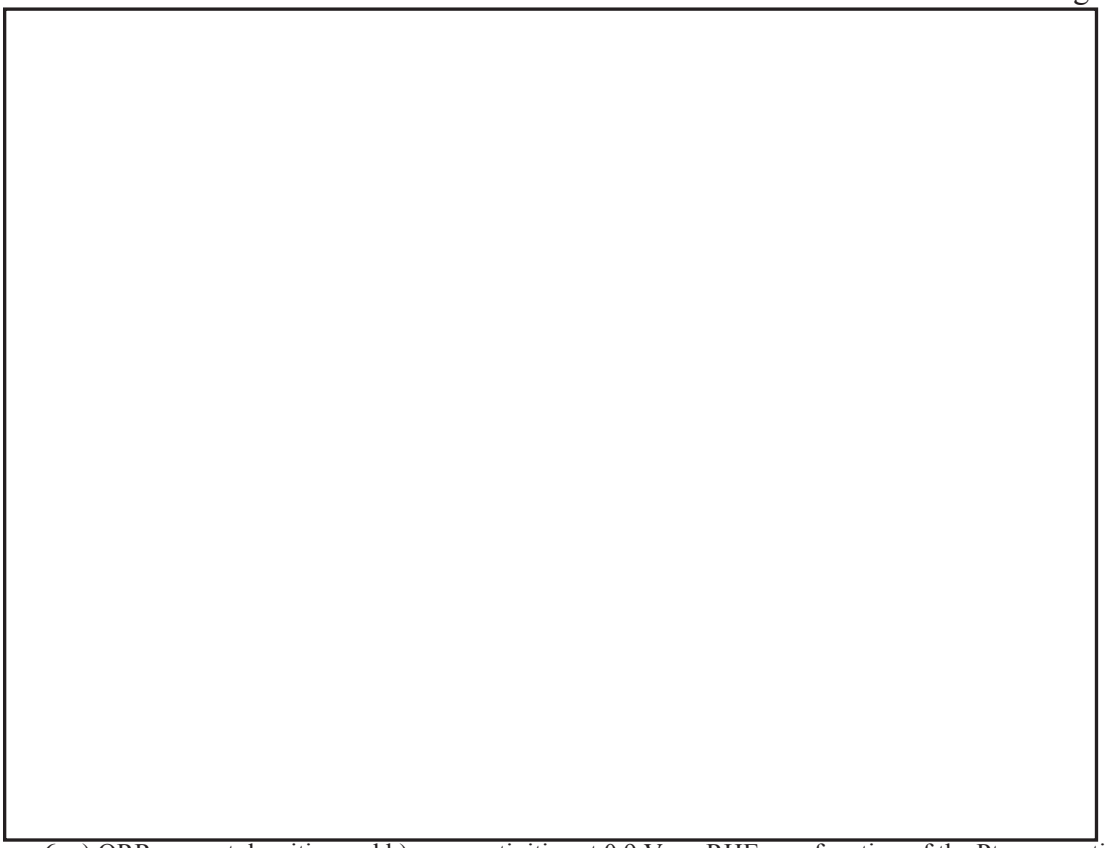

Figure 6. a) ORR current densities and b) mass activities at 0.9 V *vs.* RHE as a function of the Pt nanoparticles size. O_2 saturated 0.1 M $HClO_4$ solution at 23°C, 1600 rpm and 50 $mV.s^{-1}$. Reproduced from ref[26]

Note that replacing Pt by non-noble metal catalyst is a hot research field, for example hydrogenase like catalyst[28] (containing Fe and/or Ni) can be used for the HOR and nitrogen dopped carbon nanotubes[29] or heteroatomic polymers[30] have proved to be catalytically active for the ORR. But despite those effort Pt is still the best catalyst so far and will certainly remain essential on a short to medium time scale.[16] Efficient, versatile and easily scalable synthesis procedures are thus required.

1.3. Synthesis of supported nanoparticles

The synthesis of supported nanoparticles can be carried out using various methods, the most common[31] are i) salt impregnation by Incipient Wetness Impregnation (IWI), ii) ion exchange, iii) sol gel process with the addition of metal precursors, after various thermal treatments, nanoparticles are trapped into the matrix. Those methods are mature and are used for the preparation of large scale industrial catalysts. We will here focus on two methods that are less employed, Chemical Vapor Deposition (CVD) and the controlled decomposition of oxide grafted metallic complexes (also called surface organometallic chemistry – SOMC).

1.3.1. Metal Organic Chemical Vapor Deposition (MOCVD)

Metal Organic Chemical Vapor Deposition (MOCVD) is a technology initially dedicated to the deposition of metallic films onto 2D substrates. It is nowadays a mature process widely used in the microelectronic industry for film deposition onto wafers and for the treatment of large flat surfaces like windshields. This technique is indeed industrially very efficient as continuous processes are available. The deposition of many metals was described, *e.g.* Ni,[32] Al,[33] W,[33] Au,[34] Ag, Cu[35] or even alloys such as Fe-Ni.[36] This technique has then been successfully applied to the synthesis of nanoparticles onto various substrates, whether being 2D or 3D; this research topic has been thoroughly reviewed.[37]

1.3.1.1. MOCVD principles

The principle of MOCVD is to vaporize a metal precursor, usually an organometallic complex that will subsequently be decomposed onto the substrate and form either a metallic layer or nanoparticles depending on the process conditions. The vaporization is obtained under low pressure and specific temperature conditions. The decomposition of the metallic precursor can be induced by various methods as thermal, laser induced, plasma enhanced, electron beam induced decomposition.[38] A schematic representation of the process is presented Figure 7.

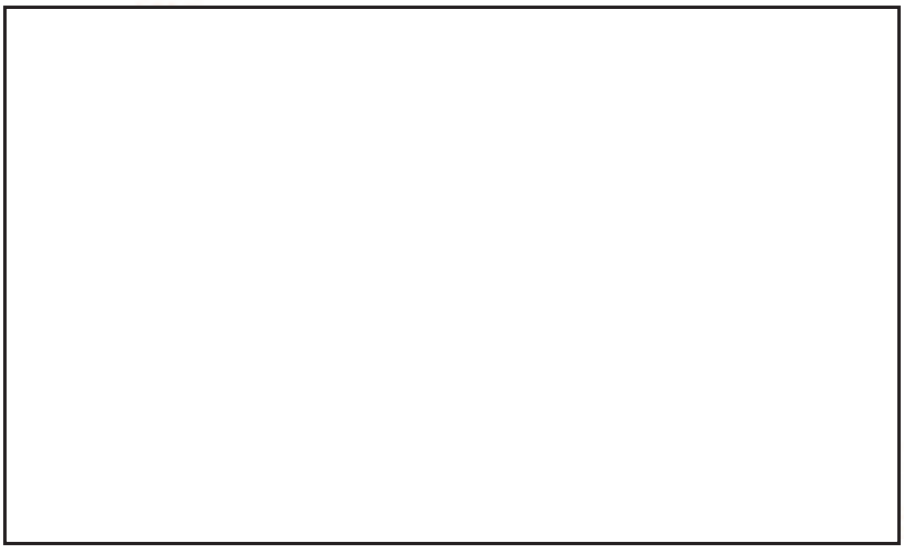

Figure 7. Schematic representation of the MOCVD process, reproduced from ref.[38]

1) convection of the gaseous reagents
2) diffusion of the reagents towards the substrate
3) adsorption of the reagents onto the substrate
4) degradation of the complex and film/nanoparticles formation
5) desorption of the gas products of the reaction

6) diffusion of these products through the boundary layer
7) gas evacuation of the system

The deposition condition used can have a strong impact on the purity, the adhesion of the film/nanoparticles and their morphology. Among those conditions, the gas composition, the temperature, the nature of the substrate surface and the solvent are the most important. Hydrogen can be used to help the reduction of the metallic precursor. For example Hierso *et al.*[39] synthesized Pt nanoparticles supported onto silica in a fluidized-bed MOCVD set-up, they showed that the addition of H_2 decreased the decomposition temperature of $(COD)Pt(Me)_2$ (COD = 1,5-cyclooctadiene) from 240°C to as low as 90°C. This proceeded through the catalytic hydrogenation of COD into cyclooctane and methyl elimination yielding methane. The substrate surface chemistry is of importance at it strongly influences the adsorption parameters, for example nucleation was found to be promoted by surface hydroxyl groups comparing the nanoparticle formation onto SiO_2 (high OH coverage), as prepared carbon nanotubes (low OH coverage) and acid treated nanotubes (high OH coverage - COOH functions).[40]

1.3.1.2. Platinum organometallic complexes for MOCVD

The literature on platinum MOCVD demonstrates the relative maturity of this process; recently mainly process conditions modification or set-up improvements are reported. Applications in the preparation of electrodes for microelectronic,[41] highly resistant coatings[42] and catalyst[37] can be found. The variety of platinum complexes is fairly large and has been thoroughly reviewed by Thurier *et al.*[38] A good MOCVD precursor must present a sufficient volatility, an adequate stability window, a low production cost and lead to films of high purity with a fast deposition rate. Moreover, stability (against water and oxygen), toxicity and of course cost are important parameters that have to be taken into account.
Most of the platinum complexes (Figure 8) used are either from the β-diketonates family, Pt^{II} diene complexes such as $(COD)Pt(X)_2$ or derivatives of the $CpPtMe_3$ complex (Cp = cyclopentadienyle). $(COD)Pt(Me)_2$ is widely used, despite being less volatile than β-diketonates or $CpPtMe_3$, as it is commercially available, synthesized in high yields and relatively stable under air.

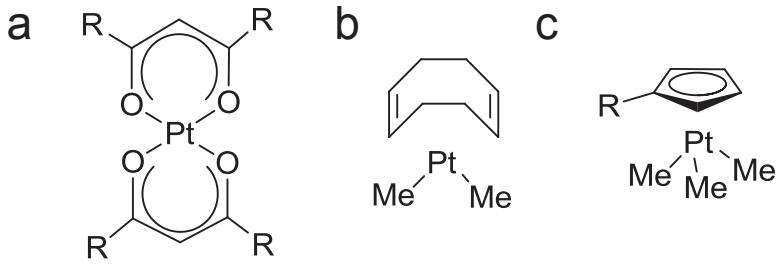

Figure 8. a) β-diketonates, R = Me, C_5H_{11}, CF_3, b) (CODPt((Me)$_2$, c) R = H, Me, Et with increased volatility

Compared to impregnation methods widely used for the synthesis of supported nanoparticles, MOCVD present several advantages. Indeed this method avoids many steps as impregnation, washing, drying, calcination and activation that consume both time and energy. This method is thus fast and economical.

1.3.2. Surface Organometallic Chemistry (SOMC)

1.3.2.1. Principle

The goal of surface organometallic chemistry is the synthesis of efficient heterogeneous catalysts. The idea behind this chemistry is to bridge the gap between molecular chemistry/homogeneous catalysis and solid-state chemistry/heterogeneous catalysis.[43,44] By this approach, single-site heterogeneous catalysts are synthesized by reacting tailor made organometallic complexes with anchoring sites onto various substrates. Controlled grafting takes place onto silica surface silanols, their nature and density being controlled by thermal treatment under vacuum or an inert gas (dehydroxylation). As depicted in Figure 9, the grafted species can be further modified by various methods, allowing fine tuning of the metal coordination sphere. This chemistry led to the synthesis of catalysts designed for various reactions such as olefin polymerization,[45-47] hydrogenation of olefins,[48] oxidation of olefins[49-51] and olefin metathesis.[52-56]

Surface species are mainly characterized by infrared spectroscopy, elemental analysis, X-Ray Photoelectron Spectroscopy (XPS), Extended X-Ray Absorption Fine Structure (EXAFS) and solid-state nuclear magnetic resonance (NMR).

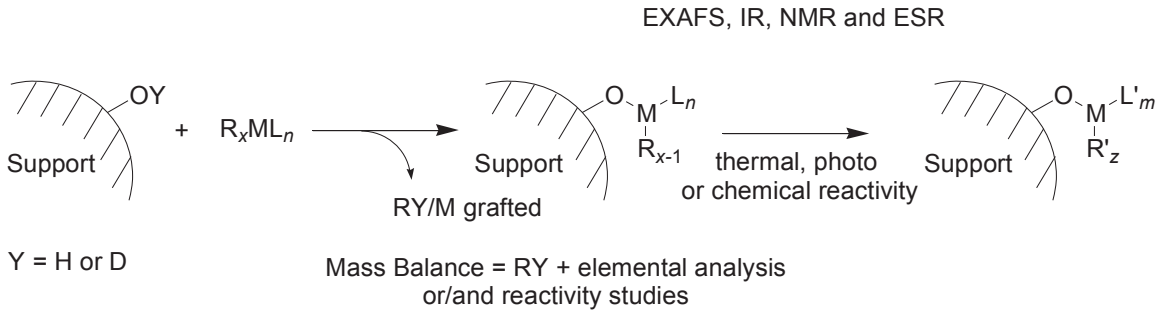

Figure 9. SOMC, schematic representation of the grafting and modification steps[44]

1.3.2.2. Supports

Historically, SOM chemistry has been thoroughly studied using silica as a support as it presents a relatively simple surface chemistry and a high surface area (Aerosil – 200 $m^2.g^{-1}$). A deep understanding of the surface chemistry of the supports used for this chemistry is necessary. The nature and density of the surface anchoring site is a key point to generate well-defined surface species, the support being here considered as a ligand of the grafted metal.

1.3.2.2.1. Silica

The silica surface is composed of 3 types of silanol functionalities, isolated, vicinal and geminal as depicted Figure 10.

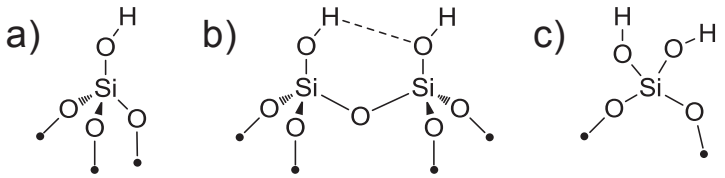

Figure 10. Silanols on silica, a) isolated, b) vicinal, d) geminal

The silanol surface density can be controlled by thermal treatment under vacuum, the so called dehydroxylation process originating from the condensation of silanols into siloxane brigdes (Figure 11).[57] The loss of surface area is limited up to 700°C, while above that temperature a significant drop is noticed due to silica nanoparticles sintering.

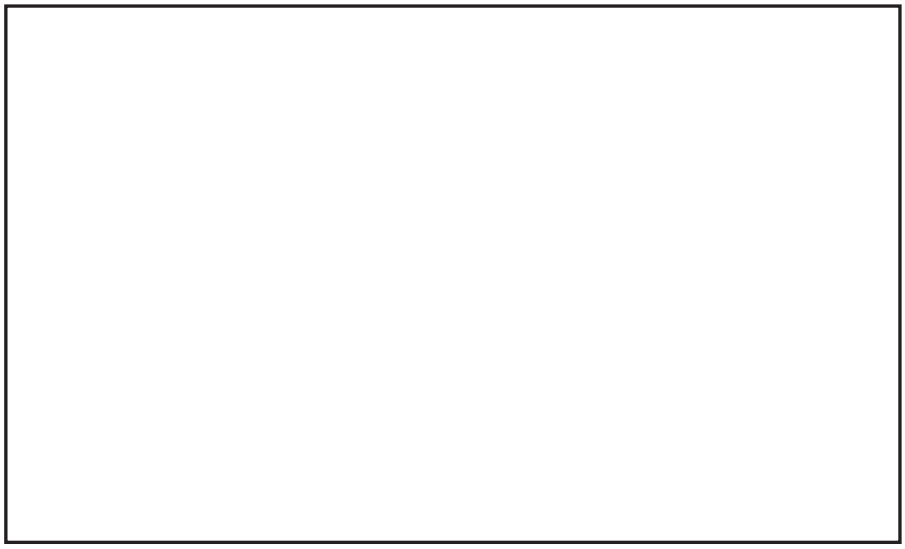

Figure 11. Silanol surface density vs. the dehydroxylation temperature, reproduced from ref[58]

Infra-red spectroscopy is the tool of choice to study silica surface composition, spectra of silica dehydroxylated at 200 and 700°C ($SiO_{2\text{-}200}$ and $SiO_{2\text{-}700}$) are presented in Figure 12. $SiO_{2\text{-}200}$ presents one sharp peak at 3747 cm^{-1} attributed to isolated silanols whereas the large absorption band centered around 3600 cm^{-1} was attributed to silanols in interaction which each other, i.e. vicinal and geminal silanols. On $SiO_{2\text{-}700}$ only isolated silanols are present as witnessed by the sharp peak at 3747 cm^{-1}. The three absorption bands at 1980, 1866 and 1633 cm^{-1} were attributed to deformation vibration of siloxane bridges. From its relative simplicity and well-defined surface chemistry, silica is a support particularly suitable to understand surface organometallic chemistry at a molecular level.

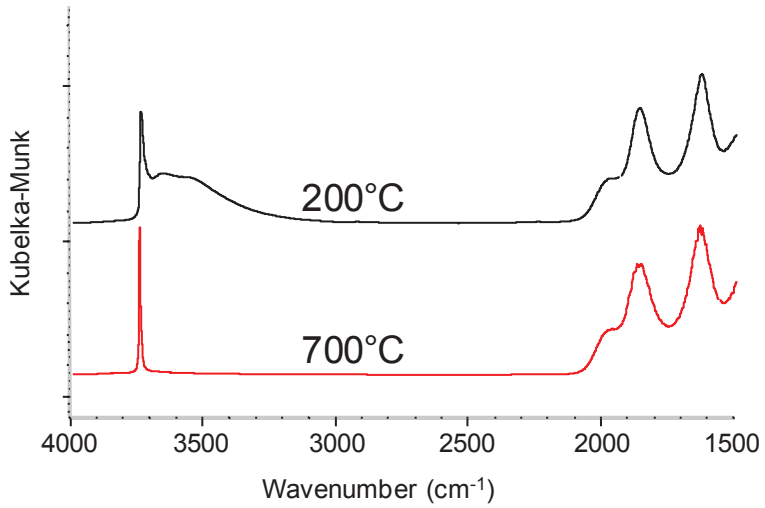

Figure 12. DRIFT spectra of silica dehydroxylated at 200 and 700°C

1.3.2.2.2. Cerium oxide

Cerium oxide, also called ceria, has a long history of academic research and industrial applications as it is a key component of three-way catalyst for car exhaust depollution as previously discussed. We are interested in developing SOMC onto this substrate for the design of Diesel Oxidation Catalysts. It has a general formula of CeO_2 and present a fluorite-like (CaF_2) cubic structure in which each cerium site, in a face-centered cubic (fcc) arrangement, is surrounded by eight oxygen atoms.

We will here mainly focus on the surface composition of ceria as it is of major interest in order to further develop surface organometallic chemistry onto this oxide. The surface chemistry of ceria has been studied notably by the group of Jean-Claude Lavalley in the ninety's. IR spectroscopy is the tool of choice to study the surface composition of ceria. Three types of surface OH have been characterized, mono-coordinated μ^1-OH (3710 cm^{-1}), doubly bridging μ^2-OH of two types (μ^2-A 3650 and μ^2-B 3634 cm^{-1} - Figure 14) and triply bridging μ^3-OH (3500 cm^{-1}).[59] The IR spectra of ceria calcined at 400°C and further reduced with H_2 at various temperature is presented Figure 13. The reduction of ceria by H_2 was limited to nonexistent at 200°C whereas at 400°C the reduction was emphasized by a strong modification of the surface OH composition. Only μ^2-OH remained, of both A and B types. Those two OH comes from the oxidation state of the ceria atom as depicted in Figure 14. The reduction by H_2 is concomitant to the formation of water.[60] Here spectra are recorded after evacuation at the same reduction temperature, and therefore water wass removed. The large band at 3450 cm^{-1} was thus attributed to the formation of surface hydroxyl groups resulting from the dissociation of H_2. Ceria presents more IR bands bellow 1600 cm^{-1} attributed to carbonate species.[61,62]

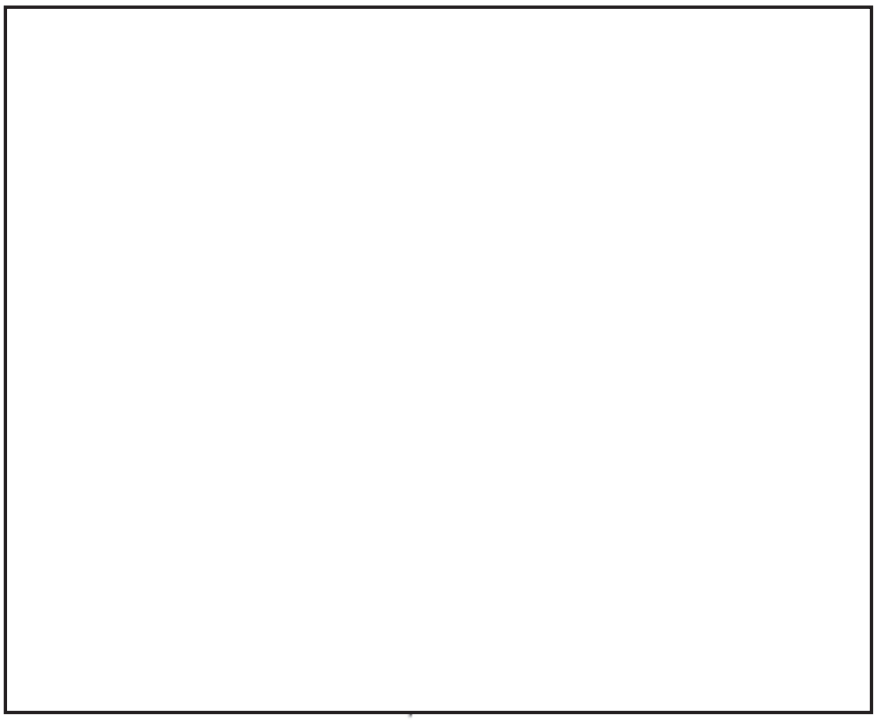

Figure 13. IR spectra of a ceria pellet 1) calcined under dry air at 400°C, 2) reduced by H_2 at 200°C, 3) at 400°C, reproduced from ref[59].

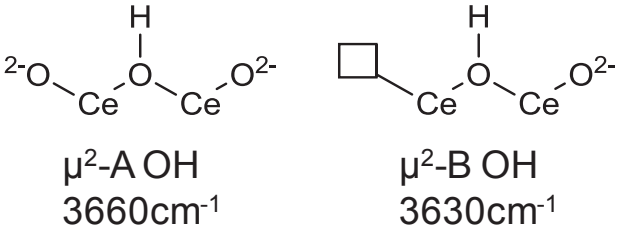

Figure 14. The two types of μ^2-OH onto ceria

The formation and modification of the surface OH species onto ceria has been widely studied but to our knowledge no effort have been done towards the rational control and the fine tuning of the surface OH composition. Moreover, to our knowledge, no surface organometallic chemistry onto ceria has been reported so far.

1.3.2.3. Nanoparticles synthesis

Ermakov *et al.*[63] proposed in the seventies to control the growth of nanoparticles through the careful decomposition of grafted surface species prepared via Surface Organometallic Chemistry (SOMC). This approach has been recently used by several groups working on the mechanism and the kinetic of formation of Ir nanoparticles supported on γ-Al_2O_3[64] or the controlled formation of silica-supported Ru,[65] Pd[66] and Pt[67,68] nanoparticles. In the case of

Rh,[65] the reaction of $Rh(\eta^3\text{-}C_3H_5)_3$ with silica, alumina and titania yielded $(\equiv EO)(\equiv EOE\equiv)Rh(\eta^3\text{-}C_3H_5)_2$ (E = Si, Al, Ti) along with the release of one mole of propylene (Figure 15). Then, reaction of $(\equiv EO)(\equiv EOE\equiv)Rh(\eta^3\text{-}C_3H_5)_2$ (E = Si, Al, Ti) surface species with H_2 led to metal particles. The mean sizes of the particles obtained are 1.5 nm on SiO_2 and TiO_2 supports, and 1.0 nm on Al_2O_3, which suggests that the oxide support plays a significant role on the final nanoparticle size.

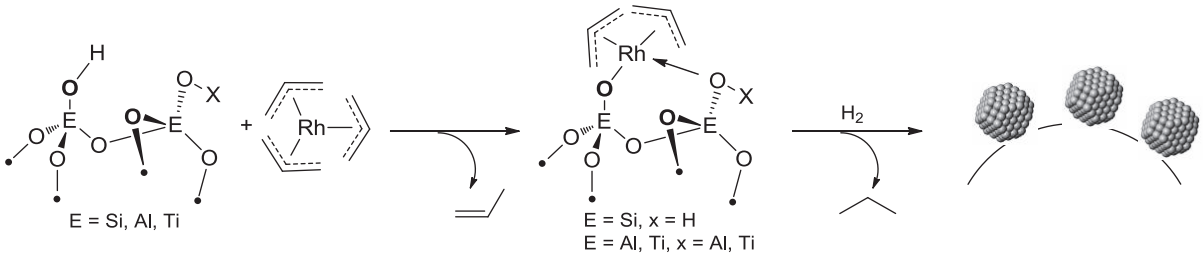

Figure 15. Grafting of Rh onto oxide supports and nanoparticles formation under H_2

Moreover, our group has shown that controlling the size and the interface of gold nanoparticles on the silica support via SOMC required the use of specific molecular precursor with the right ligands.[69] For instance, the reaction of an Au(I) bis(trimethylsilyl)-amido complex on silica partially dehydroxylated at 700 °C allowed to obtain a Au density of 0.5 $Au^I.nm^{-2}$ coordinated to $(Me_3Si)_xNH_{2-x}$ and surrounded by trimethylsilyloxy surface species (Figure 16). This was crucial to generate 1.8 nm sized supported gold nanoparticles upon subsequent treatment under H_2 at 300 °C; such particles supported on passivated silica showed improved performances in PROX and liquid phase aerobic epoxidation of stilbene.

SOMC is thus a valuable tool for the synthesis of well-dispersed nanoparticles onto various supports but suffers from a lack of understanding of the parameters influencing the nanoparticle final size.

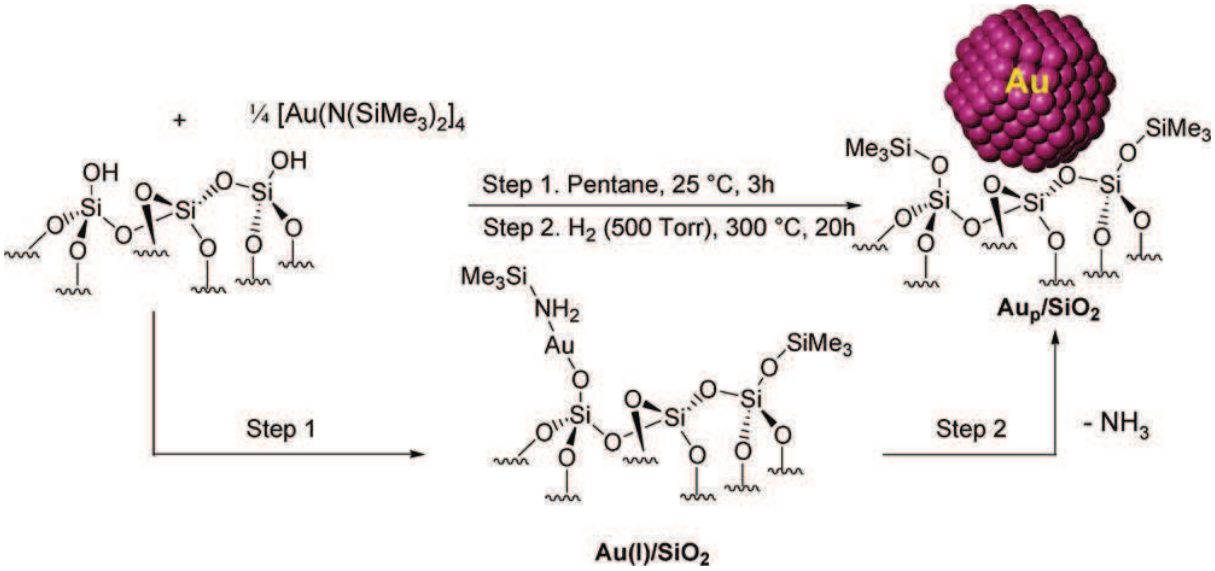

Figure 16. Schematic representation of the grafting of gold I onto $SiO_{2\text{-}700}$ and the subsequent formation of nanoparticles under H2 at 300°C. Reproduced from ref.[69]

1.4. Colloidal route to the synthesis of nanoparticles

Besides synthesizing supported nanoparticles, a large research effort has been devoted to the synthesis of colloidal suspensions of nanoparticles. The main advantage here is the synthesis of nanoparticles with narrow size dispersion, a fine control of the shape/size and of the chemical composition.

The synthesis of colloidal nanoparticles demands three components, i) a metallic precursor that can either be metal salts or organometallic complexes, ii) a reductant such as an alcohol, $NaBH_4$ or H_2 and iii) a stabilizing agent such as polymers or dendrimers. Note that the solvent can be of importance, for example in the case of ionic liquid where it can act as a stabilizing agent.[70]

Chaudret *et al.* have devoted their effort to the synthesis of colloidal nanoparticles from organometallic precursors,[71,72] they demonstrated the efficient nanoparticles synthesis under mild conditions. Ru(COD)(COT) (1,5-cyclooctadiene, and 1,3,5-cyclooctatriene) was used for the synthesis of Ru nanoparticles stabilized by alkylamines or polyvinylpyrrolidone (PVP)[73] and more recently by N-heterocyclic carbenes (NHC).[74] Those reactions were carried at room temperature in THF or pentane under 1-3 bars of H_2 and led to the synthesis of stable monodispersed nanoparticles from 1 to 3 nm in diameter. The synthesis of platinum and palladium nanoparticles were studied too from $M(dba)_2$ (dba = dibenzylideneacetone) complexes. Pd and Pt nanoparticles were stabilized by PVP[75] or nitrocellulose[76] and synthesized by reduction under H_2. Those systems present the advantage of having stabilizing

ligands weakly bonded to the nanoparticles allowing a full access to the surface for catalytic applications. Moreover bimetallic nanoparticles for example of Pd-Cu,[77] Pt-Ru[78] have been synthesized using similar procedures.

Sun *et al.* described the synthesis of Pt[79] and Pd[80] nanoparticles stabilized by oleylamine from $M(acac)_2$ complexes (acac = acetylacetone) using borane tributylamine as reductant. Oleylamine, as stabilizing agent, presents the advantage of being easily washed out under acidic conditions after supporting nanoparticles and was moreover used as the solvent for the synthesis. The drawback of this method is its relative complexity as the temperature has a strong effect on the final nanoparticles size. Very recently, they describe the synthesis of Pt/Pd bimetallic nanoparticles using similar procedures.[23] Nanoparticles from 3.5 to 6 nm, depending on the final reduction temperature, were synthesized. The initial introduced Pt/Pd ratio proved to drive the final Pt/Pd ratio found into single nanoparticles. These nanoparticles demonstrated enhancement in the Methanol Oxydation Reaction for Direct Methanol Fuel Cells and composition dependent catalytic properties.

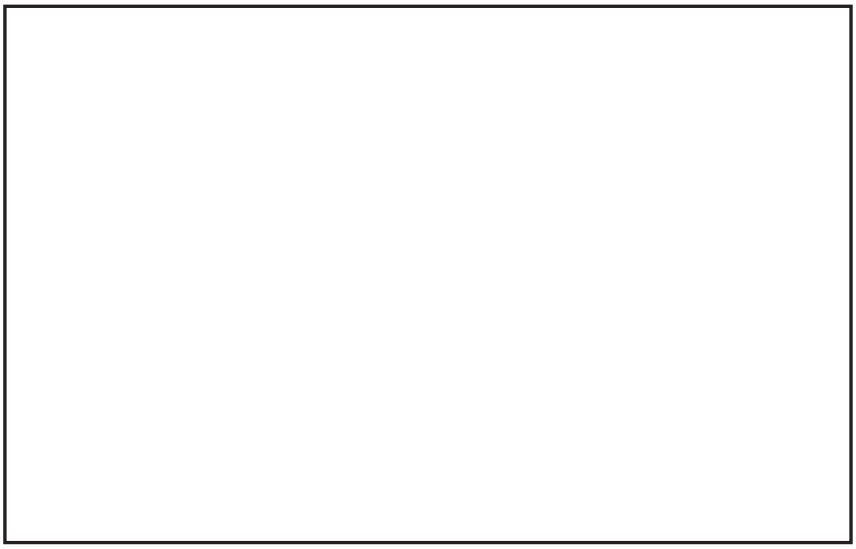

Figure 17. a)TEM image of the 5 nm$Pd_{67}Pt_{33}$ NPs, b) High resolution HAADF-STEM image (left) and bright field image (right) of a single $Pd_{67}Pt_{33}$ NP, c) HAADF-STEM image and the corresponding elemental map of several representative 5 nm $Pd_{67}Pt_{33}$ NPs, d) Correlation between the amount of Pt(acac)2 added and the amount of Pt obtained in the final PdPt NP product. Reproduced from ref.[23]

Recently in our group, we demonstrated the efficient synthesis of nanoparticles stabilized by covalently bound ligands. Ru[81,82] (Figure 18) nanoparticles have been synthesized in THF at room temperature under 3 bars of H_2 using n-octylsilane ($C_8H_{17}SiH_3$) as the stabilizing agent. This strategy was successfully implemented to Au[83] and Pt for the synthesis of hydrophobic[84] (stabilized by n-octylsilane) or hydrophilic[85] nanoparticles (stabilized by 3-chloropropylilane). Both systems led to 1.8 ± 0.4 nm well dispersed nanoparticles. This modification of the

surface chemistry led either to the integration of the nanoparticles in the walls or in the pores of a mesoporous silica matrix synthesized by sol-gel chemistry. Note that other stabilizing agents can be used such as tributyltin hydride ($(n\text{-}Bu)_3SnH$) leading to the formation of stable Pt_3Sn nanoparticles.[86]

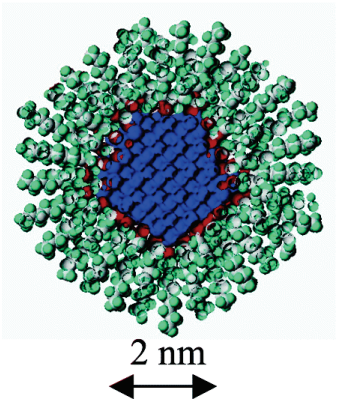

Figure 18. Ru nanoparticles stabilized by n-octylsilane, reproduced from ref[81]

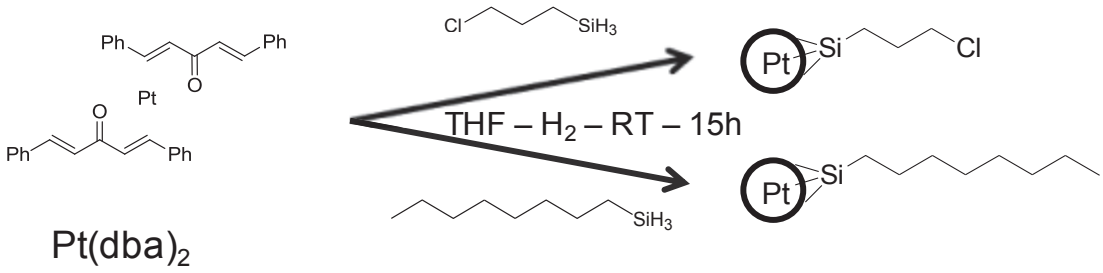

Figure 19. Hydrophilic and hydrophobic Pt nanoparticles syntheses

Finally, the use of a reductant can be avoided, several systems are able to act as both stabilizer and reductant, for example oleylamine has found to be able to both reduce and stabilize gold nanoparticles[87] or magnetite (Fe_3O_4) nanoparticles[88] thus acting as a bi-functional stabilizer. For Pt and Pd nanoparticles, different systems are able to both react as a reductant agent and stabilizer, for exemple Coccia *et al.* used lignin and fulvic acid under thermal decomposition conditions (80°C) but this process yielded poorly stabilized nanoparticles of about 20 nm and with irregular shape. To our knowledge, few have been reported on the preparation of Pt or Pd nanoparticles under mild conditions using a bi-functional molecules acting as reductant and stabilizer.

Figure 20. Synthesis of Fe_3O_4 nanoparticles (7 to 10 nm) using oleylamine as both reductant and stabilizer

1.5. Research project

The synthesis of Pt and Pd based nanoparticles for catalysis can be done *via in-situ* and *ex-situ* methodologies. While *in-situ* methods such as dry impregnation are widely used, those methods demonstrated a lack of control of the nanoparticles size and shape. On another hand, *ex-situ* syntheses, as the colloidal approach, lead to well dispersed nanoparticles with a narrow size distribution and demonstrate a good control over both size and shape. The first question was thus: can we control the synthesis of supported Pt nanoparticles the way the colloidal approach does this? In the meantime, the goal of this project in partnership between the CEA Grenoble and the CNRS, was to explore different routes to the synthesis of nanoparticles with a stress on the industrial viability of the methods developed.

This work has therefore been divided into three main chapters:

In chapter 2, we investigate the synthesis of new Pt complexes and their grafting onto silica and ceria leading to well-defined Pt^{II} surface species. The further treatment, under H_2 at 300°C yielding nanoparticles, is described and the influence of the support and the Pt complex chemistry on the final nanoparticles size is discussed.

In chapter 3, we describe the preparation and characterization of Pt nanoparticles through the use of $(COD)Pt(OSi(O\textit{t}Bu)_3)_2$ as a precursor for Metal Organic Chemical Vapor Deposition and the further catalytic properties of such nanoparticles for the Oxygen Reduction Reaction.

In chapter 4, we focus on the preparation of colloidal dispersion of Pt and Pd nanoparticles using octylsilane acting as both the reducing agent and the stabilizer. The effect of the precursor chemistry is discussed for the synthesis of Pt nanoparticles. The further implementation of this methodology towards the synthesis of Pt/Pd bimetallic nanoparticles with various compositions is presented. The catalytic properties of those nanoparticles are again tested for the Oxygen Reduction Reaction.

In chapter 5, we conclude on this thesis work and briefly discuss the perspectives.

2. From well-defined Pt^{II} surface species to the controlled growth of oxide supported Pt nanoparticles

2.1. Introduction

Following work done in our group on gold nanoparticles supported onto silica[69] (as discussed in bibliography) we wanted to tune the structure of the grated precursor in order to control the final nanoparticles sizes and in view of generating Diesel Oxydation Catalysts (DOC). We thus decided to explore the formation of platinum nanoparticles through surface organometallic chemistry by grafting various species onto silica, used as a model surface, and ceria, of more interest as a support for DOC. The synthesis of new Pt complexes will be described followed by the grafting onto silica and finally ceria.

2.2. Synthesis and characterization of Pt^{II} complexes

Symmetrical and dissymmetrical molecular complexes of general formula (COD)Pt(X)(Y) were first prepared and characterized prior to investigate grafting. While the synthesis of the molecular complexes with (X = Y = Cl)[89], (X = Y = Me)[90], (X = Me Y = Cl)[91], (X = Y = $OSi(O\textit{t}Bu)_3$)[92] and (X = Cl, Y = $N(SiMe_3)_2$)[93] were reported, the following Pt^{II} organometallic complexes with complementary ligands sets were developed: (X = CH_3, Y = $OSi(O\textit{t}Bu)_3$), (X = CH_3, Y = $N(Si(Me_3)_2)$ and (X = $OSi(O\textit{t}Bu)_3$, Y = $N(Si(Me_3)_2)$. Note however that the bis-amido complex (X = Y = $N(Si(Me_3)_2)$ as well as (COD)Pt(Cl)($OSi(O\textit{t}Bu)_3$) could not be prepared so far.

Suitable crystals for single-crystal X-Ray diffraction were obtained for (COD)Pt(Me)($OSi(O\textit{t}Bu)_3$) and (COD)Pt($N(SiMe_3)_2$)($OSi(O\textit{t}Bu)_3$); selected bond distances are given in Table 1 and crystallographic data are available in Appendix 1. They both display the expected square planar geometry for Pt^{II} d^8 molecular complexes (Figure 21). Comparing the two complexes, a shorter Pt-(C=C) distance (2.185 versus 2.268 Å) and a longer C=C bond length are observed for the alkene moiety *trans* to the amido vs. the methyl ligand (1.386 vs. 1.346 Å). This illustrates the greater π-back donation in the amido complex, and it is consistent with the weaker σ-donating and the greater π-donating ability of this ligand compared to methyl. The Pt-(OSi) bond lengths are 1.987 and 1.998 Å for the amido and the methyl complexes respectively; they are slightly longer than that observed in the bis-siloxy complex (1.982 Å)[92] and increases as the complementary ligands become more σ-donating ($OSi(O\textit{t}Bu)_3$ < $N(SiMe_3)_2$ < Me). Table 2 summarizes the characteristic signals in proton and carbon-13 NMR data (chemical shift and J_{P-X} coupling) of all prepared molecular complexes

(COD)Pt(X)(Y). As reported previously, chemical shifts and coupling constants of the olefinic protons of the COD ligand with $^{195}Pt^{94}$ are characteristic spectroscopic signatures for such type of complexes, providing precious information about the nature of the X and Y ligands attached to Pt (σ- and π-donation); these data will be particularly useful to assign the structure of surface species (vide infra).

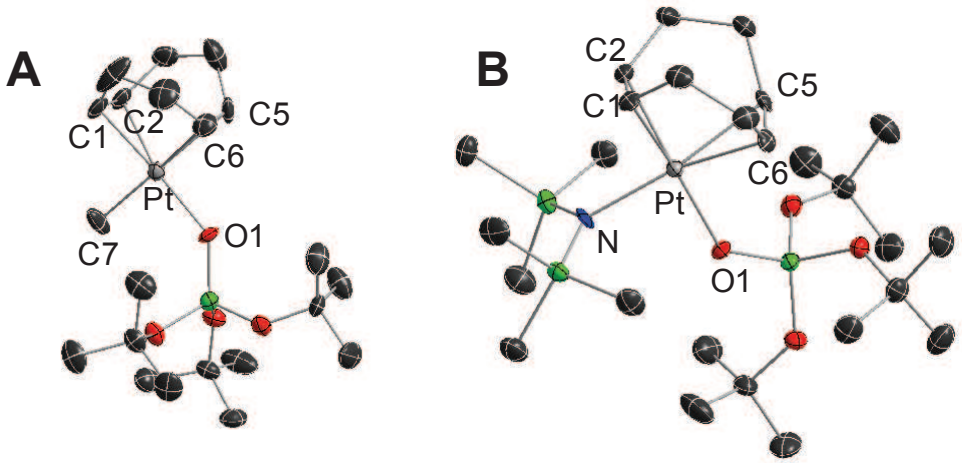

Figure 21. ORTEP drawing of compound A) (COD)Pt(Me)(OSi(O*t*Bu)$_3$) and (COD)Pt(OSi(O*t*Bu)$_3$)(N(SiMe$_3$)). H atoms are omitted for clarity.

Table 1. Selected bond lengths and angles for (COD)Pt(X)(Y) compounds. [a]: this work.

X	Y	Pt-(C=C$^{trans\ X}$)	Pt-(C=C$^{trans\ Y}$)	Pt1-X	Pt1-Y	C=C$^{trans\ X}$	C=C$^{trans\ Y}$	Ref.
Cl	Cl	2.164	2.177	2.315	2.309	1.376	1.388	[89]
Me	Cl	2.280	2.14	2.085	2.316	1.347	1.383	[91]
Me	Me	2.234	2.229	2.068	2.056	1.374	1.374	[90]
OSi(O*t*Bu)$_3$	OSi(O*t*Bu)$_3$	2.129	2.129	1.982	1.982	1.331	1.331	[92]
Me	OSi(O*t*Bu)$_3$	2.268	2.11	2.042	1.987	1.346	1.413	[a]
Cl	N(SiMe$_3$)$_2$	2.156	2.201	2.322	2.045	1.383	1.361	[a]
OSi(O*t*Bu)$_3$	N(SiMe$_3$)$_2$	2.131	2.185	1.998	2.054	1.390	1.386	[a]

Table 2. NMR data of platinum compounds (COD)Pt(X)(Y) in C_6D_6, Pt-H coupling constants are given into brackets. δ HXC= is the chemical shift of the olefinic proton of the COD trans to the X ligand.

		^{1}H			^{13}C		
X	Y	δ H^XC=	δ H^YC=	δ Pt-CH_3	δ ^{X}C=	δ ^{Y}C=	δ Pt-CH_3
Cl	Cl	4.98 (66)	4.98 (66)	-	98.8 (152)	98.8 (152)	-
Me	Cl	5.35 (33)	3.75 (72)	1.23 (75)	113 (30)	82.5 (211)	6.0 (623)
Me	Me	4.56 (39)	4.56 (39)	1.26 (84)	98.3 (56)	98,3 (56)	6.0 (785)
OSi(O*t*Bu)$_3$	OSi(O*t*Bu)$_3$	5.71 (63)	5.71 (63)	-	89.6 (178)	89.6	-
Me	OSi(O*t*Bu)$_3$	5.9 (30)	3.57 (66)	1.16 (75)	113.3 (27)	73.4 (227)	6.9 (700)
Me	N(SiMe$_3$)$_2$	5.18 (30)	3.79 (60)	1.05 (81)	111.6 (29)	84 (161)	5.8 (727)
Cl	N(SiMe$_3$)$_2$	4.68 (69)	5.00 (53)	-	94.8 (107)	101 (182)	-
OSi(O*t*Bu)$_3$	N(SiMe$_3$)$_2$	4.55 (66)	6.01 (51)	-	84.3 (198)	100.8 (86)	-

2.3. Grafting onto silica

2.3.1. Symmetrical complexes

We first compared the reactivity of symmetrical Pt^{II} complexes (COD)Pt(X)(Y) with X = Y = OSi(OtBu)$_3$ or Me using SiO_{2-200} as support. The reactivity of (COD)Pt(Cl)$_2$ could not be evaluated in view of its poor solubility in most solvents. In the case of (COD)Pt(Me)$_2$, while the formation of CH_4 clearly indicate an grafting reaction, only a partial consumption of surface isolated silanols of SiO_{2-200} was observed as evidenced by the presence of residual isolated silanols (ν(OH) = 3747 cm^{-1}) according to IR-DRIFT spectroscopy. This is accompanied with the concomitant appearance of the characteristic bands associated with the COD and methyl groups, albeit in a very low intensity (Figure S1 – Figure SX referred to figures available in the appendix section). This indicates a partial grafting of the Pt complex, and in fact the Pt content was only 3.0 wt% (0.16 mmol of Pt.g^{-1} or 0.5 Pt.nm^{-2}), which correspond to a grafting on ca. 18% of the surface silanols, referred thereafter as grafting yield. The carbon-13 cross-polarization (CP) NMR spectrum (Figure S2) of (COD)Pt(Me)$_2$@SiO_{2-200} under magic angle spinning (MAS) exhibits peaks at 118, 78, 32, 29 ppm and 6 ppm. The first two signals at low fields correspond to the alkene moiety of the coordinated COD, respectively trans to a Me and to a siloxy group, clearly indicating the formation of (COD)Pt(Me)(OSi≡) (Figure 22) by comparison with (COD)Pt(Me)(OSi(OtBu)$_3$ (Table 1) and as recently disclosed as we were preparing this manuscript.[95] The peaks at 32 and 29 ppm are also consistent with the proposed structure as the two aliphatic carbon atoms of the COD ligand are no longer equivalent. Finally, the peak at 6 ppm is also a characteristic

of the methyl ligand attached to Pt. On $SiO_{2\text{-}700}$, similar results are obtained, albeit with a lower Pt loading (1.1 %wt, 0.06 mmol of $Pt.g^{-1}$ or 0.2 $Pt.nm^{-2}$), but similar grafting yield (21 %).

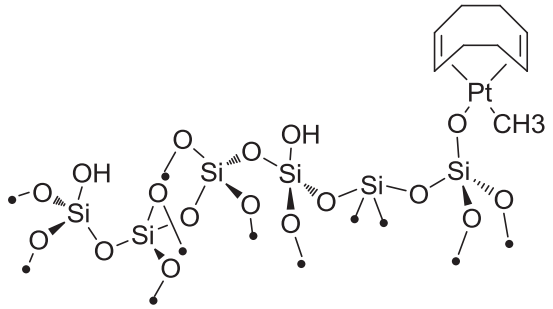

Figure 22. Surface Pt^{II} species after grafting $(COD)Pt(Me)_2$

While the grafting of $(COD)Pt(OSi(OtBu)_3)_2$ was already reported on ordered mesoporous silica (SBA type) materials,[92] here we discuss the grafting on non-porous silica partially dehydroxylated at 200°C and 700°C. IR-DRIFT spectroscopy (Figure S4) shows that the characteristic ν(OH) silanols vibration (3747 cm^{-1}) disappeared whereas characteristic bands – ν(C-H) – corresponding to the COD ligand and the *t*Bu appeared. Again stronger signals are found on $SiO_{2\text{-}200}$ than on $SiO_{2\text{-}700}$ in good correlation with the higher Pt loading, 3.9 wt.% (0.6 $Pt.nm^{-2}$, grafting yield = 23 %) versus 2.3 wt% (0.3 $Pt.nm^{-2}$, grafting yield = 44 %), respectively. Note also two additional broad ν(OH) peaks at 3700 cm^{-1} (weak) and 3360 cm^{-1} (intense), which are attributed to surface SiOH interacting with adjacent ligands and adsorbed $(tBuO)_3SiOH$ -ν(O-H), respectively. The structure of the surface species was further assessed by carbon-13 CP-MAS solid-state NMR (Figure S5). The olefinic carbon atoms of COD appear as a broad signal at 93 ppm, which is close to that observed in the starting molecular complex (89.6 ppm). The slight downfield shift effect induced by the exchange of $(tBuO)_3SiO$- by a surface siloxy ligand would indicate that the surface siloxy are somewhat less σ-donating. Moreover, signals at 72 and 30 ppm are observed and associated with the quaternary carbon and the methyl group of the $(tBuO)_3SiO$- ligand; the signal at 28 ppm corresponds to the nearly equivalent **C**H_2 of the COD ligand. The surface species can thus be depicted as $(COD)Pt(OSi(OtBu)_3(OSiO\equiv)$.

2.3.2. Dissymmetrical complexes

In view of the low reactivity of the Pt-Me bond compared to the Pt-OSi bond towards protonolysis by surface silanols, we decided to investigate the grafting of dissymmetrical systems having a methyl and a more labile ligand (i.e. siloxy group) in order to hopefully generate higher grafting yield of Pt-Me surface species. We also investigated the corresponding bis(trimethylsilyl)amido and chloro complexes, namely (COD)Pt(Me)($N(SiMe_3)_2$, (COD)Pt(Me)(Cl), as well as (COD)Pt(Cl)($N(SiMe_3)_2$).

2.3.2.1. (COD)Pt(Me)($OSi(OtBu)_3$)

The reaction of (COD)Pt(Me)($OSi(O*t*Bu)_3$) on SiO_{2-200} is evidenced by the disappearance of the IR peak at 3747 cm^{-1} corresponding to isolated silanols (Figure S8). Note the presence of broad absorption bands centered around 3640 and 3413 cm^{-1}, corresponding to bonded silanol and adsorbed $HOSi(O*t*Bu)_3$, respectively. This is also accompanied with the appearance of ν(C-H) absorption bands associated with perhydrocarbyl ligands. The Pt loading is 6.8 wt% on SiO_{2-200} (0.35 mmol.g-1 or 1 $Pt.nm^{-2}$, grafting yield = 40 %). Grafting also leads to the formation of 0.34 mmol of $HOSiO(*t*Bu)_3$ per g of silica, which is close to 1 equiv. per grafted Pt. Note the absence of CH_4 formation upon grafting. In fact, carbon-13 CP-MAS NMR (Figure S9) shows peaks at 115 and 73 ppm for the olefinic carbons of the COD ligand, those peaks are respectively attributed to the olefinic carbons of the COD ligand in *trans* to the methyl ligand and to the surface siloxy. In addition, the peak at 27 ppm corresponds to the $\mathbf{C}H_2$ of the COD, and the one at 30 ppm is attributed to absorbed $HOSi(OC(\mathbf{C}H_3)_3)_3$ on the silica surface as demonstrated by a blank experiment (Appendix 8). Comparison with the carbon-13 CP-MAS NMR of (COD)$Pt(Me)_2$@SiO_{2-200} demonstrates the presence of very similar chemical shifts (118-78 ppm for the olefinic carbons of COD and 6 ppm for the methyl ligand). In addition, the similarity of the spectrum with the molecular equivalent (COD)Pt(Me)($OSi(O*t*Bu)_3$) (113.3-73.4 and 6.9 ppm) clearly shows that the structure of the surface complex is (COD)Pt(Me)(SiO≡). For SiO_{2-700}, similar data are obtained; the only difference is the lower loading 4.1 wt% (0.20 mmol of $Pt.g^{-1}$ or 0.6 $Pt.nm^{-2}$) and the higher efficiency of grafting yield (79 %).

2.3.2.2. (COD)Pt(Me)(Cl)

In contrast, grafting of (COD)Pt(Me)(Cl) shows no consumption of the surface silanols and no appearance of typical ν(C-H) absorption bands related to COD or the methyl ligand by IR-DRIFT. Thus this molecular precursor is clearly unreactive towards surface silanols.

2.3.2.3. (COD)Pt(Me)(N(SiMe$_3$)$_2$)

For (COD)Pt(Me)(N(SiMe$_3$)$_2$), the reaction with $SiO_{2\text{-}200}$ is evidenced by the disappearance of the absorption peak at 3747 cm^{-1} corresponding to isolated silanols (Figure S12). The large absorption band centered around 3640 cm^{-1} corresponding to bonded silanols is still present, but in much lower intensity thus showing that bonded OH are also involved in the grafting process. The characteristics ν(C-H) absorption bands from COD (3013 cm^{-1}), Me (2927-2845 cm^{-1}) and $SiMe_3$ (2952-2890 cm^{-1}) also appeared. High loading, which was implied by the removal of a large number of OH groups, is confirmed by elemental analysis, with 7.4 wt% Pt found (0.38 mmol of Pt.g^{-1} or 1.1 Pt.nm^{-2}, grafting yield = 44%). The carbon-13 CP-MAS NMR spectrum (Figure S13) of this solid exhibits peaks at 114, 72, 28, 5 and 0 ppm. The peak at 0 ppm can be assigned to $OSiMe_3$, which results from the reaction of surface silanol groups with liberated $(Me_3Si)_{3-x}NH_x$.[69,96] Moreover, the peaks corresponding to the olefinic carbons of the COD ligand at 114 ppm and 72 ppm are attributed to the carbon atoms *trans* to the methyl and the surface siloxy ligands, respectively. This clearly points to a mono-grafting of (COD)Pt(Me)(N(SiMe$_3$)$_2$) *via* the selective cleavage of the Pt-N bond. It is noteworthy that on $SiO_{2\text{-}700}$ an additional peak of weaker intensity at 100 ppm is observed, which would imply the formation of (COD)Pt(N(SiMe$_3$)$_2$)(OSi≡) as a minor species. In fact, 0.05 to 0.10 equiv. of methane per grafted platinum is detected in the gas phase upon grafting. Again on $SiO_{2\text{-}700}$ a lower loading is found, 3.8 wt% Pt (0.19 mmol of Pt.g^{-1} or 0.6 Pt.nm^{-2}), highlighting the efficient reactivity of the surface silanols with this complex as 72 % of initial SiOH have reacted versus 44% for $SiO_{2\text{-}200}$.

2.3.2.4. (COD)Pt(Cl)(N(SiMe$_3$)$_2$)

The reaction of (COD)Pt(Cl)(N(SiMe$_3$)$_2$) towards silica was also investigated. In this case, a total disappearance of the isolated silanols according to IR spectroscopy was noticed (Figure S15); this was accompanied by the appearance of the characteristic ν(C-H) of COD (3022 and 3008 cm^{-1}) and -$SiMe_3$ (2966 and 2934 cm^{-1}). This translates into 4.2 wt% Pt loading (0.21 mmol of Pt.g^{-1} or 0.6 Pt.nm^{-2}, grafting yield = 25 %). The carbon-13 CP-MAS solid-state-NMR spectrum (Figure S16) displays 4 peaks at 104, 94, 31 and 0 ppm. The appearance of the olefinic protons of the COD ligand at 94 and 104 ppm is consistent with (COD)Pt(Cl)(OSi≡). This is also corroborated by the peak at 0 ppm attributed to passivated surface (≡$SiOSiMe_3$). Similar observations are obtained on $SiO_{2\text{-}700}$: consumption of OH group upon grafting, a Pt loading of 3.1% (0.15 mmol of Pt.g^{-1} or 0.5 Pt.nm^{-2}, grafting yield = 59%) and a similar NMR spectrum.

2.3.2.5. (COD)Pt(OSi(OtBu)$_3$)(N(SiMe$_3$)$_2$)

Finally, the reaction of (COD)Pt(OSi(O*t*Bu)$_3$)(N(SiMe$_3$)$_2$) on SiO_{2-200} leads to a full consumption of isolated silanols as evidenced by the disappearance of the corresponding ν(OH) at 3747 cm^{-1}, while bonded silanols at 3640 cm^{-1} remained untouched (Figure S19). This is associated with the appearance of ν(C-H) of the three ligands. Note also, a broad absorption band centered around 3360 cm^{-1}, which is probably associated with the adsorption of NH functionalities or (*t*BuO)$_3$SiOH. This leads to a Pt loading of 4.8 wt% (0.25 mmol of Pt.g^{-1} or 0.7 Pt.nm^{-2}, grafting yield = 29 %). Here again, the carbon-13 CP-MAS NMR spectrum (Figure S20) is very informative: two peaks at 105 and 95 (broad) for the olefinic COD, the former clearly attributed to a COD *trans* to N(SiMe$_3$)$_2$, the latter being *trans* to the surface siloxy ligand. The two other peaks at 75 and 30 are typical of O*t*Bu ligand, this at 28 ppm corresponds to the aliphatic carbons of COD, while the peaks at 4.5 and 0 ppm can be respectively attributed to Pt-N(SiMe$_3$) and ≡SiOSiMe$_3$. Those data highlights the existence of two competing grafting modes whether involving the cleavage of the Pt-N or the Pt-O bond. On SiO_{2-700} similar data are obtained, the only differences are again the lower Pt loading of 3.7 wt% (0.18 mmol of Pt.g^{-1} or 0.6 Pt.nm^{-2}, grafting yield = 71%) and the presence of remaining isolated silanols interacting with adjacent ligands as evidenced by a peak at 3700 cm^{-1} in IR spectrum.

Overall, grafting occurs readily for most Pt^{II} complexes independently of the silica used (SiO_{2-200} and SiO_{2-700}, Figure 23-A and -B) at the exception of (COD)Pt(Me)$_2$ for which Pt loading is much lower, e.g. 1.1 and 3.0 wt% on SiO_{2-700} and SiO_{2-200}, respectively; (COD)Pt(Cl)(Me) being unreactive towards silanols in our hands. This confirms the poorer reactivity of Pt-C bonds towards surface silanols by comparison with Pt-O and Pt-N bonds (Table 3). The structures of surface species are readily assigned from the carbon-13 CP-MAS NMR spectra as the isotropic chemical shift of the olefinic moiety of the COD ligand display very specific chemical shifts as a function of its ligand in *trans* (Figure S25 and Table 4).

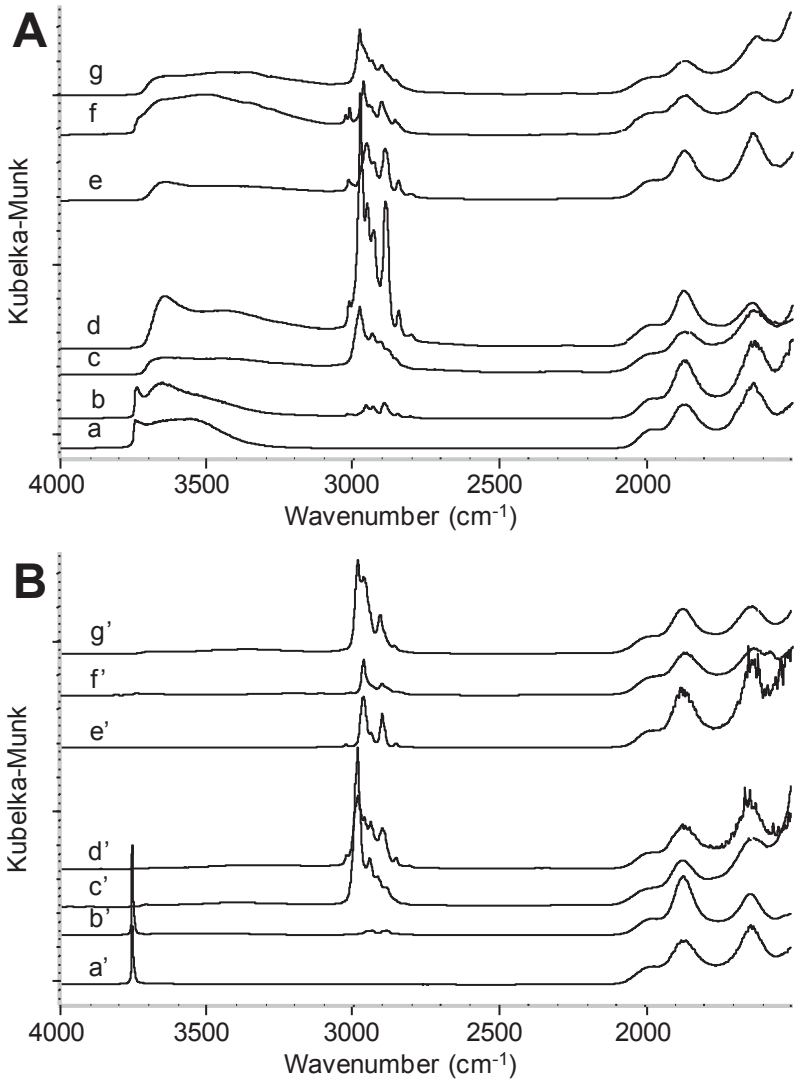

Figure 23. **A** IR-DRIFT spectra of a) $SiO_{2\text{-}200}$, b) $(COD)Pt(Me)_2@SiO_{2\text{-}200}$, c) $(COD)Pt(OSi(OtBu)_3)_2@SiO_{2\text{-}200}$, d) $(COD)Pt(Me)(OSi(OtBu)_3)@SiO_{2\text{-}200}$, e) $(COD)Pt(Me)(N(SiMe_3)_2)@SiO_{2\text{-}200}$, f) $(COD)Pt(Cl)(N(SiMe_3)_2@SiO_{2\text{-}200}$, g) $(COD)Pt(OSi(OtBu)_3)(N(SiMe_3)_2@SiO_{2\text{-}200}$

B a) IR-DRIFT spectra of a) $SiO_{2\text{-}700}$, b) $(COD)Pt(Me)_2@SiO_{2\text{-}700}$, c) $(COD)Pt(OSi(OtBu)_3)_2@SiO_{2\text{-}700}$, d) $(COD)Pt(Me)(OSi(OtBu)_3)@SiO_{2\text{-}700}$, e) $(COD)Pt(Me)(N(SiMe_3)_2)@SiO_{2\text{-}700}$, f) $(COD)Pt(Cl)(N(SiMe_3)_2@SiO_{2\text{-}700}$, g) $(COD)Pt(OSi(OtBu)_3)(N(SiMe_3)_2@SiO_{2\text{-}700}$

Table 3. The percentage of reacted silanols is calculated considering 0.86 mmol $OH.g^{-1}$ on SiO_{2-200} and 0.26 mmol $OH.g^{-1}$ on SiO_{2-700}.

	SiO_{2-200}			SiO_{2-700}		
	Pt (wt.%)	Pt/≡SiOH (A)	$Pt.nm^{-2}$	Pt (wt.%)	Pt/≡SiOH (B)	$Pt.nm^{-2}$
$(COD)Pt(Me)_2$	3,00%	18.1%	0.5	1.1%	21.3%	0.2
$(COD)Pt(OSi(OtBu)_3)_2$	3.9%	23.4%	0.6	2.3%	44.3%	0.3
$(COD)Pt(Me)(OSi(OtBu)_3)$	6.8%	40.3%	1,0	4.1%	78.6%	0.6
$(COD)Pt(Me)(N(SiMe_3)_2)$	7.4%	44.1%	1.1	3.8%	72.2%	0.6
$(COD)Pt(Cl)(N(SiMe_3)_2)$	4.2%	24.8%	0.6	3.1%	58.9%	0.5
$(COD)Pt(N(SiMe_3)_2)(OSi(OtBu)_3)$	4.8%	28.8%	0.7	3.7%	70.5%	0.6

Table 4. Carbon-13 solid-state NMR data for complexes grafted onto SiO_{2-200}

X	Y	$\delta\ ^{X}C=$	$\delta\ ^{Y}C=$	$\delta\ ^{\equiv OSi}C=$	δ Pt-CH_3
Me	Me	118	-	78	6
$OSi(OtBu)_3$	$OSi(OtBu)_3$	93	-	93	-
Me	$OSi(OtBu)_3$	115	-	73	5
Me	$N(SiMe_3)_2$	114	-	72	5
Cl	$N(SiMe_3)_2$	104	-	94	-
$OSi(OtBu)_3$	$N(SiMe_3)_2$	95	105	95	-

It is noteworthy that grafting on both SiO_{2-200} or SiO_{2-700} leads to mono-grafted complexes, which is in sharp contrast to what is observed for the grafting of earlier transition-metal complexes (up to group 6), for which lower dehydroxylation temperature favors bis-grafted systems and higher dehydroxylation temperature mono-grafted species.[44,97,98] Thus, the high OH density on SiO_{2-200} leads to a much higher Pt loading. Yet full loading (reaction of all surface silanols), which would lead to Pt loading of 17 wt.% (2.6 $Pt.nm^{-2}$) on SiO_{2-200} and 5wt.% (0.8 $Pt.nm^{-2}$) on SiO_{2-700}, respectively, have never been reached. The theoretical maximum coverage has been calculated for all (COD)Pt(X)(OSi≡) species based on the projected surface area of these complexes (Appendix 10). Note that for (COD)Pt(Me)(OSi≡) and (COD)Pt(Cl)(OSi≡) the maximum surface coverage is calculated to be respectively 2.6 and 2.8 $Pt.nm^{-2}$ assuming mono-grafting on all surface silanols on SiO_{2-200} (2.6 $OH.nm^{-2}$); grafting is thus limited by the reactivity of the molecular complexes or the complementary ligand (e.g. if passivation or adsorption occurs) and not by surface coverage. On the contrary, for the bis-siloxy complex and the amido-siloxy complex, the theoretical maximum surface coverage are between 1.0 and 1.3 $Pt.nm^{-2}$, thus no full consumption of surface silanols can be achieved and indeed on SiO_{2-200} lower Pt density are found (0.6 and 0.7 $Pt.nm^{-2}$). On SiO_{2-700}

the theoretical maximum surface coverage could be obtained but again lower values are found. While this would indicate the presence of residual silanols, they were in most cases not observed after grafting. This demonstrates the probable interaction of residual silanols with adjacent ligands, either attached to Pt or just present as adsorbed species, thus limiting their reactivity. For instance, $(t\text{BuO})_3\text{SiOH}$ interacts strongly with surface silanols as evidenced by the presence of broad bands at 3640 cm^{-1}, and $NH(SiMe_3)_2$ reacts with surface silanols to yield $\equiv SiOSiMe_3$ and ammonia (see Figure S24).

Overall, well-defined platinum (II) surface species have been effectively synthesized, by grafting on $SiO_{2\text{-}200}$ and $SiO_{2\text{-}700}$ and characterized at a molecular level. Complexes with O- or N-bound ligands ($OSi(O\textit{t}Bu)_3$ and $N(SiMe_3)_2$) have been proved to be more reactive towards protonolysis by surface silanols than C-bound ligands (Me); the O- and N-bound ligands have however similar reactivity.[99] This explains the selective grafting *via* cleavage of the M-X bond in dissymmetric complexes (COD)Pt(Me)(X) as well as the lower Pt loading upon grafting of $(COD)Pt(Me)_2$.

2.3.3. Nanoparticles formation

To generate nanoparticles, the Pt^{II} surface species were treated under H_2 either in static (150 mBar) or continuous flow conditions (1 bar, flow rate = 100 $mL.min^{-1}$) at 300°C for 15 h following a heating ramp of 5 $K.min^{-1}$. In all cases, this treatment induces a dramatic change in coloration from white to black in agreement with the formation of supported Pt particles (Figure 24). This is accompanied with the recovery of surface silanols in all cases as evidenced by the reappearance of the sharp band at 3747 cm^{-1} associated with isolated silanols in the IR spectrum (Figure 25-A). This is in line with the cleavage of Pt-O bond and the formation of Pt nanoparticles.

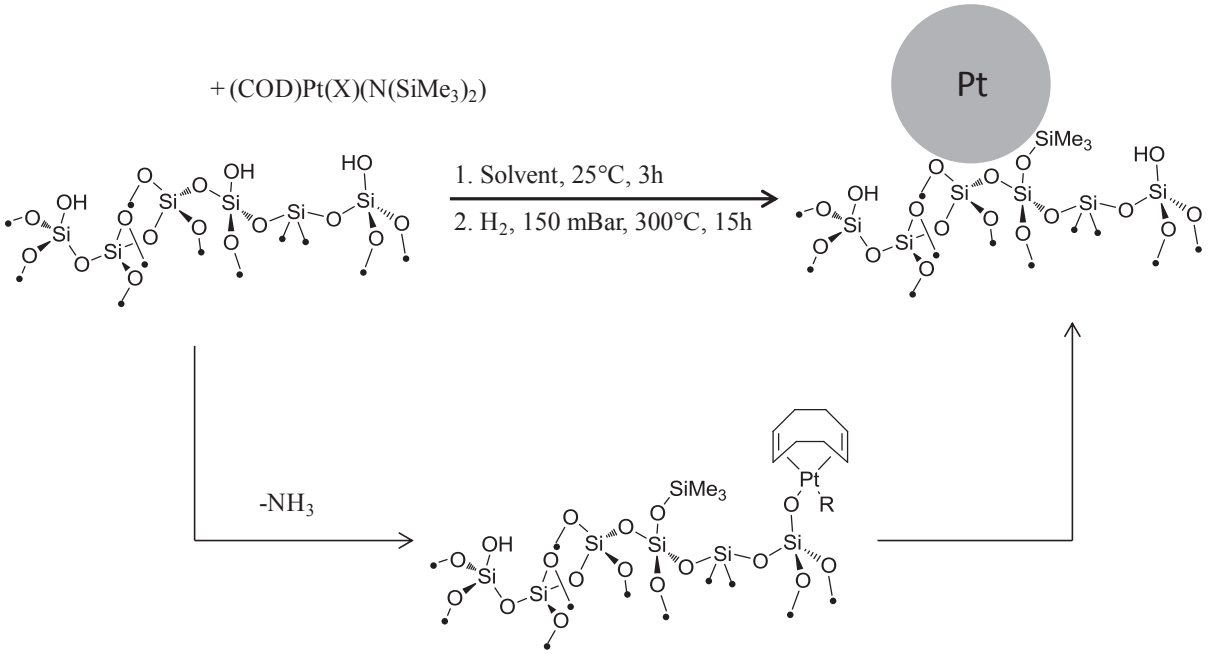

Figure 24. Schematic representation of the nanoparticles formation from (COD)Pt(X)($N(SiMe_3)_2$)@$SiO_{2\text{-}700}$

In the specific case of the supported bistrimethylsilyl amido complexes, two bands at 2965 and 2905 cm^{-1} are systematically found after calcination, which correspond to the asymmetric and symmetric stretching vibrations of "$OSi(CH_3)_3$" species. For tris(tert-butoxy)siloxy complexes, one main band is found at 2984 cm^{-1} corresponding to the asymmetric stretching of CH_3 along with three additional and less intense bands found at 2937, 2911 and 2878 cm^{-1} matching the absorption bands of the tBu fragments (Figure 25-B), $HOSi(OtBu)_3$ remains attached at the surface probably *via* a SiO bond as Si-O-Si(O*t*Bu)$_3$ surface species (Figure S23). Note that the other perhydrocarbyl ligands (COD and methyl) are efficiently eliminated yielding bare nanoparticles. Gas phase chromatography reveals indeed the formation of methane and alkanes from C_2 to C_4, which results from the catalytic hydrogenolysis of COD at the Pt surface.

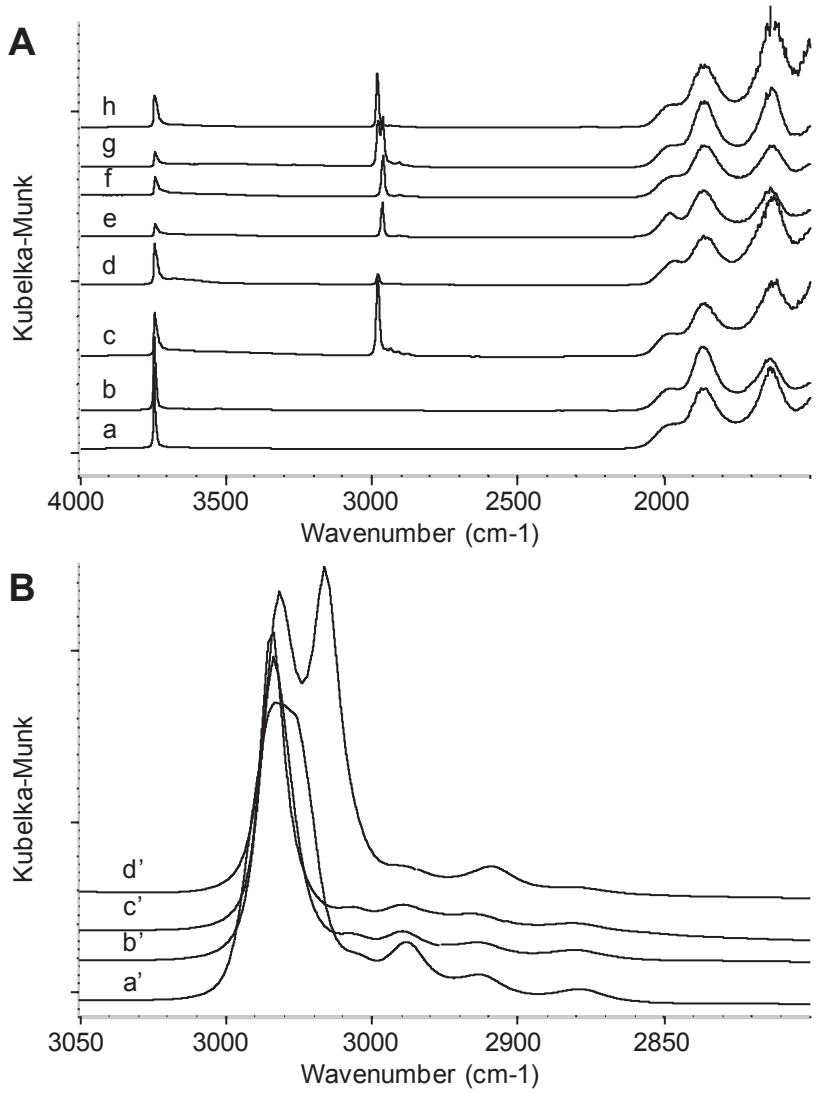

Figure 25-**A.** IR-DRIFT spectra of complexes grafted on $SiO_{2\text{-}700}$ and treated under static H_2 a) $SiO_{2\text{-}700,}$ b) $(COD)Pt(Me)_2$, c) $(COD)Pt(OSi(OtBu)_3)_2$, d) $(COD)Pt(Me)(OSi(OtBu)_3)$, e) $(COD)Pt(Me)(N(SiMe_3)_2)$, f) $(COD)Pt(Cl)(N(SiMe_3)_2)$, g) $(COD)Pt(OSi(OtBu)_3)(N(SiMe_3)_2)$ h) $HOSi(OtBu)_3$

B. a') $HOSi(OtBu)_3@SiO_{2\text{-}700}$, b') $(COD)Pt(OSi(OtBu)_3)_2@SiO_{2\text{-}700}$, c') $(COD)Pt(Me)(OSi(OtBu)_3)@SiO_{2\text{-}700}$, d') $(COD)Pt(OSi(OtBu)_3)(N(SiMe_3)_2)@SiO_{2\text{-}700}$

Transmission electron microscopy (TEM) was performed on all samples and always confirmed the presence of Pt nanoparticles. Mean size and standard deviation after static H_2 treatments are given in Table 5. A representative picture of the obtained nanoparticles is given in Figure 26; all transmission electron micrographs can be found in appendix 2-7.

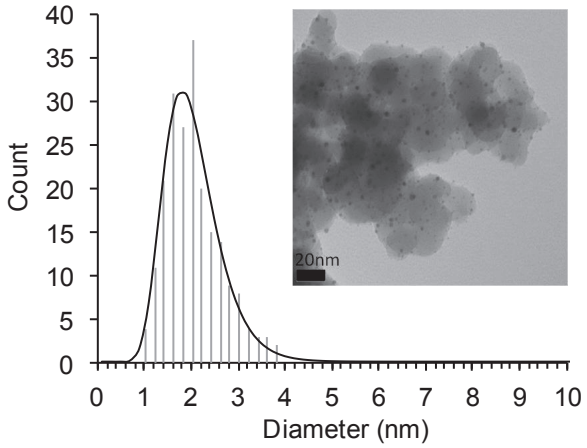

Figure 26 .TEM picture (COD)Pt(Me)(OSi(O*t*Bu)$_3$)@SiO$_{2\text{-}700}$ after H_2 static treatment

Table 5. Mean nanoparticles size, standard deviation and platinum loading.

	SiO$_{2\text{-}200}$			SiO$_{2\text{-}700}$		
	mean size (nm)	std. dev. (nm)	Pt wt.%	mean size (nm)	std. dev. (nm)	Pt wt.%
(COD)Pt(Me)$_2$	3.0	(0.7)	3.0%	2.4	(0.9)	1.1%
(COD)Pt(OSi(O*t*Bu)$_3$)$_2$	2.1	(0.9)	3.9%	2.0	(0.6)	2.3%
(COD)Pt(Me)(OSi(O*t*Bu)$_3$)	2.6	(1.2)	6.8%	2.0	(0.6)	4.1%
(COD)Pt(Me)(N(SiMe$_3$)$_2$)	3.3	(1.0)	7.4%	2,1	(0.9)	3.8%
(COD)Pt(Cl)(N(SiMe$_3$)$_2$)	5 to 40	-	4.2%	5 to 18	-	3.1%
CODPt(OSi(O*t*Bu)$_3$)(N(SiMe$_3$)$_2$)	3.2	(0.5)	5.0%	2.1	(0.6)	3.7%

We can first notice that most silica-supported nanoparticles synthesized from grafted Pt^{II} species display a relatively small size from 2.1 to 3.3 nm and narrow distribution, the standard deviation ranging from 0.6 to 1.2 nm depending on the precursor; the exception being found for the chlorinated Pt complex (nanoparticles size from 5 to 40 nm). When comparing the silica supports, nanoparticles are systematically found larger on SiO$_{2\text{-}200}$ than on SiO$_{2\text{-}700}$ by factors ranging from 9 to 36%, which is to be related to the higher density of metal and the OH coverage. Additionally, in contrast to what was observed for Au,[69] surface passivation does not lead to smaller nanoparticles: in fact silica supported (COD)Pt(Me)$_2$, (COD)Pt(Me)(OSi(O*t*Bu)$_3$) and CODPt(Me)(N(SiMe$_3$)$_2$), which presents the same surface species, albeit with different Pt density (respectively 0.2, 0.6 and 0.6 Pt.nm^{-2}) and SiMe$_3$ coverage, provide supported nanoparticles of similar sizes on SiO$_{2\text{-}700}$ i.e. 2.4, 2.0 and 3.0 nm, respectively. In fact, the most dramatic effect comes from the presence of a pendant Cl ligand.

For instance, while grafted (COD)Pt(Cl)($N(SiMe_3)_2$) associated with the surface species (COD)Pt(Cl)(OSi≡) yields large aggregates from 5 to 40 nm and 5 to 18 nm on $SiO_{2\text{-}200}$ and $SiO_{2\text{-}700}$, respectively; grafted (COD)Pt(CH_3)($N(SiMe_3)_2$) associated with (COD)Pt(CH_3)(OSi≡) surface species, provides well dispersed nanoparticles with a mean size of 3.3 nm on $SiO_{2\text{-}200}$ and 2.1 nm on $SiO_{2\text{-}700}$ (Table 6). Note that few larger aggregates are also found in this case. The formation of very large particle (> 20 nm) is prevented in part when flow conditions are used (Figure 27). Elemental analyses (Table 7) after H_2 treatment of (COD)Pt(Cl)($N(SiMe_3)_2$)@$SiO_{2\text{-}700}$ revealed the presence of chlorine, 0.7 (± 0.2) Cl/Pt ratio, for static H_2 treatment, whereas no chlorine is detected when a flow was used. This indicates that HCl formed under H_2 needs to be absent and at least eliminated to avoid the growth of nanoparticles.

Table 6. Particle size in nm and associated standard deviation from compounds grafted at $SiO_{2\text{-}700}$.

	static		flow	
(COD)Pt(Me)($N(SiMe_3)_2$)	2.1	(0.9)	1.7	(0.8)
(COD)Pt(Cl)($N(SiMe_3)_2$)	5 to 18	-	6.3	(2.4)
(COD)Pt($OSi(OtBu)_3$)$_2$	2.0	(0.6)	1.8	(0.4)

Table 7. Elemental analyses after grafting and H_2 treatments.

	Pt	C		N		Cl	
	wt.%	wt.%	C/Pt	wt.%	N/Pt	wt.%	Cl/Pt
(COD)Pt(Cl)($N(SiMe_3)_2$)	3.1%	2.5%	13.3	0.4%	1.7	0.4%	0.7
H_2-static	2.9%	0.9%	5.1	0.3%	1.3	0.2%	0.4
H_2-flow	2.9%	0.9%	5.3	0.2%	0.9	<0.1%	<0.2
(COD)Pt(Me)($N(SiMe_3)_2$)	3.8%	3.0%	12.8	0.3%	1.2	-	
H_2-static	3.9%	0.9%	3.6	0.2%	0.8	-	
H_2-flow	3.9%	0.9%	3.7	0.2%	0.8	-	

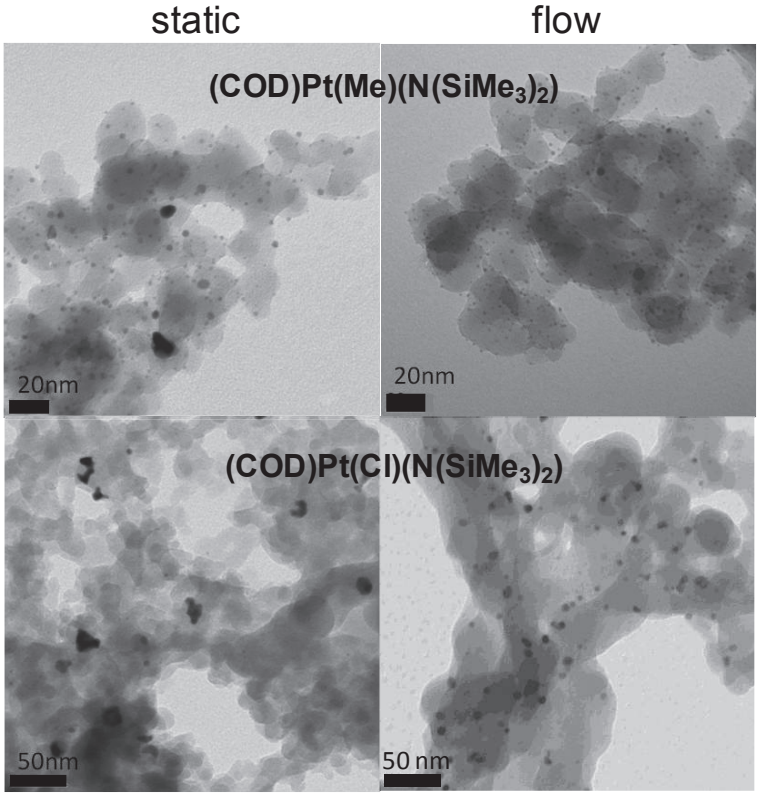

Figure 27. Comparative TEM pictures of complexes grafted on $SiO_{2\text{-}700}$

2.3.4. Conclusion

Overall, cyclooctadienyl Pt^{II} complexes of general formula (COD)Pt(X)(Y) are convenient precursors to prepare well-defined Pt^{II} surface species and supported Pt nanoparticles with a small size, typically around 2 nm, and a narrow distribution; the smaller nanoparticles being obtained on highly dehydroxylated supports and lower Pt loading. For the grafting step, it is notable that the COD ligand is a good reporter of the coordination sphere around Pt, even showing that a surface siloxy group is a slightly less strong donor ligand than the corresponding molecular tris(tert-butoxy) siloxy one. Overall, Pt^{II}-complexes with at least one O- and N-bound ligands are more reactive and preferred over those having Cl or only C-bound ligands; this allows the implantation of higher density of Pt at the silica surface and *in-fine* higher metal loading. Of the various ligands studied – $(t\text{BuO})_3\text{SiO}$, $(Me_3Si)_2N$, Me and Cl – chloride is the only one that dramatically influences and increases the mean size and the size distribution of Pt nanoparticles, probably through the formation of HCl, which helps Pt migration; but this can be partially controlled by using flow conditions in place of static ones.

2.4. Ceria surface organometallic chemistry

2.4.1. Ceria surface chemistry

Following this work on silica, we wanted to transpose it onto ceria. Ceria is indeed the support of choice for generating Diesel Oxydation Catalyst, mostly due to its O_2 storage properties. Before any grafting, the surface chemistry has to be controlled, Surface Organometallic Chemistry indeed supposes a good understanding of the surface oxide support in order to define at the molecular level the structure and reactivity of the grafted species.

2.4.1.1. Surface morphology

Ceria (Evonik Degussa VP60) is a crystalline material with a relatively low surface area (~ 60 $m^2.g^{-1}$). In analogy with silica, ceria will be treated under vacuum at various temperatures in order to clean the surface from organic pollutants and to control the water coverage and surface OH (≡Ce-OH) density. Ceria was first calcined under air followed by dehydroxylation under secondary vacuum. The surface area was measured by N_2 adsorption and desorption at -196°C. A type II adsorption isotherm is recorded and linked to intergrain macroporosity, results are summarized in Table 8. Ceria presented a relatively good thermal stability with a loss of less than 10% of its surface area between 200 and 800°C.

Table 8. Ceria BET surface area as a function of the calcination and dehydroxylation temperature. Error on the surface area is ± 3 $m^2.g^{-1}$

Calcination and dehydroxylation temperature (°C)	BET Surface area ($m^2.g^{-1}$)
200	58
400	57
600	54
800	52

2.4.1.2. IR-Study

The surface chemistry of ceria was studied by mean of IR spectroscopy. Ceria pellets were prepared and treated under various conditions into a set-up allowing *in-situ* analyses (Figure 28). On the spectrum of the as prepared pellet, bands at 3367 and 1637 cm^{-1} were associated

with absorbed water ((ν(OH) and δ(OH)). Bands at 2963, 2937 and 2886 cm^{-1} corresponded to the ν(C-H) of organic pollution of the sample. The large absorption area between 1600 and 900 cm^{-1} was related to carbonate species[100] (δ(OH) and ν(C-O)) and δ(C-C) of hydrocarbons -pollution). After calcination, here at 450°C, the bands associated with the hydrocarbon pollution disappeared and the absorbed water was efficiently eliminated. Bands from ν(OH) at 3709, 3659 and 3630 cm^{-1} were found and associated respectively to monodentate OH (μ^1) and two types of bidentate OH (μ^2-A and μ^2-B - Figure 29). Only polydentate carbonate species[100] remained as demonstrated by the IR bands at 1460 and 1400 cm^{-1}. After dehydroxylation, only the μ^1-OH band disappeared, all other bands, compared to the calcined sample, remained unchanged. Note that during the dehydroxylation process, a coloration change was noticed, the pellet turning from yellow to grey. This was indicative of an oxidation state modification from Ce(IV) to Ce(III).

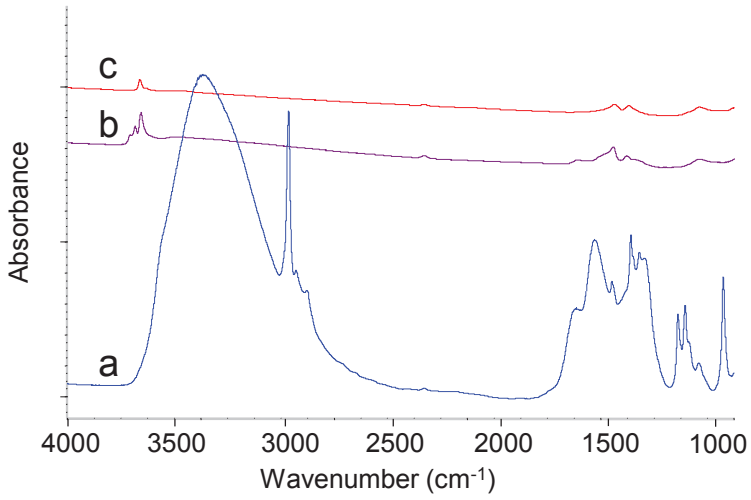

Figure 28. IR spectra of a ceria pellet a) as prepared, b) calcined at 450°C, c) dehydroxylated at 450°C.

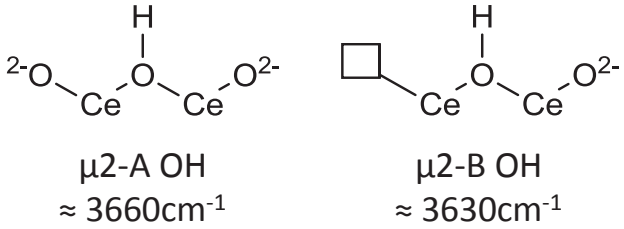

Figure 29. Schematic representation of the μ2 type of surface OH on ceria

2.4.1.3. OH titration

The OH titration was performed on ceria partially dehydroxylated at 200°C by reacting ceria with methylmagnesium bromide yielding methane. Methane evolvement was measured by gas

chromatography. A mean value of 3.6 ± 0.1 OH.nm^{-2} was measured, which is slightly higher than this found on silica dehydroxylated at 200°C, 2.5 OH.nm^{-2}.

OH was also titrated by integrating the OH bands by transmission IR spectroscopy. A ceria pellet was calcined at 200°C under air and further dehydroxylated under secondary vacuum at increasing temperature (Figure 30). From yellow after calcination, the pellet turned grey after dehydroxylation at 200°C. Between each temperature increase, the pellet was cooled down and a transmission infrared spectrum was recorded at room temperature. Results are presented in Figure 30. The peak at 2130 cm^{-1} was associated with electronic transition[101] of Ce^{3+} or to CO arising from the decomposition of carbonate surface species[59] and the peak at 2339 cm^{-1} corresponded to residual gaseous CO_2. As expected, the ν(OH) intensity was found to decrease with increasing dehydroxylation temperature. At 600°C, an OH and carbonates free surface was obtained.

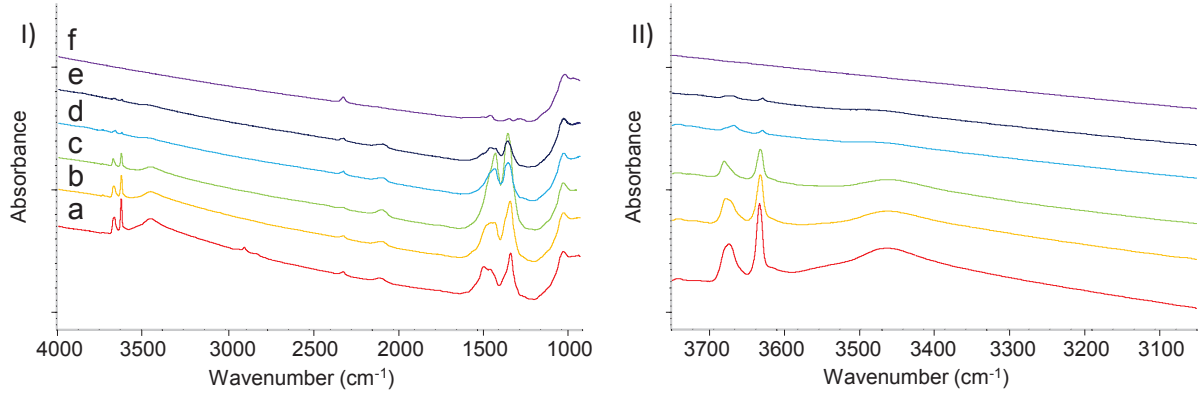

Figure 30. I) Transmission IR spectra of a ceria pellet calcined at 200°C under air and dehydroxylated for 5 to 12 hours at a) 200°C, b)300°C, c) 400°C, d) 450°C, e) 500°c and f) 600°C. II) Zoom 3750 to 3050 cm^{-1} region.

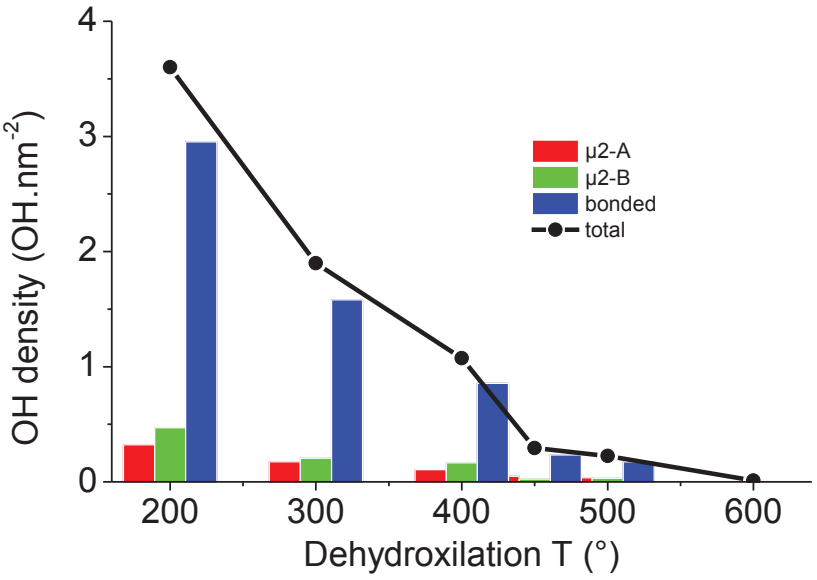

Figure 31. Surface OH density versus the ceria dehydroxylation temperature

The total OH density was plotted versus the dehydroxylation temperature (Figure 31), an exponential type decay was observed as previously described for silica[57] and alumina.[102] The surface composition could be estimated by integrating each band and considering equal extinction parameters for μ^2-A, μ^2-B and bonded OH. The μ^2-A/μ^2-B ratio was found constant, equal to 0.8 (±0.1).

Attempts to rationalize the surface composition were made by reducing ceria under H_2. Ceria reacts indeed with H_2 at 150°C to form water and reduced ceria as depicted below:

$$CeO_2 + H_2 \rightleftarrows Ce_2O_3 + H_2O$$

Ceria reduction

A ceria pellet was first calcined under air at 200°C and dehydroxylated at 200°C for at least 14 hours (sample 1). After this first process, H_2 was added (150 mBar) and the pellet was heated at 150°C for at least 6 hours. The pellet was then again dehydroxylated at 200°C for 15 hours. After each step, an IR spectrum was recorded at room temperature. Four reduction/dehydroxylation cycles were performed and the surface chemistry was monitored by IR spectroscopy (Figure 32).

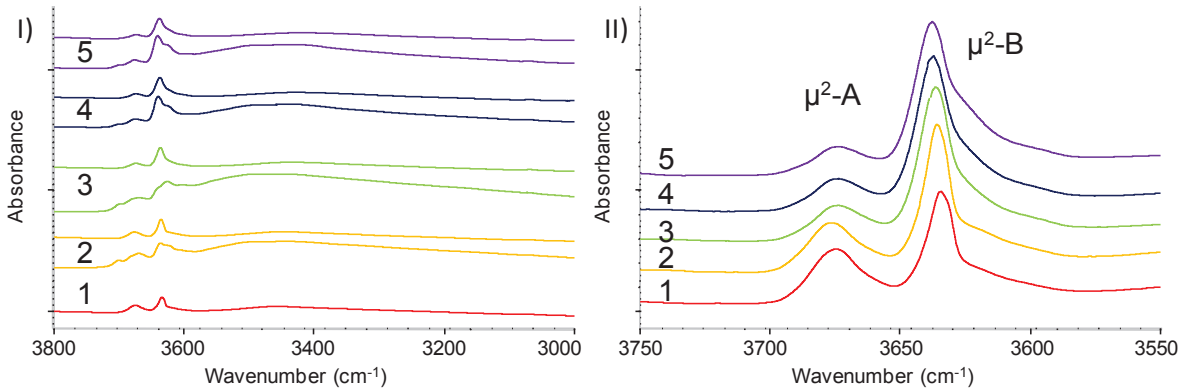

Figure 32. I) Transmission IR spectra after reduction/dehydroxylation cycles. II) Only spectra after dehydroxylation are presented.

The formation of water was confirmed by the large band at 3450 cm^{-1} and the appearance of a band of low intensity at 1630 cm^{-1} (not shown). Peaks corresponding to μ^2-A and μ^2-B species were integrated and plotted versus the reduction/dehydroxylation cycle numbers (Figure 33). The total OH content was plotted in black and correspond to the integration of the ν(OH) band from 3100 to 3710 cm^{-1}.

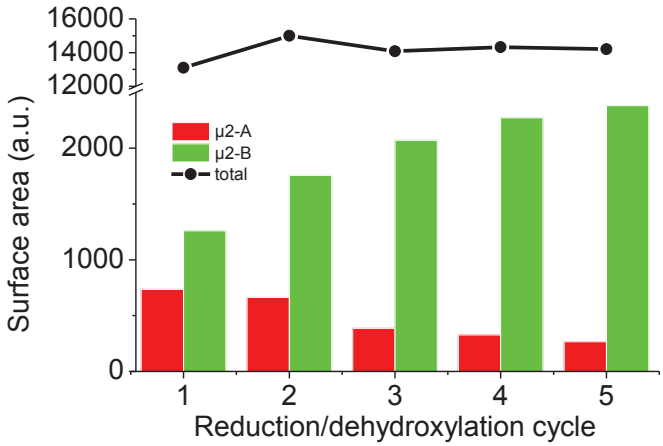

Figure 33. Integration of the bands under μ^2-A, μ^2-B and total integrated from 3700 cm^{-1} to 3100 cm^{-1}.

The total OH density remained constant after 5 cycles. Interestingly the reduction of the support was confirmed by the Ce-OH nature modification from μ^2-A type to μ^2-B type. Overall the composition of the μ^2-OH was switched from 37% of type A after the first cycle to less than 10% after 5 cycles. Note that at this low dehydroxylation temperature, most of the surface Ce-OH remained bonded (about 82 %).

Note here that surface organometallic chemistry on ceria will be made difficult by the high reactivity of ceria with O_2 and CO_2. Indeed, the modification of the DRIFT spectra of dehydroxylated ceria showed the formation of carbonates species after storing it several weeks in a clean glove-box. Moreover, the dehydroxylation process on ceria powder did not

give repeatable results. It was necessary to calcine ceria, and then reduce it under H_2 and finally dehydroxylate it to obtain repeatable spectra.

2.4.2. Platinum complexes grafting

The grafting of platinum species onto ceria was performed following the work done onto silica using similar procedures. Ceria calcined at 400°C under air, reduced under H_2 at 150°C and finally dehydroxylated at 400°C ($CeO_{2\text{-}400}$) was used for grafting, the hydroxyl coverage being estimated to be 1.1 OH.nm^{-2}, comparable to values found on $SiO_{2\text{-}700}$ (0.8 OH.nm^{-2}). $(COD)Pt(Me)_2$, $(COD)Pt(Me)(N(SiMe)_3)_2$ and $(COD)Pt(Cl)(N(SiMe)_3)_2$ were tested for grafting.

The efficient grafting of $(COD)Pt(Me)_2$ was monitored by IR-DRIFT (Figure 34). Similarly to silica, this complex poorly reacted with the OH functionality of the ceria surface, indeed only a partial consumption of surface hydroxyls was not found. Bonded hydroxyls did not react as the broad signal centered on 3350 cm^{-1} remained unchanged. The μ^2 type ν(OH) band was only partially consumed. The presence of the complex onto the surface was witnessed by the formation of absorption bands corresponding to ν(CH) of the Pt ligands below 3010 cm^{-1}.

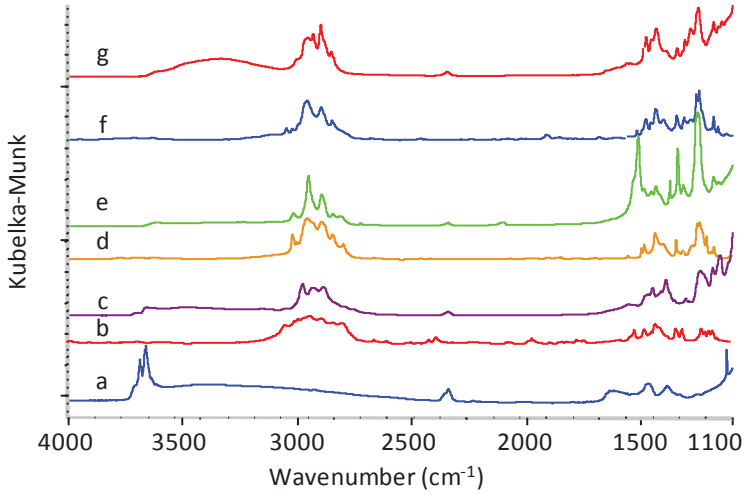

Figure 34. IR-DRIFT spectra of complexes grafted on $CeO_{2\text{-}400}$ a) $CeO2\text{-}_{400}$, b) $(COD)Pt(Me)_2$, c) $(COD)Pt(Me)_2$ @CeO2-400, d) $(COD)Pt(Me)(N(SiMe_3)_2)$, e) $(COD)Pt(Me)(N(SiMe_3)_2)@CeO_{2\text{-}400}$, f) $(COD)Pt(Cl)(N(SiMe_3)_2)@CeO_{2\text{-}400}$, g) $(COD)Pt(Cl)(N(SiMe_3)_2)$.

For $(COD)Pt(Me)(N(SiMe)_3)_2$ (Figure 34 e) the spectrum showed the full consumption of the μ^2-OH. Bonded surface OH seemed to react as no more broad band around 3350 cm^{-1} was found. Moreover, comparatively to $CeO_{2\text{-}400}$ and the pure $(COD)Pt(Me)(N(SiMe_3)_2)$ spectra a new band at 1510 cm^{-1} was found and not attributed yet.

Again, similar observations were made for (COD)Pt(Cl)($N(SiMe)_3)_2$ (Figure 34 g). The consumption of μ^2-OH and the concomitant appearance of ν(CH) vibration bands bellow 3010 cm^{-1} indicated the formation of surface species. Here, bonded surface OH remained untouched as witnessed by the large absorption band centered on 3350 cm^{-1}. For this latter complex carbon-13 CP-MAS solid-state NMR was used to characterize the surface species (Figure 35). The peaks at 92 and 74 ppm were attributed to the olefinic carbons of the COD onto Pt respectively in *trans* to the chlorine and to the surface (≡Ce-O-) ligands. The large peak at 27 ppm was attributed to the CH_2 of the COD ligand. Similarly to what was observed for silica, the peak at 0 ppm was attributed to passivated surface (≡$CeOSiMe_3$ surface species). The peaks at 67 and 12 ppm were attributed to diethyl ether (grafting solvent) absorbed onto the surface as verified by a blank experiment (Appendix 11). The peak at 133 ppm was likely attributed to free COD that could result from a degradation of instable surface species or to carbonated species due to contamination.[103] The carbon-13 CP-MAS solid-state NMR of the freshly $CeO_{2\text{-}400}$ presented no signal between -10 and 260 ppm.

Overall, the Pt complexes seemed to graft on ceria similarly to what was observed on silica but the full characterization has not been done yet and requires further analyses (elemental analyses, solid-state NMR).

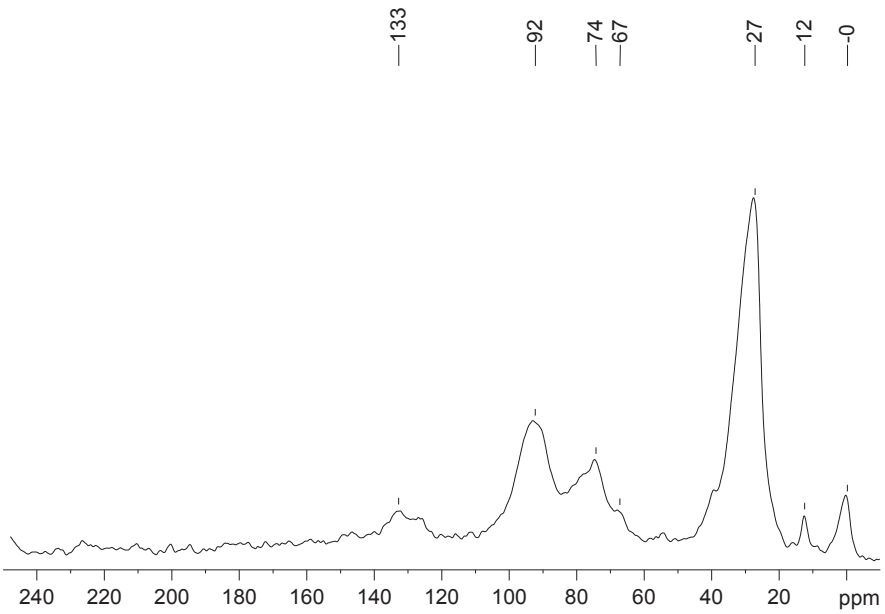

Figure 35. ^{13}C CP/MAS solid state NMR spectra of (COD)Pt(Cl)($N(SiMe_3)_2$)@CeO_2 (d1 = 2 s, 30000 scans, lb=100Hz)

2.4.3. Nanoparticles formation

The formation of nanoparticles was tested in the same static conditions than those used for silica support, i.e. under 150 mbar of hydrogen at 300°C. The formation of nanoparticles was visually attested by the coloration change from light yellow to black. From IR-DRIFT spectra recorded after treatment (Appendix 12), the total elimination of the ligands was checked by the full disappearance of the ν(CH) vibration bands bellow 3010 cm^{-1}. The formation of platinum nanoparticles occurred by the cleavage of the Ce-O-Pt bonds as witnessed by the recovery of isolated μ^2-OH. Note here that ceria itself was affected by H_2 at 300°C, as partial reduction and thus formation of water occurred. The samples being evacuated at 300°C no free water was found but the large OH band centered on 3350 cm^{-1} was associated to newly formed surface OH as already reported.[60]

Nanoparticles were observed by TEM. For (COD)Pt$(Me)_2$, nanoparticles were barely visible probably due to their very low size (0.8 nm nanoparticles were found - Appendix 13) and low Pt loading. For (COD)Pt(Me)$(NSiMe)_3$), nanoparticles of 1.2 nm were found with a narrow size dispersion of 0.2 nm. For (COD)Pt(Cl)$(NSiMe)_3$), nanoparticles were bigger with a diameter of 1.5 nm and a size dispersion of 0.3 nm. This is in strong contrast with what was observed onto silica where Cl, as a ligand, led to a dramatic increase of the nanoparticles size. Here this size increase effect was probably limited by the influence of the substrate. Ceria is indeed known for giving rise to stronger metal/support interactions than silica[104] thus stabilizing nanoparticles even at high temperature under oxidizing conditions.[105] We hypothesized that this interaction counterbalanced the detrimental effect of Cl over the nanoparticles growth.

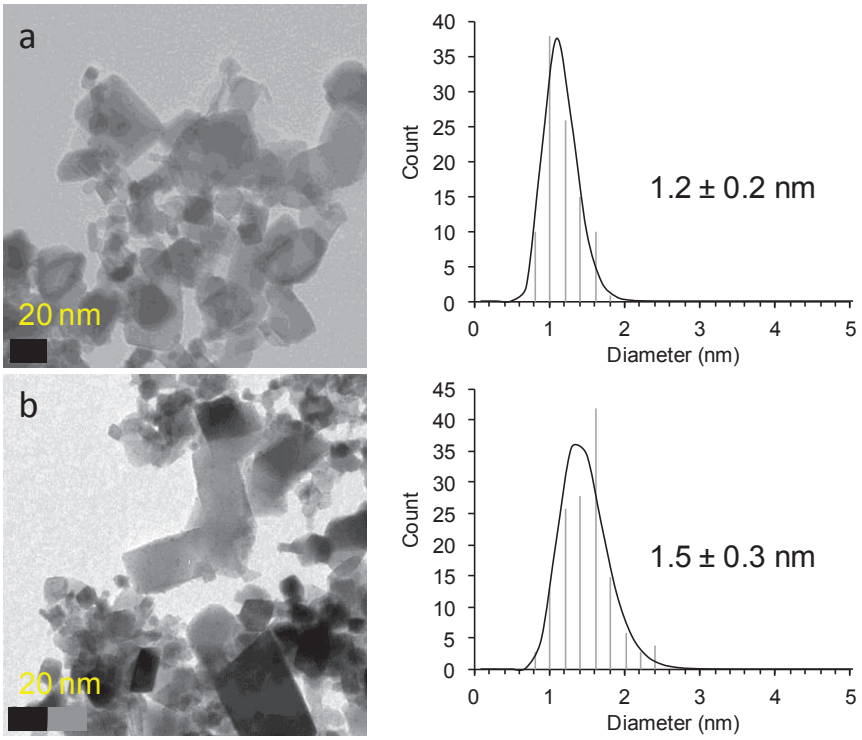

Figure 36. TEM picture after static H2 treatment of a) (COD)Pt(Me)(N(SiMe$_3$)$_2$)@CeO$_{2\text{-}400}$, b) (COD)Pt(Cl)(N(SiMe$_3$)$_2$)@CeO$_{2\text{-}400}$

2.4.4. Conclusion

Through calcination and dehydroxylation procedure the ceria surface composition can be easily modified. The OH type and their concentration are respectively triggered by the oxidation state of ceria and the dehydroxylation temperature. Despite its relative complexity, grafting of isolated complexes onto ceria has been successfully achieved by using tools and methods previously developed for silica. The further treatment under H_2 and heating led to the formation of well dispersed nanoparticles. The platinum surface species chemistry, and particularly the presence of chlorine, proved to led to slightly larger nanoparticles, as observed for silica albeit with less dramatic effect. The strong metal support interaction encountered onto ceria is probably responsible for this limited growth.

2.5. Chapter conclusion

Surface organometallic chemistry was used to produce well dispersed Pt nanoparticles onto silica or ceria. Onto silica the surface OH concentration proved to be a key parameter to control the Pt loading. On both oxides the influence of the precursor chemistry, notably leading or not to the passivation of the surface was found to have little impact on the

nanoparticles growth. On another hand Cl containing precursor led to a strong increase in the nanoparticles size through the probable formation of HCl. This phenomenon could be limited by treating the grafted samples under an H_2 flow as demonstrated for silica support. This first SOMC study onto ceria paves the way to further research on this support. For example, the study of the formation mechanism of nanoparticles from isolated species could be key to better understand and characterize the strong metal support interaction or the redispersion of agglomerated Pt nanoparticles as described recently.[12]

2.6. Experimental

2.6.1. General procedures

All experiments were carried out under a controlled atmosphere (Ar), using Schlenk and glove-box techniques for organometallic synthesis and silica surface modifications. Silica dehydroxylated at 700 °C, referred as SiO_{2-700}, was obtained as follow: silica (Aerosil Degussa, 200 $m^2.g^{-1}$) was compacted with distilled water, dried at 110 °C for 2 days, calcined (500°C under air for 4 hours) and partially dehydroxylated under secondary vacuum (10^{-5} mBar) at 500°C for 12 h and then at 700°C for 4 h. Silica dehydroxylated at 200 °C, referred as SiO_{2-200}, was dehydroxylated at 200°C under secondary vacuum for 15 hours, just after compacting. The density of surface silanols as determined by titration with methylmagnesium bromide was respectively 0.86 and 0.26 $mmol.g^{-1}$ for SiO_{2-200} and SiO_{2-700}. [57,106] Ceria (Evonik Degussa VP 60) pellets were produced by finely grinding ceria using a mortar, 40 mg were placed in a mold (17 mm diameter) between two mica sheets and pressed using an hydraulic press applying a pressure of 1 t for 1 min. For grafting, ceria was first calcined under air at 400°C for 15 h, then reduced under static H_2 atmosphere at 150°C for 15 h and finally dehydroxylated at 400°C for 15 h.

K_2PtCl_4 99.9 % was purchased from Strem Inc. 1,5-cyclooctadiene 99+ % (COD), was purchased from Sigma-Aldrich, filtered over dried alumina and degassed prior to use. Tris(tert-butoxy)silanol 99.999 % ($HOSi(OtBu)_3$), lithium bis(trimethylsilyl)amide ($LiN(SiMe_3)_2$) and methyl lithium 1.6 M in Et_2O (MeLi) were purchased from Sigma-Aldrich and used as received. Pentane, diethylether and dichloromethane were dried using an MBraun solvent purification system, contacted with MS 4 Å and degassed under vacuum. Dihydrogen was purified over R3-11 BASF catalyst / MS 4 Å prior to use. Benzene was dried under Na/K/benzophenone and distilled prior to use. The molecular complexes $(COD)Pt(Cl)_2$,[89]

(COD)Pt(Me)$_2$,[90] (COD)Pt(Cl)(Me),[91] (COD)Pt(OSi(O*t*Bu)$_3$)$_2$[92] and (COD)Pt(Cl)(N(SiMe$_3$)$_2$)[93] were prepared as described in the literature.

Infra-Red spectra were recorded on a Nicolet Magna 550 FT spectrometer using a custom infrared cell equipped with CaF_2 windows, allowing *in-situ* studies. Typically, 64 scans were accumulated for each spectrum (resolution 4 cm^{-1}).

Elemental analyses were performed at "Mikroanalytisches Labor Pascher" in Germany. Transmission Electron Micrographs (TEM) were obtained on a Philips CM120 Transmission Electron Microscope at the "Centre Technologique des Microstructures Université Lyon 1" in France the acceleration voltage was set to 120 kV, and the grids were prepared by directly "dipping" the grid into the silica powder (this method avoided the use of a solvent and the potential leaching or aggregation of particles on the support).

^{1}H magic angle spinning (MAS) and ^{13}C cross polarization (CP)-MAS solid-state NMR spectra were recorded on a Brüker Avance 500 MHz spectrometer with a conventional double resonance 4 mm CP-MAS probe. The samples were introduced under Ar in a zirconia rotor, which was then tightly closed. In all experiments, the rotation frequency was set to ca. 10 kHz. Chemical shifts are given with respect to TMS as the external reference for both ^{1}H and ^{13}C NMR. ^{1}H and ^{13}C liquid-state NMR spectra were recorded on a Brüker Avance 300 MHz spectrometer. Chemical shifts are given with respect to the residual solvent peak chemical shift.

2.6.2. Platinum complexes preparation

Preparation of (COD)Pt(Me)(N(SiMe$_3$)$_2$).

To a suspension of (COD)Pt(Cl)(Me) (500 mg – 1.4 mmol) in pentane (15 mL) was added a solution of LiN(SiMe$_3$)$_2$ (237 mg – 1.4 mmol) in pentane (6 mL). The colorless reaction mixture turned light yellow, while LiCl precipitated. After 90 min at 25 °C, stirring was stopped allowing LiCl to settle, and the reaction mixture was filtered and evaporated to dryness to afford 521 mg of a targeted complex as a white to light yellow solid (77%). ^{1}H NMR (C_6D_6; δ, ppm): 0.46 (s, 18H, -Si*Me$_3$*), 1.05 (t, 3H, Pt-C*H$_3$*, J_{Pt-H} = 80Hz), 1.47 (m, 4H, endo C*H$_2$*), 1.80 (m, 4H, exo C*H$_2$*), 3.79 (t, 2H, =C*H*, *trans* to N(SiMe$_3$)$_2$, J_{Pt-H} = 60 Hz), 5.18 (t, 2H, =C*H*, *trans* to CH_3, J_{Pt-H} = 30 Hz). ^{13}C NMR (C_6D_6; δ, ppm): 5.8 (t, *C*H$_3$, Me, JPt-C=726.8 Hz), 7.0 (m, Si*C*H3), 28.1 (t, *C*H$_2$, JPt-C=12.9 Hz), 30.8 (t, *C*H$_2$, JPt-C=15.9 Hz), 84.0 (t, =*C*H, *trans* to N, JPt-C=161.3 Hz), 111.6 (s, =*C*H, *trans* to CH_3, JPt-C=29.4 Hz). High-resolution mass spectrometry (m/z): $[M+H]^+$ 479.1876 measured (Δm = -0.9 ppm), 479.1872 calculated from $C_{15}H_{33}NPtSi_2$. Elemental analysis: Pt/Si/N/C/H calculated for

$C_{15}H_{33}NPtSi_2$ 37.6/6.9/2.9/40.8/11.7; found, 38.0/7.0/3.0/40.6/11.4. IR (cm^{-1}): 3019, 3000, 2955, 2924, 2888, 2843, 2795, 1493, 1478, 1433, 1397, 1339, 1312, 1251, 1214, 1180.

Alternative preparation of (COD)Pt(Me)(N(SiMe$_3$)$_2$).

Complex **1** can also be prepared in 60 % yield using the above procedure from (COD)Pt(Cl)($NSiMe_3$)$_2$ and MeLi.

Preparation of (COD)Pt(Me)(OSi(OtBu)$_3$).

To (COD)Pt(Cl)(Me) (800 mg – 2.3 mmol) suspended in pentane (10 mL) was added a solution of NaOSi(O*t*Bu)$_3$ (648 mg – 2.3 mmol) in pentane (10 mL). After 16 h at 25 °C, stirring was stopped, NaCl was filtered off, and the uncolored solution was concentrated at -30°C. After removal of the supernatant, 835 mg (64%) of complex **2** was recovered as white crystalline solid. ^{1}H NMR (C_6D_6; δ, ppm): 1.16 (t, 3H, C*H$_3$,* JPt-H=75Hz), 1.50 (m, 4H, endo C*H$_2$*), 1.62 (s, 27H, OC*Me$_3$*), 1.80 (m, 4H, exo C*H$_2$*), 3.57 (t, 2H, =C*H*, *trans* to OSi, JPt-H=66 Hz), 5.90 (t, 2H, =C*H*, *trans* to CH_3, JPt-H=30Hz). ^{13}C NMR (C_6D_6; δ, ppm): 6.9 (s, *C*H$_3$, JPt-C=700 Hz), 27.6 (s, *C*H$_2$), 31.6 (s, *C*H$_2$), 32.2 (s, OC*Me$_3$*), 71.4 (s, O*C*Me$_3$), 73.4 (s, =CH, *trans* to OSi, JPt-C=227 Hz), 113.3 (s, =CH, *trans* to CH_3, JPt-C=26.5 Hz). IR (cm^{-1}): 3011, 2973, 2923, 2894, 2842, 1473, 1449, 1419, 1385, 1363, 1243, 1215, 1200, 1063.

Preparation of (COD)Pt(N(SiMe$_3$)$_2$)(OSi(OtBu)$_3$).

To a mixture of (COD)Pt(Cl)($N(SiMe_3)_2$) (200 mg – 0.4 mmol) in benzene (5 mL) was added a solution of NaOSi(O*t*Bu)$_3$ (115 mg – 0.4 mmol) in benzene (10 mL). The reaction mixture was kept at reflux for 16 h, filtered and evaporated to dryness. The resulting solid was dissolved in pentane and crystallized at -30 °C yielding 150 mg (52%) of complex as yellow crystals suitable for X-Ray structure determination. ^{1}H NMR (C_6D_6; δ, ppm): 0.54 (s, 18H, -Si*Me$_3$*), 1.31 (m, 4H, endo C*H$_2$*), 1.54 (s, 27H, OC*Me$_3$*), 1.94 (m, 4H, exo C*H$_2$*), 4.55 (t, 2H, =C*H*, *trans* to OSi, J_{Pt-H} = 66 Hz), 6.01 (t, 2H, =C*H*, *trans* to $N(SiMe_3)_2$, J_{Pt-H} = 51 Hz). ^{13}C NMR (C_6D_6; δ, ppm): 7.0 (s, Si*Me$_3$*), 29.2 (s, *C*H$_2$), 30.7 (s, *C*H$_2$, COD), 32.3 (s, OC*Me$_3$*), 71.8 (s, O*C*Me$_3$), 84.4 (s, =CH, *trans* to OSi(O*t*Bu)$_3$), 100.8 (s, =CH, *trans* to $N(SiMe_3)_2$). IR (cm^{-1}): 3056, 2963, 2935, 2895, 2846, 1474, 1456, 1434, 1387, 1363, 1247, 1198, 1065.

2.6.3. Grafting procedures

Grafting of (COD)PtMe$_2$ on SiO$_{2-700}$: (COD)PtMe$_2$@SiO$_{2-700}$. Representative Procedure.

Using a schlenk with double compartments separated with a glass filter, (COD)Pt(Me)$_2$ (1.2 equiv.; 53 mg; 0,16 mmol) in pentane (5mL) was contacted with SiO$_{2-700}$ (0.50 g, 0.13 mmol SiOH) at 25°C. After 3 h, the solid is decanted, the supernatant was filtered, and the resulting solid was washed with pentane (4 × 5 mL) and dried under vacuum (10^{-5} mBar) for 1 h to yield a white solid. Elemental Analysis (wt%): Pt/C 1.1/1.0. IR-DRIFT: 3410/3057/3001/2945/2927/2877/2842/2801. Solid-state ^{13}C NMR (ppm): 118/78/33/30/6.

Grafting of (COD)PtMe$_2$ on SiO$_{2-200}$: (COD)PtMe$_2$@SiO$_{2-200}$.

The experimental procedure described above was carried out in pentane using (COD)Pt(Me)$_2$ (1.2 equiv.; 173 mg; 0,52 mmol) and SiO$_{2-200}$ (0.50 g, 0.43 mmol SiOH). Elemental Analysis (wt%): Pt/C 3.0/2.1. IR-DRIFT: 3018/3005/2955/2930/2894/2648/2802. Solid-state ^{13}C NMR (ppm): 118/78/32/29/6.

Grafting of (COD)PtMe$_2$ on CeO$_{2-400}$: (COD)PtMe$_2$@CeO$_{2-400}$.

The experimental procedure described above was carried out in pentane using (COD)Pt(Me)$_2$ (1.2 equiv.; 72 mg; 0,22mmol) and CeO$_{2-400}$ (0.50 g, 0.18 mmol CeOH).

Grafting of (COD)Pt(OSi(OtBu)$_3$)$_2$ on SiO$_{2-700}$: (COD)Pt(OSi(OtBu)$_3$)$_2$@SiO$_{2-700}$.

The experimental procedure described above was carried out in pentane using (COD)Pt(OSi(O*t*Bu)$_3$)$_2$ (1.2 equiv.; 53 mg; 0.064 mmol) and SiO$_{2-700}$ (0.20 g, 0.053 mmol SiOH). Elemental Analysis (wt%): Pt/C 2.3/5.4. IR-DRIFT: 3370/2975/2933/2905/2876. Solid-state ^{13}C NMR (ppm): 92/72/30/28.

Grafting of (COD)Pt(OSi(OtBu)$_3$)$_2$ on SiO$_{2-200}$: (COD)Pt(OSi(OtBu)$_3$)$_2$@SiO$_{2-200}$.

The experimental procedure described above was carried out in pentane using (COD)Pt(OSi(O*t*Bu)$_3$)$_2$ (1.2 equiv.; 172 mg; 0.21 mmol) and SiO$_{2-200}$ (0.20 g, 0.17 mmol SiOH). Elemental Analysis (wt%): Pt/C 3.9/5.3. IR-DRIFT: 3420/2975/2931/2905/2876/2850. Solid-state ^{13}C NMR (ppm): 93/72/30/27.

Grafting of (COD)Pt(Me)(OSi(OtBu)$_3$) on SiO$_{2-700}$: (COD)Pt(Me)(OSi(OtBu)$_3$)@SiO$_{2-700}$.

The experimental procedure described above was carried out in pentane using (COD)Pt(Me)(OSi(O*t*Bu)$_3$) (1.2 equiv.; 37 mg; 0.064 mmol) and SiO$_{2-700}$ (0.20 g, 0.053 mmol

SiOH). Elemental Analysis (wt%): Pt/C 4.1/4.8. IR-DRIFT: 3015/2977/2954/2932/2893/2888/2846/2800. Solid-state ^{13}C NMR (ppm): 115/73/30/27/4.

Grafting of (COD)Pt(Me)(OSi(OtBu)$_3$) on SiO$_{2-200}$: (COD)Pt(Me)(OSi(OtBu)$_3$)@SiO$_{2-200}$.

The experimental procedure described above was carried out in pentane using (COD)Pt(Me)(OSi(OtBu)$_3$) (1.2 equiv.; 121 mg; 0.21 mmol) and SiO$_{2-200}$ (0.20 g, 0.17 mmol SiOH). Elemental Analysis (wt%): Pt/C 6.8/5.4. IR-DRIFT: 3013/2975/2951/2928/2890/2844/2801. Solid-state ^{13}C NMR (ppm): 115/73/30/27/5.

Grafting of (COD)Pt(Me)(N(SiMe$_3$)$_2$) on SiO$_{2-700}$: (COD)Pt(Me)(N(SiMe$_3$)$_2$)@SiO$_{2-700}$.

The experimental procedure described above was carried out in pentane using (COD)Pt(Me)(N(SiMe$_3$)$_2$) (1.2 equiv.; 30 mg; 0.064 mmol) and SiO$_{2-700}$ (0.20 g, 0.053 mmol SiOH). Elemental Analysis (wt%): Pt/C 3.8/3.0. IR-DRIFT: 3017/3002/2962/2957/2932/2895/2846/2802. Solid-state ^{13}C NMR (ppm): 117/101/76/32/29/7/0.

Grafting of (COD)Pt(Me)(N(SiMe$_3$)$_2$) on SiO$_{2-200}$: (COD)Pt(Me)(N(SiMe$_3$)$_2$)@SiO$_{2-200}$.

The experimental procedure described above was carried out in pentane using (COD)Pt(Me)(N(SiMe$_3$)$_2$) (1.2 equiv.; 98 mg; 0.21 mmol) and SiO$_{2-200}$ (0.20 g, 0.17 mmol SiOH). Elemental Analysis (wt%): Pt/C 7.4/4.9. IR-DRIFT: 3014/3000/2954/2927/2890/2844/2796. Solid-state ^{13}C NMR (ppm): 114/72/28/5/0.

Grafting of (COD)Pt(Me)(N(SiMe$_3$)$_2$) on CeO$_{2-400}$: (COD)Pt(Me)(N(SiMe$_3$)$_2$)@CeO$_{2-400}$.

The experimental procedure described above was carried out in pentane using (COD)Pt(Me)(N(SiMe)$_3$) (1.2 equiv.; 105 mg; 0,22mmol) and CeO$_{2-400}$ (0.50 g, 0.18 mmol CeOH).

Grafting of (COD)Pt(Cl)(N(SiMe$_3$)$_2$) on SiO$_{2-700}$: (COD)Pt(Cl)(N(SiMe$_3$)$_2$)@SiO$_{2-700}$.

The experimental procedure described above was carried out in diethyl ether using (COD)Pt(Cl)(N(SiMe$_3$)$_2$) (1.2 equiv.; 103 mg; 0,16 mmol) and SiO$_{2-700}$ (0.50 g, 0.13 mmol SiOH). Elemental Analysis (wt%): Pt/C 3.1/2.5. IR-DRIFT: 3022/3008/2964/2934/2902/2888. Solid-state ^{13}C NMR (ppm): 106/88/60/35/32/0.

Grafting of (COD)Pt(Cl)(N(SiMe$_3$)$_2$) on SiO$_{2-200}$: (COD)Pt(Cl)(N(SiMe$_3$)$_2$)@SiO$_{2-200}$.

The experimental procedure described above was carried out using (COD)Pt(Cl)($N(SiMe_3)_2$) (1.2 equiv.; 258 mg; 0,52 mmol) and $SiO_{2\text{-}200}$ (0.5g, 0.43 mmol SiOH). Elemental Analysis (wt%): Pt/C 4.2/2.8. IR-DRIFT: 3023/3009/2962/2942/2934/2900/2853. Solid-state ^{13}C NMR (ppm): 104/94/31/0.

Grafting of (COD)Pt(Cl)($N(SiMe_3)_2$) on $CeO_{2\text{-}400}$: (COD)Pt(Cl)($N(SiMe_3)_2$)@$CeO_{2\text{-}400}$.

The experimental procedure described above was carried out in pentane using (COD)$Pt(Me)_2$ (1.2 equiv.; 108 mg; 0,22mmol) and $CeO_{2\text{-}400}$ (0.50 g, 0.18 mmol CeOH).

Grafting of (COD)Pt($N(SiMe_3)_2$)($OSi(OtBu)_3$) on $SiO_{2\text{-}700}$: (COD)Pt($N(SiMe_3)_2$)($OSi(OtBu)_3$) @$SiO_{2\text{-}700}$.

The experimental procedure described above was carried out in pentane using (COD)Pt($N(SiMe_3)_2$)($OSi(OtBu)_3$) (1.2 equiv.; 46 mg; 0.064 mmol) and $SiO_{2\text{-}700}$ (0.20 g, 0.053 mmol SiOH). Elemental Analysis (wt%): Pt/C 3.7/4.6. IR-DRIFT: 2976/2956/2951/2899/2851. Solid-state ^{13}C NMR (ppm): 105/89/75/31/5/0.

Grafting of (COD)Pt($N(SiMe_3)_2$)($OSi(OtBu)_3$) on $SiO_{2\text{-}200}$: (COD)Pt($N(SiMe_3)_2$)($OSi(OtBu)_3$)@$SiO_{2\text{-}200}$.

The experimental procedure described above was carried out in pentane using (COD)Pt(($N(SiMe_3)_2$)($OSi(OtBu)_3$) (1.2 equiv.; 151 mg; 0.21 mmol) and $SiO_{2\text{-}200}$ (0.20 g, 0.17 mmol SiOH). Elemental Analysis (wt%): Pt/C 4.8/4.8. IR-DRIFT: 2977/2958/2933/2900/2852. Solid-state ^{13}C NMR (ppm): 105/95/75/30/28/5/0.

Grafting of (COD)Pt(Cl)(Me) on $SiO_{2\text{-}200}$: (COD)Pt(Cl)(Me)@$SiO_{2\text{-}200}$.

The experimental procedure described above was carried out in dichloromethane using (COD)Pt(Cl)(Me) (1.2 equiv.; 73 mg; 0.21 mmol) and $SiO_{2\text{-}200}$ (0.20 g, 0.17 mmol SiOH). No signals were found neither by IR-DRIFT nor by solid-state ^{13}C NMR.

Grafting of (COD)$Pt(Cl)_2$

No attempt to graft (COD)$Pt(Cl)_2$ was done as no solvent was found to solubilize this complex.

2.6.4. Nanoparticles formation

Preparation of supported Pt nanoparticles from oxides supported Pt precursors under static H_2 atmosphere.

Representative procedure. In a glove box, 80 mg of the silica supported Pt precursor was transferred in a 200-mL glass reactor. After evacuation of the reactor (10^{-5} mBar), H_2 was added (150 mBar), and the system was kept at 300°C for 15 h following a heating ramp of 5 K.min^{-1} from 25 °C. After cooling down to 25 °C, the reactor was evacuated (10^{-5} mBar), and the solid (dark grey to black) was transferred and stored in a glove-box.

Preparation of silica-supported Pt nanoparticles from silica supported Pt precursors under a continuous flow of H_2.

Representative procedure. To a reactor equipped with a glass frit, 80 mg of the silica supported Pt precursor were placed on the frit in the glove-box. After connection to the H_2 line and purging the tubing, the reactor was opened, put under H_2 flow (ca. 100 mL.min^{-1}), and heated up to 300°C with a heating ramp of 1 to 5 K.min^{-1}. After 15 h, the gas flow was switched off, the reactor was cooled down to room temperature and evacuated. The resulting solid (dark grey to black) was transferred and stored in a glove-box.

2.7. Appendix

Appendix 1. Single Crystal X-Ray diffraction Table S-1.

	(COD)Pt(Me)(OSi(O*t*Bu)$_3$) (**2**)	(COD)Pt(OSi(O*t*Bu)$_3$)(N(SiMe)$_3$) (**3**)
Formula	$C_{21}H_{42}PtO_4Si$	$C_{26}H_{57}NPtO_4Si_3$
Formula weight (g.mol^{-1})	581.74	727.09
Crystal size (mm)	0.38x0.21x0.13	0.63x0.53x0.45
Color, morphology	coloreless	light yellow
ρ (g.cm^{-3})	1.563	1.452
Lattice type, crystal system	Monoclinic	Triclinic
Space group	$P2_1/n$	P -1
Z	2	2
Cell constant		
a (Å)	9.465(1)	10.5195(5)
b (Å)	8.6144(9)	11.5936(6)
c (Å)	30.436(3)	14.5167(8)
α (°)	90	72.425(5)
β (°)	95.187(9)	80.632(4)
γ (°)	90	89.822(4)
V (Å^3)	2471.4(4)	1663.3(2)
F_{000}	1168	744
μ (Mo Kα) (mm^{-1})	5.75	4.36
θ (°)	3.6-29.5	3.5-29.5
Scan type	ω scans	ω scans
Temperature (K)	150	150
Measured reflections	22806	43516
Refinement	full least-square matrix on F^2	full least-square matrix on F^2
Independent relections	6069	8476
No. Parameters	244	317
$R[F^2>2\sigma(F^2)]/ wR_2$	0.047/ 0.149	0.031/ 0.066
GoF	0.99	1
Max peak in final diff. map (e- Å^{-3})	2.09	1.86
Min peak in final diff. map (e- Å-3)	-3.57	-1.76

Appendix 2. (COD)Pt(Me)$_2$

Figure S1. IR-DRIFT

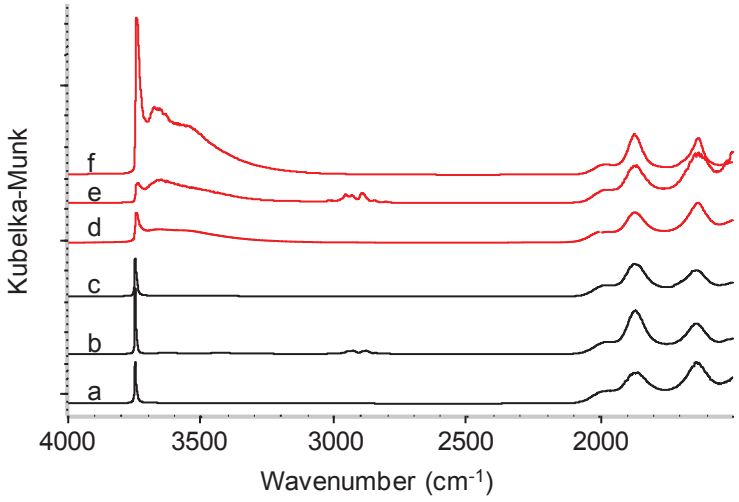

a) $SiO_{2\text{-}700}$, b) (COD)Pt(Me)$_2$@$SiO_{2\text{-}700}$, c) after static H_2 treatment, d) $SiO_{2\text{-}200}$, e) (COD)Pt(Me)$_2$@$SiO_{2\text{-}200}$, f) after static H_2 treatment

	grafted	after H_2
$SiO_{2\text{-}700}$	3057/3001/2945/2927/2877/2842/2801	-
$SiO_{2\text{-}200}$	3018/3005/2955/2930/2894/2648/2802	-

Figure S2.

Solid-state NMR of (COD)Pt(Me)$_2$@SiO2$_{-200}$

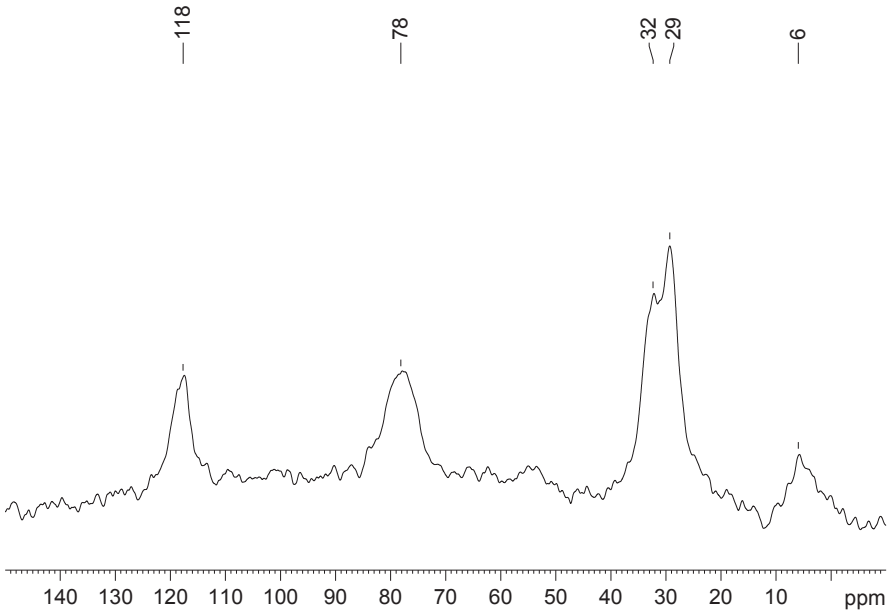

^{13}C CP/MAS solid state NMR spectra of (COD)Pt(Me)$_2$@SiO$_{2\text{-}200}$ (d1 = 6 s, 10484 scans, lb=100Hz)

Solid-state NMR of (COD)Pt(Me)$_2$@SiO$_{2\text{-}700}$

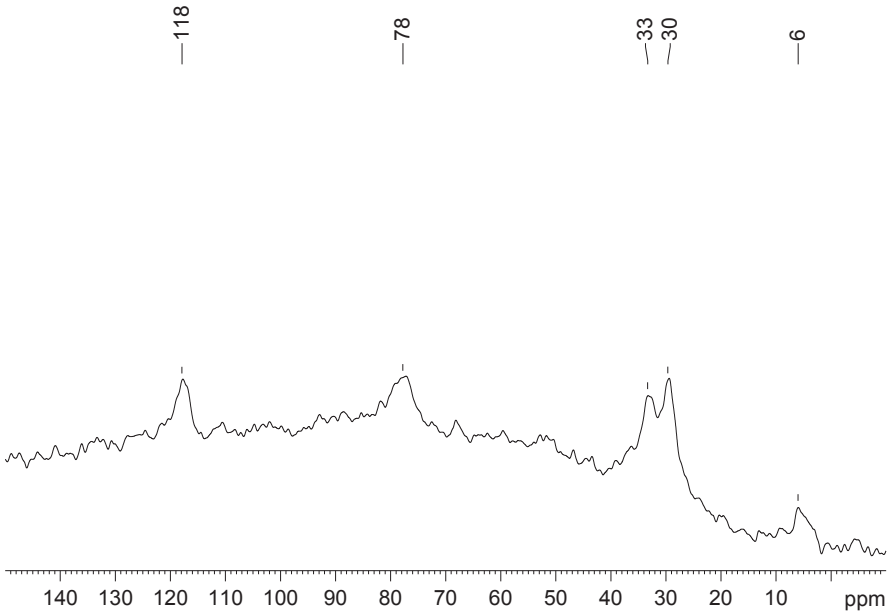

^{13}C CP/MAS solid state NMR spectra of (COD)Pt(Me)$_2$@SiO$_{2\text{-}700}$ (d1 = 4 s, 33702 scans, lb=100Hz)

Solid-state NMR of (COD)Pt(Me)$_2$ mixed in the solid state with SiO$_{2\text{-}700}$

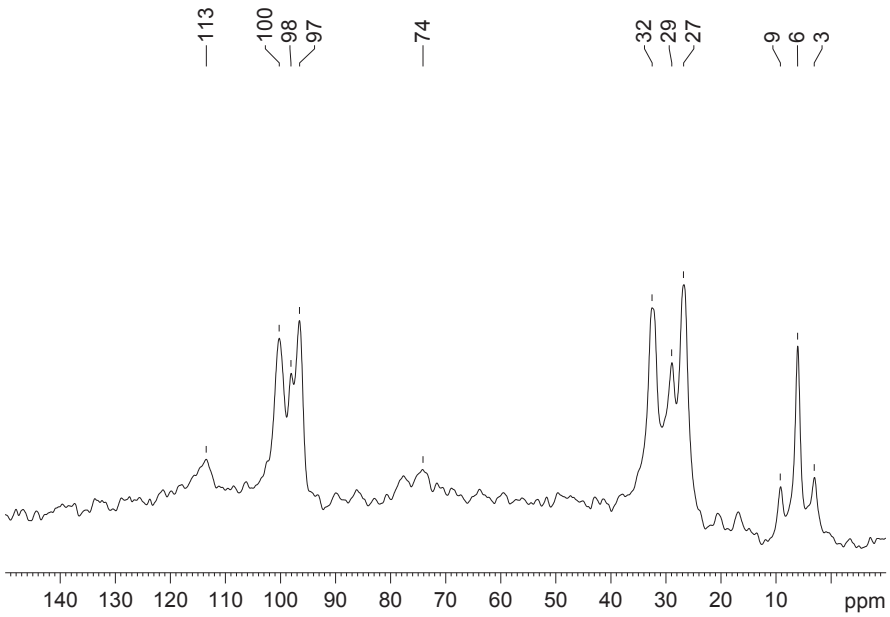

^{13}C CP/MAS solid state NMR spectra of (COD)Pt(Me)$_2$ + SiO$_{2\text{-}700}$ (d1 = 2 s, 3433 scans, lb=100Hz)

Figure S3. TEM

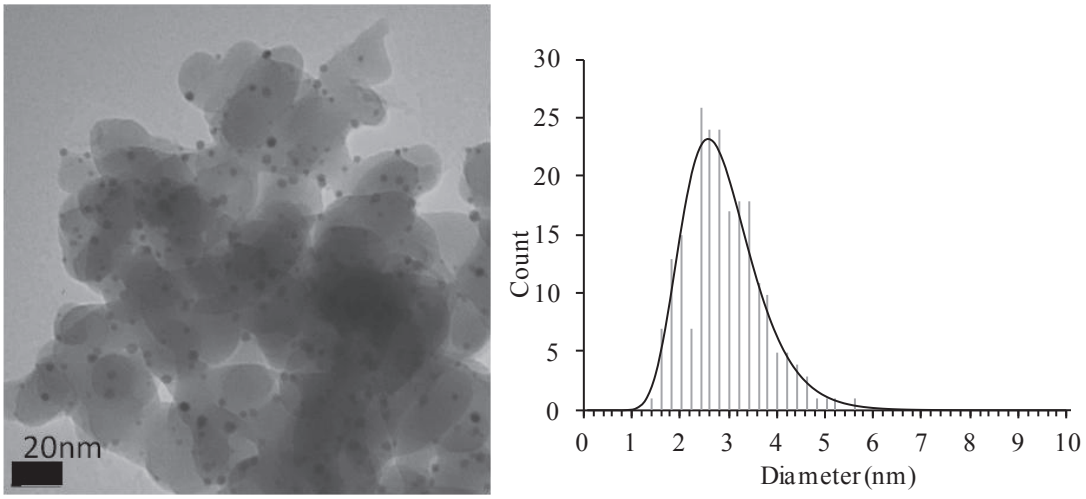

(COD)Pt(Me)$_2$@SiO$_{2\text{-}200}$ treated under static H_2 atmosphere. 170 nanoparticles count. Mean size 3.0 (σ = 0.7) nm.

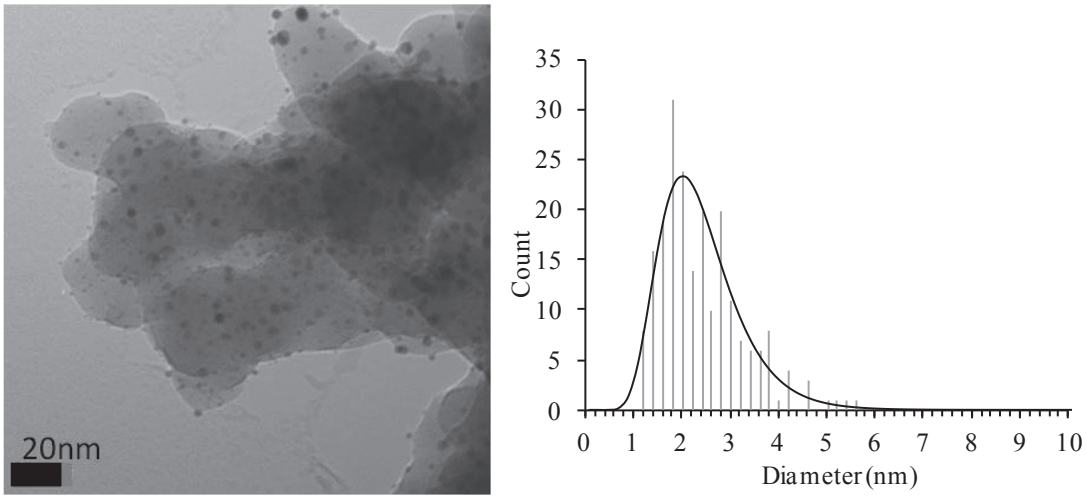

(COD)Pt(Me)$_2$@SiO$_{2\text{-}700}$ treated under static H2 atmosphere. 212 nanoparticles count. Mean size 2.4 (σ = 0.9) nm.

Appendix 3. (COD)Pt(OSi(O*t*Bu)$_3$)$_2$

Figure S4. IR-DRIFT

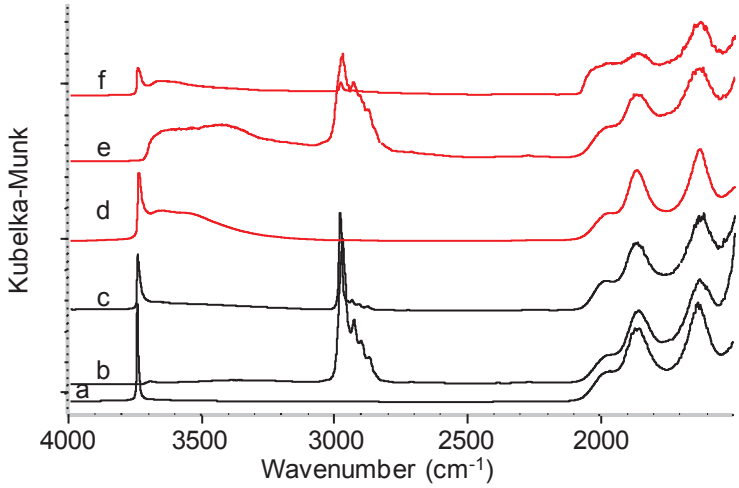

a) $SiO_{2\text{-}700,}$ b) (COD)Pt(OSi(OtBu)$_3$)$_2$@$SiO_{2\text{-}700}$, c) after static H_2 treatment, d) $SiO_{2\text{-}200}$, e) (COD)Pt(OSi(OtBu)$_3$)$_2$@$SiO_{2\text{-}200}$, f) after static H_2 treatment

	grafted	after H_2
$SiO_{2\text{-}700}$	3370/2975/2933/2905/2876	2982/2955/2938/2913/2880
$SiO_{2\text{-}200}$	3420/2975/2931/2905/2876/2850	2984/2040

Figure S5.

Solid-state NMR of (COD)Pt(OSi(OtBu)$_3$)$_2$@SiO$_{2\text{-}200}$

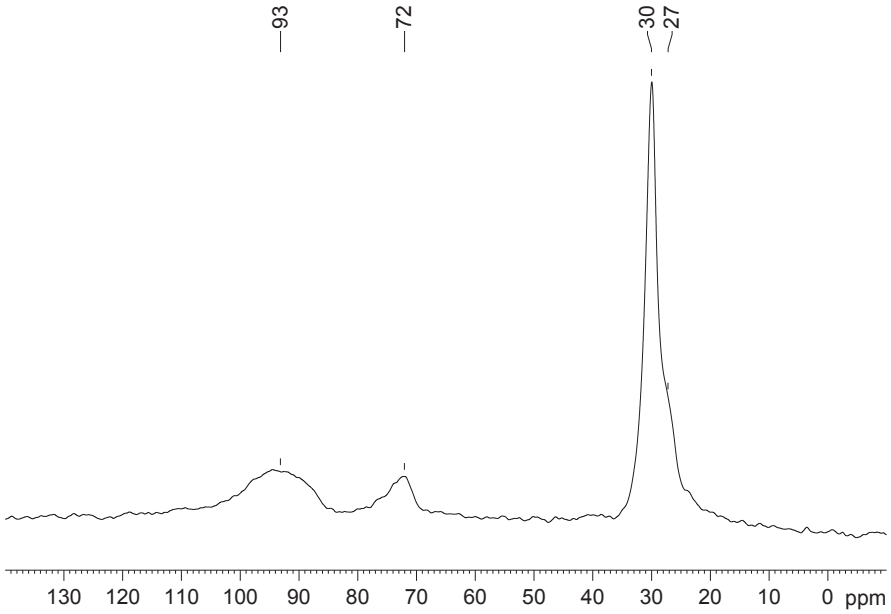

13C CP/MAS solid state NMR spectra of (COD)Pt(OSi(OtBu)$_3$)$_2$@SiO$_{2\text{-}200}$ (d1 = 4 s, 12766 scans, lb=100Hz)

Solid-state NMR of (COD)Pt(OSi(OtBu)$_3$)$_2$@SiO$_{2\text{-}700}$

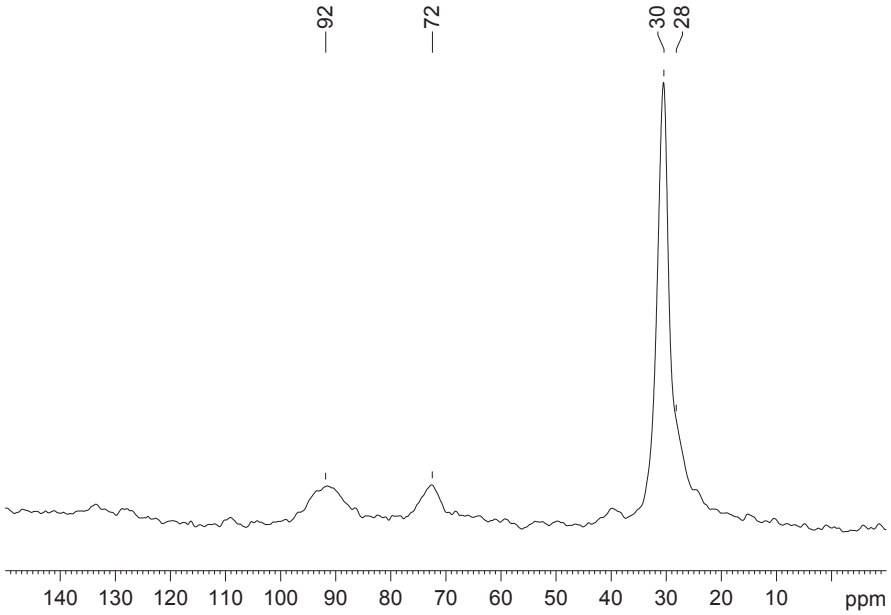

13C CP/MAS solid state NMR spectra of (COD)Pt(OSi(O*t*Bu)$_3$)$_2$@SiO$_{2\text{-}700}$ (d1 = 2 s,2618 scans, lb=50Hz)

Figure S6. TEM

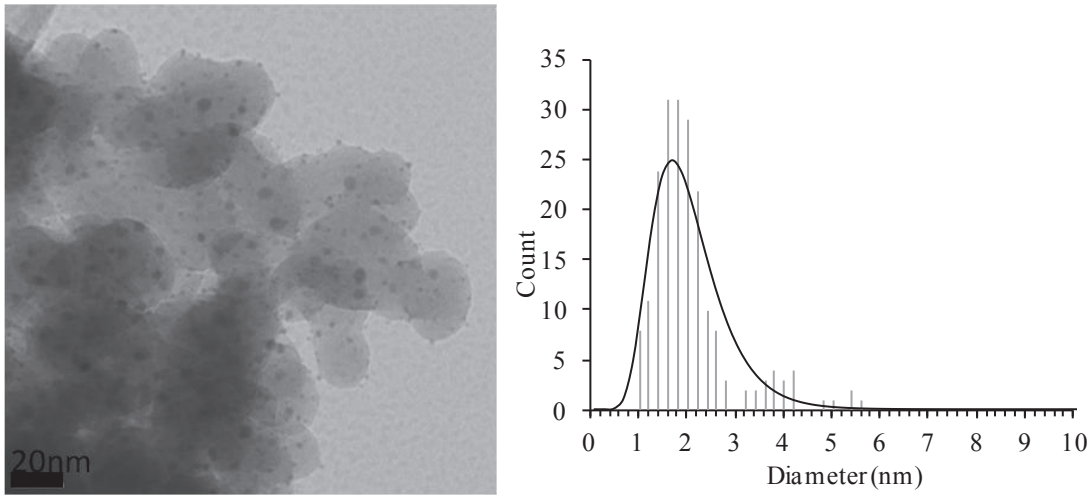

(COD)Pt(OSi(O*t*Bu)$_3$)$_2$@SiO$_{2\text{-}200}$ treated under static H_2 atmosphere. 200 nanoparticles count. Mean size 2.1 (σ = 0.9) nm.

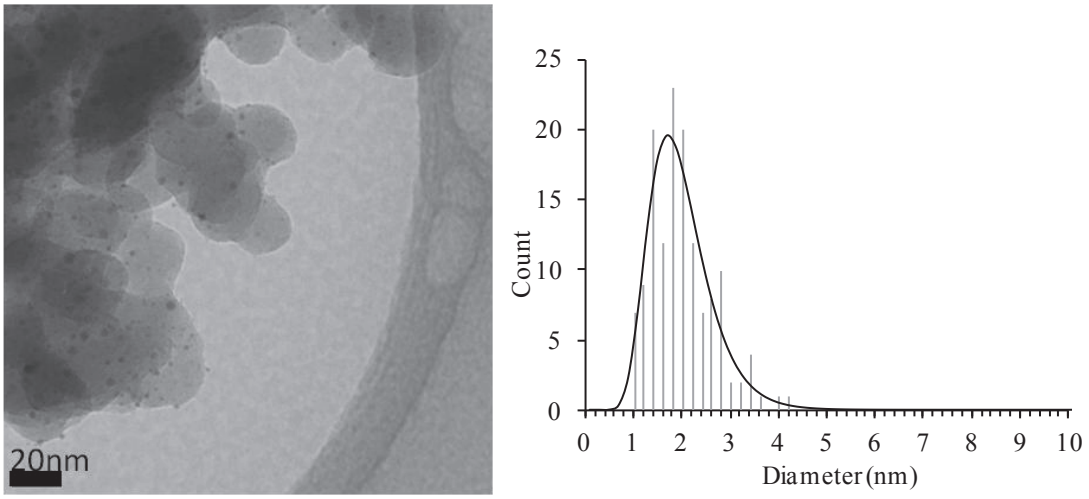

(COD)Pt(OSi(OtBu)$_3$)$_2$@SiO$_{2\text{-}700}$ treated under static H_2 atmosphere. 200 nanoparticles count. Mean size 2.0 (σ = 0.6) nm.

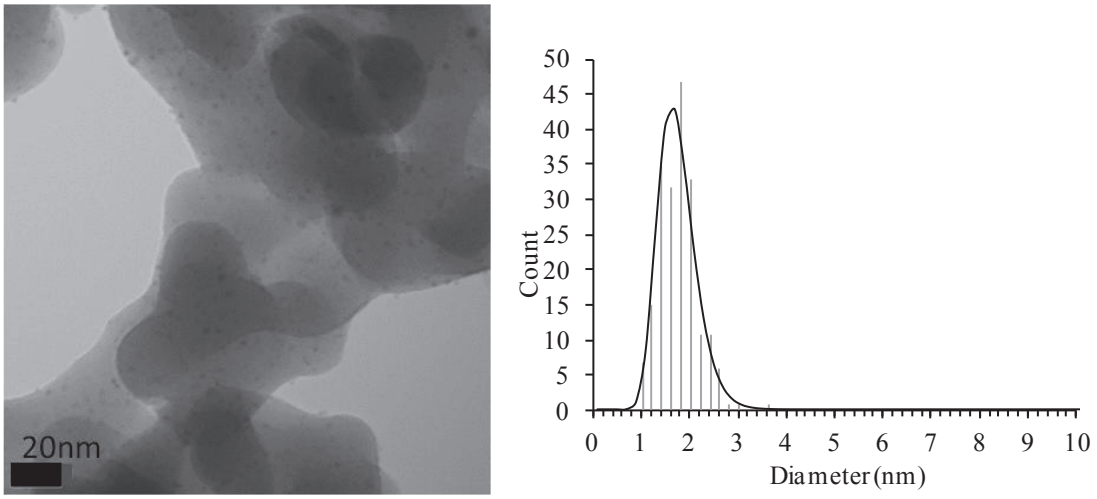

(COD)Pt(OSi(OtBu)$_3$)$_2$@SiO$_{2\text{-}700}$ treated under H_2 flow. 200 nanoparticles count. Mean size 1.8 (σ=0.4) nm.

Appendix 4. (COD)Pt(Me)(OSi(OtBu)$_3$)

Figure S7.

Liquid NMR of 2 (COD)Pt(Me)(OSi(OtBu)$_3$) in C_6D_6.

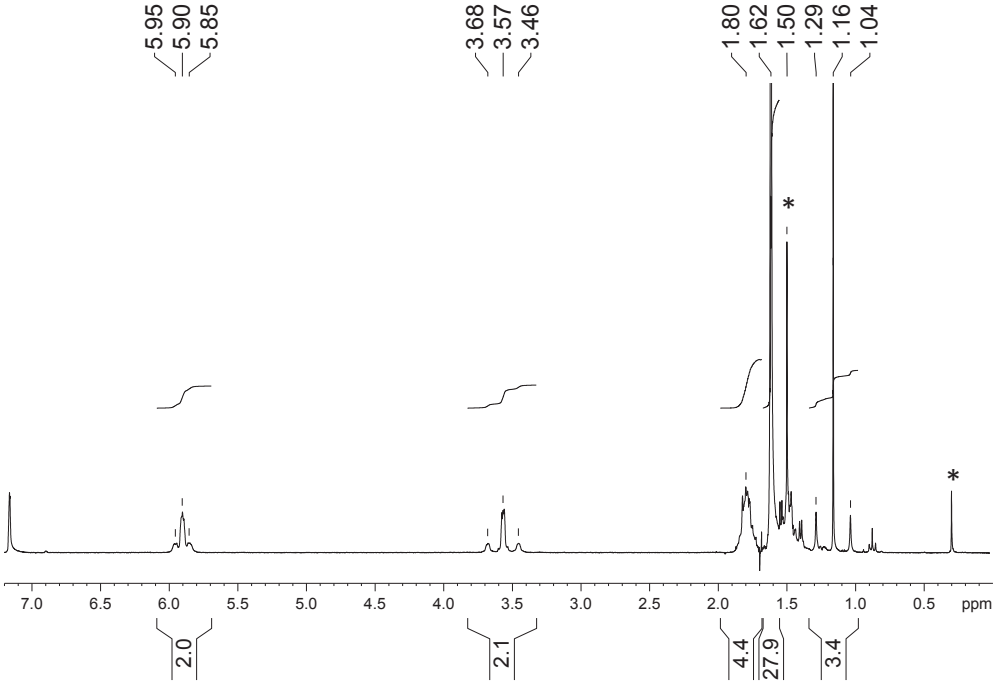

^{1}H NMR, d1=1sec, 8 scans.

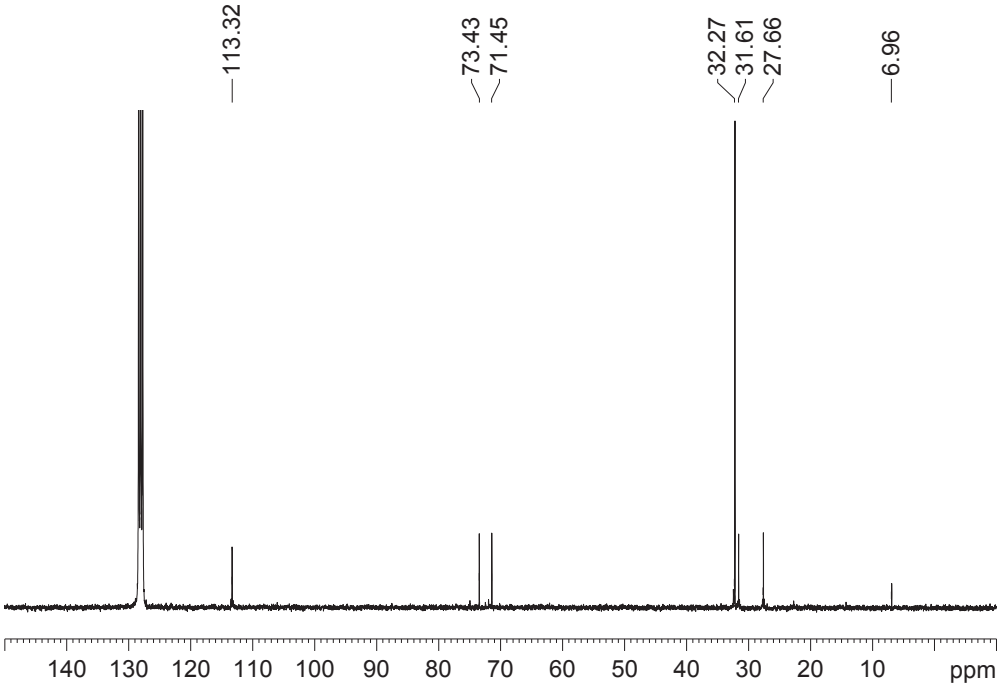

^{13}C NMR in C6D6, d1=1sec, 17709 scans

^{1}H NMR (C_6D_6; δ, ppm): 1.16 (t, 3H, C*H$_3$,* JPt-H=75Hz), 1.50 (m, 4H, endo C*H$_2$*), 1.62 (s, 27H, OC*Me$_3$*), 1.80 (m, 4H, exo C*H$_2$*), 3.57 (t, 2H, =C*H*, trans to OSi, JPt-H=66 Hz), 5.90 (t, 2H, =C*H*, trans to CH_3, JPt-H=30Hz).

^{13}C NMR (C_6D_6; δ, ppm): 6.9 (s, *C*H_3, JPt-C=700 Hz), 27.6 (s, *C*H_2), 31.6 (s, *C*H_2), 32.2 (s, OC*Me*$_3$), 71.4 (s, O*C*Me$_3$), 73.4 (s, =CH, trans to OSi, JPt-C=227 Hz), 113.3 (s, =CH, trans to CH_3, JPt-C=26.5 Hz).

Figure S8. IR-DRIFT

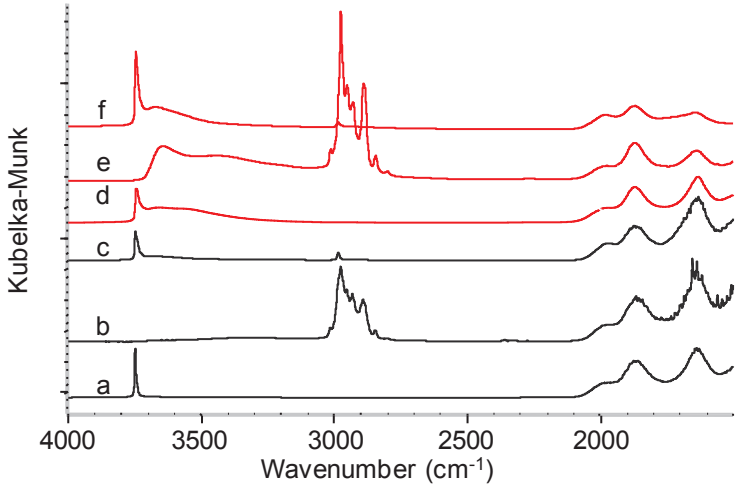

a) $SiO_{2\text{-}700}$, b) (COD)Pt(Me)(OSi(OtBu)$_3$)@$SiO_{2\text{-}700}$, c) after static H_2 treatment, d) $SiO_{2\text{-}200}$, e) (COD)Pt(Me)(OSi(OtBu)$_3$)@$SiO_{2\text{-}200}$, f) after static H_2 treatment

	grafted	after H_2
$SiO_{2\text{-}700}$	3015/2977/2954/2932/2893/2888/2846/2800	2983
$SiO_{2\text{-}200}$	3413/3013/2975/2951/2928/2890/2844/2801	2984

Figure S9.

Solid-state NMR of (COD)Pt(Me)(OSi(OtBu)$_3$@SiO$_{2\text{-}200}$

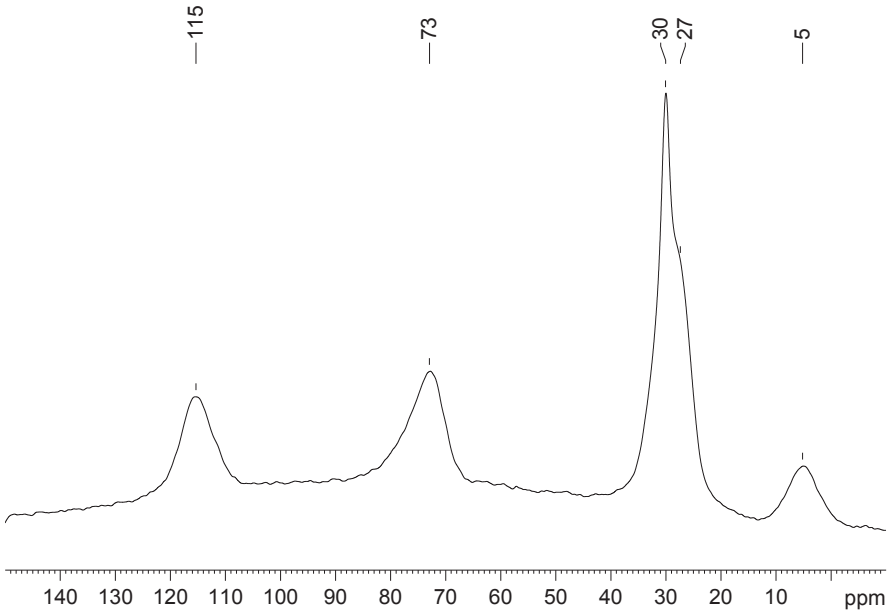

13C CP/MAS solid state NMR spectra of (COD)Pt(Me)(OSi(O*t*Bu)$_3$)@SiO$_{2\text{-}200}$ (d1 = 2 s, 100000 scans, lb=100Hz)

Solid-state NMR of CODPt(Me)(OSi(OtBu)$_3$)@SiO$_{2\text{-}700}$

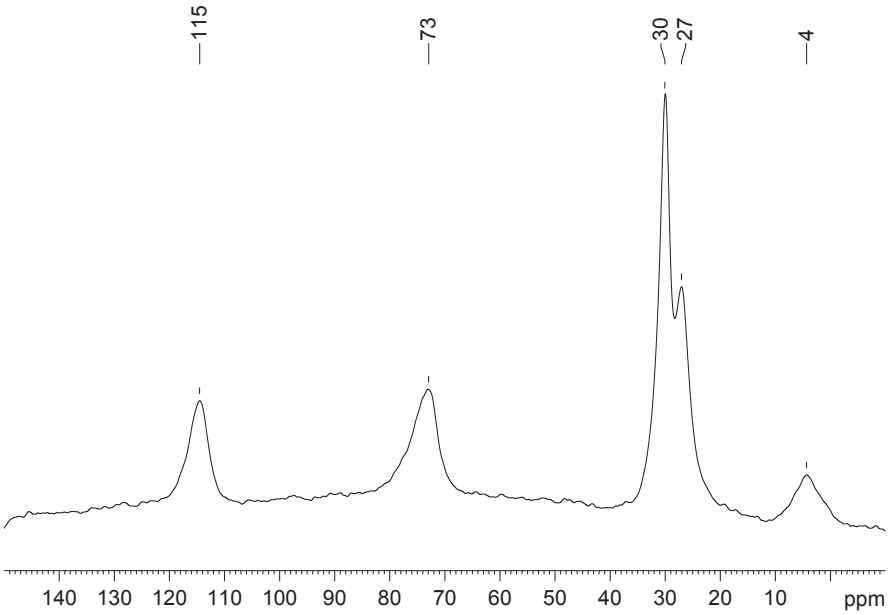

^{13}C CP/MAS solid state NMR spectra of (COD)Pt(Me)((OSi(O*t*Bu)$_3$)@SiO$_{2\text{-}700}$ (d1 = 6 s, 38069 scans, lb=100Hz)

Figure S10. TEM

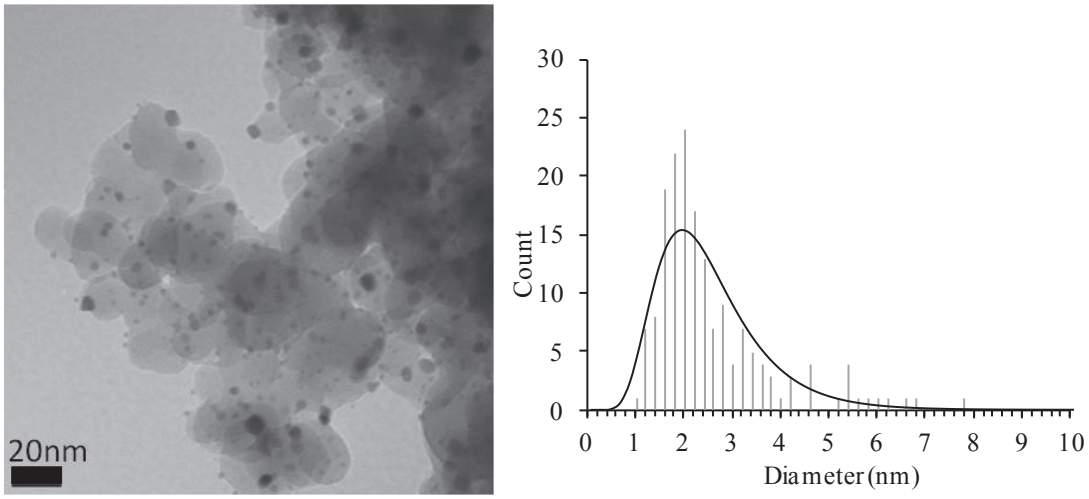

(COD)Pt(Me)((OSi(O*t*Bu)$_3$)@$SiO_{2\text{-}200}$ treated under static H_2. 170 nanoparticles count. Mean size 2.6 (σ = 1.2) nm.

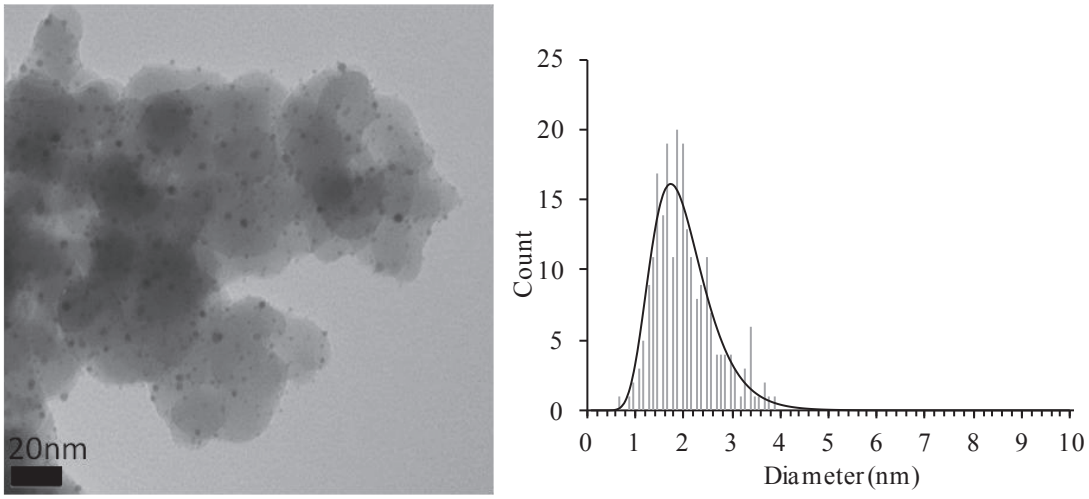

(COD)Pt(Me)(OSi(O*t*Bu)$_3$)/$SiO_{2\text{-}700}$ treated under static H_2. 226 nanoparticles count. Mean size 2.0 (σ = 0.6) nm.

Appendix 5. (COD)Pt(Me)N(SiMe$_3$)$_2$

Figure S11. Liquid NMR of 1 (COD)Pt(Me)N(SiMe$_3$)$_2$ in C_6D_6.

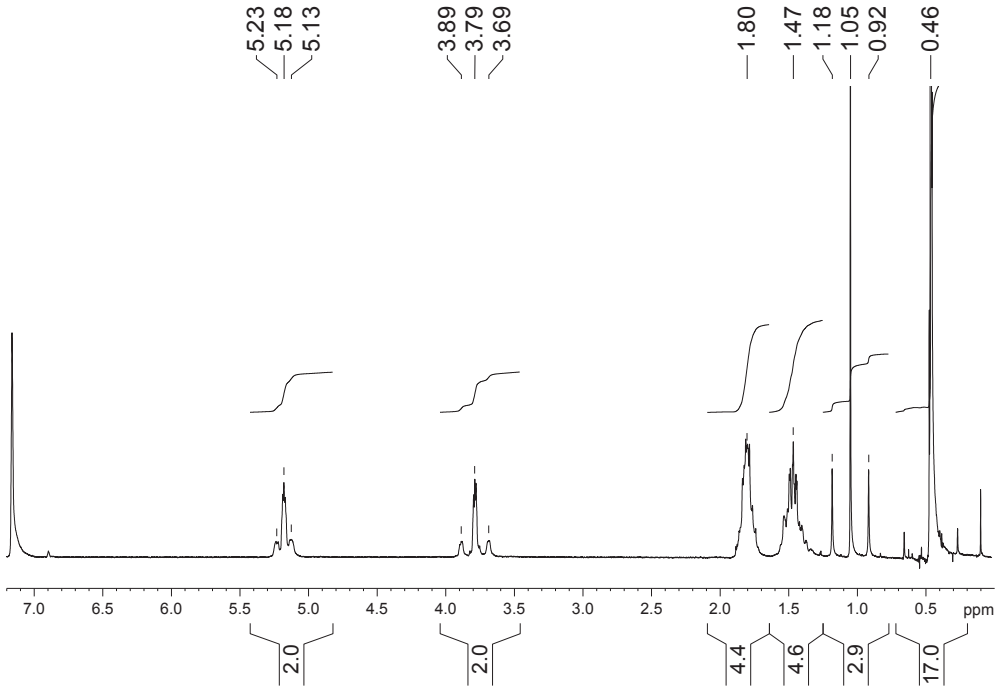

^{1}H NMR, d1=1sec, 8 scans.

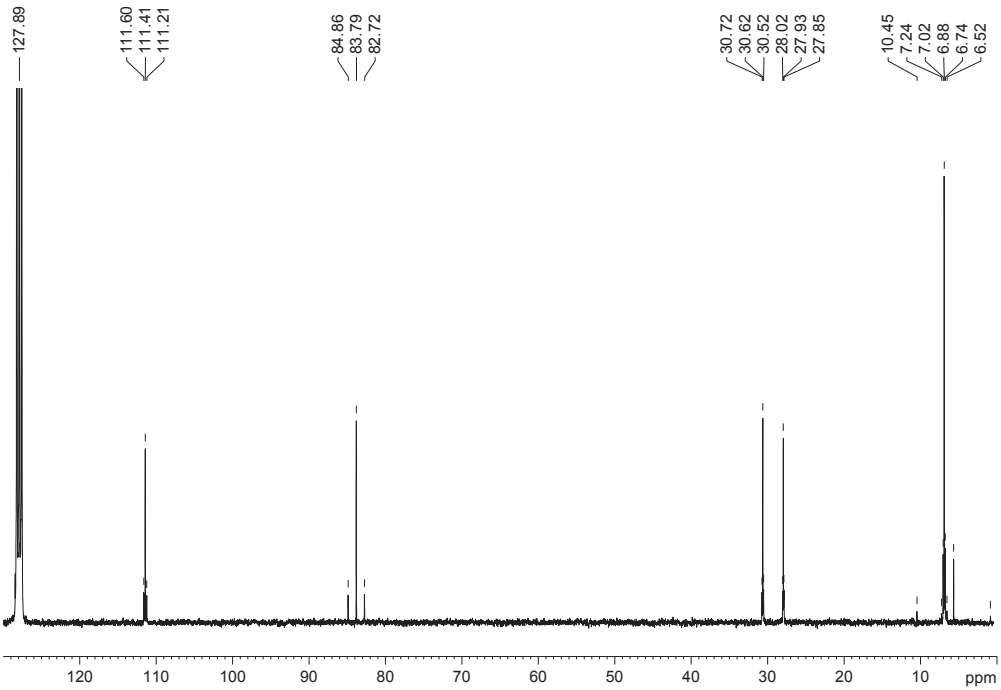

^{13}C NMR, d1=1sec, 10000 scans

^{1}H NMR (C6D6; δ, ppm): 0.46 (s, 18H, -Si*Me$_3$*), 1.05 (t, 3H, Pt-C*H$_3$*, JPt-H=80Hz), 1.47 (m, 4H, endo C*H$_2$*), 1.80 (m, 4H, exo C*H$_2$*), 3.79 (t, 2H, =C*H*, trans to N, JPt-H=60 Hz), 5.18 (t, 2H, =C*H*, trans to CH_3, JPt-H=30Hz).

^{13}C NMR (C6D6; δ, ppm): 5.8 (t, *C*H_3, Me, JPt-C=726.8 Hz), 6.8 (m, Si*C*H3), 28.1 (t, *C*H_2, JPt-C=12.9 Hz), 30.8 (t, *C*H_2, JPt-C=15.9 Hz), 83.9 (t, =*C*H, trans to N, JPt-C=161.3 Hz), 111.6 (s, =*C*H, trans to CH_3, JPt-C=29.4 Hz).

Figure S12. IR-DRIFT

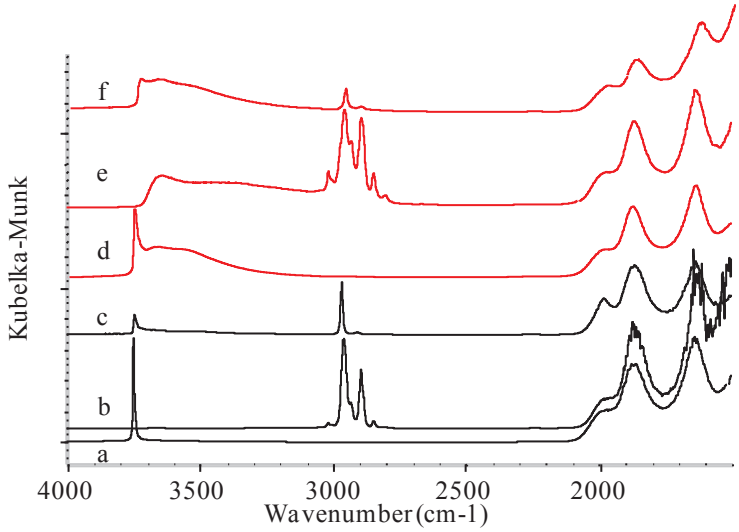

a) $SiO_{2\text{-}700}$, b) (COD)Pt(Me)($N(SiMe_3)_2$)@$SiO_{2\text{-}700}$, c) after static H_2 treatment, d) $SiO_{2\text{-}200}$, e) (COD)Pt(Me)($N(SiMe_3)_2$)@$SiO_{2\text{-}200}$, f) after static H_2 treatment

	grafted	after H_2
$SiO_{2\text{-}700}$	3017/3002/2962/2957/2932/2895/2846/2802	3747/2966//2907/1980
$SiO_{2\text{-}200}$	3014/3000/2954/2927/2890/2844/2796	2965/2905/1982

Figure S13.

Solid-state NMR of (COD)Pt(Me)(N(SiMe$_3$)$_2$)@SiO$_{2\text{-}200}$

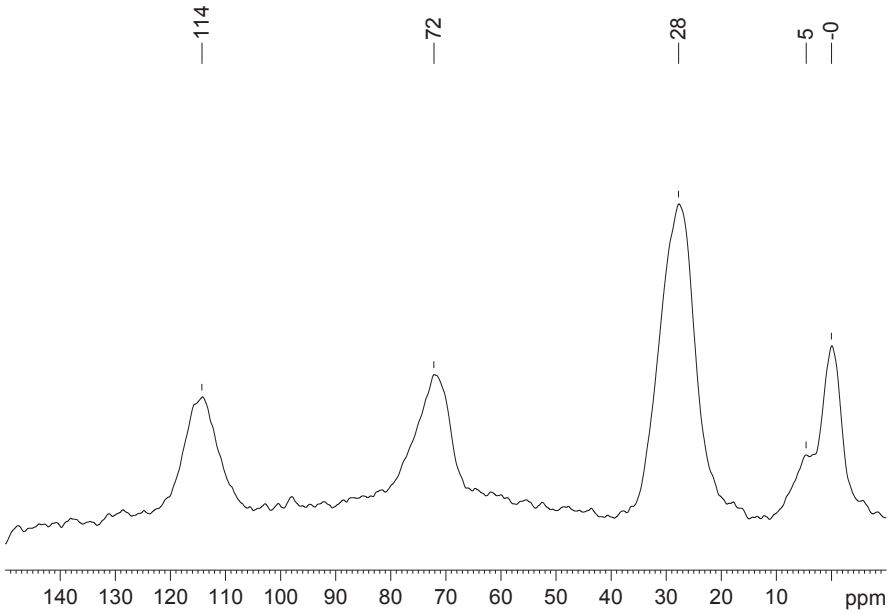

^{13}C CP/MAS solid state NMR spectra of (COD)Pt(Me)(N(SiMe$_3$)$_2$)/SiO$_{2\text{-}(200)}$ (d1 = 2 s, 26482 scans, lb=100Hz)

Solid-state NMR of (COD)Pt(Me)N(SiMe$_3$)$_2$@SiO$_{2\text{-}700}$

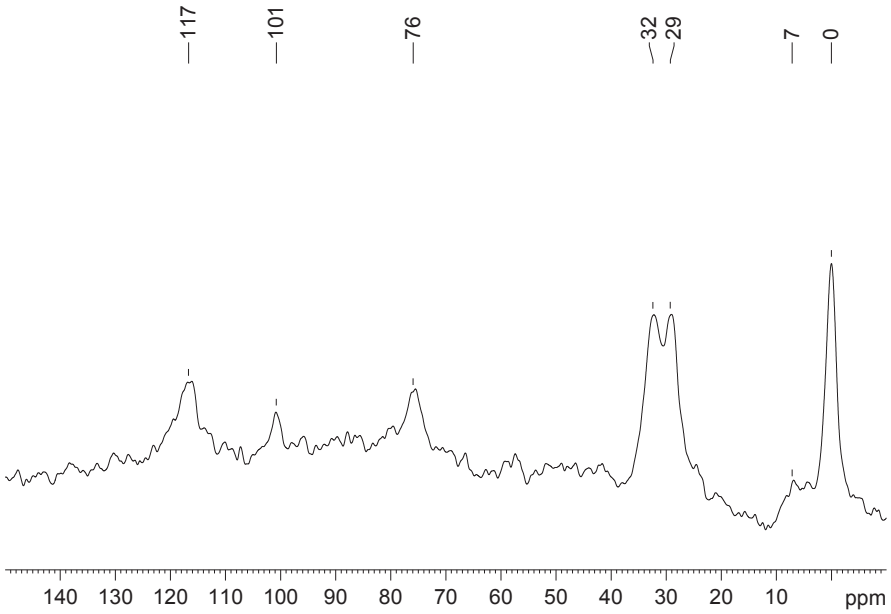

^{13}C CP/MAS solid state NMR spectra of (COD)Pt(Me)(N(SiMe$_3$)$_2$)@SiO$_{2\text{-}700}$ (d1 = 2 s, 10379 scans, lb=100Hz)

Figure S14. TEM

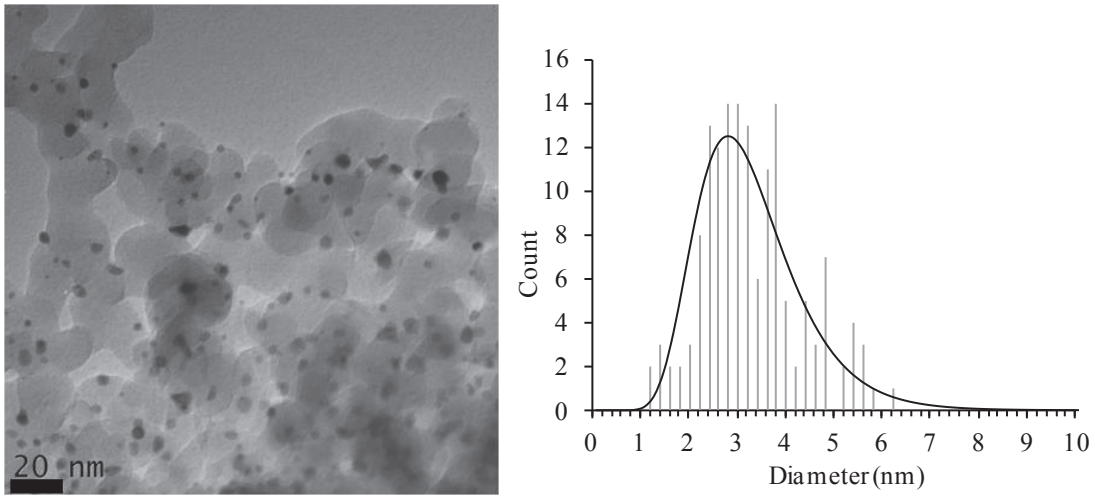

(COD)Pt(Me)(N(SiMe$_3$)$_2$)@SiO$_{2\text{-}200}$ treated under static H_2. 150 nanoparticles count. Mean size 3.3 (σ = 1.0) nm.

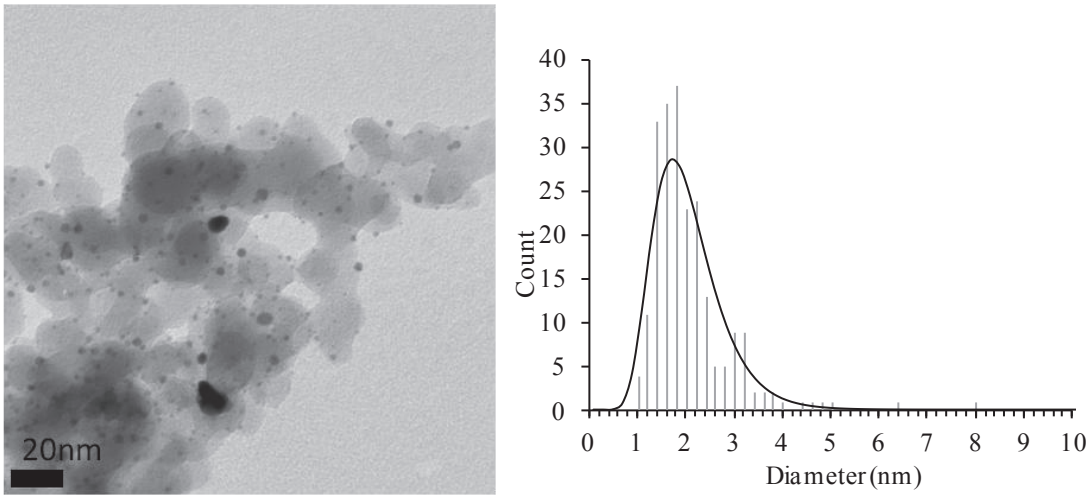

(COD)Pt(Me)(N(SiMe$_3$)$_2$)@SiO$_{2\text{-}700}$ treated under static H_2 atmosphere. 221 nanoparticles count. Mean size 2.1 (σ = 0.9) nm.

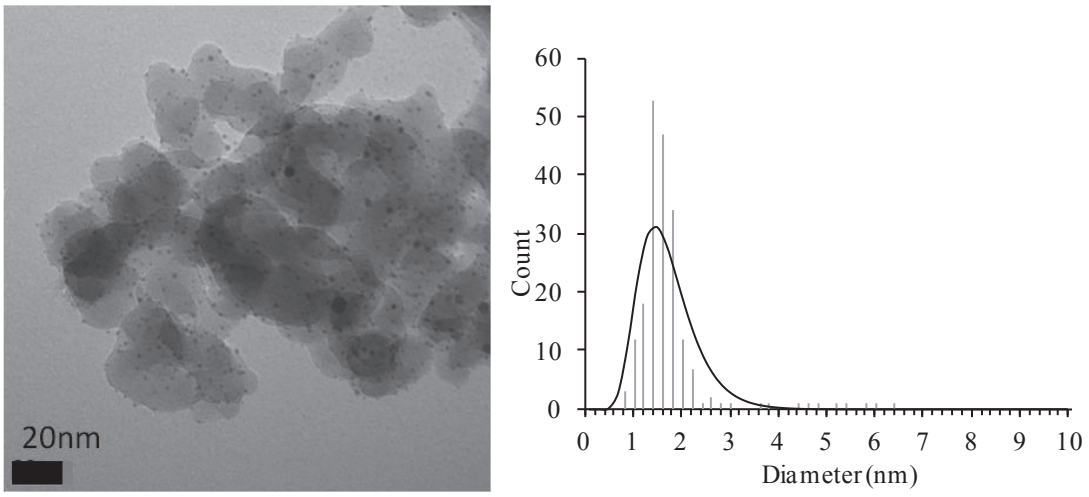

(COD)Pt(Me)(N(SiMe$_3$)$_2$)@SiO$_{2\text{-}700}$ treated under H_2 flow. 221 nanoparticles count. Mean size 1.7 (σ = 0.8) nm.

Appendix 6. (COD)Pt(Cl)(N(SiMe$_3$)$_2$)

Figure S15. IR-DRIFT

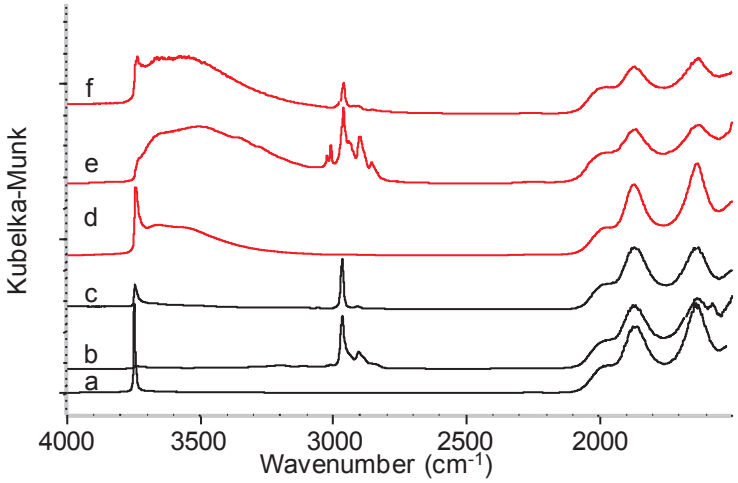

a) $SiO_{2\text{-}700}$, b) (COD)Pt(Cl)(N(SiMe$_3$)$_2$)@$SiO_{2\text{-}700}$, c) after static H_2 treatment, d) $SiO_{2\text{-}200}$, e) (COD)Pt(Cl)(N(SiMe$_3$)$_2$)@$SiO_{2\text{-}200}$, f) after static H_2 treatment

	grafted	after H_2
$SiO_{2\text{-}700}$	3022/3008/2964/2934/2902/2888	2966/2907
$SiO_{2\text{-}200}$	3023/3009/2962/2942/2934/2900/2853	2964/2907

Figure S16.

Solid-state NMR of (COD)Pt(Cl)(N(SiMe$_3$)$_2$@SiO$_{2\text{-}200}$

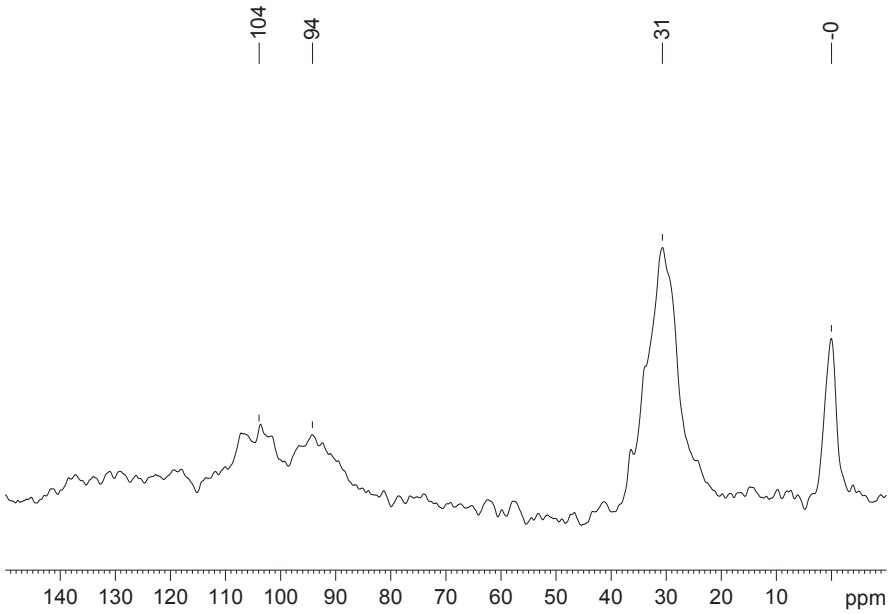

^{13}C CP/MAS solid state NMR spectra of (COD)Pt(Cl)(N(SiMe$_3$)$_2$)@SiO$_{2\text{-}200}$ (d1 = 14 s, 12312 scans, lb=100Hz)

Solid-state NMR of (COD)Pt(Cl)(N(SiMe$_3$)$_2$@SiO$_{2\text{-}700}$

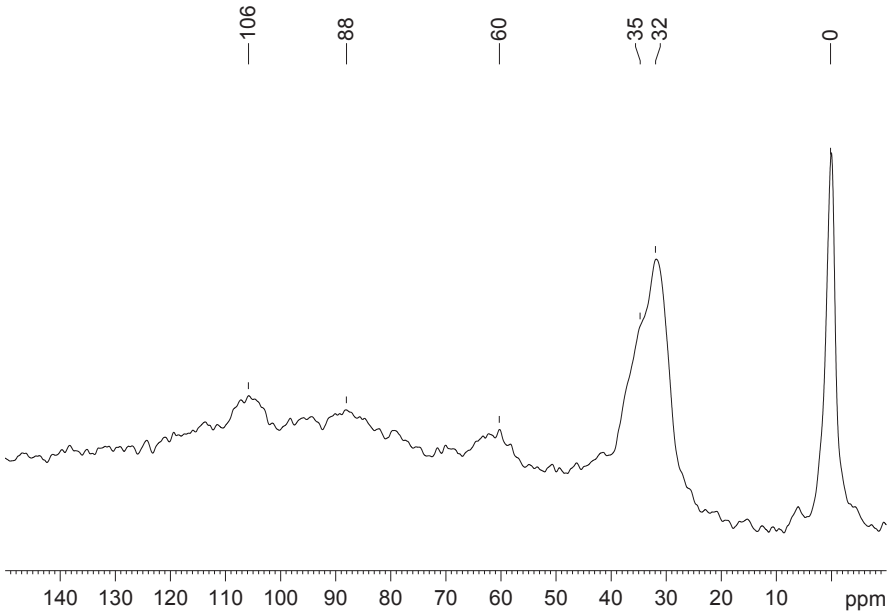

^{13}C CP/MAS solid state NMR spectra of (COD)Pt(Cl)(N(SiMe$_3$)$_2$)@SiO$_{2\text{-}700}$ (d1 = 4 s, 39207 scans, lb=100Hz)

Note: the additional peak at 60 ppm is attributed to physisorbed diethylether.

Figure S17. TEM

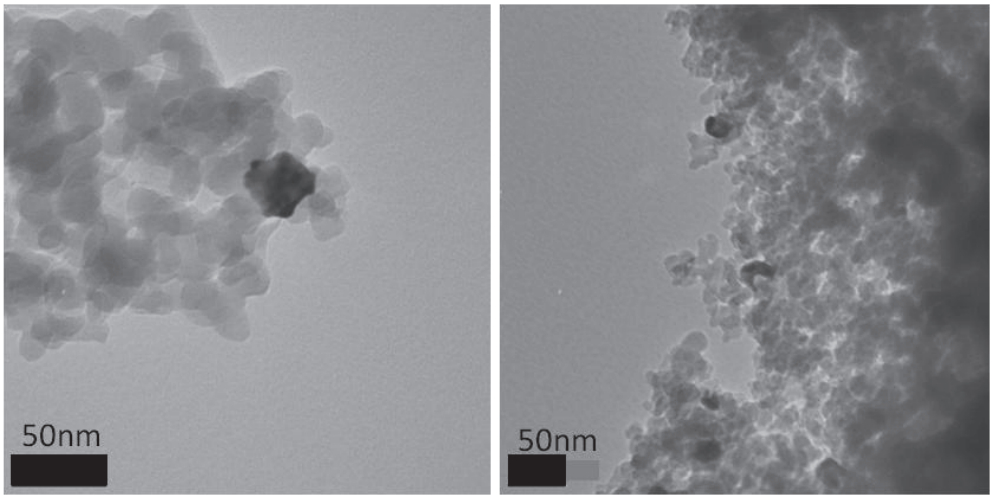

(COD)Pt(Cl)(N(SiMe$_3$)$_2$)@SiO$_{2\text{-}200}$ treated under static H_2 atmosphere.

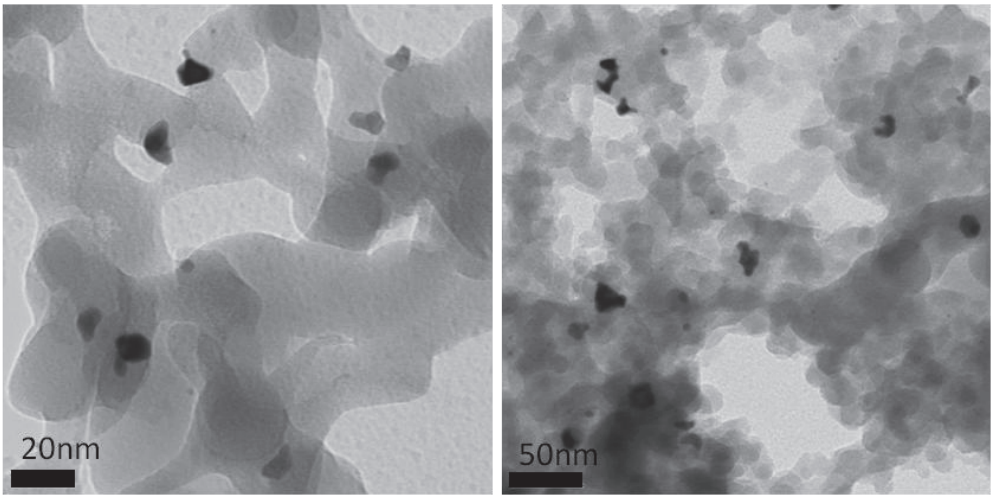

(COD)Pt(Cl)(N(SiMe$_3$)$_2$)@SiO$_{2\text{-}700}$ treated under static H_2 atmosphere.

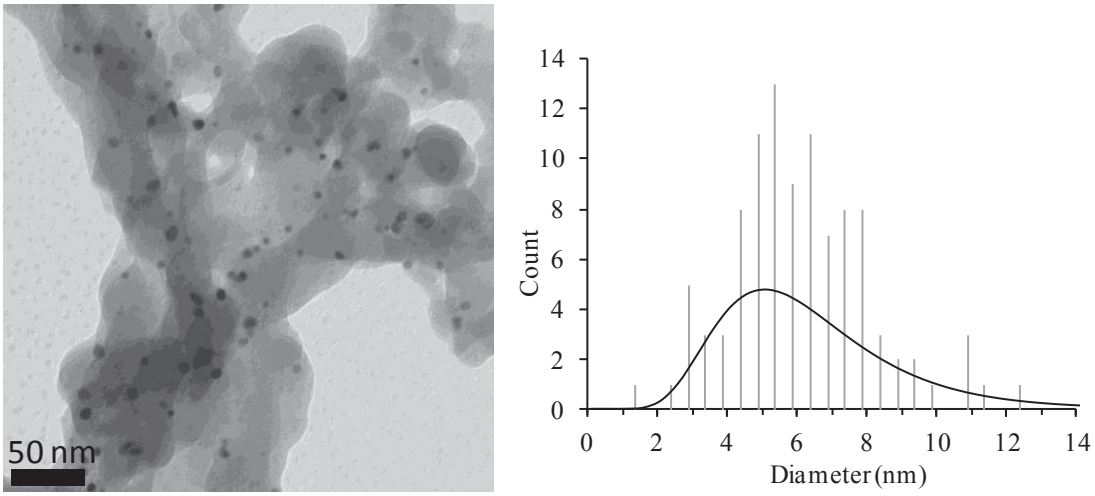

(COD)Pt(Cl)(N(SiMe$_3$)$_2$)@SiO$_{2\text{-}700}$ treated under H_2 flow. 103 nanoparticles count. Mean size 6.3 (σ = 2.4) nm.

Appendix 7. (COD)Pt(OSi(O*t*Bu)$_3$)(N(SiMe$_3$)$_2$)

Figure S18. Liquid state NMR of 3 (COD)Pt(OSi(OtBu)$_3$)(N(SiMe$_3$)$_2$) in C_6D_6.

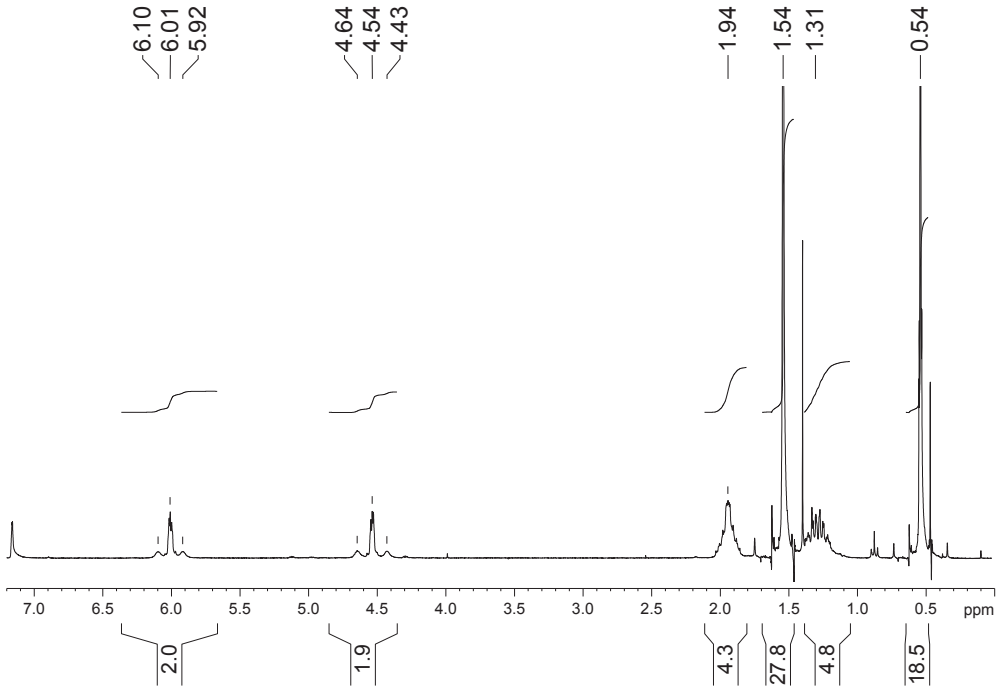

^{1}H NMR , d1=1sec, 8 scans.

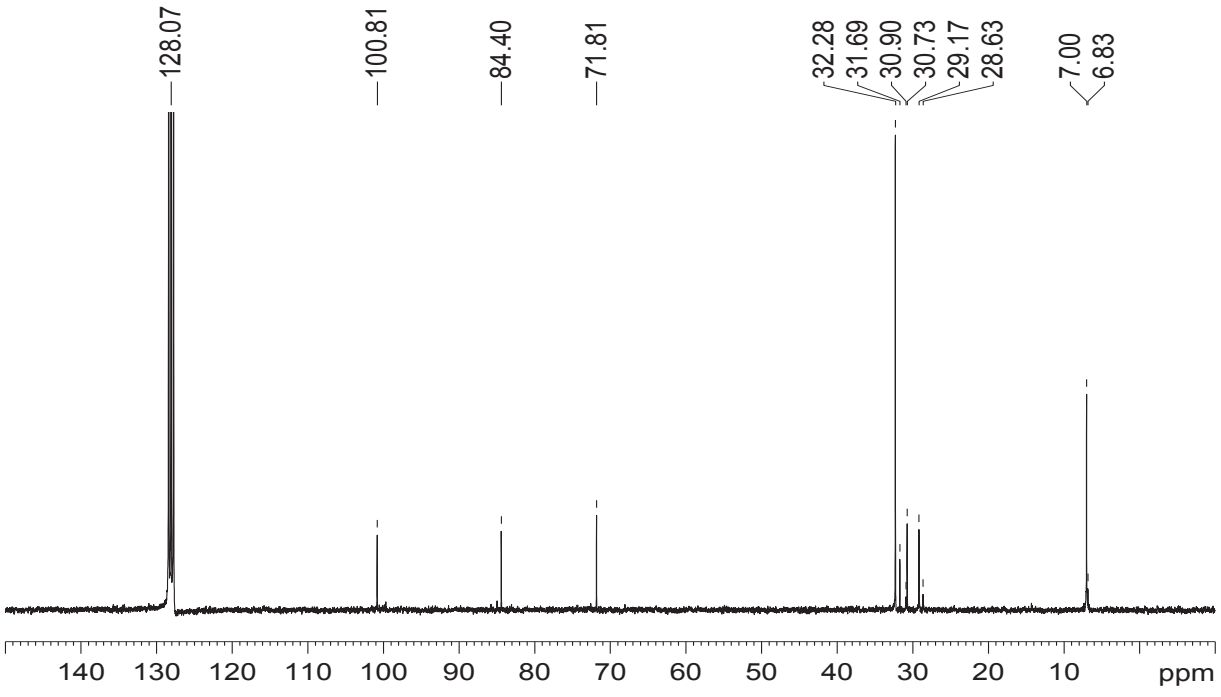

^{13}C NMR, d1=1sec, 1875 scans.

^{1}H NMR (C6D6; δ, ppm): 0.54 (s, 18H, -Si*Me$_3$*), 1.31 (m, 4H, endo C*H$_2$*), 1.54 (s, 27H, OC*Me$_3$*), 1.94 (m, 4H, exo C*H$_2$*), 4.55 (t, 2H, =C*H*, trans to OSi, JPt-H=66 Hz), 6.01 (t, 2H, =C*H*, trans to N, JPt-H=51Hz).

^{13}C NMR (C6D6; δ, ppm): 6.8 (s, OC*Me*$_3$), 7.0 (s, Si*Me*$_3$), 29.2 (s, *C*H$_2$), 30.7 (s, *C*H$_2$, COD), 32.3 (s, OC*Me*$_3$), 71.8 (s, O*C*Me$_3$), 84.4 (s, =CH, trans to OSi), 100.8 (s, =CH, trans to N).

Figure S19. IR-DRIFT

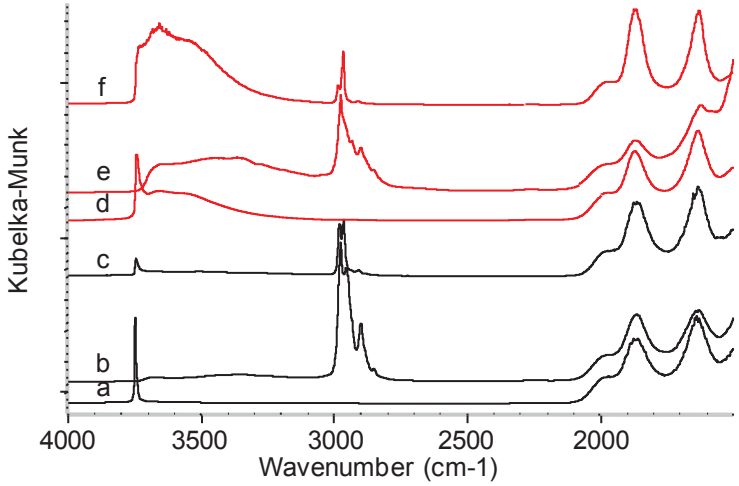

a) $SiO_{2\text{-}700}$, b) (COD)Pt(OSi(O*t*Bu)$_3$)(N(SiMe$_3$)$_2$)@$SiO_{2\text{-}700}$, c) after static H_2 treatment, d) $SiO_{2\text{-}200}$, e) (COD)Pt(OSi(O*t*Bu)$_3$)(N(SiMe$_3$)$_2$)@$SiO_{2\text{-}200}$, f) after static H_2 treatment

	grafted	after H_2
$SiO_{2\text{-}700}$	2976/2956/2951/2899/2851	2981/2965/2909
$SiO_{2\text{-}200}$	2977/2958/2933/2900/2852	2983/2964/2906

Figure S20.

Solid-state NMR of (COD)Pt(N(SiMe$_3$)$_2$)(OSi(OtBu)$_3$)@SiO$_{2\text{-}200}$

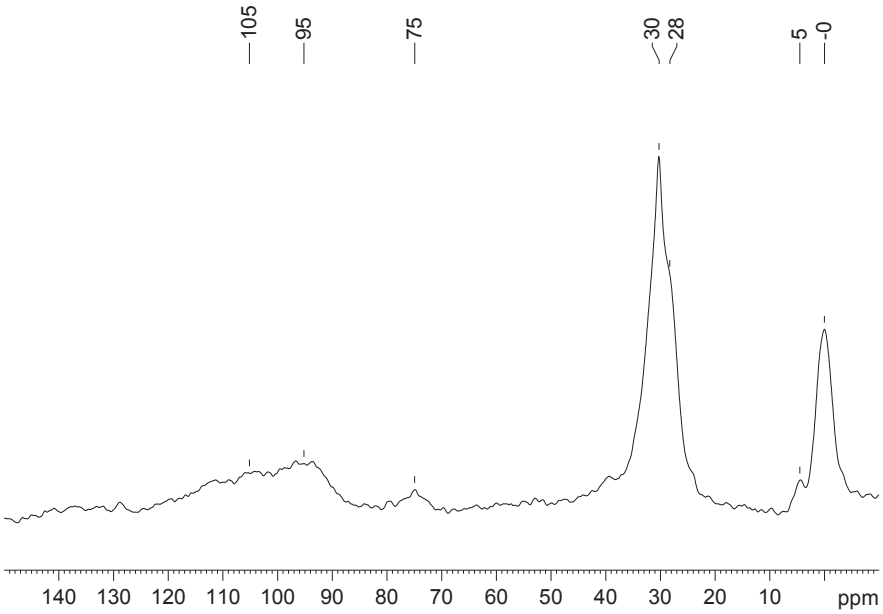

^{13}C CP/MAS solid state NMR spectra of (COD)Pt(N(SiMe$_3$)$_2$)(OSi(O*t*Bu)$_3$)@SiO$_{2\text{-}200}$ (d1 = 4 s, 12490 scans, lb=100Hz)

Solid-state NMR of CODPt(N(SiMe$_3$)$_2$)(OSi(OtBu)3)@SiO$_{2\text{-}700}$

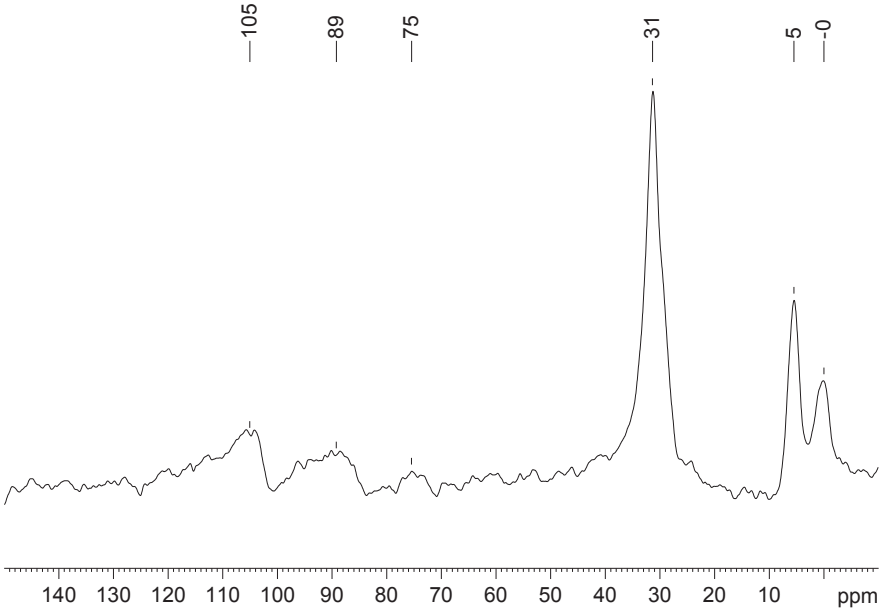

^{13}C CP/MAS solid state NMR spectra of CODPt(N(SiMe$_3$)$_2$)(OSi(O*t*Bu)$_3$)@SiO$_{2\text{-}700}$ (d1 = 2 s, 10416 scans, lb=100Hz)

Figure S21. TEM

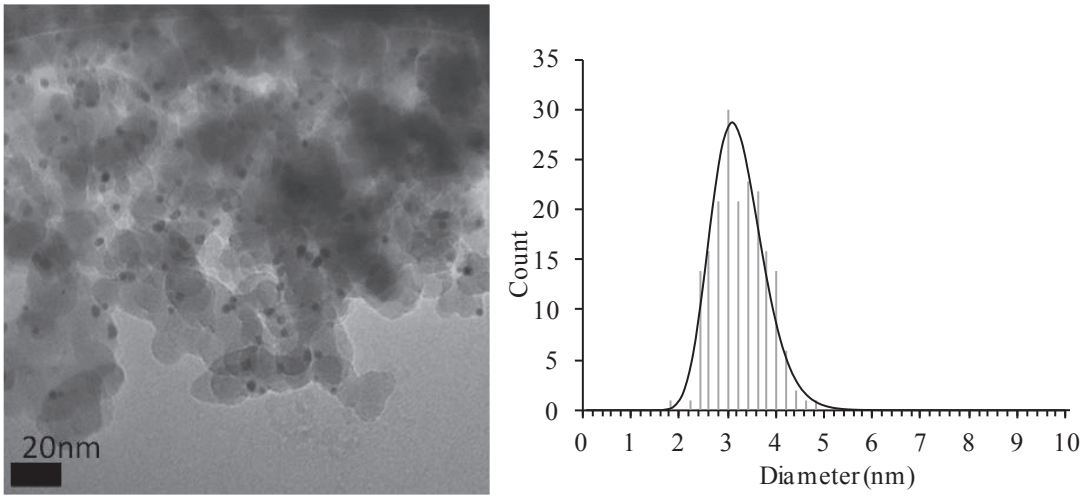

(COD)Pt(OSi(O*t*Bu)$_3$)(N(SiMe$_3$)$_2$)@SiO$_{2\text{-}200}$ treated under static H_2 atmosphere. 189 nanoparticles count. Mean size 3.2 (σ = 0.5).

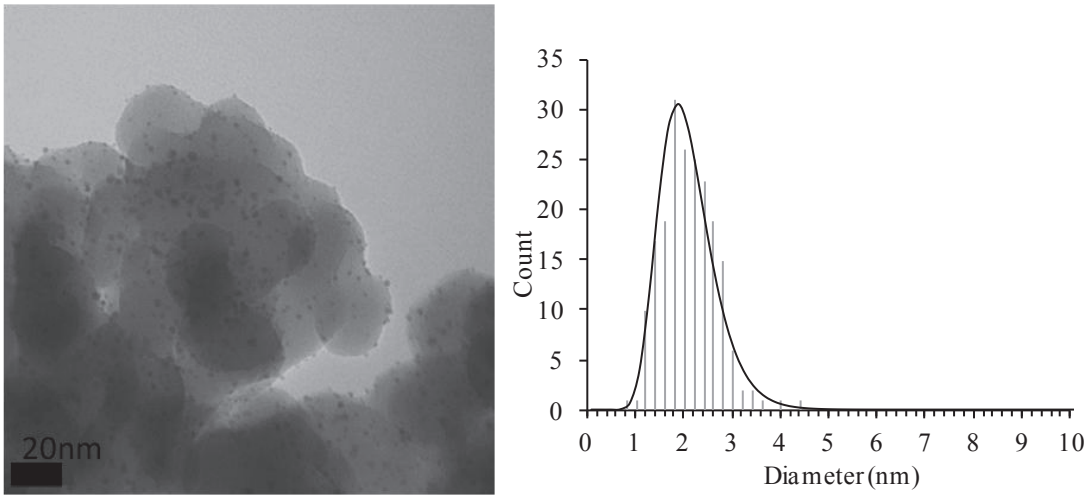

(COD)Pt(OSi(OtBu)$_3$)(N(SiMe$_3$)$_2$)@SiO$_{2\text{-}700}$ treated under static H_2 atmosphere. 200 nanoparticles count. Mean size 2.1 (σ = 0.6).

Appendix 8. HOSi(O*t*Bu)$_3$

For the methyl-siloxy complexes grafting, IR-DRIFT reveals the presence of tBu units on the surface, to address the question whether the silanol is absorbed or grafted on the surface, $SiO_{2\text{-}700}$ was contacted with 1.2 equivalents of tris(tert-butoxy)silanol in pentane for 3 hours followed by multiple washings and secondary vacuum drying, mimicking the full process of a grafting procedure. Typical tBu ν(C-H) vibrations at 2982, 2938, 2912 and 2877 cm^{-1} are observed by IR-DRIFT. A large IR-band is observed at 3360 cm^{-1} and can be attributed to the silanol of absorbed tris(tert-butoxy)silanol. By ^{13}C SS-NMR the **C**(CH$_3$)$_3$ and C(**C**H$_3$)$_3$ are respectively found at 71 and 30 ppm.

After treatment under H_2 under static atmosphere *t*Bu unit are still present at the surface as demonstrated by IR-DRIFT spectroscopy and consumption of surface OH is evidenced by the intensity diminution of the band at 3747 cm^{-1}. Those observations indicates the probable formation of SiO bonds thus anchoring the tris(tert-butoxy)silanol to the surface.

Figure S22. Solid-state NMR of HOSi(OtBu)$_3$ absorbed onto SiO$_{2\text{-}700}$

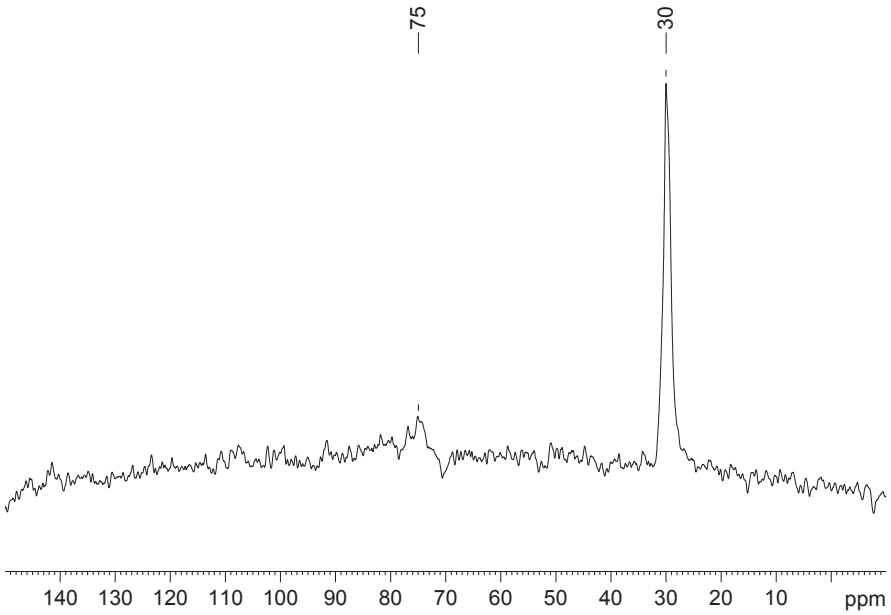

^{13}C CP/MAS solid state NMR spectra of HOSi(O*t*Bu)$_3$@SiO$_{2\text{-}700}$ (d1 = 2 s, 28529 scans, lb=100Hz)

Figure S23. IR-DRIFT

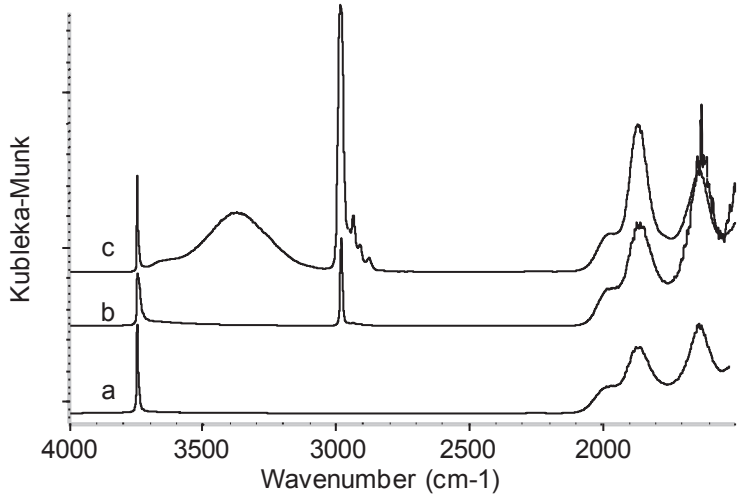

a) $SiO_{2\text{-}700}$, b) after static H_2 treatment, c) $HOSiO(tBu_3)_3@SiO_{2\text{-}700}$

	grafted	after H_2
$SiO_{2\text{-}700}$	3370/2983/2937/2911/2878	3747/2983

Figure S24

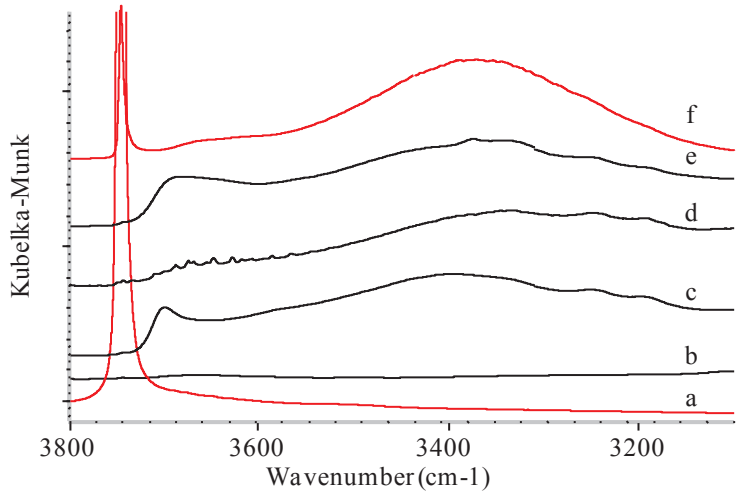

IR-DRIFT spectra of a) $SiO_{2\text{-}700}$, b) $(COD)Pt(Me)(N(SiMe_3)_2@SiO_{2\text{-}700}$, c) $(COD)Pt(OSi(OtBu)_3)_2@SiO_{2\text{-}700}$, d) $(COD)Pt(Me)(OSi(OtBu)_3)@SiO_{2\text{-}700}$, e) $(COD)Pt(OSi(OtBu)_3)(N(SiMe_3)_2@SiO_{2\text{-}700}$, f) $HOSi(OtBu)_3@SiO_{2\text{-}700}$ (smaller Y scale).

Appendix 9. ^{13}C SS-NMR spectra of Pt complexes grafted onto SiO_{2-200}.

Figure S25.

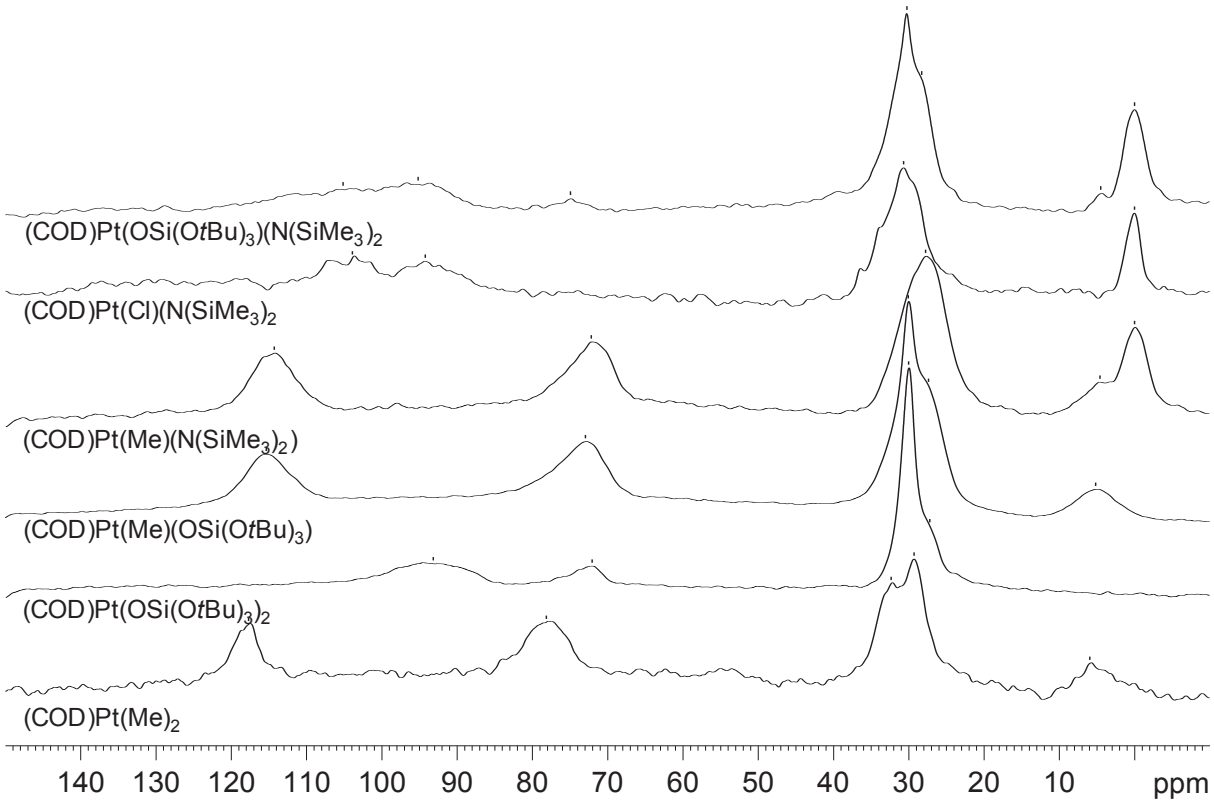

Appendix 10. Maximum surface coverage for (COD)Pt(R)(OSi≡) species

The maximum radius of the grafted molecule is determined from DRX data of (COD)Pt(R)(OSi(O*t*Bu)$_3$) when available. For (COD)Pt(Cl)(OSi≡) the measure is derived from the (COD)Pt(CH$_3$)(OSi(O*t*Bu)$_3$) complex, considering the carbon atom of the methyl ligand as a chlorine atom. We consider the molecules as discs in dense packing, with a surface density of 0.9069.

R	radius Å	disc surface nm^2	Pt.nm^{-2}
Me	0.37	0,43	2,6
Cl	0.36	0,40	2,8
OSi(OtBu)3	0.60	1,12	1,0
N(SiMe3)2	0.52	0,83	1,3

Appendix 11. Blank experiment, absorption of Et_2O onto ceria, 13C CP/MAS NMR spectrum.

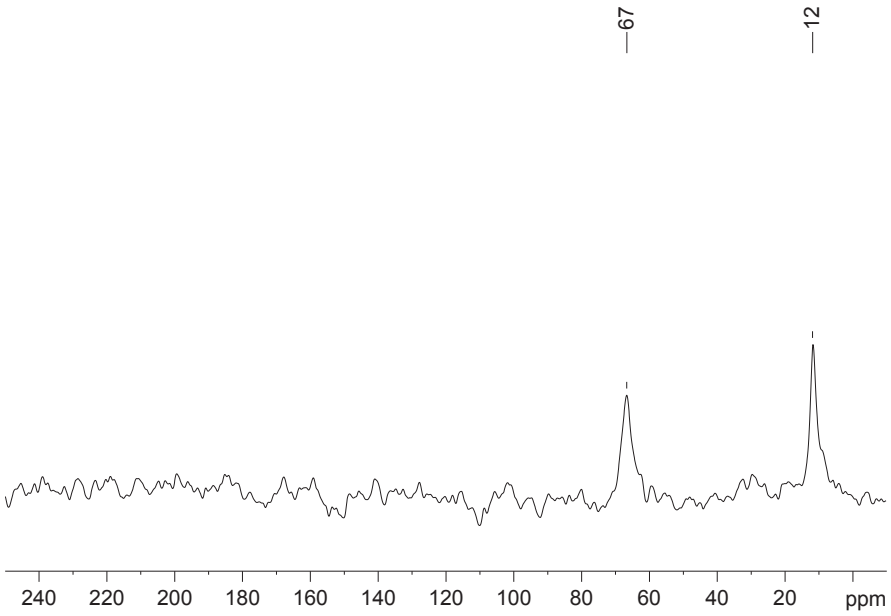

30000 scans, d1 = 2 sec, lb = 100 Hz

Appendix 12. Grafting onto $CeO_{2\text{-}400}$

(COD)Pt(Me)$_2$

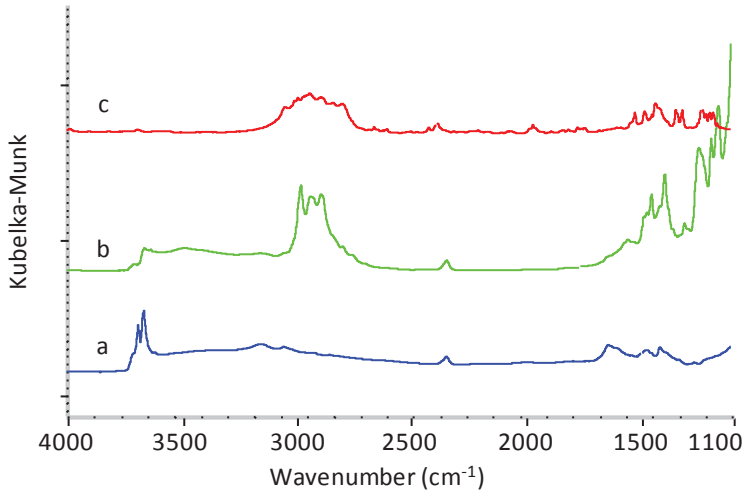

a) $CeO_{2\text{-}400}$, b) $(COD)Pt(Me)_2@CeO_{2\text{-}400}$, c) $(COD)Pt(Me)_2$

(COD)Pt(Me)(N(SiMe$_3$)$_2$)

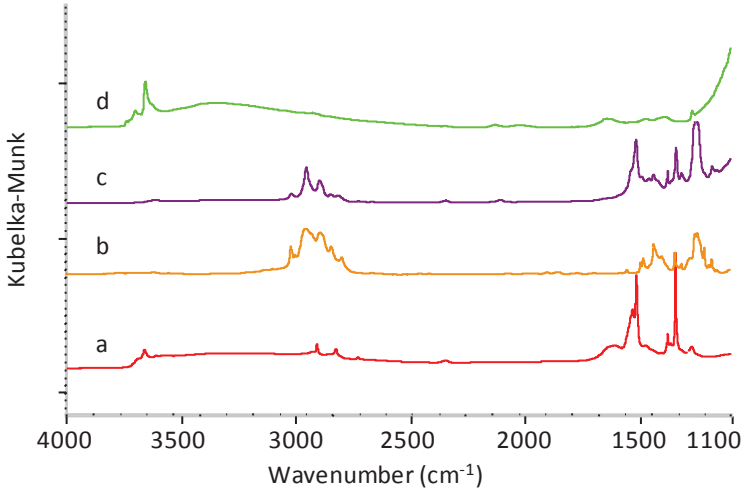

a) $CeO_{2\text{-}400}$, b) (COD)Pt(Me)(N(SiMe$_3$)$_2$)@$CeO_{2\text{-}400}$, c) (COD)Pt(Me)(N(SiMe$_3$)$_2$), d) after static H_2, 300°C, 15 h.

(COD)Pt(Cl)(N(SiMe$_3$)$_2$)

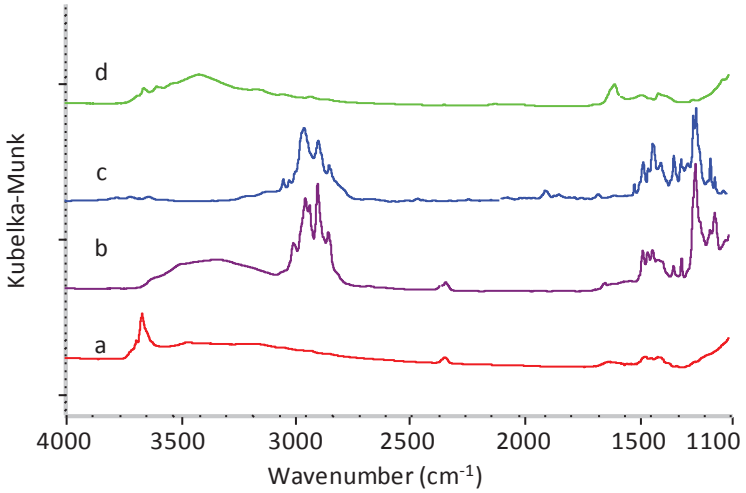

a) $CeO_{2\text{-}400}$, b) (COD)Pt(Cl)(N(SiMe$_3$)$_2$)@$CeO_{2\text{-}400}$, c) (COD)Pt(Cl)(N(SiMe$_3$)$_2$), d) after static H_2, 300°C, 15 h.

Appendix 13. TEM picture, (COD)Pt(Me)$_2$@CeO$_{2\text{-}400}$ treated under static H$_2$ atmosphere (150 mBar, 300°C, 15 h).

The red arrows are pointing to Pt nanoparticles.

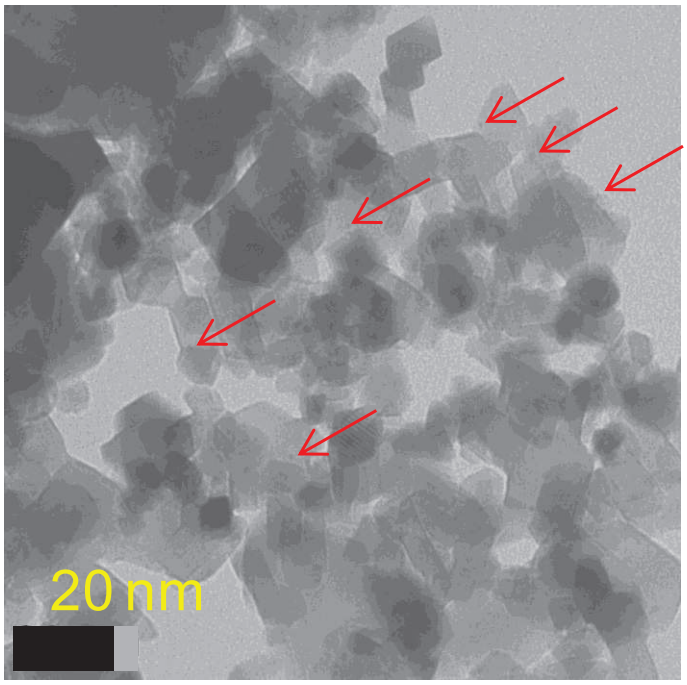

3. Platinum Nanoparticles deposited from (COD)Pt(OSi(O*t*Bu)$_3$)$_2$ on GDLs by DLI-MOCVD and application in fuel-cell catalysis

3.1. Introduction

New Platinum precursors are required for nanoparticles deposition by Metal Organic Chemical Vapor Deposition.[38] One of the aims is to lower the deposition temperature for process, cost and method versatility issues. For example at temperature above 300°C, gas diffusion layers used in fuel-cells are partially calcined and thus damaged, a lower deposition temperature would broaden the number of possible substrates used in MOCVD and thus possible applications of this technology. For this purpose a recently described platinum complex with a low degradation temperature,[92] (COD)Pt(OSi(O*t*Bu)$_3$)$_2$, was tested. Indeed, during thermogravimetric experiments under an N_2 flow and a heating ramp of 10°C/min Tilley *et al.*observed the decomposition of the product yielding pure Pt (ceramic yield 22.7 wt% vs 23.5 wt% theoretically), the loss of 1.8 equivalent of HOSi(O*t*Bu)$_3$ beeing shown by ^{1}H NMR experiments. The onset decomposition temperature is about 150°C and total decomposition is achieved around 230°C. This low decomposition temperature makes this precursor a good candidate for MOCVD as lower temperature will induce broader uses on fragile supports and lower costs.

3.2. Results and discussion

3.2.1. Precursor characterization

(COD)Pt(OSi(O*t*Bu)$_3$)$_2$ was synthesized according to the procedure developed by Tilley *et al.*[92] from (COD)Pt(Cl)$_2$ and NaOSi(O*t*Bu)$_3$)$_2$ with high yields (>80 %) and purity (for NMR see Appendix 14).

Platinum was then deposited starting from the thus-prepared Pt^{II} precursor onto gas diffusion layers (GDLs) used as fuel-cell catalyst supports.[107] Five deposition times were tested; experimental details can be found in part 4. The MOCVD process[108,109] was carried out on two types of GDLs: 24BC and E-TEK, note that 24BC (104.1 g.m^{-2}) has a paper-like morphology whereas E-TEK (178.8 g.m^{-2}) has a fabric-like structure; they are both coated on one side with microporous carbon. GDLs are preimpregnated with polytetrafluoroethylene (PTFE). This polymer has two functions: binding together the carbon fibers and giving hydrophobic properties to the GDL to avoid flooding at the cathode;[110] those

two GDLs being widely used for research purposes and current applications of PEM fuel cells.

3.2.2. Nanoparticles characterization

3.2.2.1. Elemental analysis results

Elemental analyses were performed by Inductively Coupled Plasma method (ICP), samples mainly contains carbon (80 wt%) and fluorine (20 wt%) from PTFE; all the results are summarized in Table 9.

Table 9. Elemental analyses, results in wt% are given with a ± 0.01 wt% error. This corresponds to 100 µg.cm^{-2} for 24BC and 180 µg.cm^{-2} for E-TEK.

deposition time (min)			20	45	60	75	100
24BC	wt%	Pt	0.02	0.02	0.04	0.02	0.06
		Si	0.03	0.02	0.03	0.03	0.02
	µg/cm²	Pt	208	208	416	208	625
		Si	312	208	312	312	208
molar ratio Si/Pt			10.4	6.9	5.2	10.4	2.3
E-TEK	wt%	Pt	0.01	0.01	0.02	0.02	0.03
		Si	0.03	0.03	0.04	0.03	0.04
	µg/cm²	Pt	179	179	358	358	536
		Si	536	536	715	536	715
molar ratio Si/Pt			20.8	20.8	13.9	10.4	9.3

Platinum loadings from 200 to 650 µg.cm^{-2} were obtained. A trend, showing the linear increase of the platinum loading versus the deposition time, can be obtained (Figure 37). By MOCVD, the deposition rate depends on the wettability of the support by the metallic precursors. Here the deposition rate is estimated to 5 µgPt.cm^{-2}.min^{-1} for the two GDL supports, which both exhibit similar physical properties.

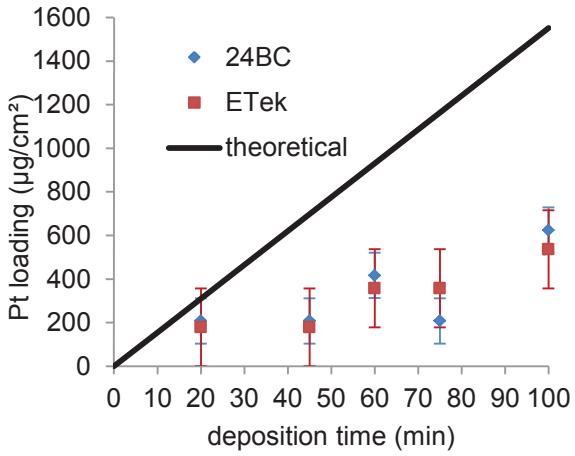

Figure 37. Platinum loading vs. deposition time

From this deposition rate, a deposition yield, defined as the ratio between the amounts of platinum effectively deposited over the one introduced, can be calculated. Measurements of the mass of solution (and thus the volume) used at each run were attempted but due to set up constraints the measured values were smaller than the error. After numerous runs the injector tends to be stuck with early decomposed precursor. This made it difficult to reliably link the deposition time with the amount of precursor introduced. A test was performed with pure toluene; in the present conditions we found a flow rate of about 0.75 mL.min^{-1}. Based on those values and given the diameter of the deposition chamber (20 cm) the theoretical platinum deposition rate is 15.5 µgPt.cm^{-2}.min^{-1}. The deposition yield is thus 32% in agreement with yields generally obtained in MOCVD (15 to 30 %)[111]. Work is under progress to recover the non-reacted precursors by trapping the MOCVD exhaust gas in order to increase the overall yield of this deposition method and thus make it more economically viable.

Note that at very low loadings, values found by elemental analyses fall within the experimental error. This explains the inconsistent results found for 75 minutes deposition time. Platinum loadings are comparable on either E-TEK or 24BC, showing that there is no major influence of the GDL type.

On both types of GDL the ratio of silicium to platinum decreases with increasing deposition time as depicted Figure 38. On E-TEK the total amount of silica is about twice the one found on 24BC. Those high ratio (a theoretical ratio of 2 would have been expected) could come from the early decomposition of platinum at the injector level leading to an atmosphere enriched with –OSi(O*t*Bu)$_3$ and the subsequent thermal decomposition of this ligand onto the GDLs.

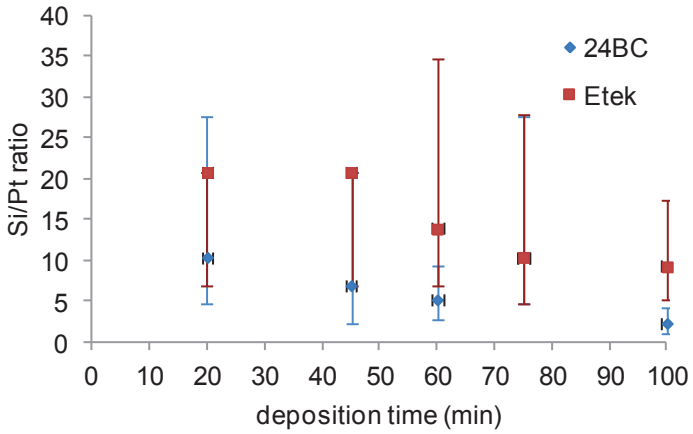

Figure 38. Evolution of the Si to Pt ratio versus deposition time

3.2.2.2. Transmission Electron Microscopy (TEM)

In order to evaluate the particle morphology, TEM grids have been introduced into the deposition chamber and used as substrates for MOCVD.

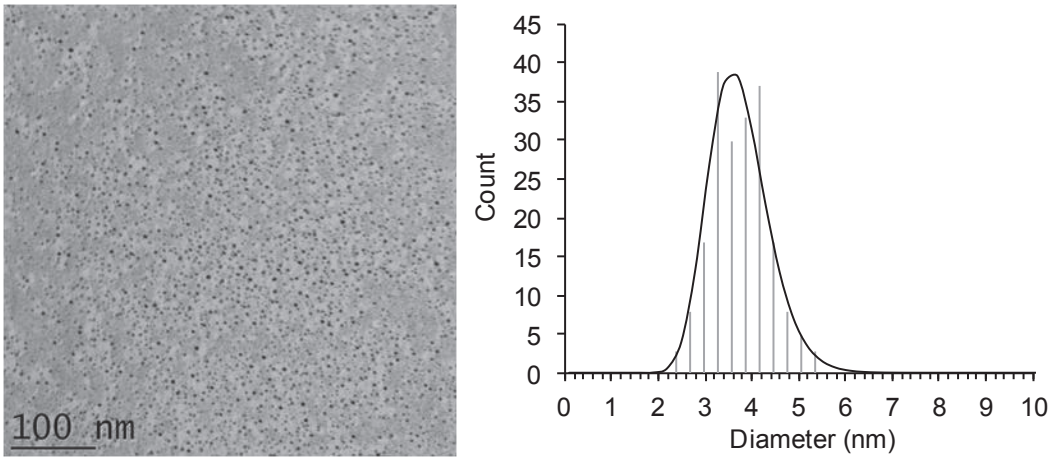

Figure 39. TEM picture and size repartition diagram, 20 min deposition. 200 nanoparticles count: 3.7 nm (± 0.6)

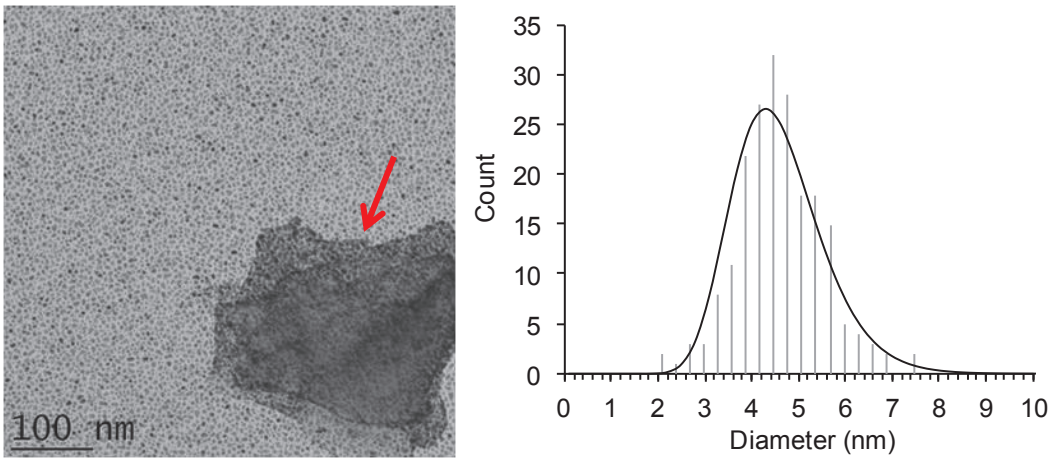

Figure 40. TEM picture and size repartition diagram, 100 min deposition. 200 nanoparticles count, 4.5 nm (± 0.9). The arrow points to an impurity.

TEM analysis confirms the formation of platinum nanoparticles, a small increase in size from 3.7 to 4.5 nm being observed when increasing the deposition time. Relatively narrow size dispersions are measured, standard deviations being respectively 0.6 and 0.9 nm after 20 and 100 minutes of deposition. The small size increase is concomitant to an increase of the nanoparticles density onto the TEM grids. Indeed this density is increased from 216 nanoparticles per 100 nm² after 20 minutes of deposition to 274 nanoparticles per 100 nm^2 after 100 minutes of deposition. This indicates that two processes happened in the meantime, nucleation of new nanoparticles and limited growing of preexisting ones. Those nanoparticles densities associated with mean nanoparticle size allow us to calculate loadings; results compared to loadings obtained on GDLs are presented Table 10. The ratio between the loading after 100 and 20 minutes of deposition is quite similar in both cases (respectively 2.3 on TEM grids and 3.0 on GDL) but the absolute value is two orders of magnitude lower on TEM grids. This result is not surprising since GDLs are coated with a microporous carbon layer and thus develop a high surface area.

Table 10.

		Pt loading ($\mu g.cm^{-2}$)	
deposition time	nanoparticle density (NP.100 cm^{-2})	calculated (on TEM grids)	by ICP (on GDL)
20	216	1.2	208
100	274	2.8	625

The Z-contrast between the elements of the sample is outlined by TEM. In Figure 39 and Figure 40 particles of similar sizes but either black or light grey are observed, supporting the hypothesis of the formation of platinum particles along with silica particles.

3.2.2.3. Scanning Electron Microscopy (SEM)

After deposition and without further treatments GDLs are observed by SEM.

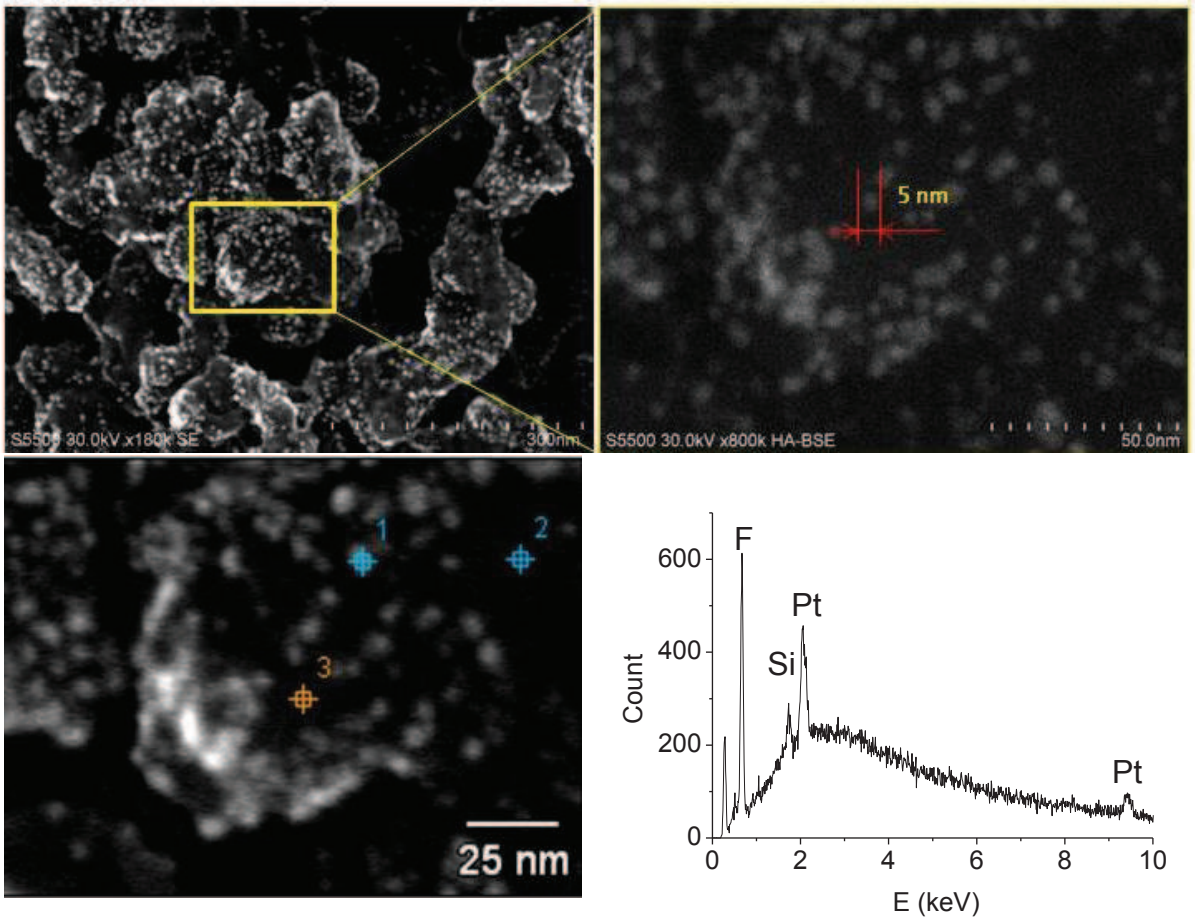

Figure 41. SEM picture (30 keV) and EDX spectrum, GDL 24BC, 100 min deposition.

Well dispersed nanoparticles are observed, the mean particle size is about 4 to 6 nm. EDX analyses have been carried out on part of the sample. The EDX analysis presented here corresponds to the marked zone 1. Zones 2 and 3 display the same spectra. As expected, platinum (2.048 and 9.441 keV) is found. The presence of silicium (1.739 keV) along with oxygen (0.525 keV) is also confirmed. Carbon (0.277 keV) is present on the support as a conductor. The presence of fluorine (0.677 keV) arises from PTFE.

SEM analysis confirms the formation of 4 to 6 nm platinum nanoparticles onto the GDLs as previously observed on TEM grids. The support, whether being TEM grids or GDLs does not

seem to have a dramatic impact on the nanoparticles formation process. EDX analysis confirmed the deposition of silicium along with platinum. This indicates the probable degradation of the –OSi(O*t*Bu)$_3$ fragment onto the surface under MOCVD conditions when the elimination in the gas phase would have been expected.

3.2.2.4. X-Ray Diffraction (XRD)

Silicon wafer ontroduced into the deposition chamber were used for those experiments. After deposition, wafers were analyzed by mean of X-Ray diffraction (XRD) to confirm the formation of crystalline platinum nanoparticles. Typical diffraction peaks (39.8, 46.2 and 67.2°) from platinum[112] are found, confirming the formation of crystalline platinum nanoparticles (see Figure 42). The peaks at 52.8, 54.4 and 55.8° are intrinsic to the silicon wafer support (see Appendix 15 for bare wafer XRD spectra). The platinum crystallites size can be evaluated using the Scherrer equation (see Appendix 16). For 20 and 100 minutes of deposition time, 3.3 (±1) nm and 2.3 (±1) nm crystallites are respectively found. Those values are slightly smaller those found on TEM grids (3.7 and 4.5 nm) and GDL (4 to 6 nm). This can either indicate a different deposition behavior on silica wafers leading to smaller nanoparticles or that nanoparticles on GDL are formed by the agglomeration of several crystallites. Unfortunately no SEM pictures of the deposited wafers are available to validate this hypothesis. Moreover, no silica crystalline phases were detected showing that the deposited silica was amorphous.

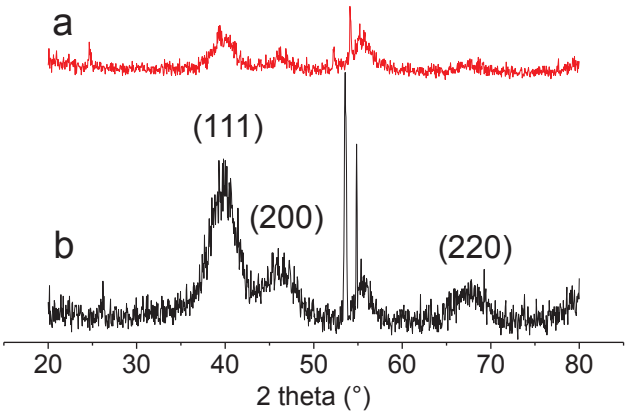

Figure 42. XRD spectrum of a wafer deposited with (COD)Pt(O(SiO*t*Bu)$_3$)$_2$, a) 20 minutes, b) 100 minutes

3.2.2.5. X-Ray Photoelectron spectroscopy (XPS)

For XPS analyses, Ti was chosen as a support for deposition by MOCVD as its orbital energy levels do not interfere with those of interest (Si, Pt). Titanium discs of high purity (99.99+%) were used and analyzed for samples after 60 minutes of deposition. For comparison a second deposition was carried out in similar conditions using platinum norbornadiene dimethyl ((nbd)Pt(Me)$_2$) previously developed for MOCVD purposes.[113]

The atomic concentrations are evaluated by integration of the XPS peaks using CasaXPS software. The results are summarized in

Table 11.

Table 11. Atomic percentage measured by XPS

	(COD)Pt(OSi(O*t*Bu)$_3$)$_2$	(nbd)Pt(Me)$_2$
O	40.5 %	46.0%
C	44.1%	31.8 %
Pt	4.4 %	20.0 %
Si	9.0 %	-

Note that the addition of each atomic percentage does not give 100% as nitrogen and sometimes fluorine (from the grease used to sealed samples under argon) are found as contaminants (total bellow 3 at. %). Note also that the Pt:Si ratio is equal to 2 as in the molecular precursor (COD)Pt(OSi(O*t*Bu)$_3$)$_2$. A Si:Pt ratio of 2 to 20 was found onto GDLs by elemental analyses (Figure 38). This probably arises from a bigger affinity of the liberated HOSi(O*t*Bu)$_3$ with the GDL substrate compared to the titanium disc.

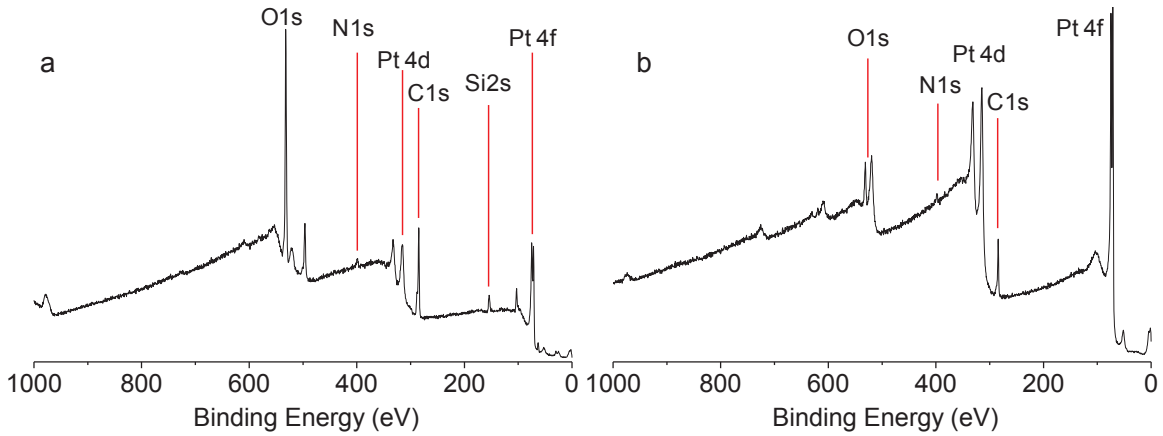

Figure 43. XPS spectra of a) (COD)Pt(OSi(OtBu)$_3$)$_2$ and b) (nbd)Pt(Me)$_2$ after MOCVD on Ti/TiO$_2$ pellets.

In both cases the Ti support signal is not seen on the XPS spectra indicating the formation of a deposited layer (Pt, C contamination, SiO$_2$) with a thickness larger than the XPS probe depth

(around 10 nm). The relative carbon contamination is higher when using the (COD)Pt(OSi(O*t*Bu)$_3$)$_2$ compared to (nbd)Pt(Me)$_2$, C:Pt ratio are respectively 10 and 1.6. The carbon contamination is higher than reported elsewhere but fine tuning of the deposition conditions is known to have a strong impact on it.[114]

The Si2p spectra, with a binding energy of 103.2 eV, is typical of SiO_2 and confirmed the deposition of silicon dioxide (Figure 44).[115]

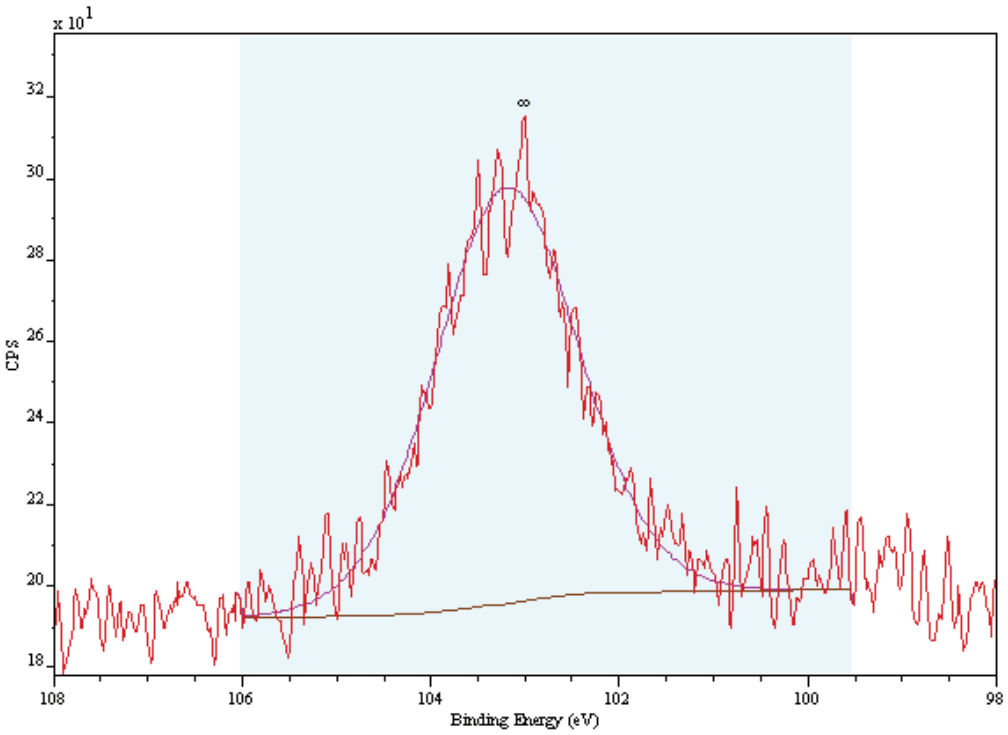

Figure 44. Si 2p spectra of deposited (COD)Pt(OSi(O*t*Bu)$_3$)$_2$

The deconvolution of the Pt4f doublet (see Figure 45 b) of the deposited (nbd)Pt(Me)$_2$ shows typical signals of metallic platinum at 71.1 and 74.2 eV and oxidized platinum at 72.5 and 75.7 eV.[115] Surprisingly, to fit the Pt4f spectrum (Figure 45 a) of the deposited (COD)Pt(OSi(O*t*Bu)$_3$)$_2$, a third contribution at higher energy (73.5 and 76.8 eV) is required. Those high energies are generally attributed to Pt^{IV} and could be here related to a specific interaction between platinum and silica.

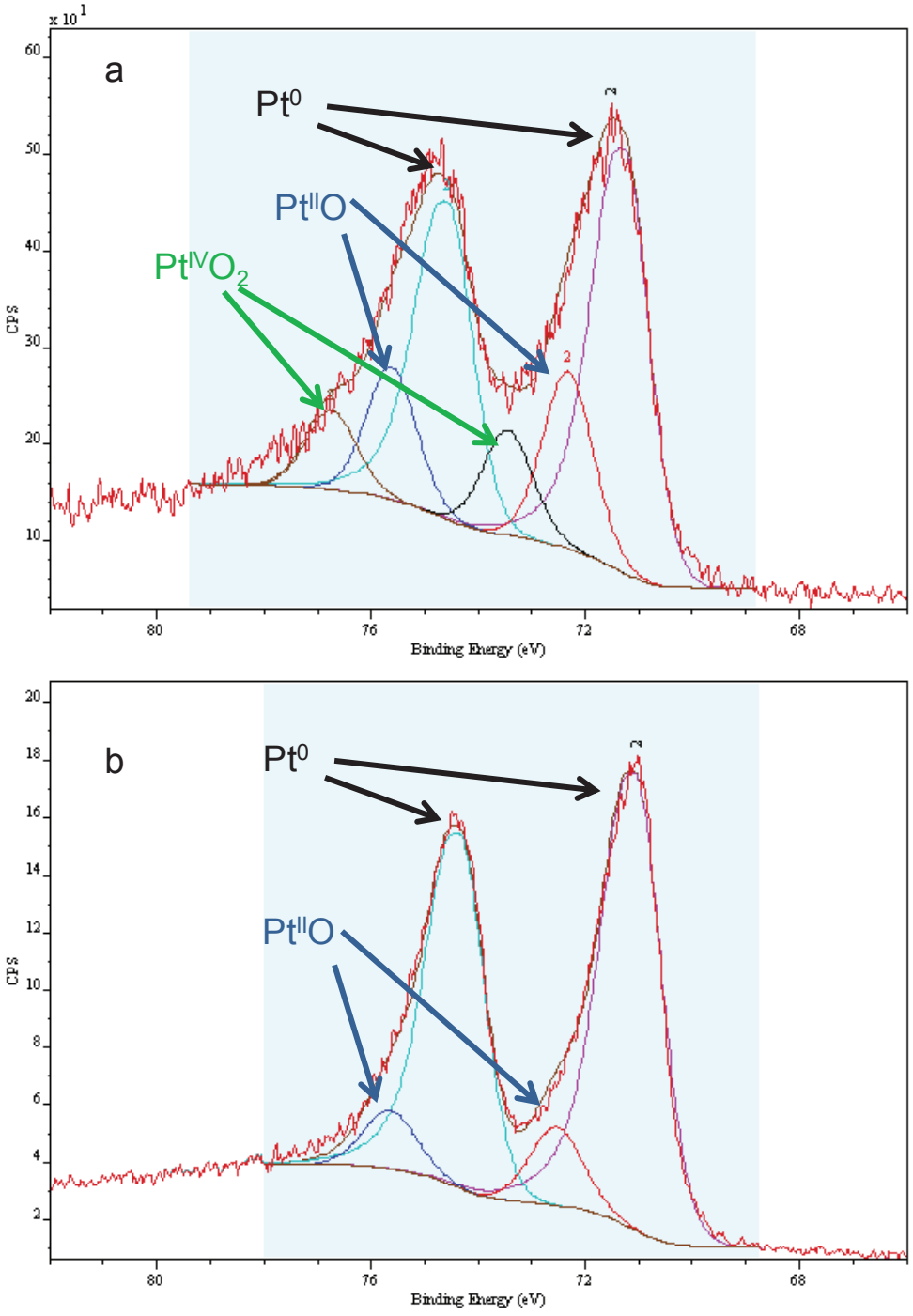

Figure 45. Pt 4f spectra of MOCVD deposited a) (COD)Pt(OSi(OtBu)$_3$)$_2$ and b) (nbd)Pt(Me)$_2$.

3.2.3. Electrocatalysis

Electrocatalysis evaluation of the catalyst was performed for the Oxygen Reduction Reaction (ORR) and Hydrogen Oxidation Reaction (HOR) in acid media in a half fuel-cell set-up,[116] please refer to experimental part for details. Main results are summarized in Table 12 and will be successively discussed.

Table 12. Main electrocatalysis results

	deposition time (min)	Pt (µg/cm²)	Pt ESA CO stripping (cm²Pt/cm²)	j at 35mV under H_2 (mA/cm²)	j at 0.8V under O_2 (µA/cm²)	A/gPt at 0.8V	µA/cm²Pt at 0.8V	dispersion
24 BC	20	208	2.2	35.0	258.0	1.2	115.2	0.2 %
	45	208	2.5	50.0	348.0	1.7	140.3	0.8 %
	60	416	2.9	39.9	216.0	0.5	75.0	0.4 %
	75	208	2.8	87.5	421.0	2,0	152.5	0.8 %
	100	625	4.8	140.0	258.0	0.4	54.2	0.5 %
E-TEK	20	179	2.6	23.3	70.0	0.4	26.9	0.8 %
	45	179	1.8	35.0	42.0	0.2	22.8	0.4 %
	60	358	2.5	21.9	30.6	0.1	12.3	0.1 %
	75	358	2.4	70.0	68.3	0.2	28.9	0.1 %
	100	536	3.4	116.7	93.0	0.2	27.4	0.4 %
REF PtCo Tanaka		540.0	108.9	155.6	17150.0	31.8	157.5	8.2 %

3.2.3.1. Electroactive surface area

3.2.3.1.1. Hydrogen adsorption

The electroactive surface area (ESA - Figure 46) has been determined by measuring the surface area under the cyclic voltammogram in the anodic part in the H-$Pt_{surface}$ removal range (or H underpotential desorbtion H_{upd} - see experimental part for details).

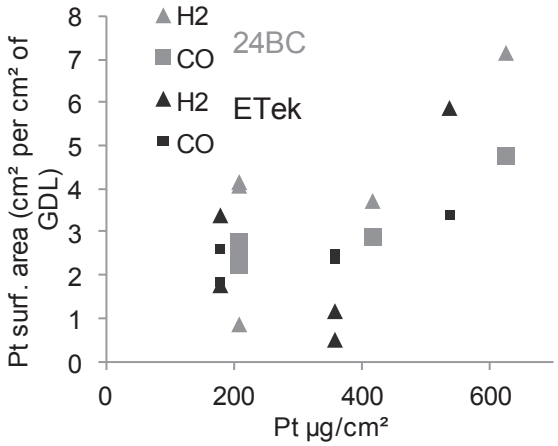

Figure 46. Comparison of the measured Pt surface area by the H_2 or the CO adsorption method on both types of GDLs. The error on the platinum surface area is ± 0.3 $cm^2_{Pt}.cm^{-2}$.

The platinum surface area increases with increasing platinum loading. This indicates the nucleation of more nanoparticles instead of the growing of pre-existing nanoparticles as previously confirmed by microscopy. CO and H_2 adsorption methods correlate well together, showing the same trend in the Pt surface area. The absolute value can differ from one method to another; the mean difference being in the 50 % range. This is probably due to the low loading of platinum on those samples and large errors on both the surface area measurements and elemental analyses.

3.2.3.1.2. CO stripping

A second method to measure the ESA is by the so called ‘‘CO stripping’’ method.[117] CO is indeed a strong poison for platinum and binds easily onto its surface. It is first adsorbed onto the surface and then oxidized into volatile CO_2 when applying a given tension to the half-cell set-up. For experimental details please refer to part 4. Results are presented and compared to ESA measured by the H_2 method in Figure 46. For the rest of the present study, Pt surface area will refer to the surface area measured by CO stripping. Indeed the surface area under the CO oxidation curve is much higher than the one observed for in the H_{upd} zone leading to a smaller error and thus more accurate values.

CO stripping is a good way to evaluate the tolerance of the catalyst towards CO poisoning. After one cyclic voltammetry under pure H_2, the gas flow is switched to H_2 + 50 ppm CO. The poisoning of the catalyst took only a few minutes. The reference, a PtCo catalyst, designed to be CO tolerant, shows no degradation of its properties in the same period of time (about 15 minutes). Typical behavior of pure Pt nanoparticles versus CO poisoning was recorded. A fast deactivation, within a few minutes range took place. Cyclic voltammograms

were recorded between -0.01 and 0.24 V *vs.* RHE and the current density can be drawn versus time. For clarity, only current density values at 0.24 V versus times are plotted (Figure 47).

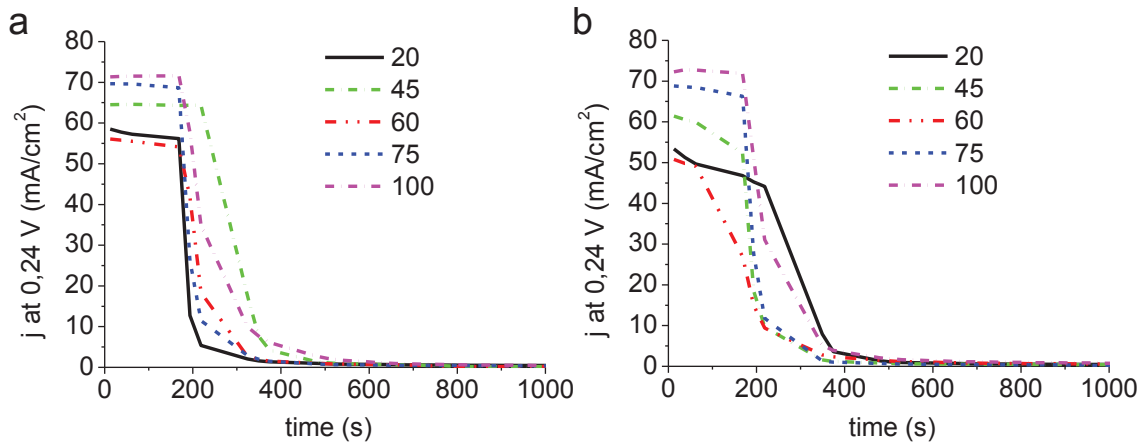

Figure 47. Current density vs. time under H_2 at 0.24 V/RHE from 0 to 200 seconds and then H_2+ CO (50ppm), a) 24BC, b) E-TEK

The final j value is directly linked to the CO coverage on the particles, this value can be calculated as follow: $CO_{cov.} = 1 - \frac{j_f}{j_{ini}}$. Values of 99% are found for all samples confirming the total poisoning of the platinum electroactive surface area.

From the platinum loading and the platinum surface area, one can calculate the metal dispersion, defined as the ratio between surface platinum atoms and the total number of atoms per nanoparticles (Equation 2).

$$Disp = \frac{Pt_{surf\ area} \times M_{Pt}}{0.08 \times A \times Pt_{loading}}$$

Equation 2

A : Avogadro's number

0.08 is the surface area per Pt atom ($nm^2.atom^{-1}$)

Dispersion is directly correlated to the particles size (see Appendix 17). Here very low dispersions are found while values between 20 and 30 % corresponding respectively to 6.6 and 4.1 nm particles are expected. The lower values indicate either very large particles (>50nm) or that only a fraction of the deposited particles are electroactive. The first hypothesis is rejected as SEM confirmed the formation of about 4 to 6 nm nanoparticles on GDLs and the absence of large platinum patches.

The theoretical platinum ESA can be evaluated considering that a 100% of the platinum nanoparticles are accessible and a mean nanoparticle size of 5 nm. Results are summarized

Table 13. νPt is defined as the catalytically active platinum over the total platinum content.

Table 13.

			Pt surface area (cm^2Pt/cm^2)		
	deposition time	Pt loading (ICP) µg/cm²	ESA (CO stripping)	calculated for 5 nm nanoparticles	νPt
24 BC	20	208.2	2.2	128.6	1.7%
	45	208.2	2.5	128.6	1.9%
	60	416.4	2.9	257.2	1.1%
	75	208.2	2.8	128.6	2.2%
	100	624.6	4.8	385.8	1.2%
E-TEK	20	178.8	2.6	110.4	2.4%
	45	178.8	1.8	110.4	1.6%
	60	357.6	2.5	220.9	1.1%
	75	357.6	2.4	220.9	1.1%
	100	536.4	3.4	331.3	1,0%
REF PtCo Tanaka		540	108.9	333.5	32.6%

Very small νPt, in the 1 to 2.4 % range, are obtained as compared to the reference where 32.6% of the platinum is catalytically active. This indicates that triple points, where gas, catalysts and electrons can meet, are not efficiently synthesized by MOCVD using the $(COD)Pt(OSi(O\textit{t}Bu)_3)_2$ precursor. This could be due to the formation of silica, an insulator, as it is the by-product of the decomposition of this very specific molecular precursor.

3.2.3.2. Hydrogen Oxidation Reaction

Hydrogen is very easily split onto Pt nanoparticles; low loadings (<50µg/cm²) of Pt meet both catalytic and economic constraints.

$$H_2 \rightarrow 2\ H^+ + 2\ e^-$$

redox potential 0 V/SHE

The oxidation of H_2 is used here as a reporter of the membrane electrode assembly (MEA) quality. Current densities are arbitrary compared at 0.35 V/RHE under a pure H_2 flow - 30 $mL.min^{-1}$ (Figure 48).

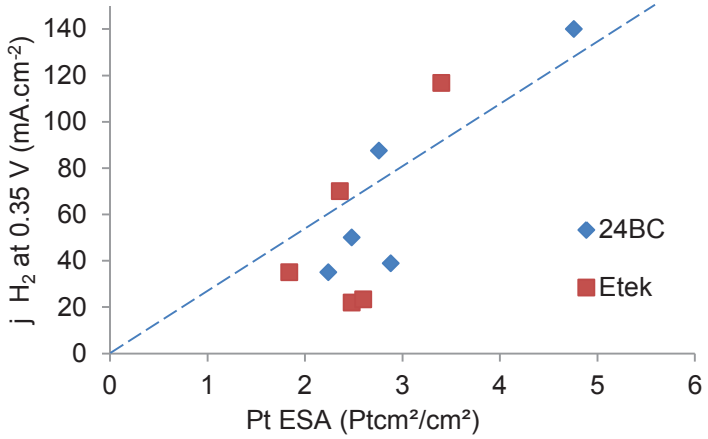

Figure 48. Current density vs. electroactive platinum surface area. The blue dashed line is a help for the eyes.

As expected, the current density is directly proportional to the electroactive surface and no influence of the GDL type is found.

3.2.3.3. Oxygen Reduction Reaction

For each sample, cyclic voltammograms (CV) were recorded under an O_2 flow (30mL.min^{-1}) at a scanning rate of 5 mV.min^{-1} (Figure 49).

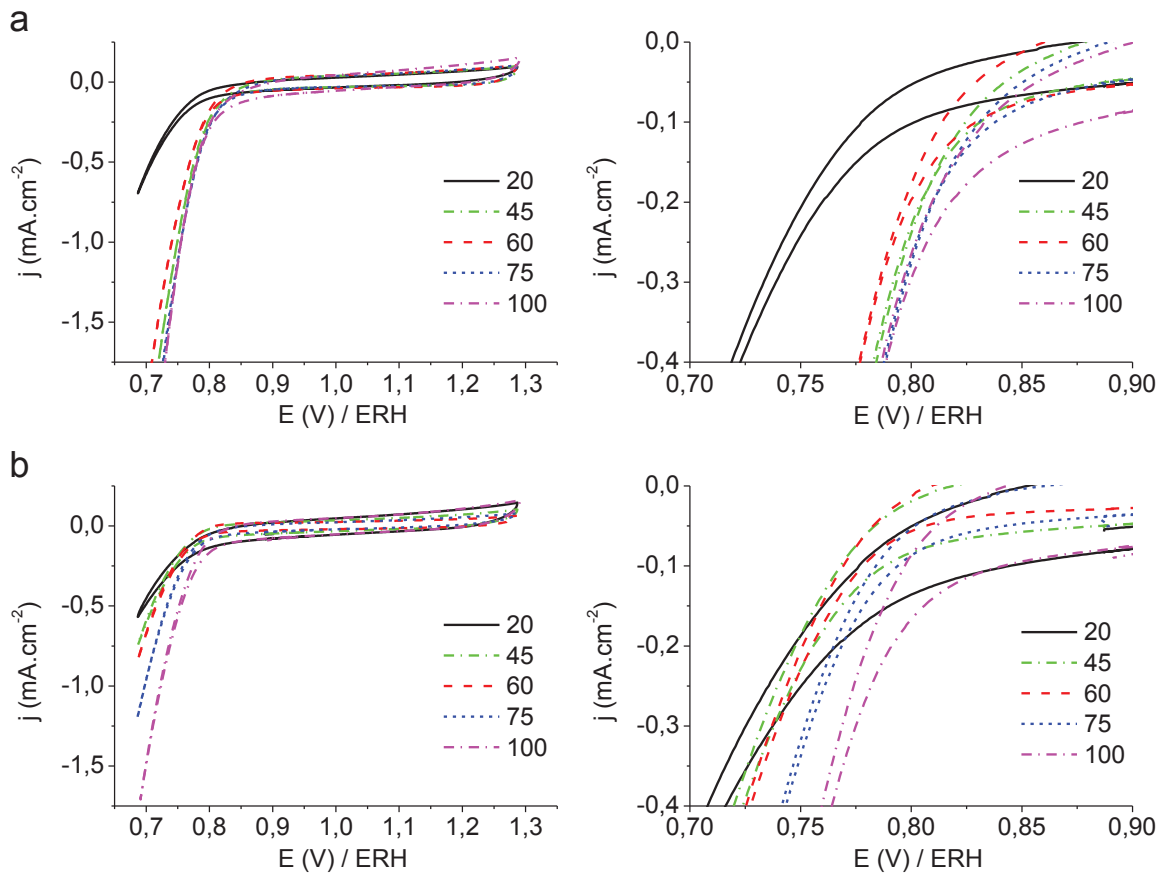

Figure 49. Cyclic voltammogram under O_2, scanning rate 5 mV.min^{-1}, gas flow 30 mL.min^{-1}, RT, a) 24BC, b) E-TEK. Deposition time from 20 to 100 min.

To easily compare the performances of each GDL, the current values at 0.8 V/RHE are compared against the electroactive surface area (Figure 50).

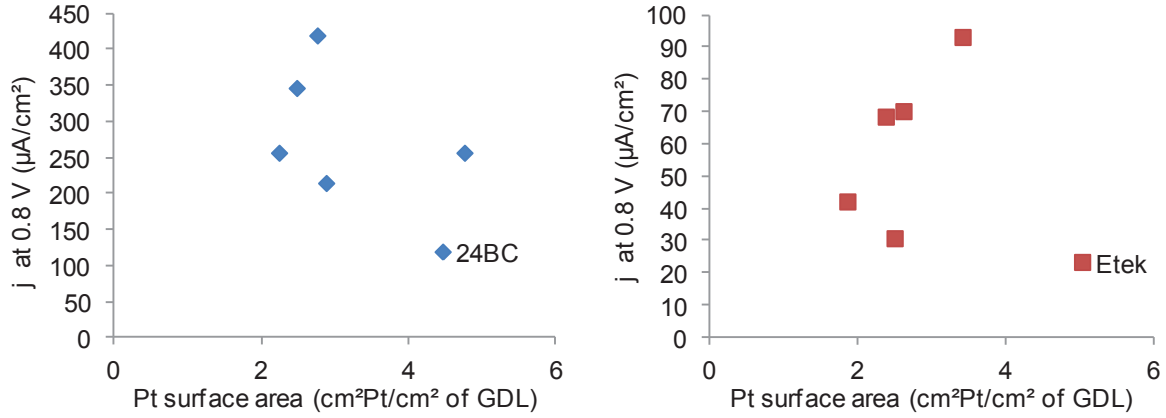

Figure 50. Current densities at 0.8 V/RHE

As expected the current density increases with electroactive platinum surface area. 24BC samples show the highest current densities above 300 µA.µg^{-1}Pt for two of them (45 and 75 minutes deposition time). Current densities are about 1 to 4 times higher on 24BC than on E-TEK GDLs and interestingly 24BC GDLs are less contaminated by silica as measured previously by ICP. The Si/Pt ratio is twice bigger on E-TEK samples. This confirms the probable electric insulation of nanoparticles due to surrounding silica.

Those results have to be compared to a reference, here a PtCo catalyst (impregnated onto 24BC) produced by Tanaka – Japan with a loading of 540 µg.cm^{-2}. This sample shows much higher platinum electroactive surface, 108.9 Ptcm^2.cm^{-2} compared to 1.8 to 4.8 Ptcm^2.cm^{-2} for our samples. The current density (µA.cm-2) at 0.8V vs. RHE is 40 to 500 times higher than for MOCVD samples. If we compare the normalized currents versus the Pt surface area the performances of our particles are ca. 1 to 12 times lower than those of the PtCo reference sample (see Table 12).

3.3. Chapter conclusion

(COD)Pt(OSi(O*t*Bu)$_3$)$_2$ proved to be an efficient precursor for the synthesis of platinum nanoparticles onto GDLs by DLI-MOCVD. Nanoparticles from 4 to 6 nm were obtained with narrow size dispersions. Platinum loadings from 100 to 600 µg.cm^{-2}, in the targeted range for

economic viability of platinum as a fuel cell catalyst,[118] were achieved. The formation of Pt nanoparticles takes place concomitantly with the formation of silicon dioxide. The evaluation of the catalytic properties of such catalyst layer was made in the Oxygen Reduction Reaction in half-cell set-up. Despite the platinum loadings achieved and the small nanoparticles sizes, low catalytic properties were measured compared to those of the reference sample. In fact, XPS demonstrated an intimate interaction between silicon oxide and platinum. Since silicon dioxide is an insulating material, it likely hinders the electrical pathway from the nanoparticles to the conductive GDLs and thus lowers the electrocatalytic properties. This poisoning could result from several effects as depicted in Figure 51 a to e.

a) Platinum and silicon dioxide nanoparticles are separately synthesized but in close relation.

b) Silicon dioxide particles surrounding platinum could limit the electrical pathway to the GDL.

c) A SiO_2 shell formed around the Pt nanoparticles could block the gas access to the catalytic sites.

d) Silicon patches around the nanoparticles could lower the accessible surface area.

e) Formation of a Pt-Si/SiO_2 solid solution.

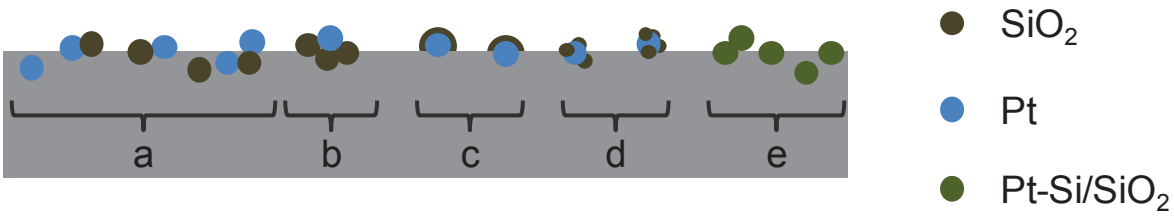

Figure 51. Scheme of the catalyst layer on GDL

The hypothesis c seems unlikely to occur as no core-shell structure was evidenced by microscopy. Hypotheses b, d and e cannot be rejected even if TEM microscopy leans towards the hypothesis b, as darker and brighter nanoparticles are found.

Despite the efficient synthesis of nanoparticles, (COD)Pt(OSi(O*t*Bu)$_3$)$_2$ gives disappointing results in electrocatalysis. In the next chapter, a different approach will be tested using colloidal nanoparticles stabilized by silanes.

Note that the intimate Pt/SiO_2 structure could result is more thermally stable nanoparticles when deposited onto oxides and could have interest in car gas exhaust depollution as oxidation catalyst for hydrocarbons and CO removal. Effort will be pursued in this way using this Pt/SiO_2 precursor for deposition onto ceria/alumina honeycomb structures used in car exhausts.

3.4. Experimental

3.4.1. General

Elemental analyses were performed at "Mikroanalytisches Labor Pascher" in Germany.

Transmission Electron Micrographs (TEM) were obtained on a Philips CM120 Transmission Electron Microscope at the "Centre Technologique des Microstructures Université Lyon 1" in France the acceleration voltage was set to 120 kV.

Scanning electron microscopy (SEM) was performed at the CEA Grenoble at an acceleration voltage of 30 kV on the XX equipment.

X-Ray diffraction analyses were performed on the LITEN, CEA Grenoble, Bruker D8 Advance diffractometer (40 kV & 30 mA) with CuKα radiation (λ = 0.154 nm). The diffraction patterns were collected in the 2θ angle range [20°-80°] at a scanning rate of 0.1°/min.

X-Ray photoelectron spectrometry (XPS): spectra were recorded at the CEA-Grenoble, LITEN, on the SSI-SProbe XPS spectrometer spectrometer with a Kα monochromated Al source. Spectra are recorded with a collection angle of 35° and a pass energy of 25 eV for high resolution spectra. The pressure in the analysis chamber was bellow 10^{-9} Pa. Peaks are calibrated toward the C1s (adventitious contamination carbon) peak set at 284.8 eV. Synthetic components on Pt4f were analyzed with a Shirley background subtraction and the peaks shape were resolved with a combination of gaussians and lorentzians (30%).

The synthesis of (COD)Pt(OSi(OtBu)$_3$)$_2$ was carried out under a controlled atmosphere (Ar), using Schlenk and glove-box techniques for organometallic synthesis. For details please refer to chapter 2.

3.4.2. MOCVD

Direct Liquid Injection Metal Organic Chemical Vapor Deposition (DLI-MOCVD) was performed at the Laboratoire des Technologies de Surface (LTS) in CEA Grenoble on the "Murielle" equipment. The precursor was first dissolved (0.025 mol.L^{-1}) in dried and

degassed toluene and placed in a sealed vessel. The solution was pushed by N_2. The carrier gas was an 80% N_2/20% O_2 100 mL.min^{-1} flow. The substrate was heated to 270°C, above the decomposition temperature of the platinum precursor. The pressure into the deposition chamber was maintained at 1 torr and the wall temperature was set to 110°C. The injector was heated at 100°C and the injection frequency set to 2 Hz with an opening time of 2 ms. A scheme and a picture of the equipment are presented Figure 52 and Figure 53.

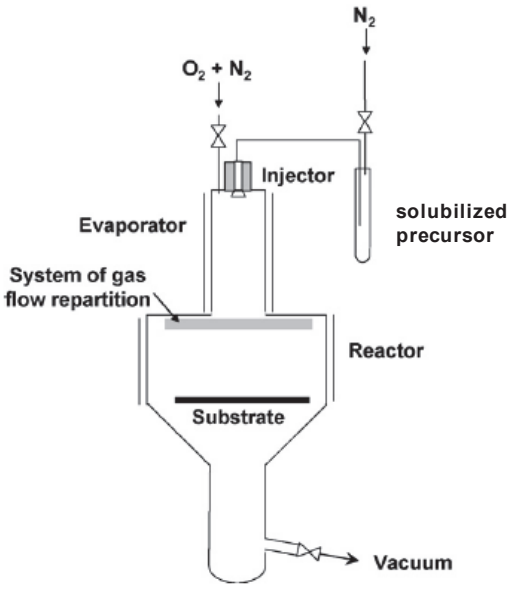

Figure 52. DLI-MOCVD set-up[113]

Figure 53. ‘‘Murielle’’ DLI-MOCVD equipment

For each deposition run a set of support was placed at the center of the substrate holder. A glass slide was used as a visual reporter of the efficient deposition as it turns grayish after deposition. A wafer (about 2×2 cm²) was used for further XRD characterization. A titanium disc (1 cm in diameter) of high purity (99.99+) from Goodfellow is used for XPS analysis, it was sonicated in acetone and air-dried prior to use. GDLs (8×8 cm²) of two types, 24BC (SGL group) and E-TEK (BASF) were used. TEM grids (carbon coated copper grids) were placed along with another supports to allow TEM characterization of the deposited nanoparticles. 5 runs were made with varying the deposition time from 20 to 100 minutes.

3.4.3. Sample preparation for half-cell tests

The catalysts deposed onto the gas diffusion layers (GDLs) were tested in fuel cell condition i.e. in the membrane electrode assembly referred as MEA. GDLs consist of a microporous mixture of carbon particles and polytretrafluoroethylene (PTFE) supported onto a macroporous carbon cloth. Platinum nanoparticles were deposited on the carbon microporous side. Two types of GDL were tested: 24BC produced by SGL and E-TEK from BASF. For half-cell set-up MEA composed of three layers were used (see Figure 54) and prepared as follow.

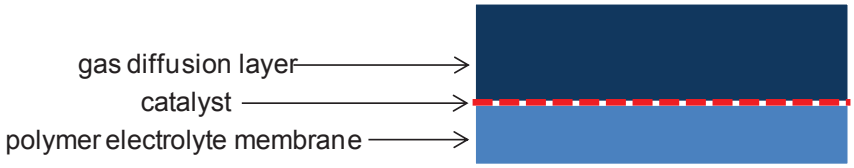

Figure 54. Membrane electrode assembly used for half fuel-cell set-up

To ensure a good contact (electrical pathway) between the catalyst nanoparticles and the Nafion membrane, Nafion was first deposited onto the GDLs. A solution of Nafion at 0.5 wt% in water/isopropanol (1:1) was prepared by mixing 1mL of Nafion 5 wt% in water, 4mL of deionized water (18.2 MΩ.cm) and 5mL of isopropanol. GDLs were impregnated using an aerograph with the appropriate amount of Nafion solution to ensure a Nafion loading of about 100 µg.cm^{-2}. After drying at 80°C for 10 min, GDLs and the Nafion membrane (NRE211 CS) were then hot casted together at 135°C for 2.5 min and then at 135°C under 40 kg.cm^{-2} for 2.5 more minutes following a previously developed method. Circular samples (ø=14 mm) were cut for testing.

3.4.4. Half-cell tests

Those tests were carried out at the Laboratoire Composants Piles à combustible, Electrolyse et Modélisation (LCPEM) of the CEA-Grenoble under the supervision of Dr. Nicolas Guillet. The characterization of our samples was performed in a half-cell set-up as described below (Figure 55.). The standard electrolyte used was a H_2SO_4 freshly prepared solution at 0.5 mol.L^{-1} and was deoxygenized by N_2 bubbling at least 20 minutes before testing. Three electrodes were used (working electrode, reference electrode and counter electrode). The counter electrode was made of platinum and the reference electrode was Hg/HgSO4 (E°= -0.698 mV vs. Reversible Hydrogen Electrode - RHE). The active part of the MEA has a geometric surface area of 0.5 cm². The feeding gas at the working electrode could be switch between N_2, O_2, H_2 or H_2 + 50ppm CO. Therefore we could evaluate the performances of the catalysts in the Oxygen Reduction Reaction (ORR), Hydrogen Oxidation Reaction (HOR) and against the CO poisoning.

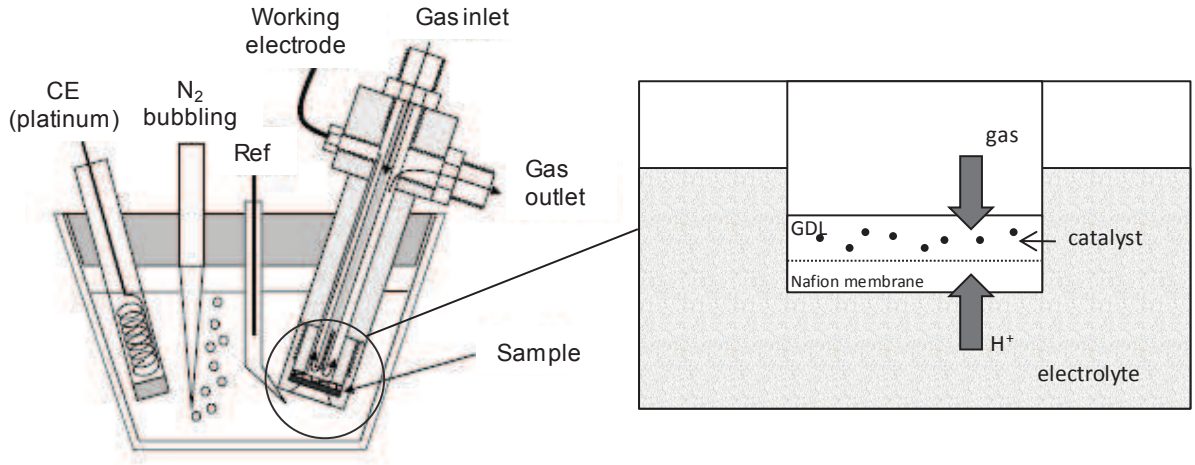

Figure 55. Half-cell set-up scheme

3.4.4.1. Electroactive surface measurement

The total numbers of reactive surface sites on platinum were measured by two methods: absorption of H_2 or CO (CO stripping) at the catalyst surface followed by oxidation. Those two methods are based on the measurement of the charge needed to remove the absorbed monolayer (of H or CO). This is done by integrating the current in the anodic scan region (I>0). One H and one CO are absorbed per surface platinum atom.

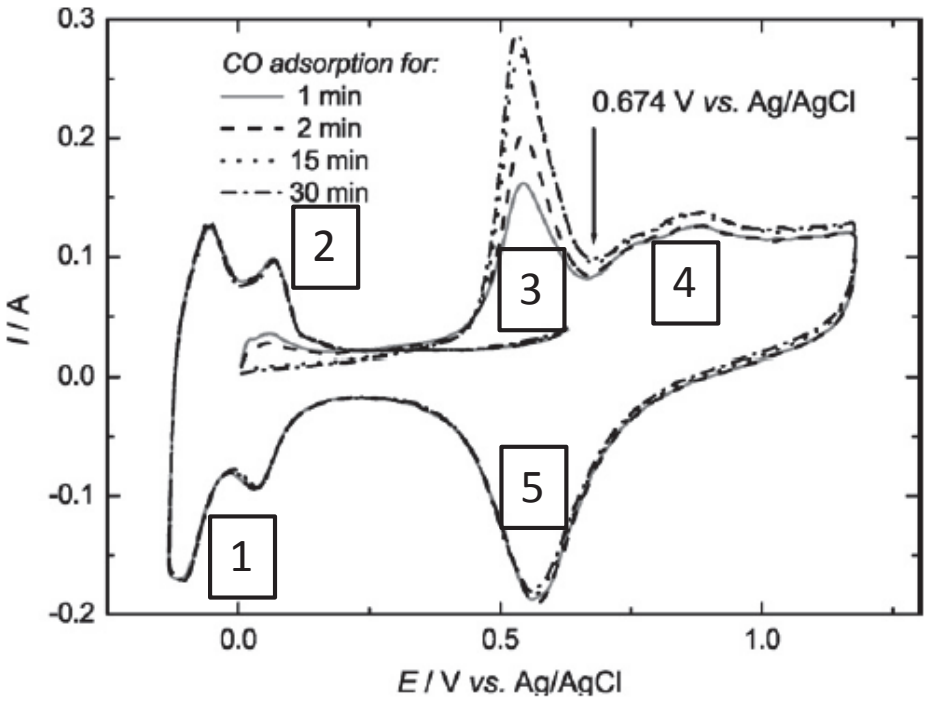

Figure 56. Typical cyclic voltammogram under N_2 after CO adsorption on a Pt catalyst[117]

1. $H^+ + Pt_{surface} + e^- \rightarrow$ H-Pt(surface)
2. H-$Pt_{surface} \rightarrow H^+ +$ Pt(surface) + e^-
3. CO-$Pt_{surface} + H_2O \rightarrow CO_2 + 2H+ + 2e- + Pt_{surface}$
4. $Pt + xH2O \rightarrow PtOx + 2xH^+ + 2xe^-$ Metal oxidation
5. $PtOx + 2xH^+ + 2xe^- \rightarrow Pt + xH2O$ Metal reduction

The electroactive surface area (ESA) can be obtained by using the two following equations:

$$S = \frac{Q_H}{0.210} \qquad S = \frac{Q_{CO}}{0.420}$$

0.210 mC.cm^{-2} being the charge needed to remove the H monolayer on 1 cm² of platinum (0.420 is the equivalent for CO removal). Q_H and Q_{CO} are measured by integrating the peaks corresponding to the H or CO monolayer removal, it is given in mC.

$$Q_x = \frac{\int IdE}{v}$$

v is the scanning rate in mV.s^{-1}.

From this equation we understand that for a given ESA and thus a given Q_x, ∫IdE increases with increasing scanning rate.

H_2 absorption:

N_2 was bubbled into the electrolyte for at least 20 minutes, and then the working electrode was flushed with N_2 (30 mL.min^{-1}). Prior to measurements, the MEA is cycled from 0 to 1.1 V/RHE at a scanning rate of 20 mV.s^{-1} to ensure stabilization of the ESA. Cyclic voltammograms (CVs) were reproducible after 4 to 5 cycles. The ESA was measured on the last voltammogram recorded. Below is given an example for the H_2 surface area peak measurement (see Figure 57). Integration is done using EC-lab software.

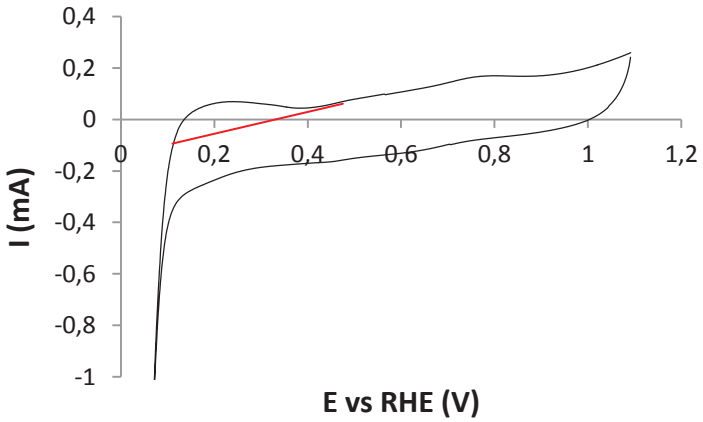

Figure 57. Cyclic voltammogram under N_2 at a 20 mV.s^{-1} scan. Sample 24BC 100 minutes.

CV under pure H_2 (Hydrogen Reduction Reaction) and CO stripping:

A first voltammogram was recorded under pure H_2 (30 mL.min^{-1}) and then the gas flow was switched to H_2 + CO (50 ppm, 30 mL.min^{-1}). CO is a strong poison for Pt and thus the current density will decrease. The faster the decrease the more rapidly the catalyst is poisoned. The poisoning of most sites on the catalyst surface took only a few minutes (<10 min). After switching for the H_2/CO mix, CV between 0 to 0.65 V/RHE were recorded every 2.5 minutes. After complete poisoning of the catalyst, typically 5 cycles, the gas at the working electrode was switched to nitrogen and a CV from 0 to 1.13 V/RHE was recorded. The absorbed CO was thus oxidized into CO_2 and the surface area under the CO oxidation peak was measured. A second CV was drawn and used as the base line for the surface measurement (see Figure 58).

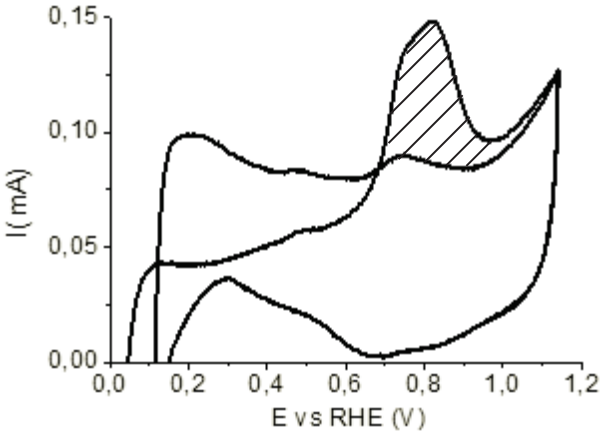

Figure 58. Cyclic voltammogram under N_2 after CO adsorption at a 5 $mV.s^{-1}$ scan rate. Sample 24BC 100 minutes.

3.4.4.2. Oxygen Reduction Reaction

N_2 was bubbled into the electrolyte for at least 20 minutes and the working electrode was flushed with oxygen (30 $mL.min^{-1}$). Cyclic voltammograms were recorded from 0.7 to 1.3 V/RHE at a scanning rate of 5 $mV.s^{-1}$. At least 4 cycles are recorded. Current densities are compared at the arbitrary chosen potential value of 0.8 V/RHE

3.5. Appendix

Appendix 14. Liquid state ^{1}H-NMR of (COD)Pt(OSi(O*t*Bu)$_3$)$_2$ in THF-d$_8$

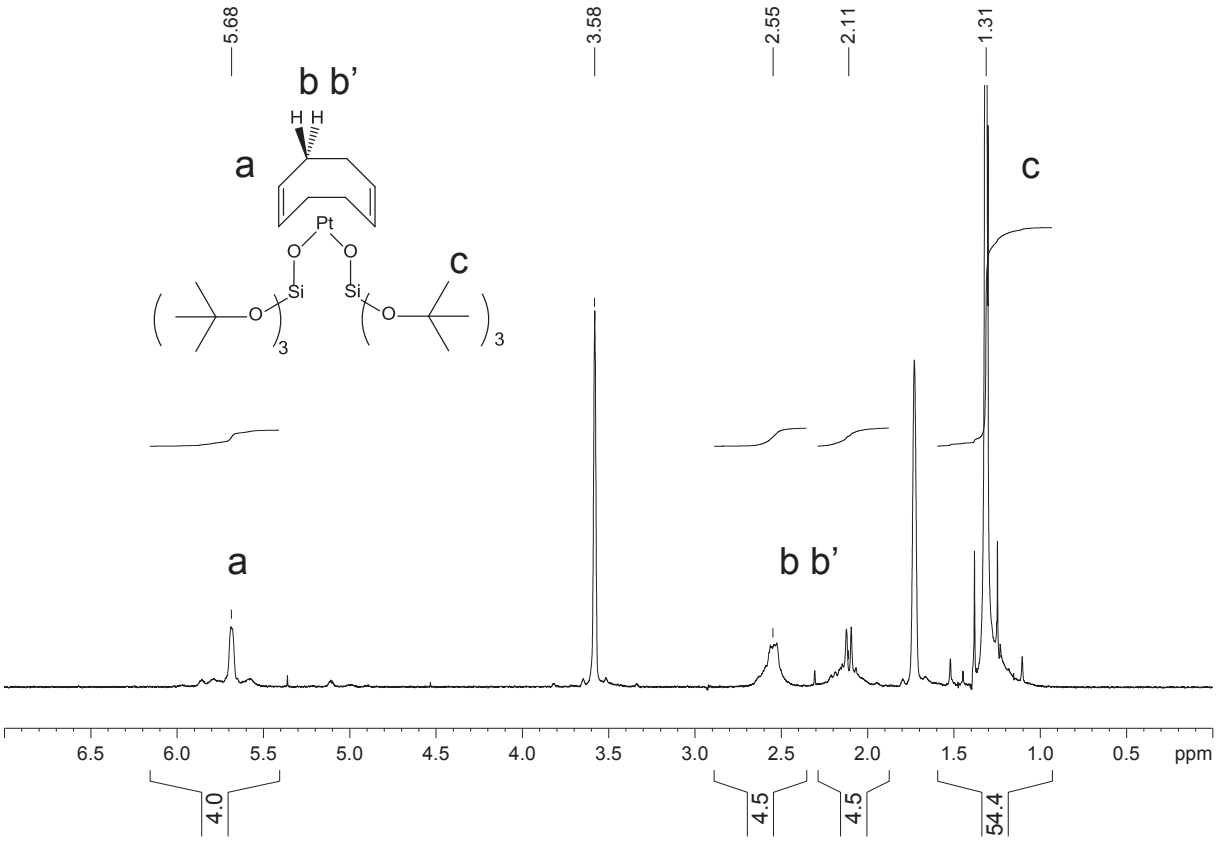

Appendix 15. XRD spectra of a bare wafer.

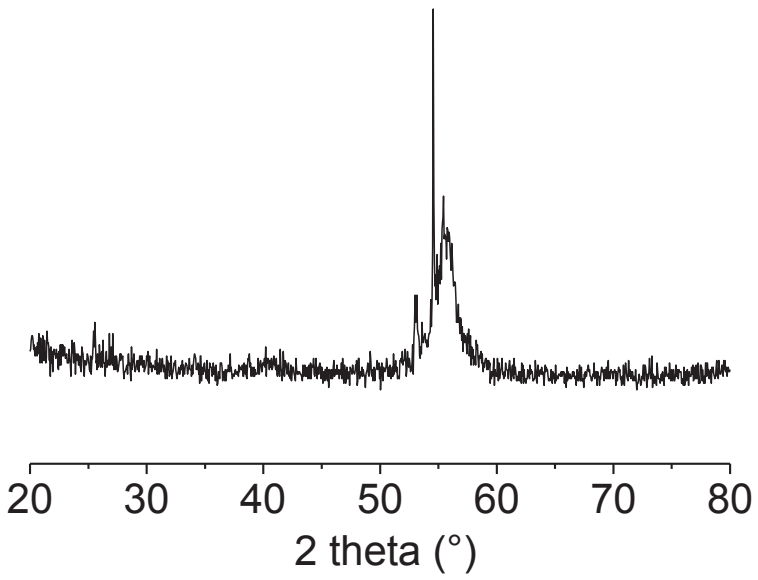

Appendix 16. Crystallites size evaluation by the Scherrer equation.

Based on the measure of the full width at half maximum (FWHM) of the diffractions peaks, the crystallites size can be evaluated by the Scherrer formula:

$$d = \frac{K\lambda}{\beta cos\vartheta}$$

With K the shape factor fixed to 0.9 for truncated cubo-octahedron nanoparticles, λ the wavelength of the X-Ray source (1.5406 Å), β the FWHM in radian and θ the Bragg angle in radian. FWHM are measured using the OriginPro 8.1 Software and a Gaussian type fitting of the peaks. The error is estimated to be in the nanometer range on the final crystallites value.

Appendix 17. Correlation between the nanoparticles size and dispersion.[119]

Calculations are based on the truncated cubo-octahedron geometry typically observed for platinum crystalline nanoparticles.

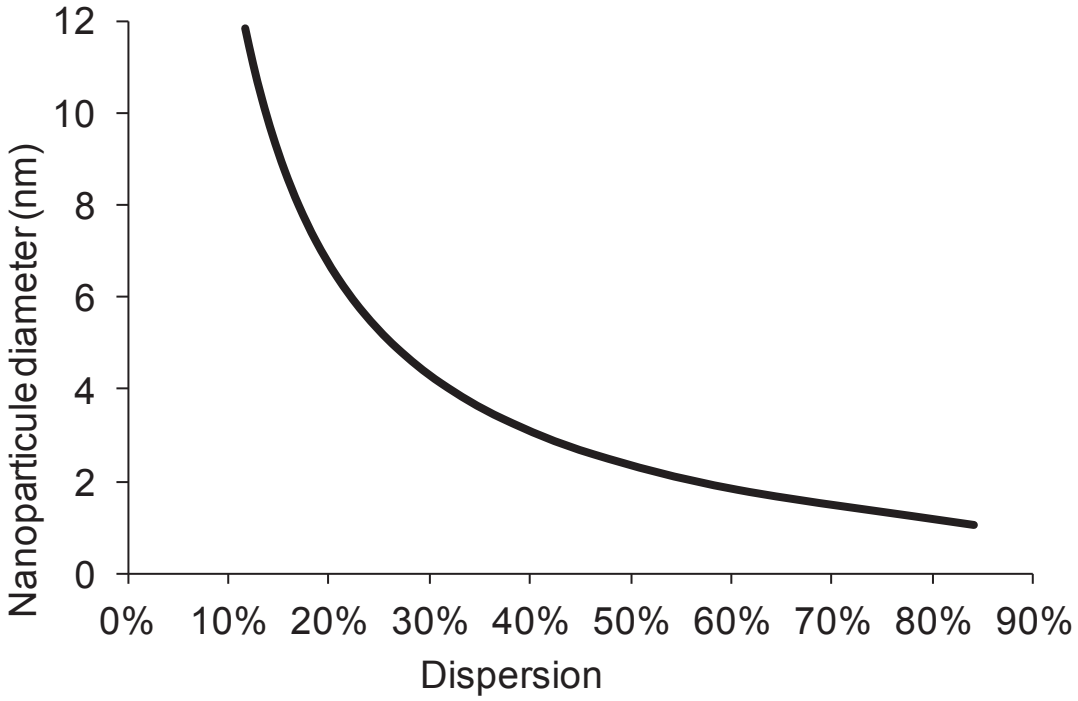

4. Colloidal nanoparticles stabilized by octylsilane, from monometallic to bimetallic systems

4.1. Introduction

The goal of this chapter is to describe the synthesis of octylsilane stabilized nanoparticles of platinum, palladium and of bimetallic Pt/Pd nanoparticles and the understanding of their synthesis pathway and final atomic composition. These syntheses were developed based on previous work performed on ruthenium,[82] platinum[84,85] and gold.[83] The catalytic properties will be tested in the Oxygen Reduction Reaction (ORR).

4.2. Platinum nanoparticles

4.2.1. From Pt^0 precursor

4.2.1.1. Synthesis using H_2 as an external reductant

The synthesis of Pt nanoparticles stabilized by octylsilane was previously published by our group[84,85] albeit with low insight into the nanoparticles growth mechanism. The starting Pt^0 complex was bis-dibenzylideneacetone platinum ($Pt(dba)_2$), an air stable compound easily synthesized.[120] Upon addition of 1 equiv. of octylsilane, pressurization under 3 bars of H_2 and mixing, the coloration change from purple (color of $Pt(dba)_2$) to black indicating the formation of nanoparticles within 8 to 10 h. Nanoparticles of 1.8 nm in diameter were obtained with narrow size dispersions 0.3 nm (Figure 59).

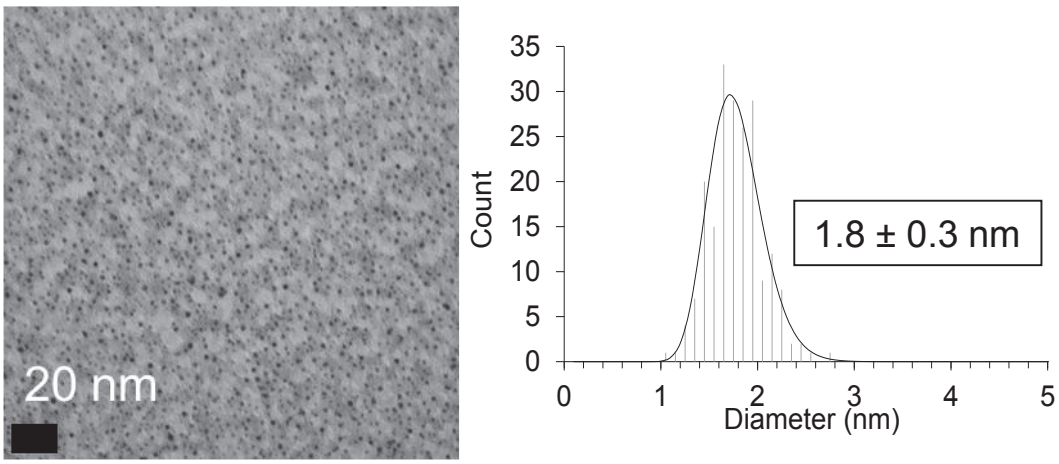

Figure 59. Pt nanoparticles synthesized from $Pt(dba)_2$ and stabilized by 1 equiv. octylsilane and the associated histogram with mean size and the associated standard deviation. 200 nanoparticles count.

The byproducts of the reaction were further analyzed. After filtration over alumina to trap the Pt nanoparticles the liquid phase was analyzed by gas chromatography coupled with mass spectrometry (GC-MS). 1-5,dicyclohexylpentane and n-octane were detected.

The release of octane indicates the probable formation of Pt-Si intermediates, the cleavage of the Si-C bond and the potential incorporation of silicium atoms within the nanoparticles structure. Part of the alkyl chains would stay pending from the surface and thus stabilizing the nanoparticles. This hypothesized mechanism (Figure 60) implies the formation of Pt-Si intermediates that have not been isolated yet. This hypothesis is supported by kinetic observations where Pd (see below) was found to react faster than Pt. The faster reaction of palladium compared to platinum is in line with previous computational studies by Sakaki *et al.*[121] which showed lower calculated activation energies for the oxidative addition of SiH_4 over $Pd(PPh_3)_2$ than over $Pt(PPh_3)_2$, this system being comparable to our $RSiH_3$ over M^0 reaction.

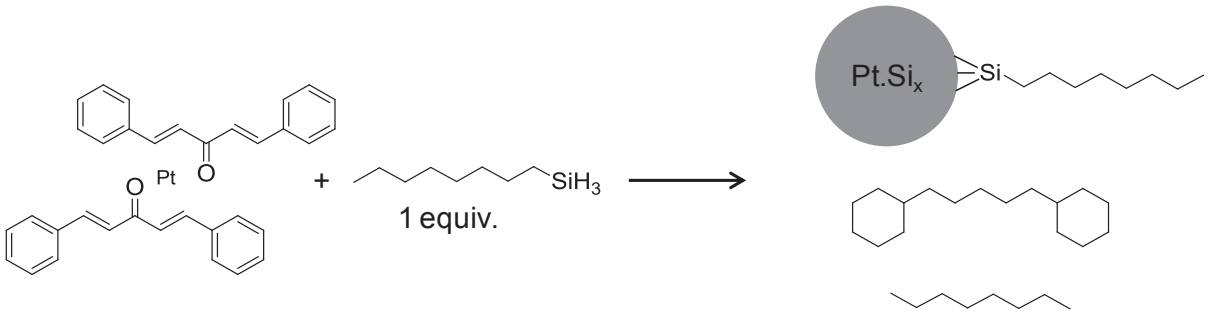

Figure 60. Platinum nanoparticles reaction scheme

4.2.1.2. Synthesis in the absence of H_2

The synthesis of platinum and palladium nanoparticles under H_2 proved to be very efficient but the explosiveness of H_2 makes it a potentially dangerous process. Moreover a solution of $Pt(dba)_2$ with one equiv. of octylsilane was left over for several hours under N_2 and a slight variation of the coloration, from deep purple to black was noticed. From this point the need for H_2 as an external reductant was questioned, and we decided to explore the synthesis in the absence of H_2 and at a higher temperature in order to speed up the nanoparticles formation process.

A $Pt(dba)_2$ solution was heated in THF at 60°C, neither coloration change nor formation of aggregates were observed after two hours demonstrating the good thermal stability of the precursors. When one equiv. of octylsilane was rapidly added (about 1 second), a dramatic coloration change from pink to dark black was noticed in about 1 min of time. TEM images of the nanoparticles after overnight reaction at 60°C are presented Figure 61. 1.6 nm nanoparticles were produced, this size being smaller than that obtained when the reaction proceeds at room temperature, while size distribution (σ = 0.3 nm) was not modified.

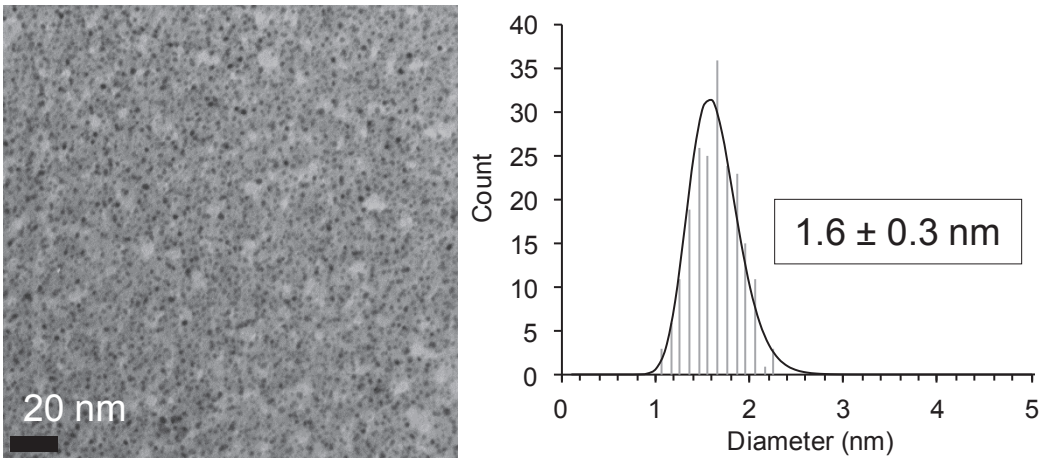

Figure 61. TEM pictures of Pt nanoparticles prepared at 60°C with one equivalent of octylsilane.

The full consumption of the Pt precursor was checked by UV-Vis spectroscopy, results are presented Figure 62. The absorption peak characteristic of $Pt(dba)_2$ at 320 nm disappeared after 15 h of reaction indicating its full consumption.

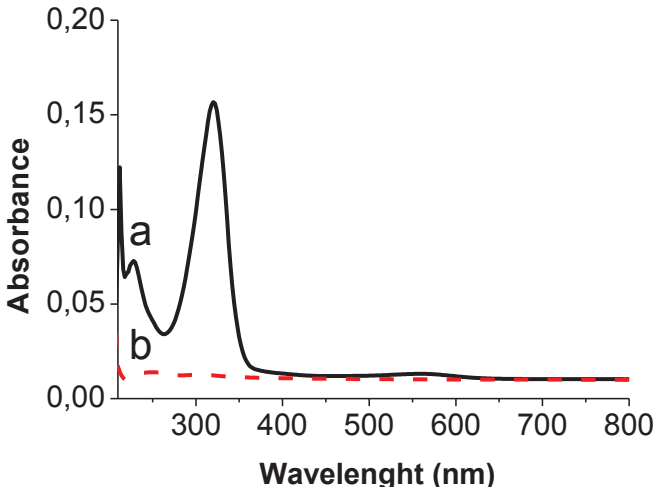

Figure 62. a) $Pt(dba)_2$, b) after reaction at 60°C, 15 h.

4.2.1.3. In-situ NMR monitoring of platinum nanoparticles formation

Despite previous work, the synthesis and structure of those nanoparticles are not yet fully understood. NMR analyses were performed in order to gain insights into the reactivity of this system. The synthesis of nanoparticles was monitored by NMR using a Young NMR tube. The final $Pt(dba)_2$ concentration in the tube was 30 $mmol.L^{-1}$ versus 1.5 $mmol.L^{-1}$ for nanoparticles synthesis experiments. This higher concentration did not have any detrimental effect on the nanoparticles as proven by TEM images (see Appendix 18, well dispersed

nanoparticles were produced). On the other hand, upon addition of 1 equiv. of octylsilane into the NMR tube, a fast coloration change was noticed demonstrating a faster kinetic. The formation of bubbles was also noticed within the first seconds after silane addition and before tightly closing the NMR tube. Spectra were recorded up to 14 h after starting the reaction (Figure 63).

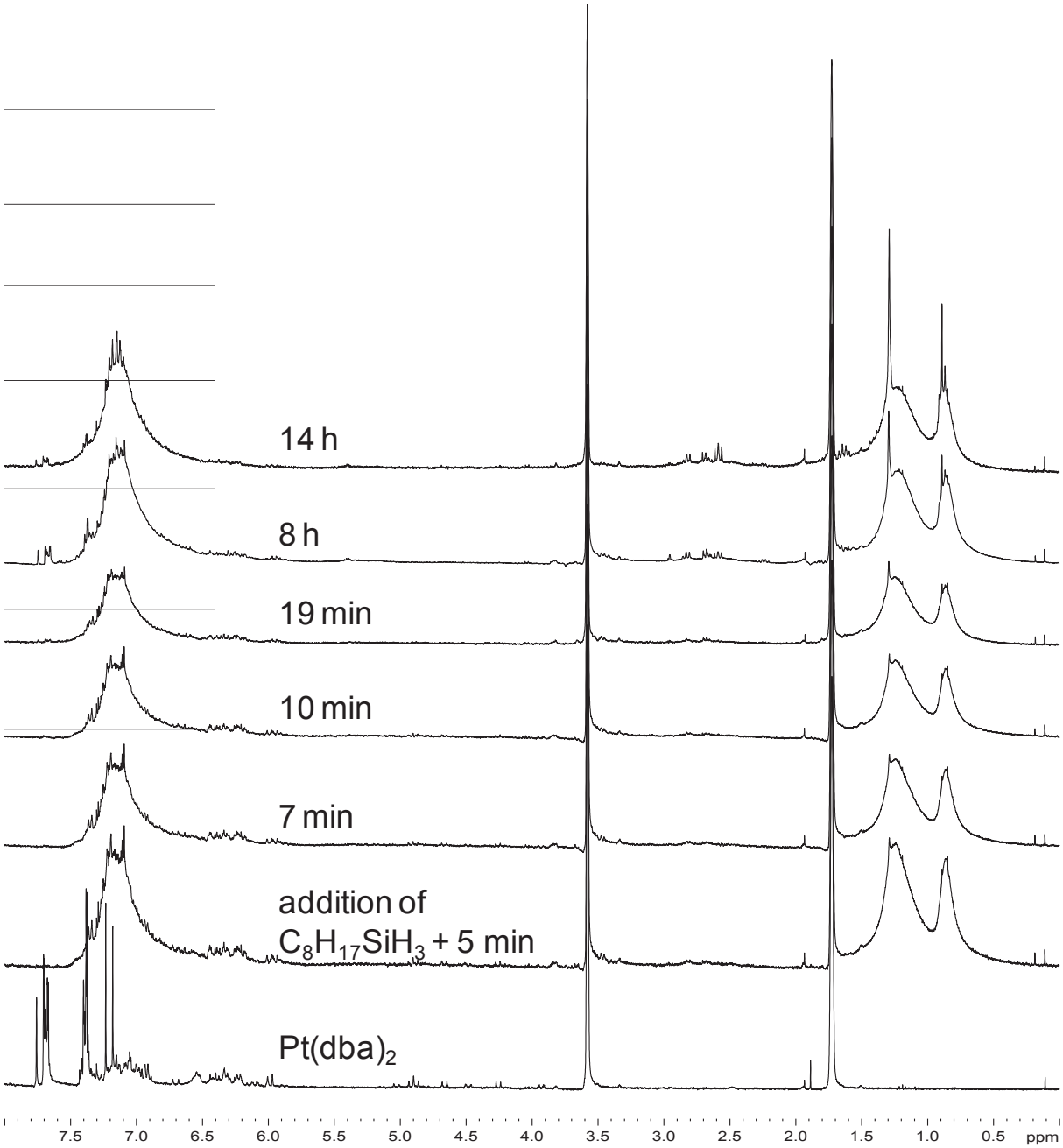

Figure 63. Liquid state NMR of Pt nanoparticles formation in THF-d_8

After addition of the silane, protons from the dba ligand between 7.2 and 7.8 ppm were not anymore visible. Strong and large peaks at 0.85 and 1.25 were attributed to both the silane

precursor (respectively C**H**$_3$ and -(C**H**$_2$)$_6$- see Appendix 20 a) and 1-5,dicyclohexylpentane. At 7.2 ppm, residual aromatic protons were attributed to non-hydrogenated dba. The broad shape of those peaks indicated the interaction of this residual dba with the nanoparticles surface. The expected H_2 signal at 4.55 ppm cannot be found indicating both its full consumption and its probable partial loss during the silane addition process. The peaks at 1.29 and 0.89 ppm were attributed to octane (see Appendix 20 b). Octane was found from the beginning of the reaction but its concentration evolves up to 14 h after the beginning of the reaction. No -Si**H**$_3$ signals was found (3.47 ppm) indicating the fast and total reaction of silane with the platinum complex. The -C**H**$_2$-Si- signal (0.77 ppm) was not seen but could be overlapped by the large peak centered on 0.85 ppm and shifted/broadened due to the formation of Pt nanoparticles as already observed by other for Au[122,123] or Ru[73] and referred to as the "Knight shift" effect.

The reactivity of octylsilane towards dibenzylideneacetone was tested without the presence of the Pt complex. When one equiv. of octylsilane and one equiv. of dibenzylideneacetone were mixed in THF-d_8 in an NMR tube, no reaction took place after overnight mixing at room temperature. Heating at 60°C for two hours did not induce either any reaction. Platinum thus proved to be necessary to induce the hydrogenation of dba into 1-5, dicyclohexylpentane. This implies the formation of H_2 at one point of the process, its splitting over the metallic nanoparticles and the further catalytic hydrogenation and reduction of dba. The reaction of silane with the metallic center yielding Pt-Si bonds and elimination of H_2 was hypothesized.

4.2.2. From Pt^{II} precursors

The influence of the precursor used for such nanoparticles synthesis was studied; platinum II precursors were tested.

4.2.2.1. (COD)Pt(Me)$_2$

We first tested (COD)Pt(Me)$_2$ as a precursor; this product presents the advantage of being air stable and commercially available, making it a perfect candidate for nanoparticles synthesis. It was found to be unreactive towards octylsilane at room temperature after 3 days as no coloration change was observed. Addition of 3 bars of H_2 as an external reductant for 15 h did not led to any improvement of the reactivity. Finally, the heating at 60°C for 15 h yielded a brown solution and TEM microscopy revealed the formation of microsize aggregates (Figure 64, grey and light grey structures comes from the supporting grid) probably *via* a thermally

induced degradation of the complex. The strong Pt-Me bonds are believed to hindered the reactivity of $(COD)Pt(Me)_2$ towards octylsilane.

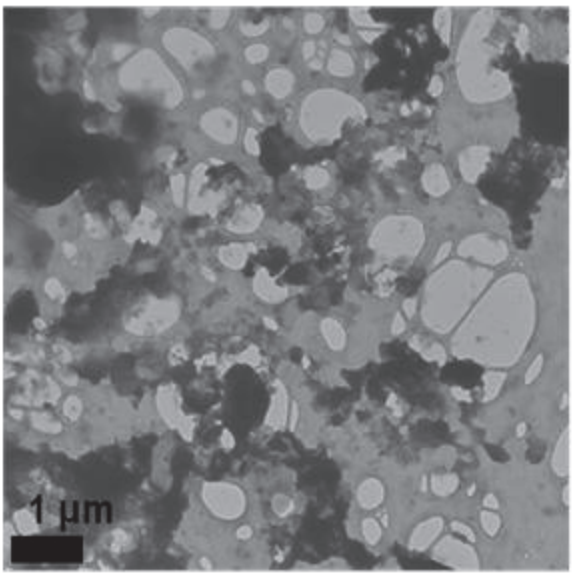

Figure 64. TEM image, $(COD)Pt(Me)_2$ + 1 equiv. octylsilane, 60°C, 15 hrs.

4.2.2.2. $(COD)Pt(OSi(OtBu)_3)_2$

Following the work performed in surface organometallic chemistry where $(COD)Pt(OSi(OtBu)_3)_2$ was found to be more reactive than $(COD)Pt(Me)_2$, we decided to investigate the nanoparticles synthesis from this bisiloxy complex.

4.2.2.2.1. Synthesis and characterization

Upon addition of 0.3 or 1 equiv. of octylsilane at room temperature, the THF solution of $(COD)Pt(OSi(OtBu)_3)_2$ turned instantaneously from color-free to brown/black.

4.2.2.2.1.1. TEM imaging

TEM grids were prepared after 30 minutes and 15 h of stirring (Figure 65).

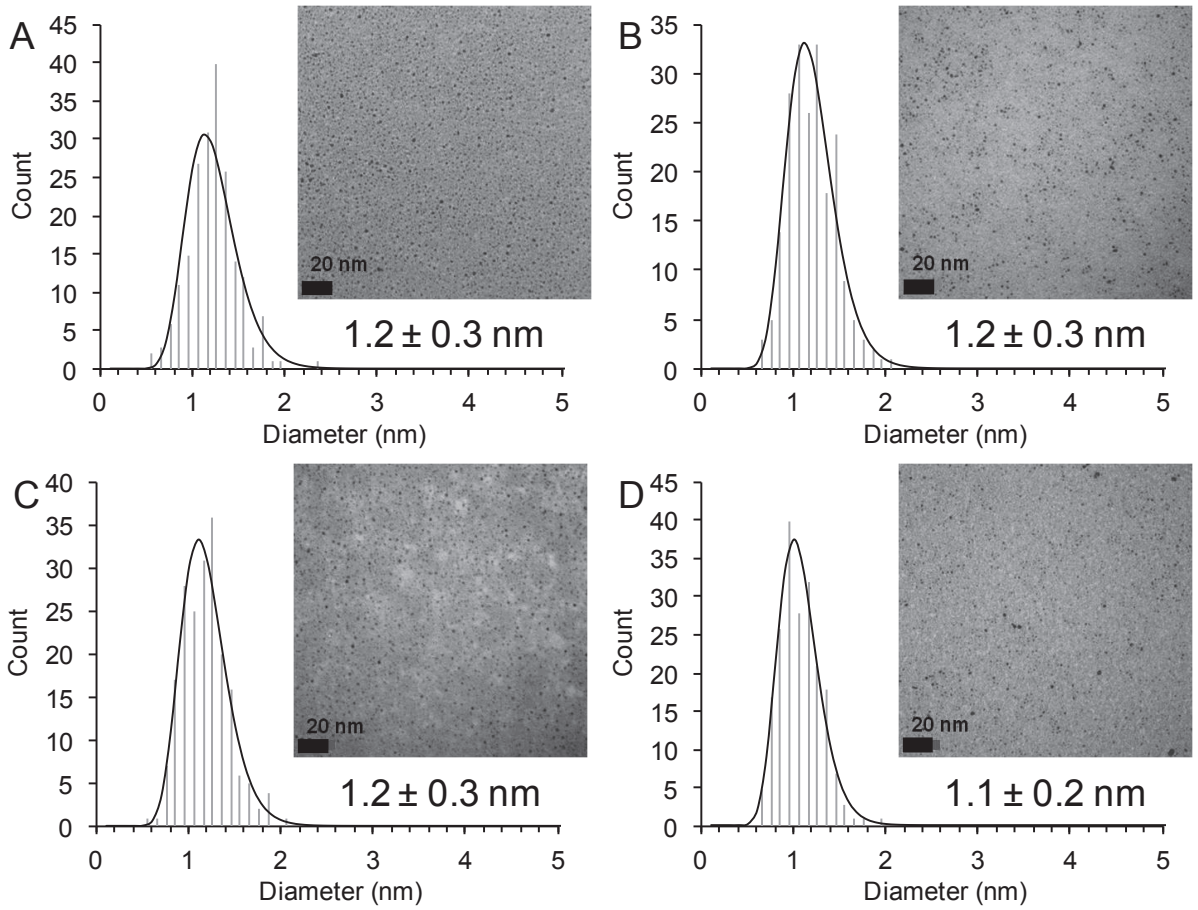

Figure 65. TEM images, a) 0.3 equiv. octylsilane, RT, 30 min., b) 0.3 equiv. octylsilane, RT, 15hrs, c) 1 equiv. octylsilane, RT, 30 min., d) 1 equiv. octylsilane, RT, 15 hrs.

Nanoparticles with a diameter of 1.2 nm and a narrow size dispersion (0.3 nm) were synthesized in a very reproducible manner. No influence of the number of equivalent of octylsilane between 0.3 and 1 was found; after 15 h of stirring, no aggregation or increase of the nanoparticles was observed. At room temperature, the total consumption of the platinum precursor was not achieved after 24 h according to NMR and longer reaction times or heating were necessary. The nanoparticles synthesis was thus carried out at room temperature (60 min) and pursued at 60°C for 15 h, NMR demonstrating the full consumption of the precursor under those conditions. No modification neither of the size nor of the dispersion was found (Figure 66). Those colloids are remarkably stable for months at room temperature, no aggregation or settling of nanoparticles was observed.

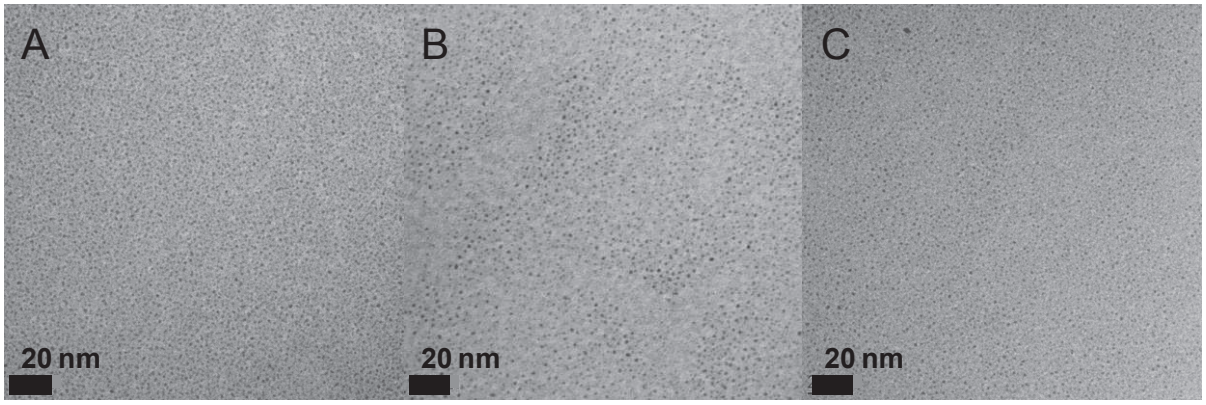

Figure 66. TEM images, (COD)Pt(OSi(O*t*Bu)$_3$)$_2$, 1 equiv. of octylsilane a) 60 min at RT, b) 90 min at 60°C, c) 15 h at 60°C

4.2.2.2.1.2. IR-monitoring of the reaction

The reaction was monitored by transmission infrared (IR) spectroscopy. After 15 h of reaction, the colloidal suspension was concentrated, one drop was placed between two KBr windows and the IR spectrum was recorded. After subtraction of the THF signal (Figure 67), the colloids spectra (d and e) showed the following peaks: the Si-H peak at 2150 cm^{-1} is no more visible indicating the full reaction of the Si-H. The C=C stretching vibration of COD at 1650 cm^{-1} as well as the C=C-H stretching band at 3007 cm^{-1} have also disappeared; these data being consistent with the hydrogenation of this ligand. The colloids spectra presented bending vibrations, δ(C-H) and δ(C-C) between 1100 and 1500 cm^{-1}, and stretching ν(CH) vibrations between 2800 and 3000 cm^{-1} comparable to those of HOSi(O*t*Bu)$_3$ and octylsilane (spectra c and f). Moreover the colloid spectra presented a broad peak at 3400 cm^{-1} similar to that of HOSi(O*t*Bu)$_3$ and associated with ν(OH). Unfortunately, due to their extremely small particle size no separation of the nanoparticles from the reaction solution was possible by centrifugation. The IR spectrum of isolated nanoparticles was thus not recorded.

Overall, the IR spectra of the colloids suggested the formation of HOSi(O*t*Bu)$_3$ as a byproduct and the probable hydrogenation of COD into cyclooctane. The full reaction of silane probably leading to ≡SiC$_8$H$_{17}$ surface species was confirmed.

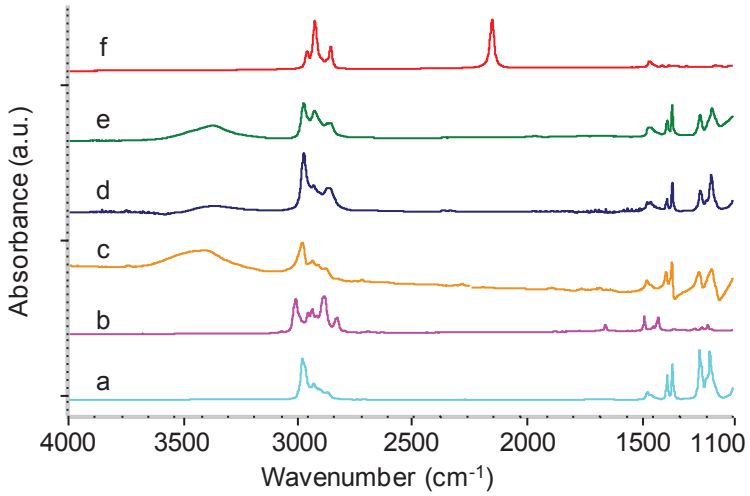

Figure 67. IR spectra of a) (COD)Pt(OSi(O*t*Bu)$_3$)$_2$, b) COD, c) HOSi(O*t*Bu)$_3$, d) 0.3 equiv. $C_8H_{17}SiH_3$, e) 1 equiv. $C_8H_{17}SiH_3$, f) $C_8H_{17}SiH_3$

4.2.2.2.1.3. H_2 chemisorption

The nanoparticles size was also evaluated by H_2 chemisorption for comparison with TEM analyses. After synthesis (1 equiv. octylsilane, 60°C overnight), the colloids were impregnated (1 wt%) onto silica by the Incipient Wetness Impregnation method[124] (IWI). Silica was previously calcined and dehydroxylated at 700°C under secondary vacuum. For IWI, a simply dried support is typically necessary (for silica a treatment at 120°C under primary vacuum would have been sufficient), but we used silica partially dehydroxylated at 700°C silica for ease of interpretation (this process ensure a simple IR-DRIFT spectrum - isolated Si-OH, ν(OH) at 3740 cm^{-1} and Si-O-Si deformation bands bellow 2000 cm^{-1}). Samples were then dried under an argon flow and finally under primary vacuum at room temperature. The DRIFT spectrum of the as-prepared sample is presented in Figure 68 b. The broad peak at 3400 cm^{-1} (νOH) was attributed to absorbed HOSi(OtBu)$_3$. To ensure a clean platinum surface ready for H_2 chemisorption and based on previous work,[84] supported nanoparticles were calcined under a dry air flow (40 mL.min^{-1}) at 320°C for 15 h. IR-DRIFT showed the disappearance of multiple C-H stretching peaks (2800 to 3000 cm^{-1} - Figure 68 c), this process ensured the efficient removal of the pending alkyl chains. The remaining peaks at 2982 and 2931 cm^{-1} were attributed to *t*Bu unit *via* the formation of HOSi(O*t*Bu)$_3$. Platinum was then reduced under a hydrogen flow (40 mL.min^{-1}) at 500°C for 6 h. The IR spectrum is presented in Figure 68 d. Under such high temperature the remaining HOSi(O*t*Bu)$_3$ was eliminated, no more ν(C-H) bands were found bellow 3000 cm^{-1}.

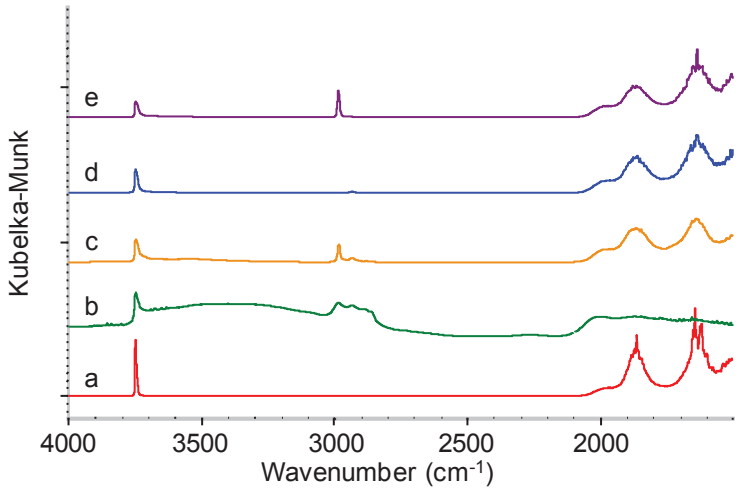

Figure 68. a) $SiO_{2\text{-}700}$, b) after IWI, c) calcined ,d) reduced ,e) HOSi(O*t*Bu)3 @ $SiO_{2\text{-}700}$ after calcination

The IWI process also ensured an efficient dispersion of the nanoparticles as no aggregate was found by TEM (Figure 69). Moreover, the subsequent thermal treatment under air and H_2 did not led to an increase of the nanoparticles size, demonstrating high stability of the nanoparticles under such conditions.

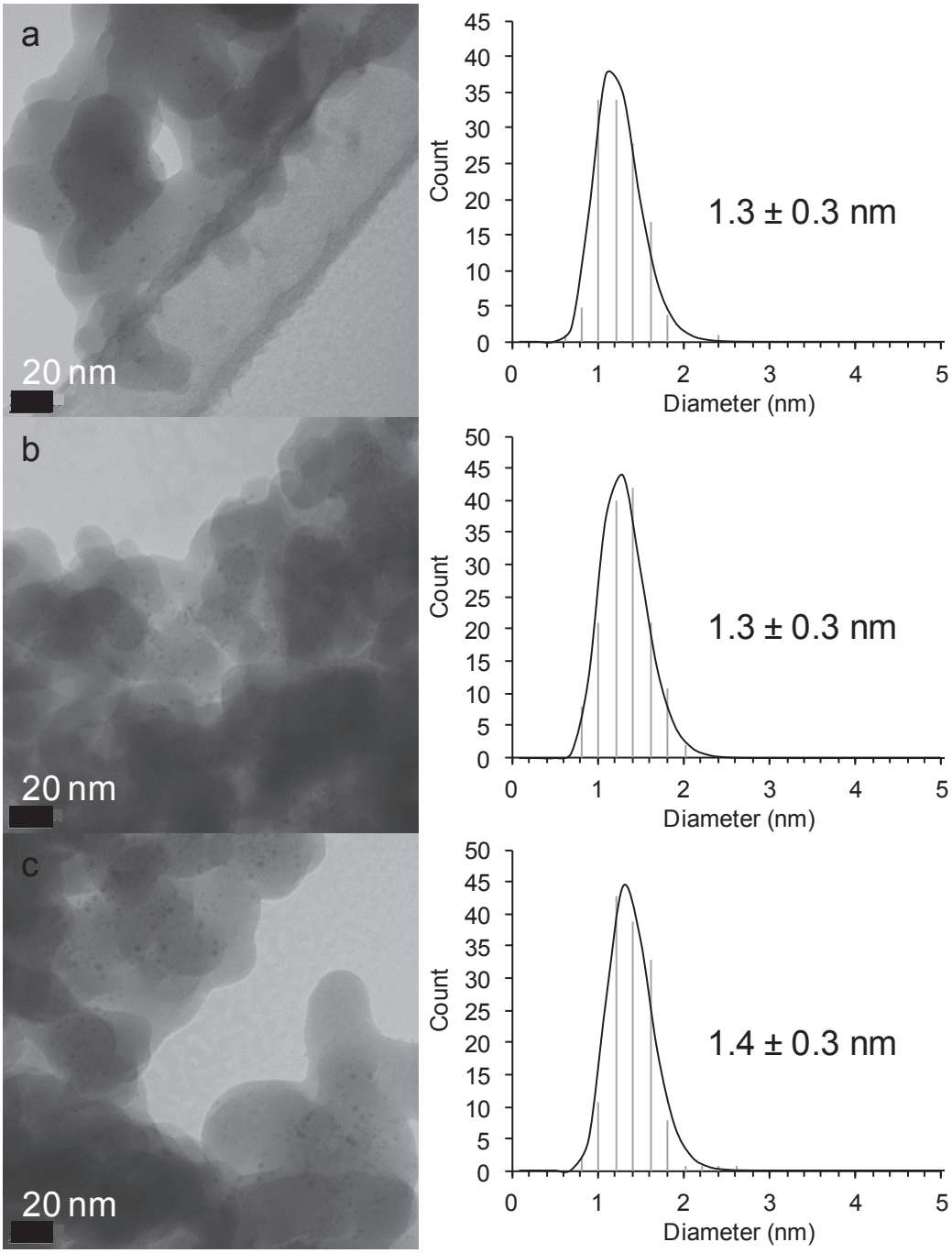

Figure 69. a) as prepared after IWI, b) calcined, c) reduced

Finally, H_2 chemisorption was performed on the reduced sample (Table 14). We consider 1.8 atom of hydrogen per surface platinum atom.[125] From the measured dispersion, the nanoparticle size was estimated considering a truncated cubic octahedron shape.[119]

Table 14. H_2 chemisorption

Pt loading	1%
n Pt mmol.g^{-1}	0.051
nH per surface Pt	1.8
Q max (mmol H_2.g^{-1})	0.039
dispersion	68%
particle size based on cubic octahedron	1.54

Based on two samples, the dispersion was defined within ±8%, the nanoparticles size found was thus 1.6 ± 0.3 nm which is in excellent correlation with TEM analysis.

4.2.2.2.2. In-situ NMR monitoring of Pt nanoparticles formation

To gain more insights into the nanoparticles synthesis mechanism, liquid state NMR experiments were carried out. The reaction of one equiv. of octylsilane with one equiv. of (COD)Pt(OSi(O*t*Bu)$_3$)$_2$ was carried out in a Young NMR tube in THF-d$_8$. Upon addition of the silane, a quick coloration change occurred from color-free to brown; few bubbles were formed. NMR spectra from 2 minutes reaction to 110 h are presented in Figure 70. The peaks at 5.50/2.32 ppm were attributed to free cyclooctadiene (=C-H and –CH_2-) and the one at 5.33 ppm to the silanol group of tris(tert-butoxy)silanol. The release of tris(tert-butoxy)silanol was further evidenced by the disappearance of the peak at 1.31 ppm associated with PtOSi(OC(C**H**$_3$)$_3$)$_3$ and the formation of a peak at 1.30 ppm attributed to the methyl signal of free tris(tert-butoxy)silanol (see Figure 71 and Appendix 20 d). The formation and further consumption of H_2 was evidenced by monitoring the peak at 4.55 ppm associated with dissolved H_2. The consumption of H_2 was concomitant with the disappearance of the COD peaks, the formation of cyclooctene (5.51 and 1.51 ppm) and then its final hydrogenation into cyclooctane (1.54 ppm). This hydrogenation process underlined the formation of platinum nanoparticles as platinum surface is needed to split hydrogen and for the hydrogenation of cyclooctadiene.

The silane reactivity was evidenced by the disappearance of the Si**H**$_3$ triplet at 3.47 ppm. In the same time, the peak at 0.77 ppm (-CH_2-Si) was shifted toward higher fields up to 0.68 ppm and the peak shape was broadened (Figure 72). Those observations are consistent with the formation of surface species as depicted in Figure 72. The formation of n-octane was evidenced by the appearance of a peak at 0.89 (C**H**$_3$) and 1.29 ppm (C**H**$_2$). The peak at 2.50

ppm observed after 110 h was associated to water from external contamination. Weak peaks at 4.63 and 4.72 ppm were formed; their attribution will be discussed later.

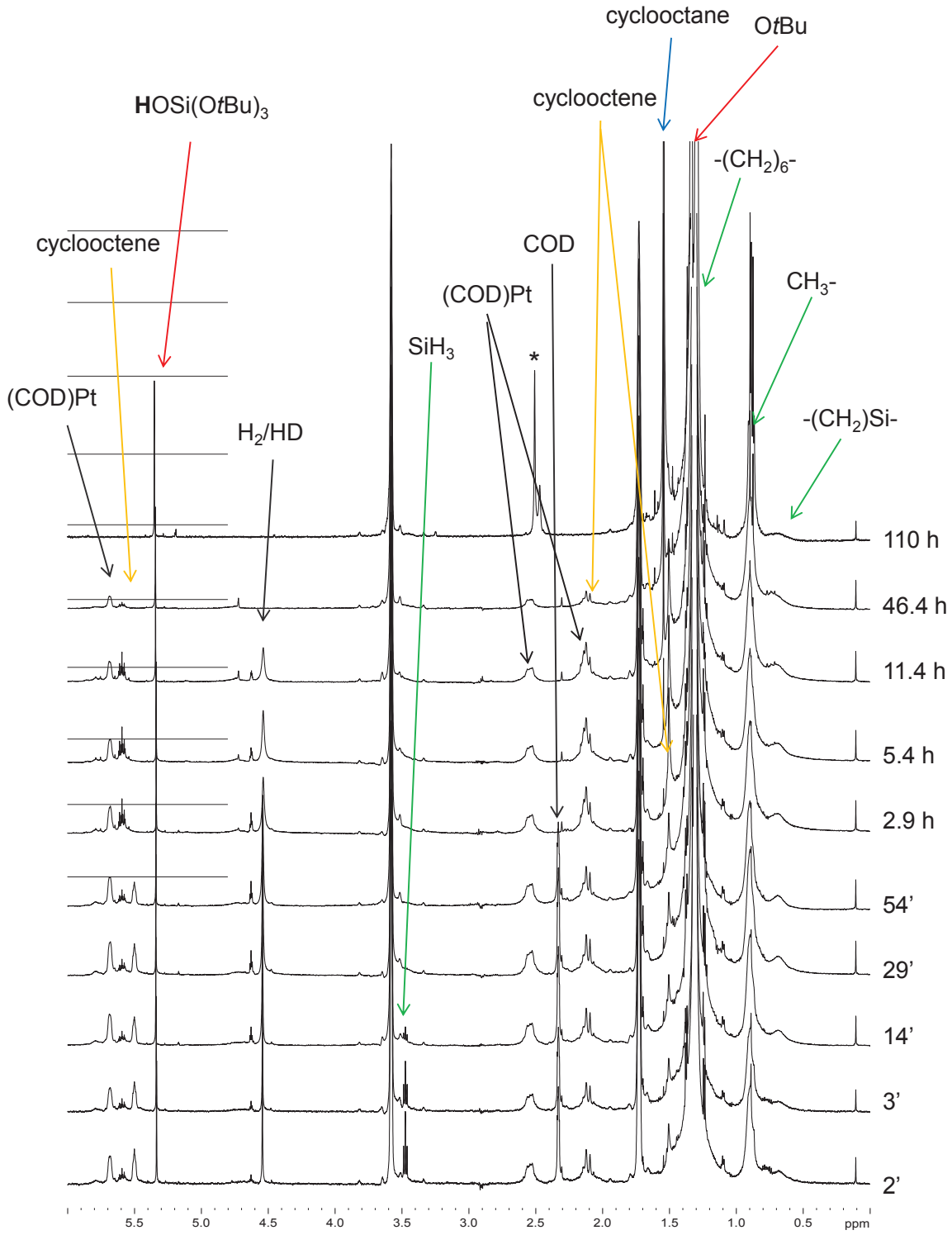

Figure 70. NMR spectra, synthesis of Pt nanoparticles from $(COD)Pt(OSi(OtBu)_3)_2$ + 1 equiv. octylsilane at RT in THF-d_8

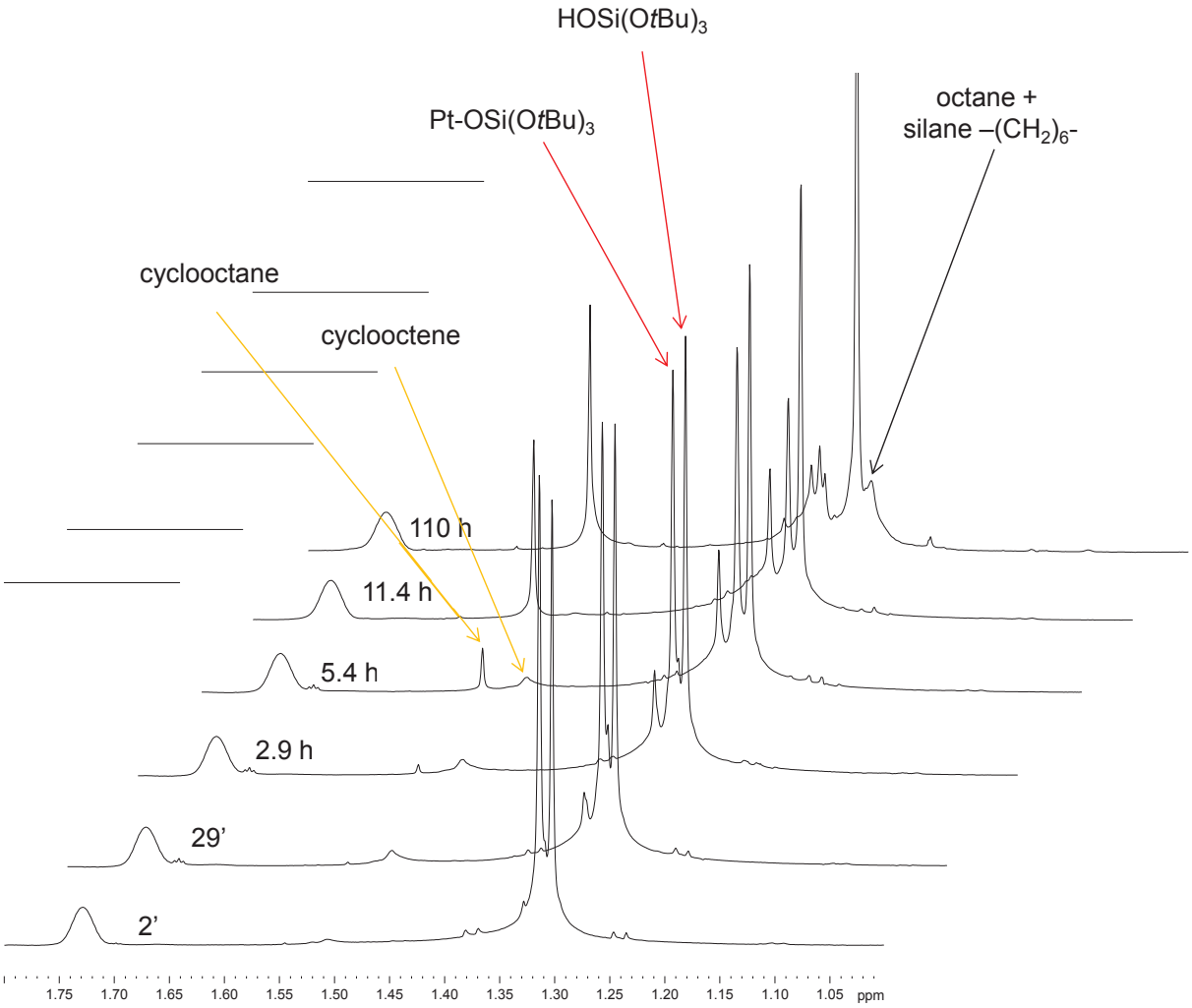

Figure 71. 1.8 to 1 ppm zoom-in

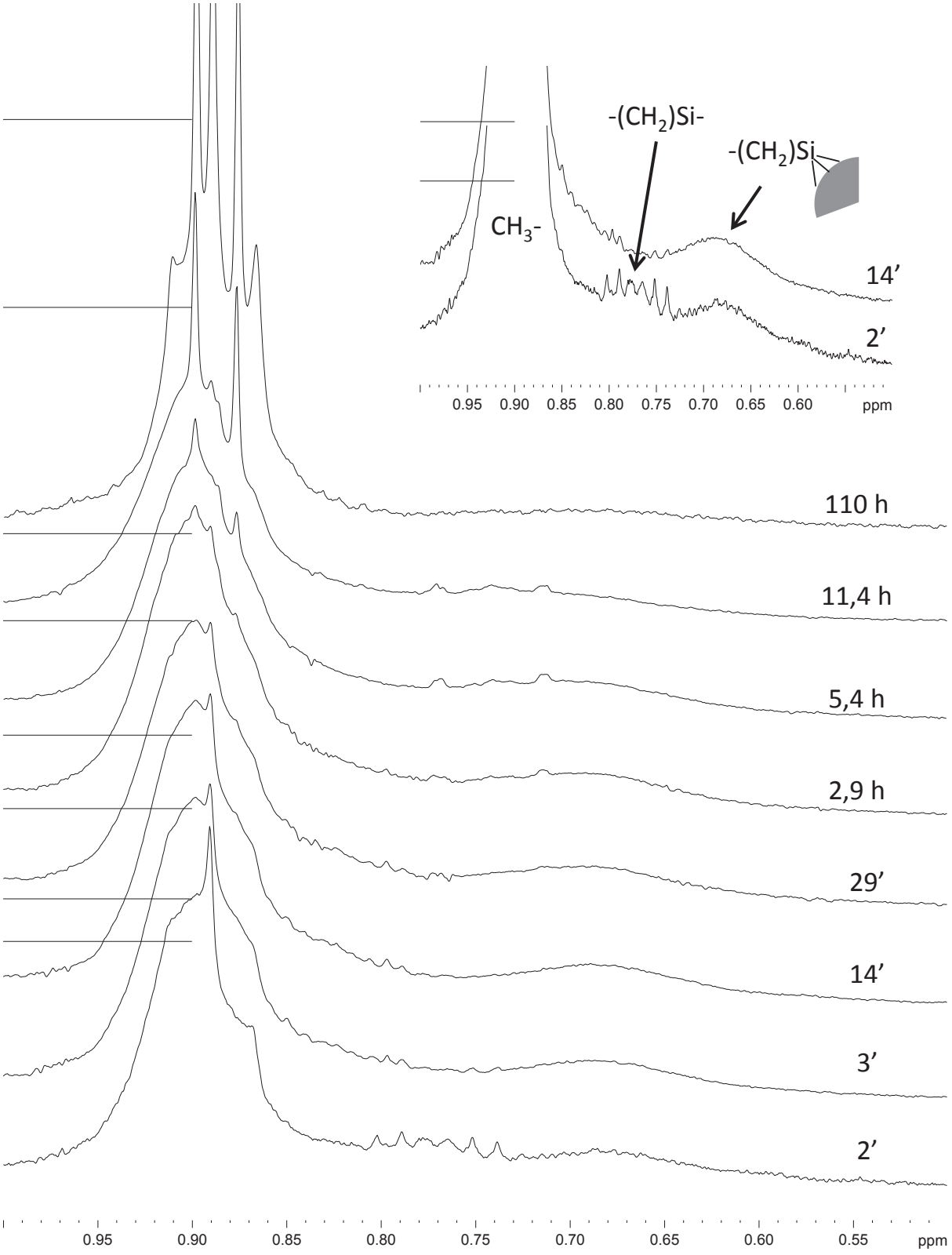

Figure 72. 1 to 0.5 ppm zoom-in

The formation of $\equiv SiC_8H_{17}$ species at the platinum nanoparticles surface is further supported by Diffusion Ordered Spectroscopy (DOSY) NMR experiments. This technique separates the

NMR signals of different species according to their diffusion coefficient. Results are presented in Figure 73.

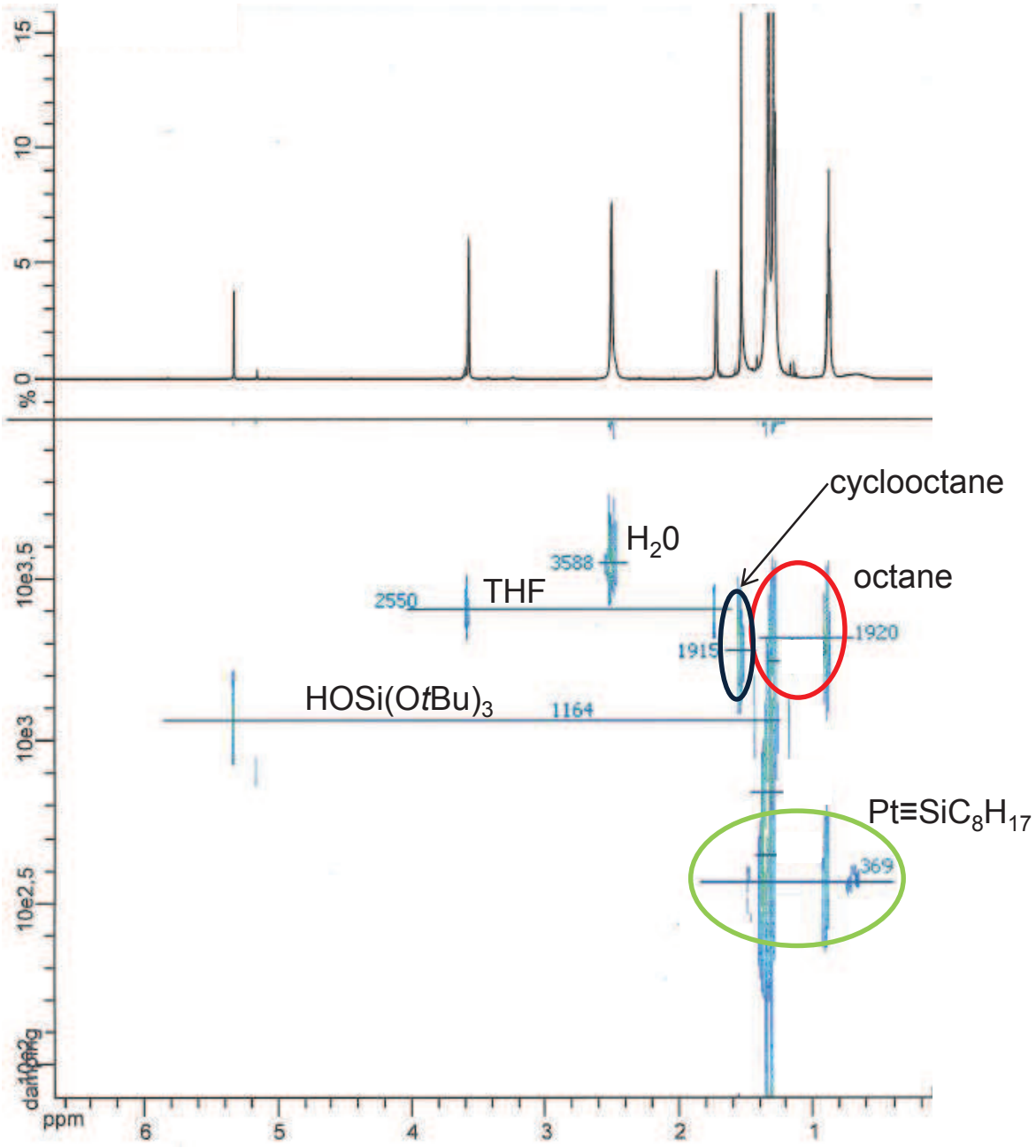

Figure 73. ^{1}H-DOSY experiment of $(COD)Pt(OSi(OtBu)_3)_2$ + 1 equiv. octylsilane after complete reaction

The 3 peaks at 1.30, 0.89 and 0.68 ppm, respectively attributed to $-(CH_2)_6-$, CH_3- and $-CH_2Si-$ of the octysilane molecule, present a very low diffusion coefficient, 369 $\mu m^2.s^{-1}$, compared to other species. The diffusion coefficient in THF of octylsilane itself was measured separately: a value of 1740 $\mu m^2.s^{-1}$ was found (Appendix 19). This clearly highlights for the formation of platinum nanoparticles covered by SiC_8H_{17} chains. The two signals presenting the same diffusion coefficient at 1.29 and 0.87 were attributed to n-octane and confirmed its formation.

Moreover, the diffusion coefficient (1920 $\mu m^2.s^{-1}$) is close to that of cyclooctane (1.54 ppm - 1915 $\mu m^2.s^{-1}$).

The diffusion coefficients are directly related to the hydrodynamic radius of molecules (Equation 3). Here the nanoparticles size could be estimated from the diffusion coefficient of grafted octylsilane molecules.[126]

$$D = \frac{k_B T}{6\pi\eta R_H}$$

Equation 3.

A hydrodynamic radius of 1.3 nm was calculated (Appendix 21) corresponding to nanoparticles with a 2.6 nm diameter. This is to be compared with TEM analysis where nanoparticles of 1.2 nm are found. By TEM the silane shell ($\equiv SiC_8H_{17}$) cannot be seen (no contrast between the carbons of the silane chains and the carbon layer deposited onto the TEM grids) and only the platinum core is imaged. The total nanoparticle diameter would thus be theoretically of 3.2 nm considering straight octylchains (Appendix 22) covering the surface as depicted in Figure 74. Note that this was likely to lead to an overestimation of the nanoparticles size. NMR confirmed the formation of nanoparticles stabilized by octylsilane. The oxidative addition of octylsilane and the further reductive elimination forming H_2 is hypothesized to explain the formation of the nanoparticles.

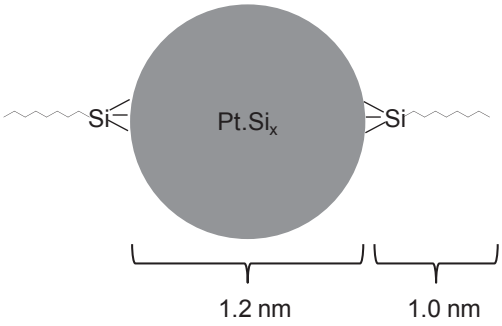

Figure 74. Schematic representation of a platinum nanoparticle stabilized by octylsilane

4.2.2.3. (COD)Pt(Me)(OSi(OtBu)$_3$) and (COD)Pt(Cl)(Me)

We further decided to test two other Pt molecular precursors, namely (COD)Pt(Me)(OSi(O*t*Bu)$_3$) and (COD)Pt(Cl)(Me) for nanoparticles synthesis *via* the colloidal approach. For both precursors, slower kinetic were observed. Upon addition of one equiv. of octylsilane, (COD)Pt(Me)(OSi(O*t*Bu)$_3$ reacted (coloration change from color-free to brown)

within 10 min and (COD)Pt(Me)(Cl) in about 15 min affording nanoparticles of respectively 1.3 (σ = 0.3) nm and 1.3 (σ = 0.2) nm in diameter (Figure 75).

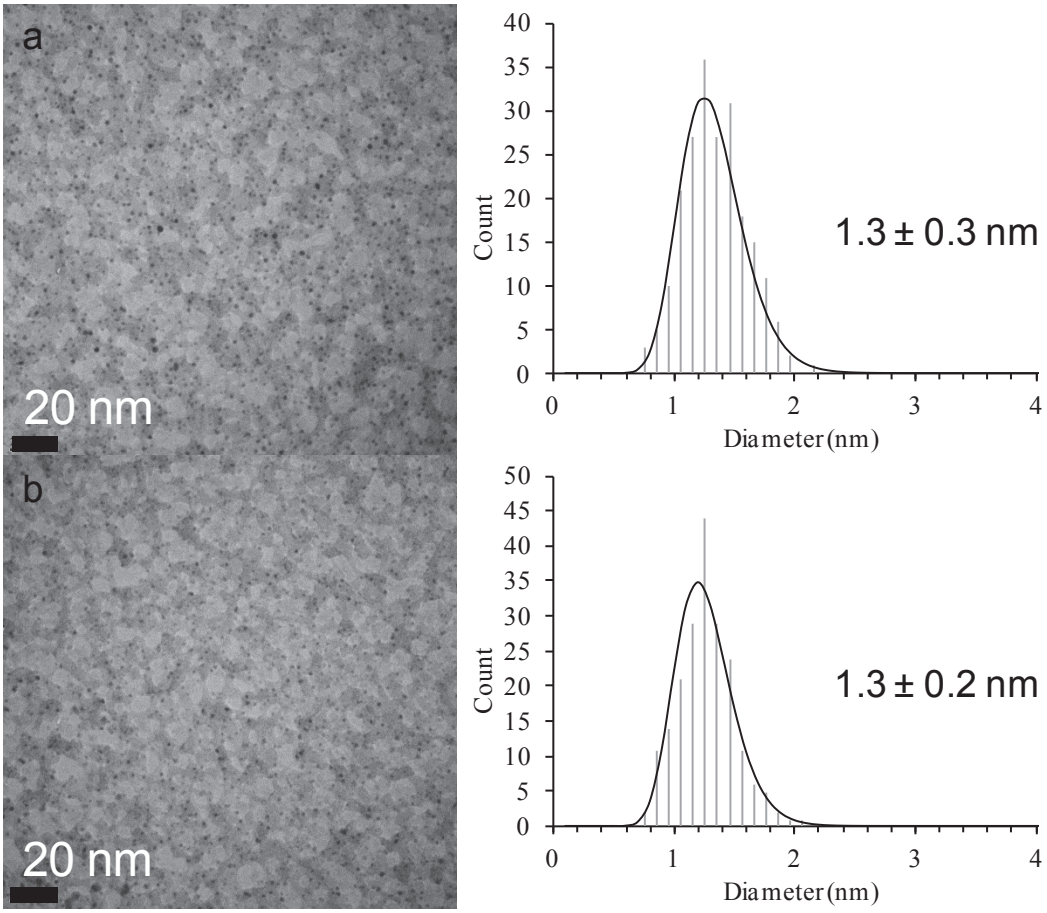

Figure 75. TEM images, colloids synthesized after 30 min. from 1 equiv. of octylsilane and a) (COD)Pt(Me)(OSi(OtBu)$_3$) and c) (COD)Pt(Cl)(Me).

The formation of nanoparticles from (COD)Pt(Me)(OSi(O*t*Bu)$_3$) was monitored by liquid-stateNMR spectroscopy; results are presented in Figure 76. One equiv. of octylsilane was added, the reaction kinetic being relatively slow, the formation and then consumption of H_2 could be easily observed. The liberated COD readily reacted with dihydrogen to yield cyclooctene (5.51 and 1.51 ppm) and finally cyclooctane (1.54 ppm). The Pt-Me bond was broken as witnessed by the diminution of the peak at 0.74 ppm (attributed to Pt-Me). This decrease was concomitant with the appearance of a peak at 0.19 ppm primarily attributed to methane. After evacuation of the NMR tube prior to new measurements, the peak at 0.19 ppm remained unchanged. 2D-^{1}H,^{29}Si HSQC NMR experiments (Heteronuclear Single Quantum Coherence) shows a coupling between the singlet protons at 0.19 ppm and a silicon atom. This peak was thus attributed to (C**H**$_3$)$_3$-Si, the Si atom having no proton. Peaks at high fields, 0.11 ppm (triplet – rapidly fading) and 0.21 ppm (doublet), were similarly attributed to C**H**$_3$-SiH$_x$- species (x being equal to 1 or 2). The peak at 1.31 ppm corresponding to the -

$OSi(O\mathit{t}Bu)_3$ ligand faded and peaks at 1.30 ppm (*t*Bu) and 5.33 ppm (O**H**) attributed to $HOSi(O\mathit{t}Bu)_3$ concomitantly appeared. The formation of a peak at 1.33 ppm was also observed and attributed to $(\mathbf{\mathit{t}Bu}O)_3SiOSiH_xR$ species. The peak at 4.72 ppm was attributed to -O-Si$\mathbf{H}_x$- species (Appendix 23) whether being intermediates species onto platinum centers or reaction byproducts arising from the formation of Me/silane and $(\mathit{t}BuO)_3SiO$/silane (peak at 1.33 ppm) coupling byproducts with the generic formula $H_wSi(CH_3)_x(OSi(O\mathit{t}Bu)_3)_y(C_8H_{17})_z$ (w+x+y+z = 4). One silane molecule probably reacts with several platinum complexes by oxidative addition followed by reductive elimination. Concerning octylsilane protons signals, observations similar to those with $(COD)Pt(OSi(O\mathit{t}Bu)_3)_2$ were made. The disappearance of the Si$\mathbf{H}_3$ triplet at 3.47 ppm evidenced the reactivity of the silane and in the same time, the peak at 0.77 ppm (-C$\mathbf{H_2}$-Si) was shifted toward higher fields up to 0.68 ppm and broadened, proving the formation of surface species. After 9 h a steady state is reached, only a fraction (about a half) of the platinum complex had reacted and the liberated COD was not fully hydrogenated. Due to the particular reactivity induced by the methyl ligand, a second equiv. of octylsilane was added and required to complete the reaction. After 12 h, full consumption of the Pt precursor was observed (Figure 76 c).

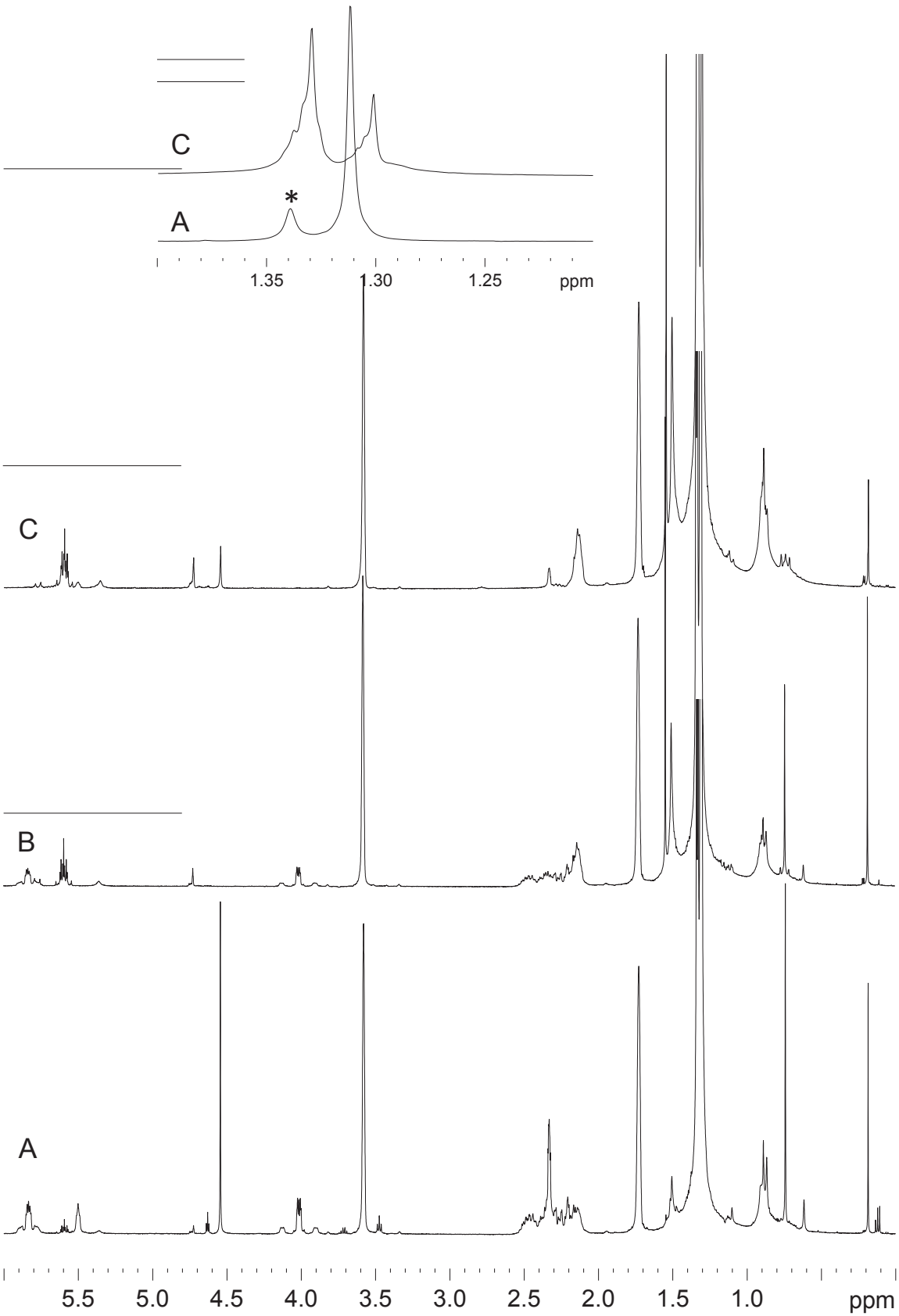

Figure 76. ^{1}H NMR spectra at RT in THF-d_8, synthesis of Pt nanoparticles from (COD)Pt(Me)(OSi(OtBu)$_3$)$_2$ A) 8 min after addition of 1 equiv. octylsilane, B) after 12.5 h, C) 12 h after addition of a second equiv. of octylsilane

4.2.3. Conclusion

In conclusion, platinum nanoparticles stabilized by octylsilane were successfully synthesized under mild conditions without the use of H_2 from Pt^0 or Pt^{II} organometallic complexes. The synthesis of even smaller nanoparticles, with a diameter of 1.1 to 1.3 nm vs. 1.8 nanoparticle generated from $Pt^0(dba)_2$, was performed from Pt^{II} complexes. The size dispersion was always found very narrow with standards deviations ranging from 0.2 to 0.3 nm. The silane played the role of both stabilizing agent and reductant by liberating H_2 upon oxidative addition followed by reductive elimination on platinum centers. The inner structure of the nanoparticles has still to be elucidated, but the full silane consumption and the formation of n-octane both point towards the formation of PtSi structures, whether being alloyed or solid solutions, the nanoparticles being stabilized by $\equiv SiC_8H_{17}$ surface species.

4.3. Palladium nanoparticles

4.3.1. Synthesis using H_2 as an external reductant

Similarly to platinum, $Pd(dba)_2$ (palladium dibenzylideneacetone), a Pd^0 commercially available palladium precursor was used. One equiv. of octylsilane ($C_8H_{17}SiH_3$) was used as stabilizing agent, THF was found to be the more appropriate solvent for this synthesis.[127] Upon addition of 3 bars of H_2 and vigorous stirring at room temperature, a coloration change from pink to black was noticed within 4 h demonstrating a faster kinetic than Pt. Stirring was maintained over night for a total of 15 h. TEM imaging is the method of choice to evaluate the morphology and size repartition of those nanoparticles. As seen in Figure 77, palladium nanoparticles were produced with a mean size of 1.7 nm and a remarkably narrow size distribution (σ = 0.4 nm).

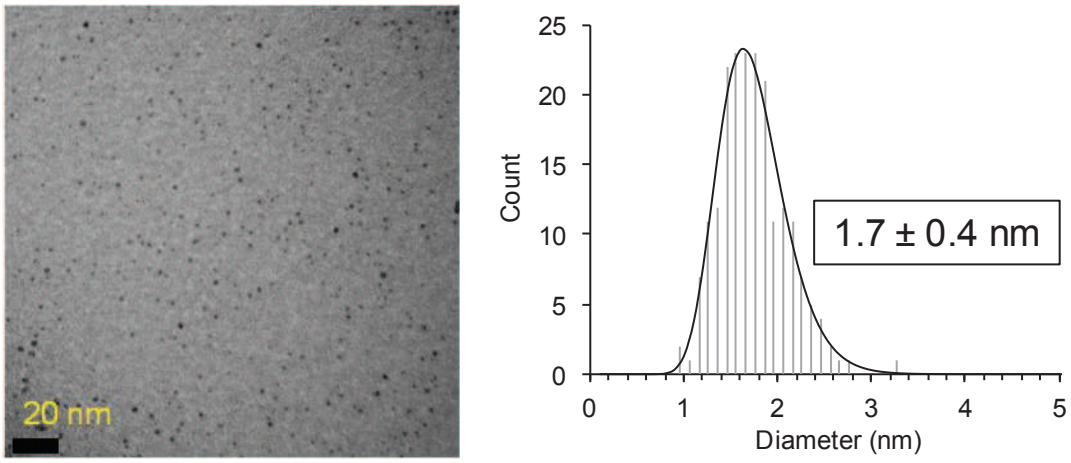

Figure 77. Palladium nanoparticles synthesized with one equiv. of octylsilane in THF

The dramatic coloration change was monitored by mean of UV-Vis spectroscopy (Figure 78). The absorption peak at 320 nm typical of $Pd(dba)_2$ faded after reaction indicating the total consumption of the precursor.

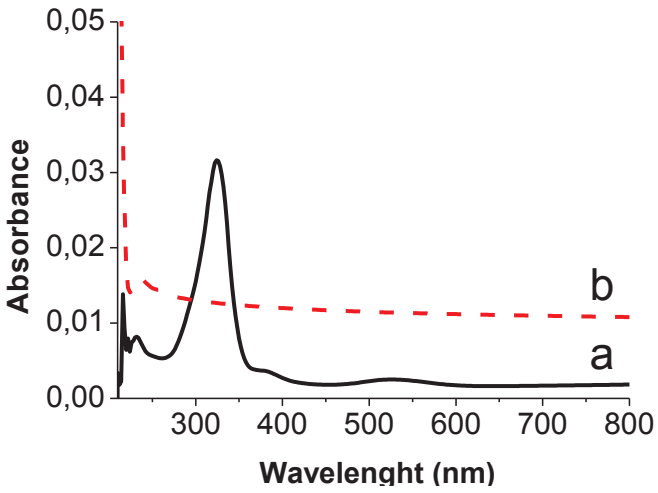

Figure 78. UV-Vis spectrum of a) $Pd(dba)_2$ and b) Pd colloidal solution

The byproducts of the reaction were further analyzed. After filtration over alumina to trap the Pd nanoparticles the liquid phase was analyzed by gas chromatography coupled with mass spectrometry (GC-MS). 1-5,dicyclohexylpentane and n-octane were detected similarly to the results obtained for $Pt(dba)_2$. The release of octane points out the formation of PdSi nanoparticles as already discussed for Pt.

4.3.2. Synthesis in the absence of H_2

As for the synthesis of platinum nanoparticles, the need for H_2 was questioned. A $Pd(dba)_2$ solution was heated in THF at 60°C, neither coloration change nor formation of aggregates were observed after two hours demonstrating the good thermal stability of the precursor.

When one equiv. of octylsilane was rapidly added (about 1 second), a dramatic coloration change from pink to dark black was noticed in a few seconds. TEM images of the nanoparticles after overnight reaction at 60°C are presented in Figure 79. No further NMR analyses were performed onto the Pd system. The formation process being probably the same as from $Pt(dba)_2$ as indicated by kinetic observations and by products analyses.

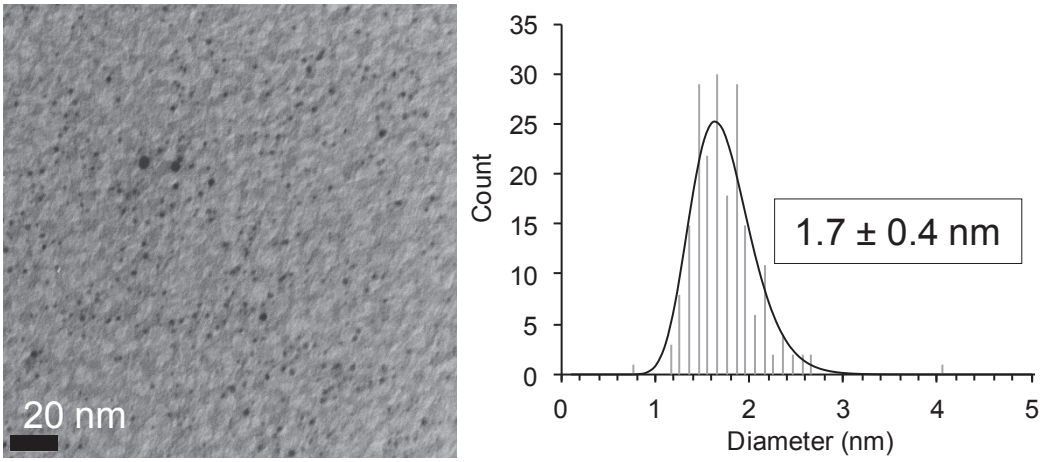

Figure 79. TEM pictures of Pd nanoparticles prepared at 60°C

4.3.3. Conclusion

In conclusion, palladium nanoparticles stabilized by octylsilane were successfully synthesized with or without H_2 following previous methods developed for platinum. They display a mean size of 1.7 nm and narrow size dispersion, the standard deviation being 0.4 nm. Based on those results we decided to test the possibility of expending this nanoparticles synthesis methodology towards the synthesis of bimetallic platinum/palladium nanoparticles.

4.4. Platinum/palladium bimetallic nanoparticles

4.4.1. Synthesis and characterization

The synthesis of bimetallic nanoparticles stabilized by octylsilane was attempted by simply mixing in THF both $Pt^0(dba)_2$ and $Pd^0(dba)_2$ precursors. They both display the same structure and have a similar reactivity towards octylsilane. The octylsilane to total metal content ratio was set to 1 as it previously demonstrated to lead to stable and well dispersed nanoparticles. The reaction was carried out under 3 bars of hydrogen at room temperature to ensure complete reaction and hydrogenation of dba. Within 4 h a coloration change from purple to

dark black was noticed. The reaction solution was further mixed at room temperature for 11 h (total reaction time of 15 h) to ensure the complete reaction of both precursors.

4.4.1.1. UV-Vis spectroscopy

UV-Vis spectroscopy was used to monitor the reaction. UV-Vis spectra of the pure precursors are very similar and present an absorption maximum at 320 nm associated with the dba ligand. The UV-Vis spectra of 3/1, 1/1 and 1/3 molar ratio of $Pt(dba)_2$ and $Pd(dba)_2$ are thus identical (Figure 80). After 15 h of reaction, an aliquot of the colloidal solution was analyzed, the intense peak due to the $M(dba)_2$ complexes at 320 nm was no more visible indicating a full consumption of both precursors. Again, GC-MS proved the formation of 1-5,dicyclohexylpentane and n-octane.

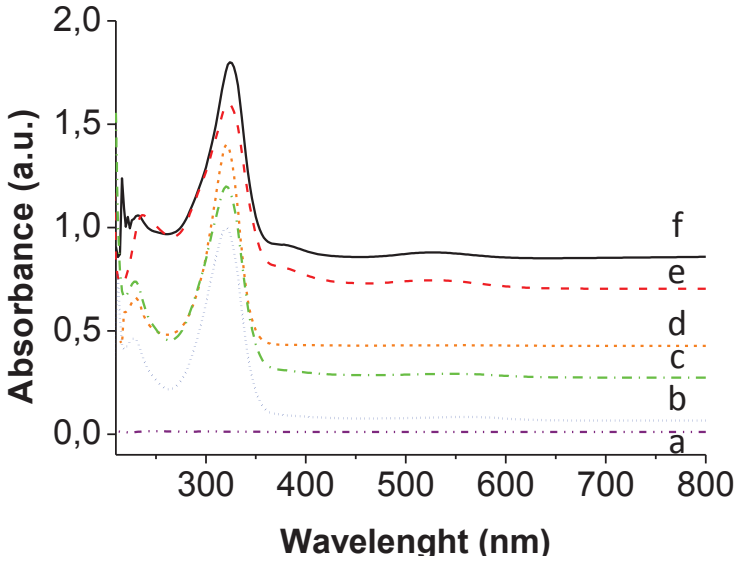

Figure 80. a) Pd colloid, b) $Pt(dba)_2$; $Pt(dba)_2/Pd(dba)_2$ molar ratio c) 3/1, d) 1/1, e) 3/1; f)$Pd(dba)_2$. Peaks are normalized to 1 at maximum intensity.

4.4.1.2. Transmission electron microscopy

After reaction, the colloidal solutions were analyzed by TEM (Figure 81). Nanoparticles from 1.4 to 1.8 nm are synthesized. For all compositions, similar size dispersion were found with a standard deviation from 0.3 to 0.5 nm (Table 15).

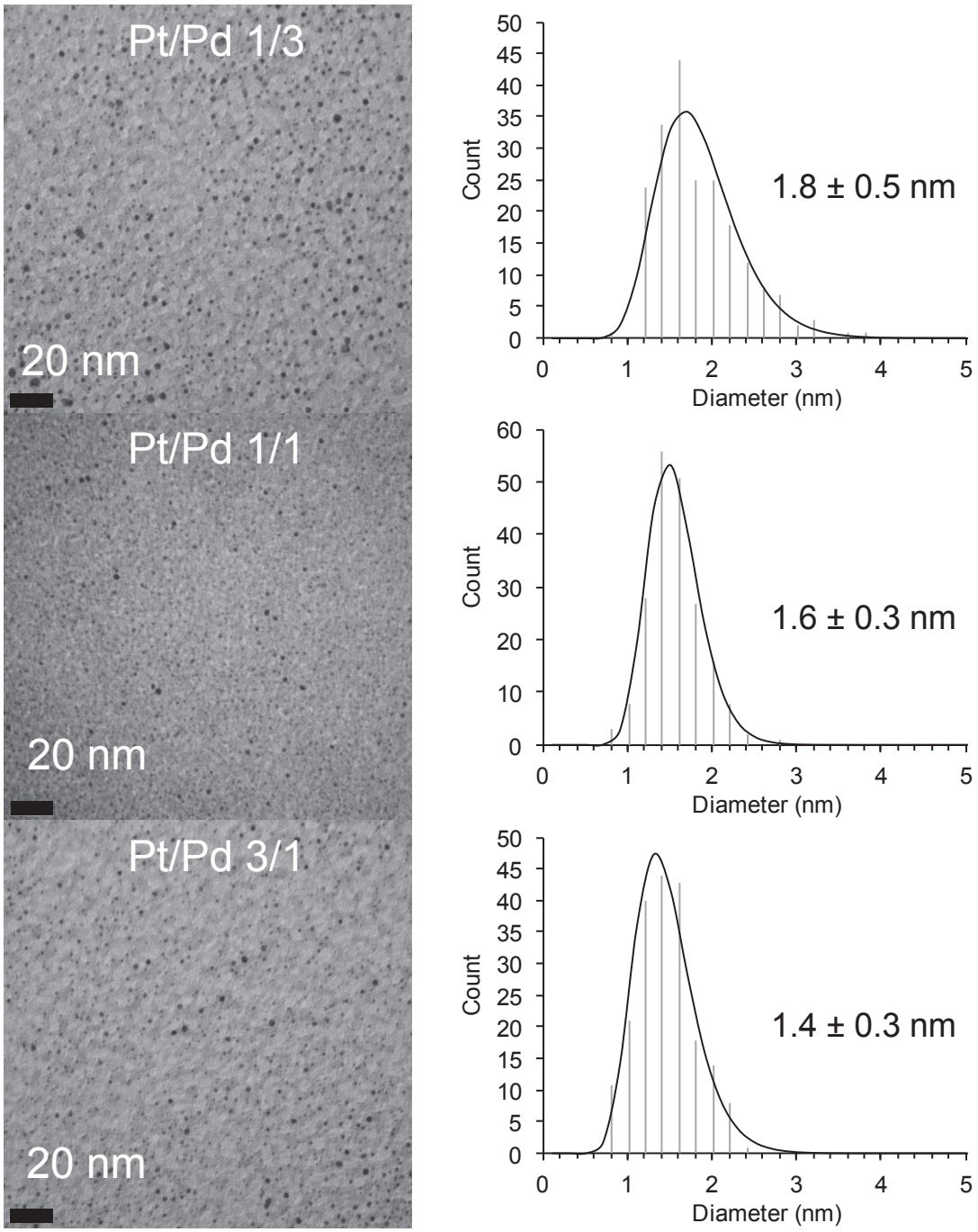

Figure 81. TEM images and corresponding size repartition diagram

Table 15. Monometallic and bimetallic nanoparticles size and standard deviation

composition Pt/Pd	size (nm)	standard deviation (nm)
1/0	1.8	0.3
3/1	1.4	0.5
1/1	1.6	0.3
1/3	1.8	0.5
0/1	1.7	0.3

The nanoparticles size did not vary very much with increasing the palladium content with a lowest value of 1.4 nm for ca. 3/1 Pt/Pd ratio.

TEM highlights the Z contrast, the formation of separated Pt and Pd nanoparticles should thus be visible (platinum nanoparticles being darker than palladium). A mix of separately prepared Pt and Pd nanoparticles was observed by TEM (Appendix 24). Unfortunately no strong Z contrast was evidenced. One cannot conclude by low resolution TEM analysis whether monometallic platinum and palladium nanoparticles or bimetallic Pt/Pd nanoparticles were synthesized.

4.4.1.3. Infrared spectroscopy

IR analyses were carried out using silica supported samples before and after calcination. IR-DRIFT of the as-prepared and calcined samples were recorded after exposure to air (Figure 82). Typical signal of the silane aliphatic chain was observed (ν(C-H) 2985, 2923 and 2855 cm^{-1}) but the ν(Si-H) band at 2150 disappeared. Signals at 3064 and 3029 cm^{-1}, associated with ν(C=C-H) from residual dba aromatic rings or partially hydrogenated dba, were still observed. There was also a large band at 3400 cm^{-1} associated with water absorbed onto silica after exposure to air. After calcination, the ν(C-H) bands dramatically decreased and only bands with a very low intensity were found. This clearly indicated the efficient degradation of the aliphatic chains grafted onto the nanoparticles. Similar results were found for pure Pt or Pd as well as for bimetallic nanoparticles.

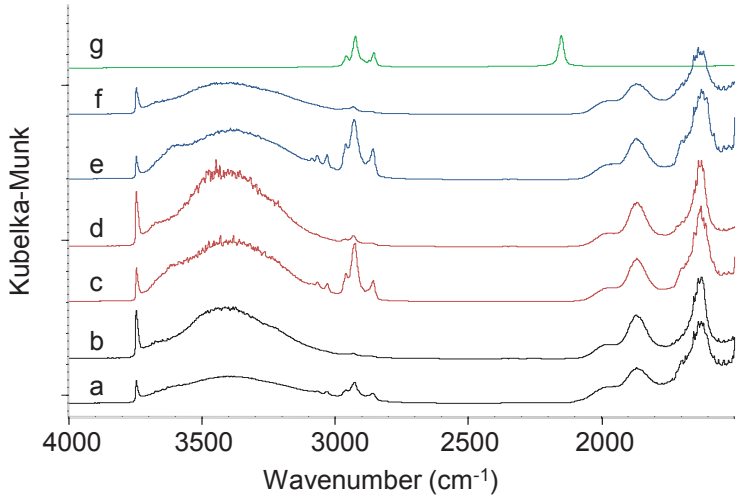

Figure 82. IR-DRIFT spectra after IWI at $SiO_{2\text{-}700}$ of a) Pt colloid, b) Pt calcined, c) Pt/Pd 1/1 colloid, d) Pt/Pd 1/1 calcined, e) Pd colloid, f) Pd calcined, g) pure octylsilane signal (absorbance)

Despite the loss of the organic ligands, the supported colloids were found to be stable as evidenced by TEM. Before and after calcination TEM pictures of the supported nanoparticles were recorded (Figure 83). Nanoparticles were evenly distributed onto the silica surface. After calcination neither aggregation nor increase of the nanoparticles size was noticed.

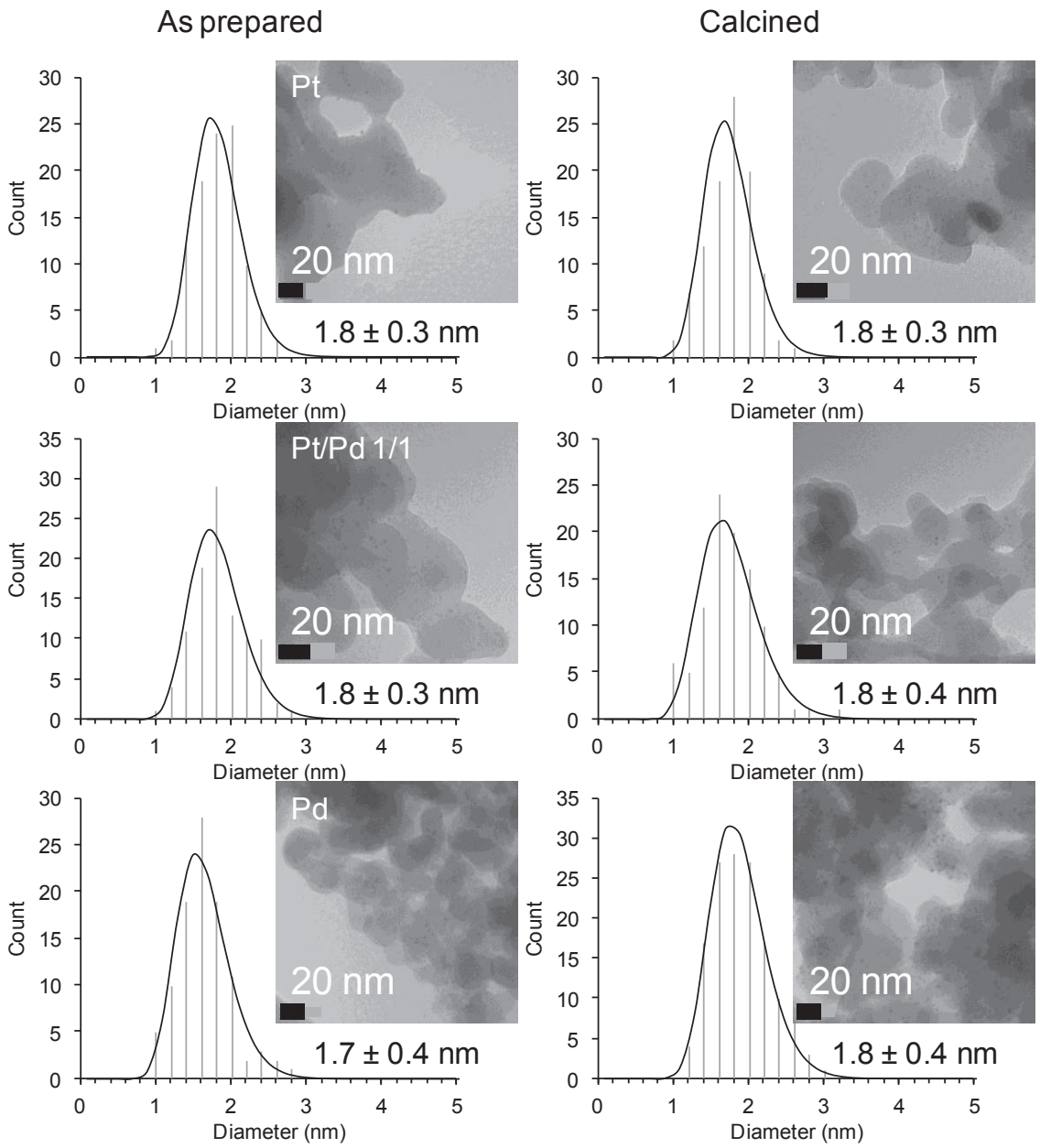

Figure 83. TEM pictures of silica supported nanoparticles, as prepared and calcined

4.4.2. Determining the nature of the nanoparticles prepared from mixtures of Pt and Pd precursors

4.4.2.1. X-Ray photoelectron spectroscopy (XPS)

The platinum, palladium and 1/1 Pt/Pd nanoparticles were studied by XPS (Figure 84) after deposition onto a titanium disc under argon. The XPS spectrum of Pt nanoparticles was already described[84] and repeated for the purpose of this study. Pt-Pt and Pt-Si bonds were evidenced by peaks at 71.6/74.9 and 72.6/75.6 eV and confirmed the formation of Pt-Si bonds

whether arising from the formation of the octylsilane shell or the incorporation of Si into the nanoparticles structure. As prepared Pd nanoparticles presented 2 broad 3d level signals that can be deconvoluted, similarly to Pt, into two pairs of peaks at 336.2/341.6 eV and 337.6/342.9 eV, these peaks were respectively attributed to Pd^0 and Pd^{2+}.[115] The Pd^{2+} signal could be interpreted as Pd-Si. The Pt 4f signal of the bimetallic nanoparticles with a 1/1 ratio was very similar to the one of the Pt monometallic which presented peaks at 71.8/75.2 and 72.8/76.1 eV attributed again to Pt-Pt and Pt-Si bonds. Surprisingly, the Pd 3d signal of the bimetallic nanoparticles presented only the Pd^0 contribution at 336.2/341.6 eV. This could be interpreted as resulting from a core shell structure, the core being Pd enriched but a Pd-Si contribution arising from the incorporation of Si into the nanoparticles structure would still have been expected. The formation of core shell Pt/Pd nanoparticles with an enriched Pd core was previously described by others[128] and was coherent with a faster reaction of the palladium precursor. This, anyhow, confirms the formation of bimetallic nanoparticles instead of separated palladium and platinum nanoparticles.

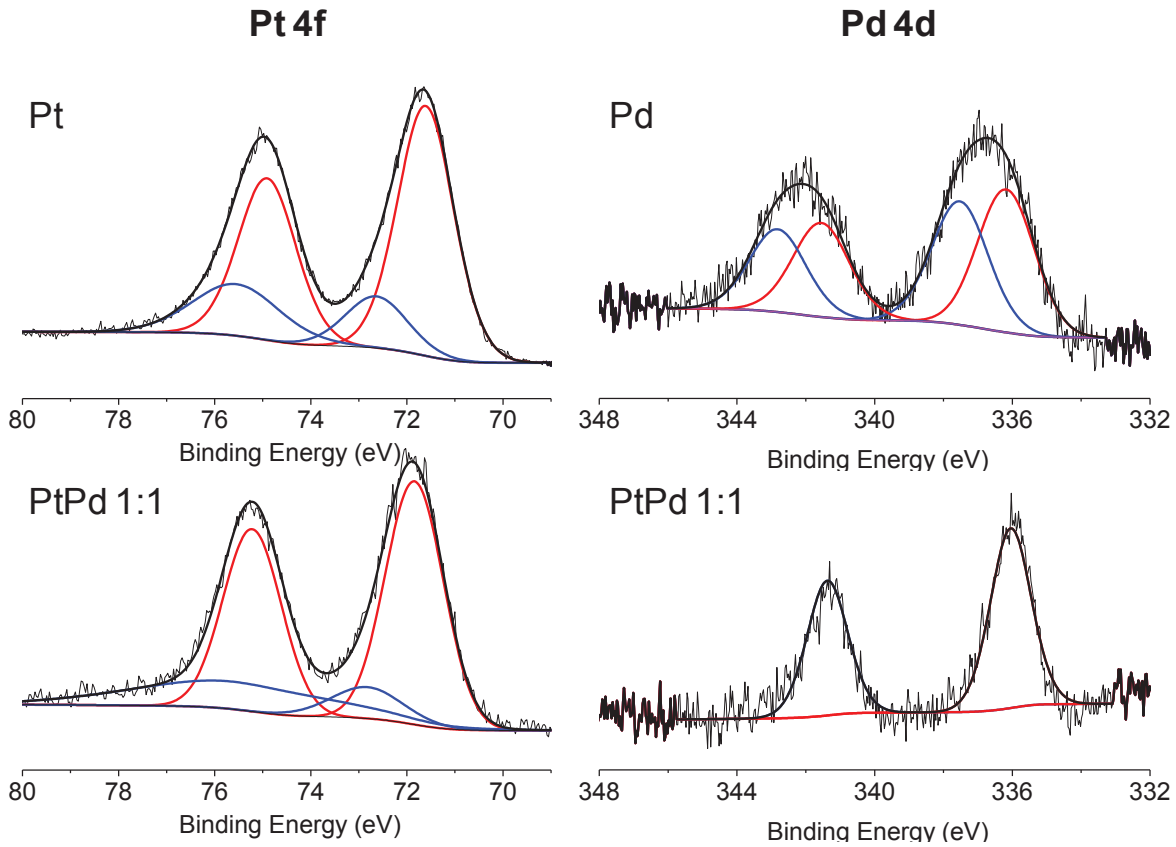

Figure 84. Pt 4f and Pd 3d level XP spectra of Pt, Pd and Pt/Pd 1:1 nanoparticles stabilized by 1 equiv. octylsilane

XP spectra were recorded after calcination under dry air at 320°C (Figure 85). Platinum presented then two main contributions attributed to Pt^0 and Pt^{2+} (PtO)[115] respectively at 71.6/74.9 and 72.9/76.2 eV, the Pt-Si contribution, if still present, was no more visible. The same phenomenon was observed for palladium, the Pd^{2+} being now the predominant species. Interestingly, spectra of the bimetallic nanoparticles displayed both for palladium and platinum a third contribution at higher energies. As in the MOCVD, chapter this could be attributed to a specific interaction between the metals and silica. The formation of silica after calcination being supported by XPS too (Figure 86). The Si 2p signal switches indeed from 102.5 to 103.4 eV, respectively attributed to partial Si oxides (and thus Pt-Si or Pd-Si) and SiO_2[115].

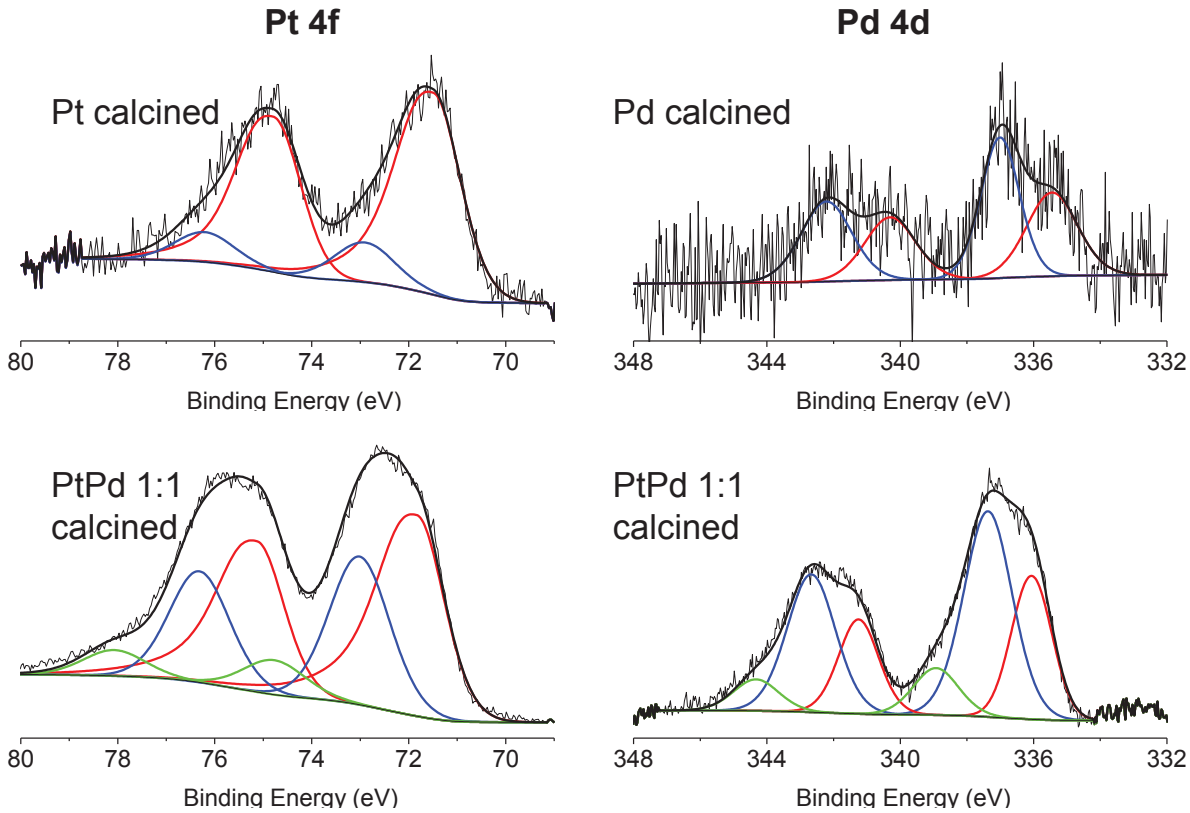

Figure 85. Pt 4f and Pd 3d level XP spectra of Pt, Pd and Pt/Pd 1:1 nanoparticles stabilized by 1 equiv. octylsilane and calcined

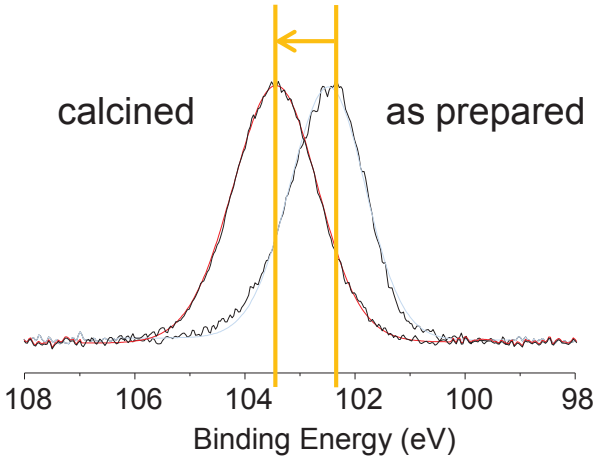

Figure 86. Si 2p XP spectra of Pt/Pd 1:1 nanoparticles before and after calcination

4.4.2.2. High-Resolution Transmission Electron Microscopy

HR-TEM analyses (Figure 87) of Pt/Pd 1:1 nanoparticles demonstrated the crystallinity of those nanoparticles. The lattice spacing measured is 0.229 nm corresponding to platinum (111) plans (0.225 nm[129] to 0.229 nm[130]). Palladium nanoparticles have a very close lattice spacing value of 0.224 nm[130]. Those results are in good agreement with XPS analysis and suggest the formation of a Pt rich shell but due to measurement errors we cannot conclude so far whether alloyed or core shell nanoparticles are obtained as shown by Tsen *et al.*[129]

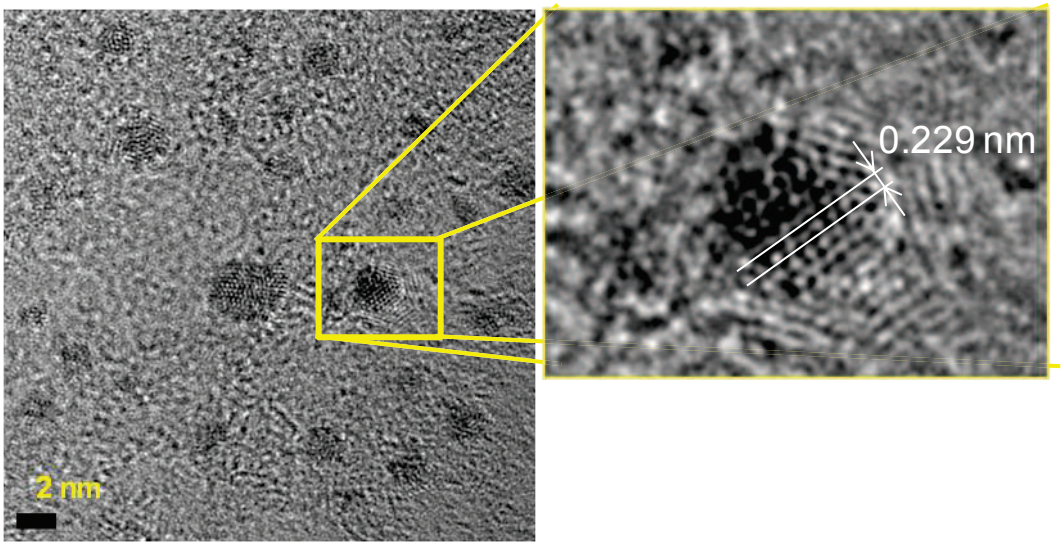

Figure 87. HR-TEM picture of Pt/Pd 1:1 nanoparticles

4.4.2.3. Energy Dispersive X-Ray spectrometry

Energy Dispersive X-Ray spectroscopy performed on single nanoparticles is a powerful tool for bimetallic characterization as shown by Krumeich *et al.*[131] It allows the unambiguous determination of single nanoparticle composition.

EDX spectra were first recorded from Pt/Pd 1:1colloids directly deposited onto copper grids. The EDX spectrum (Figure 88 a) demonstrated the presence of Pt and Pd in a 1/1 ratio along with silicium. During the EDX acquisition (about 1 minute), a drift of the sample occured, this phenomenon added to the high nanoparticles surface density did not allowed us to conclude on single nanoparticles composition. Moreover, those results were poorly reproducible due to a high carbon contamination resulting from the silane decomposition under the energetic electron beam of the HR-TEM microscope. Analyses were thus carried out on isolated nanoparticles supported onto silica and calcined. This ensured the stabilization of the nanoparticles and allowed for longer acquisition times. Those measures were repeated on 3/1 and 1/3 Pt/Pd samples, the calculated ratio came from the average of 5 to 10 measures, results are presented in Table 16. The platinum content is higher than expected for the 75/25 and 25/75 ratio. The standard deviation was ± 3 % but the error on the EDX measures was estimated to *ca.* 10 %.

Table 16. Pt/Pd ratio measured by EDX on nanoparticles impregnated on alumina and calcined

Pt/Pd theoretical composition	Pt/Pd measured
75/25	85/15
50/50	51/49
25/75	37/63

To confirm the presence of silicium into/onto the nanoparticles, an EDX spectrum was recorded on alumina supported sample after calcination (Figure 88 b). A Si signal was found at 1.75 keV confirming the Pt/Pd/Si composition of the nanoparticles but we were not able to record repeatable Si/M ratio.

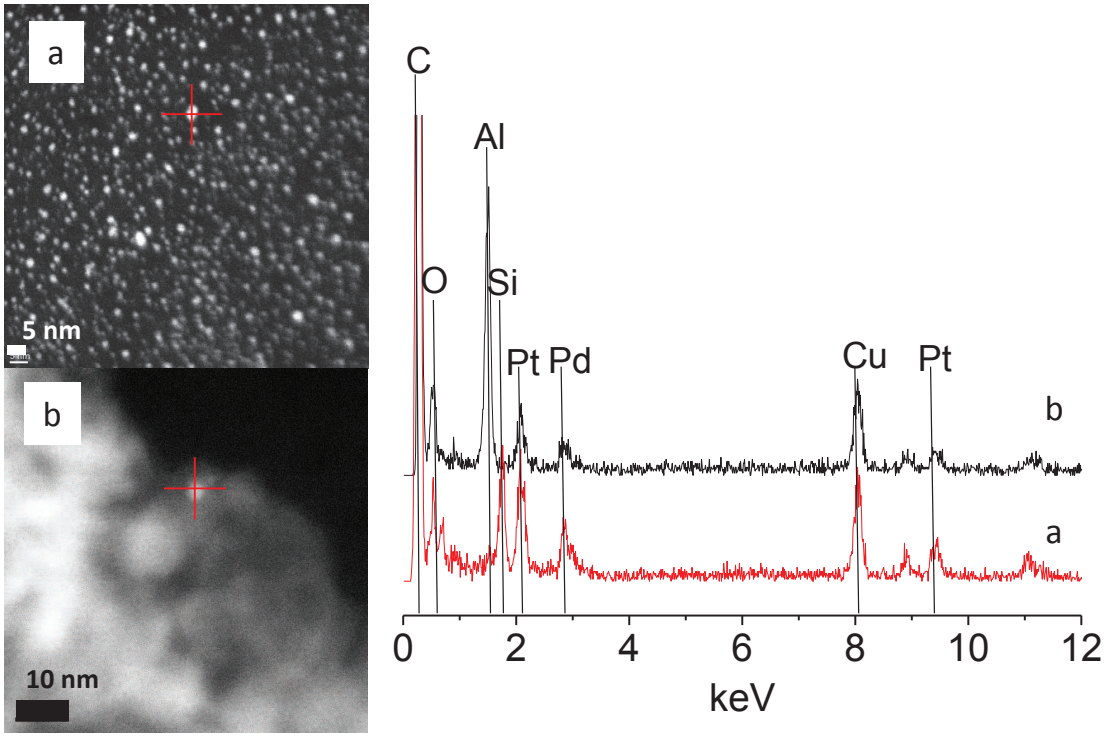

Figure 88. HAADF-STEM images and associated EDX spectra of Pt/Pd 1/1 nanoparticles, a) supported on TEM grid, b) supported on alumina and calcined

4.4.3. Conclusion

The silane stabilization methodology to synthesize nanoparticles with sizes bellow 2 nm and narrow size dispersion has been successfully implemented towards the synthesis of more complex systems, i.e. Pt/Pd bimetallic nanoparticles. The nanoparticles composition was controlled by the initial Pt/Pd ratio in coherence with the Pt/Pd phase diagram demonstrating the formation of solid solutions over the entire composition range.[132] However, the structure of those nanoparticles is still to be elucidated even if a Pd enriched core can be hypothesized from XPS analyses. Moreover silicium is believed to be embedded in those nanoparticles as suggested by the n-octane evolvement during the nanoparticles synthesis. After calcination the pending alkyl chains are efficiently eliminated and silica is formed. No silica shell was found around the nanoparticles and the definite structures of the calcined nanoparticles are not yet fully understood. X-Ray absorption spectroscopy (XANES and EXAFS) have recently been recorded on pure and bimetallic systems, before and after calcination and the data are currently examined.

4.5. Electroanalysis and catalysis

4.5.1. Loading on high surface area carbon

To study the intrinsic catalytic properties of nanoparticles, a high surface area carbon (Vulcan XC-72R) was used as support,[133-135] it presents a surface area of 242 $m^2.g^{-1}$ (Appendix 26). Pure Pt, pure Pd and 1:3, 1:1 and 3:1 bimetallic nanoparticles were impregnated with a 50 wt% loading. The efficient dispersion of nanoparticles onto the high surface area carbon was checked by TEM (Figure 89). If dispersed in THF, the supported nanoparticles leach from the support, see Figure 89-a. In a water/isopropanol 80/20 solution, in which nanoparticles were less soluble, no leaching from the carbon was observed (Figure 89-b).

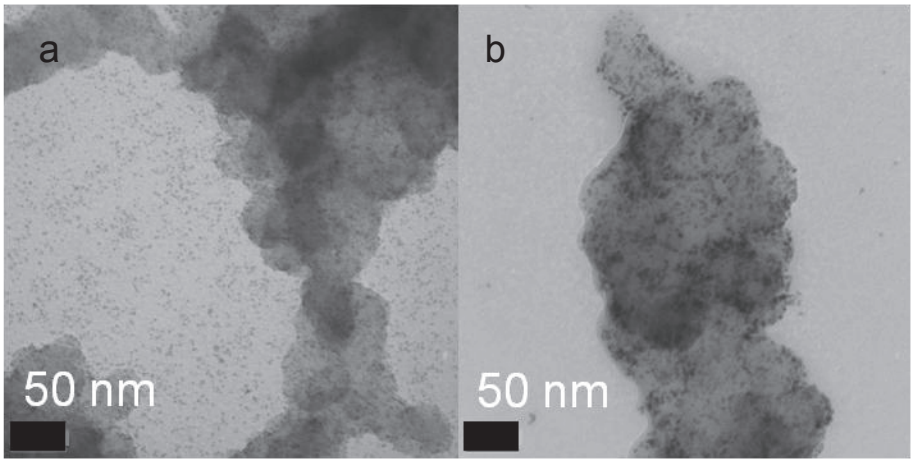

Figure 89. TEM picture of Pd nanoparticles loaded onto Vulcan XC-72R a) dispersed in THF, b) dispersed in water/isopropanol 80/80.

4.5.2. Cyclic voltamperometry

Cyclic voltammograms were recorded for each catalyst in de-aerated sulfuric acid at 0.5 $mol.L^{-1}$. The intensity was plotted versus the potential against the mercury/mercurous sulfate electrode. The potential of the $Hg/HgSO_4$ *vs.* the hydrogen reference electrode being 0.68 mV. Catalysts were scanned from -0.67 mV (0.1 mV/RHE) to increasing voltage from 0.5 to 0.7 mV (Figure 90). Voltage was increased after two cycles. In the positive scanning direction, the first broad peak corresponds to hydrogen under potential desorption (H_{upd}) on the nanoparticles surface. The second peak corresponds to the formation of a hydroxide layer onto the surface and the oxidation of the metal. In the negative scanning direction ($I < 0$ mA) the first peak corresponded to reduction of the catalyst and the second at the minimum

potential corresponded to the reduction of H^+ into H_2. We compare on Figure 90 the platinum reference produced by Tanaka to octylsilane stabilized platinum nanoparticles. On cyclic voltammogram a) no modification of the H desorption peak and thus of the electroactive surface area (ESA) was noticed. For Pt/octylsilane, integration of the H_{upd} surface area of each cycle showed no modification of the surface area too. The reduction of the platinum catalyst occured from 0.10 mV to 0.03 mV depending on the maximum potential reached during the cyclic voltamperometry (CV) experiments.[136] For Pt/octylsilane nanoparticles, this reduction occured at lower potential, from -0.10 to -0.33 mV. This is logically correlated to a stronger oxidation as seen between 0.4 and 0.7 mV in the positive scanning direction. All together those observations support the hypothesis of non-purely platinum nanoparticles and the probable incorporation of silicium inside its structure modifying its red/ox potential. No reference on Pt/Si was found but similar observations were found for alloyed nanoparticles, for example PdCo,[137] PtFe.[21]

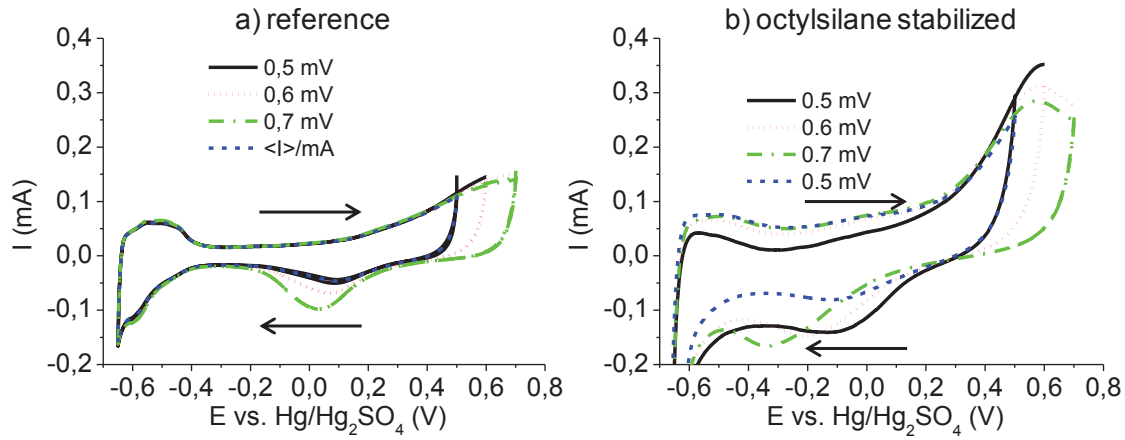

Figure 90. CV under N_2 of Pt/C with varying maximum potential: 0.5 – 0.6 – 0.7 and 0.5 mV/Hg. Arrows show the scanning direction.

CVs of colloidal nanoparticles under N_2 were compared to the reference (Figure 91). Similarly to platinum and palladium nanoparticles, shifted single reduction peaks were observed for bimetallic nanoparticles witnessing the homogeneity of the surface.[138] Moreover, the Pt-H desorption peak presented a maximum potential that was a function of the nanoparticle composition as plotted in Figure 92. A linear increase in the potential was observed *vs.* the platinum content of the nanoparticles. This support the formation of alloyed nanoparticles against core/shell Pd/Pt nanoparticles as previously hypothesized from XPS results which was in good accordance with literature.[23,139]

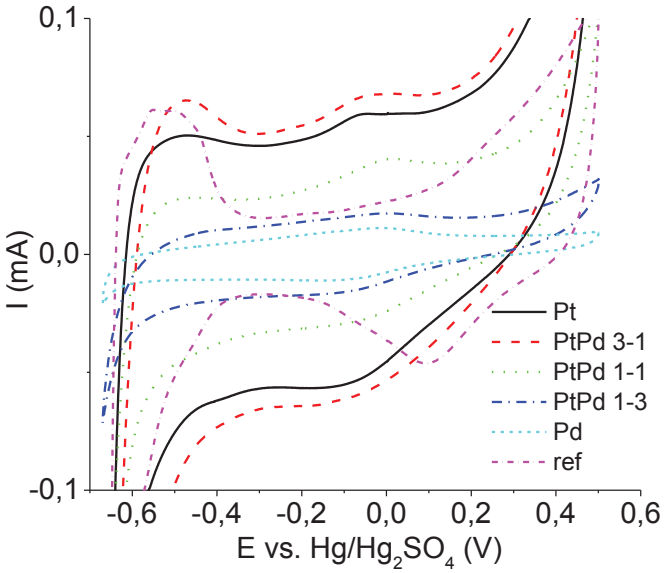

Figure 91. CV at 20 $mV.s^{-1}$ scanning rate under N_2.

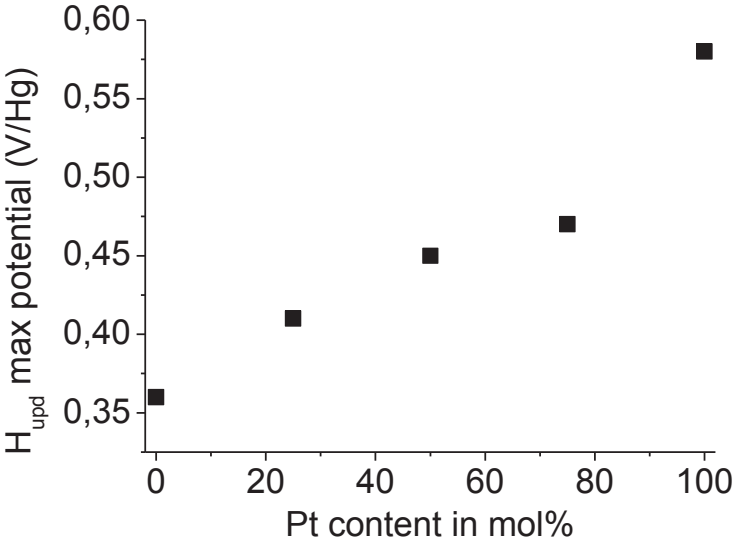

Figure 92. Potential of the Hupd peak as a function of the platinum content.

The electroactive surface area (ESA) were measured by the integration of the H_{upd} zone and reported in Table 17. The theoretical ESA was compared to the calculated one (see Chapter I) and the ratio (vM) gave the percentage of metal efficiently used for catalysis. Small ratios were found (0.1 to 28%) compared to the reference (56%); the nanoparticles being covered by octylsilane which then probably limited the surface accessibility to gases and hinder their catalytic properties.

4.5.3. Oxygen Reduction Reaction

Polarization curves were recorded under O_2 bubbling into the electrolyte and current densities were compared at the arbitrary chosen potential value of 0.2 V/Hg (0.88 V/RHE) (refer to Appendix 27). The mass current density could be calculated from the platinum loadings and plotted vs. the nanoparticles composition (Figure 93). Current densities from 0.12 to 1 $A.g^{-1}_{Pt}$ were reported. Those values were 4 to 20 times lower than the one of the reference (3.9 $A.g^{-1}_{Pt}$). Of our catalyst, the 3:1 Pt/Pd nanoparticles was found to be 1.4 times more efficient for the ORR than pure platinum or 1:1 and 1:3 Pt/Pd ratios. Those results were comparable to results recently obtained by Lee *et al.*[24] where an enhancement of the mass current density of 2 was found for 3:1 Pt/Pd nanoparticles.

Table 17.

sample	NP size (nm)	ESA (cm²/cm²) measured (H_{upd})	ESA (cm²/cm²) calculated	νM	j ($A.g^{-1}_{Pt}$)
Pt ref	2	75	133	56%	3,9
Pt	1,6	14	163	9%	0,7
Pt/Pd 3:1	1,4	51	183	28%	1,0
Pt/Pd 1:1	1,6	5	163	3%	0,1
Pt/Pd 1:3	1,8	0,2	148	0,1%	0,2

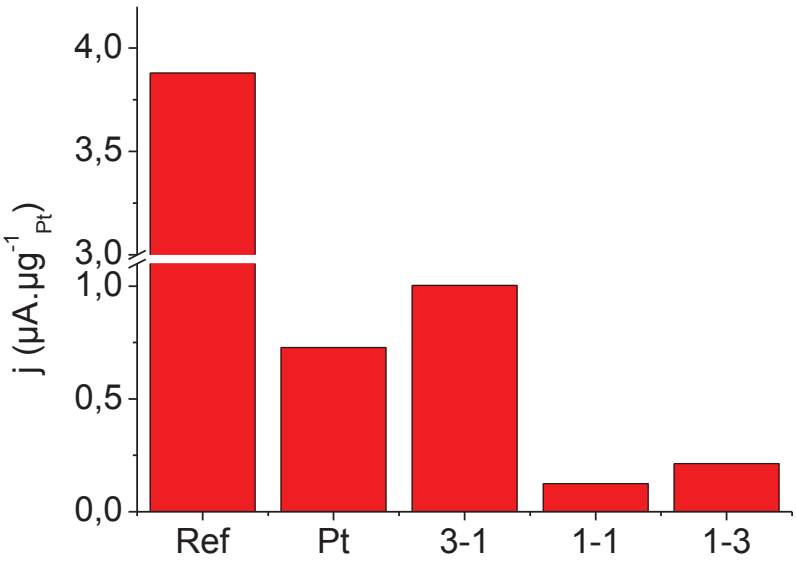

Figure 93. Current density per electrode surface area at 0.2 V/Hg *vs.* the catalyst composition.

4.5.4. Conclusion

Electroanalyses methods confirmed the formation of Pt/Pd alloys with varying composition and demonstrated to be valuable tools for the analysis of colloidal nanoparticles. The catalytic properties of these nanoparticles were tested in the Oxygen Reduction Reaction. Lower activities compared to the platinum reference were found. The surface octylsilane chains are believed to hinder the gases accessibility to the catalytic sites or could act as an insulating material between the carbon support and the nanoparticles. The elimination of those aliphatic chains is thus probably necessary to increase the electroactive surface area. The simple calcination process under air cannot be used because Vulcan has a low decomposition temperature (100 to 200°C) in the presence of platinum.[140] A previously developed process where UV irradiation is used could be tested.[141] Despite this limitation, ORR results demonstrate higher catalytic properties for the Pt/Pd 3:1 nanoparticles. The Pt/Pd alloy nanoparticles synthesis method developed is fast and reproducible. It moreover leads, to our knowledge, to the smallest Pt/Pd nanoparticles reported so far.

4.6. Chapter conclusion

The synthesis of platinum and palladium nanoparticles stabilized by octylsilane led to the formation of extremely small nanoparticles (bellow 2 nm) with narrow size dispersions (typically less than 0.4 nm). This methodology was successfully extended to Pt^{II} precursors leading to even smaller nanoparticles (1.2 nm). The use of an external reductant (H_2) proved to be unnecessary making this nanoparticles synthesis method particularly simple, fast and safe. The formation of more complex systems, i.e. bimetallic nanoparticles was tested and successfully attained for Pt/Pd nanoparticles. For catalysis applications, these nanoparticles were further dispersed onto various supports: alumina, silica and high surface area carbon. The removal of the alkyl chains is a key point for gas accessibility and is easily performed onto silica or alumina by calcination under air at 320°C. On high surface area carbon more work is necessary to achieved better catalytic performances in the Oxygen Reduction Reaction. For this reaction, 3/1 Pt/Pd nanoparticles proved to be more efficient than pure platinum.

The definite structure of octylsilane stabilized nanoparticles is not yet fully understood. From the release of n-octane during the synthesis, silicium atoms are believed to be embedded into the nanoparticles structure. After calcination, the formation of SiO_2 is proven by XPS. A core/

shell M/SiO_2 structure was expected but no evidence was found by microscopy. EXAFS results are currently under analyses and should lead to a better understanding of this system.
The straight forward synthesis of those nanoparticles and their particularly small size makes them very good candidates for catalytic applications and more work into that direction is encouraged.

4.7. Experimental

4.7.1. Preparation of palladium nanoparticles

Using dihydrogen as an external reductant

In a glove-box, 100 mg of $Pd(dba)_2$ (0.17 mmol) were introduced into a schlenk. Using schlenk lines, the complex was dissolved in freshly distilled THF and transferred into a batch reactor with thick glass walls. The THF volume was completed up to 116 mL. 0.58 mL of THF containing 25.1 mg of octylsilane (1 equiv. - 0.17 mmol) were added. After partial evacuation, the reactor was pressurized under dihydrogen at 3 bars and stirred overnight at room temperature.

In the absence of dihydrogen

In a glove-box, 100 mg of $Pd(dba)_2$ (0.17 mmol) were introduced into a schlenk. Using schlenk lines, the complex is dissolved in 116 mL of freshly distilled THF. The solution was heated up to 60°C. After stabilization of the temperature 0.58 mL of THF containing 25.1 mg of octylsilane (1 equiv. - 0.17 mmol) were rapidly added. The schlenk is quickly closed and stirred overnight at room temperature.

4.7.2. Preparation of monometallic nanoparticles

4.7.2.1. From $Pt(dba)_2$

Using dihydrogen as an external reductant

In a glove-box, 100 mg (0.15 mmol) of $Pt(dba)_2$ were introduced into a schlenk. Using schlenk lines, the complex was dissolved in freshly distilled THF (over Na/benzophenone) and transferred into a batch reactor with thick glass walls. The THF volume was completed up to 100 mL. 0.50 mL of THF containing 21.7 mg of octylsilane (1 equiv. - 0.15 mmol) were added. After partial evacuation, the reactor was pressurized under dihydrogen at 3 bars and stirred overnight at room temperature.

In the absence of dihydrogen

In a glove-box, 100 mg (0.15 mmol) of $Pt(dba)_2$ were introduced into a schlenk. Using schlenk lines, the complex was dissolved in 100 mL of freshly distilled THF. The solution was heated up to 60°C. After stabilization of the temperature 0.50 mL of THF containing 21.7 mg of octylsilane (1 equiv. - 0.15 mmol) were rapidly added. The schlenk was quickly closed and stirred overnight at room temperature.

4.7.2.2. From $Pd(dba)_2$

Using dihydrogen as an external reductant

Similar procedure to $Pt(dba)_2$ was used with 86 mg (0.15 mmol) of $Pd(dba)_2$, 100 mL THF and 0.5 mL of THF containing 21.7 mg of octylsilane (1 equiv. - 0.15 mmol).

In the absence of dihydrogen

Similar procedure to $Pt(dba)_2$ was used with 86 mg (0.15 mmol) of $Pd(dba)_2$, 100 mL THF and 0.5 mL of THF containing 21.7 mg of octylsilane (1 equiv. - 0.15 mmol).

4.7.2.3. From $(COD)Pt(OSi(OtBu)_3)_2$

In a glove-box, 125 mg (0.15 mmol) of $Pt(dba)_2$ were introduced into a schlenk. Using schlenk lines, the complex is dissolved in 100 mL of freshly distilled THF. After complete dissolution, 0.50 mL of THF containing 21.7 mg of octylsilane (1 equiv. - 0.15 mmol) were rapidly added. The schlenk is quickly closed and stirred overnight at 60°C.

4.7.2.4. From $(COD)Pt(Me)(OSi(O_tBu)_3)$

Similar procedure to $(COD)Pt(OSi(O\textit{t}Bu)_3)_2$ was used with 87 mg (0.15 mmol) of $(COD)Pt(Me)(OSi(O\textit{t}Bu)_3)$ in 100 mL THF and 0.5 mL of THF containing 21.7 mg of octylsilane (1 equiv. - 0.15 mmol).

4.7.2.5. From (COD)Pt(Cl)(Me)

Similar procedure to $(COD)Pt(OSi(O\textit{t}Bu)_3)_2$ was used with 53 mg (0.15 mmol) of (COD)Pt(Cl)(Me) in 100 mL THF and 0.5 mL of THF containing 21.7 mg of octylsilane (1 equiv. - 0.15 mmol).

4.7.3. Preparation of Bimetallic nanoparticles

Pt/Pd 1:1 nanoparticles

In a glove-box, 50 mg (0.075 mmol) of $Pt(dba)_2$ were introduced into a first schlenk and 43 mg (0.075 mmol) of $Pd(dba)_2$ were introduced in a second one. Using schlenk lines, the complexes were dissolved in freshly distilled THF and transferred successively into a batch reactor. The THF volume was completed up to 100 mL before 0.50 mL of THF containing 21.7 mg of octylsilane (0.15 mmol) were added. After partial evacuation, the reactor was pressurized under dihydrogen at 3 bars and stirred overnight at room temperature.

Pt/Pd 3:1 nanoparticles

A similar procedure was used with 75 mg (0.11 mmol) of $Pt(dba)_2$ and 22 mg (0.04 mmol) of $Pd(dba)_2$ in 100 mL of THF. 0.50 mL of THF containing 21.7 mg of octylsilane (0.15 mmol) were added.

Pt/Pd 1:3 nanoparticles

A similar procedure was used with 25 mg (0.04 mmol) of $Pt(dba)_2$ and 65 mg (0.11 mmol) of $Pd(dba)_2$ in 100 mL of THF. 0.50 mL of THF containing 21.7 mg of octylsilane (0.15 mmol) were added.

4.7.1. UV-Vis spectroscopy

UV-Vis spectra were recorded on a Perkin Elmer lambda 1050 spectrometer from 210 to 800 nm with 2 nm steps. Absorbance of the sample was measured against a reference of dry THF in a quartz cell and the samples were prepared by diluting 50 µL of colloidal solutions (initially at 1.5 mmol of metal per liter) into 3 mL of dry THF.

4.7.2. NMR experiments

4.7.2.1. Kinetic

$(COD)Pt(OSi(O\mathit{t}Bu)_3)_2$

In a glove box, 10 mg (1.2 µmol) of $(COD)Pt(OSi(O\mathit{t}Bu)_3)_2$ were introduced into a Young NMR tube and stored into a schlenk. Using a schlenk line, 0.4 mL of THF-d_8 were introduced into the NMR tube. 1.7 mg (1 equiv. - 1.2 µmol) of octylsilane in 0.1 mL THF-d_8 were added and the NMR tube was tightly closed. The tube was shaken a few seconds before being introduced into the NMR probe. ^{1}H-NMR spectra were recorded on a Brüker Avance 300 MHz spectrometer, 8 scans were recorded for each spectrum at regular intervals.

(COD)Pt(Me)(OSi(O*t*Bu)$_3$)

A similar procedure as described above was used with 7 mg (1.2 µmol) (COD)Pt(Me)(OSi(O*t*Bu)$_3$), 4 mL of THF-d8 and 1.7 mg (1 equiv. - 1.2µmol) of octylsilane in 0.1 mL THF-d_8.

After 12.5 h a second equiv. of octylsilane was added (1.7 mg in 0.1 mL THF-d_8) under argon.

4.7.2.2. DOSY

The 1H 2D NMR DOSY spectra were collected at 25°C on a Brüker spectrometer Avance III working at 500 MHz. Samples were dissolved in THF and classical 5 mm Young tubes were used. A modified Brüker dstebpgp3s sequence with π composite pulses and ZQ filter was used to improve phase stability in the spectra series. Short gradient duration pulses were obtained using a trapezoidal shape (p30=1 ms, falling and raising times of 50 µs), and the diffusion delay was set at 100 ms. Data were processed with Topspin 2.3 and NmrNotebook 2.5 with the maximum number of iterations.

4.7.3. IR

Transmission

A droplet of the concentrated colloidal suspension was placed into two KBr windows under air. IR spectra were recorded on a Nicolet Magna 550FT spectrometer. Typically 32 scans were accumulated for each spectrum (resolution 4 cm^{-1}).

Diffuse Reflectance Infrared Fourier Transformed spectroscopy (DRIFT)

DRIFT spectra were recorded on a Nicolet Magna 550 FT spectrometer using a custom infrared cell equipped with CaF_2 windows, allowing *in-situ* studies. Typically, 64 scans were accumulated for each spectrum (resolution 4 cm^{-1}).

4.7.4. Impregnation on silica and alumina

Nanoparticles were supported onto high surface area silica and alumina.

Silica dehydroxylated at 700 °C, referred as $SiO_{2\text{-}700}$, was obtained as follow: silica (Aerosil Degussa, 200 $m^2.g^{-1}$) was compacted with distilled water, dried at 110 °C for 2 days, calcined (500°C under air for 4 h) and partially dehydroxylated under secondary vacuum (10^{-5} mBar)

at 500°C for 12 h and then at 700°C for 4 h. The surface area is 185 ± 5 $m^2.g^{-1}$ as measured by N_2 adsoprtion and desorption isotherms at -196°C.

γ-alumina from SASOL (SBa-200) was used. The support was first previously calcined at 500°C under a dry air flow (40 $mL.min^{-1}$) for 12 h, evacuated for 12 h at 700°C under secondary vacuum. This ensures a stable (up to 700°C) and clean (water and organic free) support. The surface area is 243 ± 2 $m^2.g^{-1}$ as measured by N_2 adsorption and desorption isotherms at -196°C.

Nanoparticles were impregnated onto silica and alumina using the Incipient Wetness Impregnation (IWI) with a targeted final content of 1 wt%. The pore volume was measured by impregnating pure THF, and determined to be 1.45 $mL.g^{-1}$ for silica and 1.90 $mL.g^{-1}$ for alumina.

4.7.5. H_2 chemisorption

Chemisorption experiments were performed on a BELSORB-max from BEL JAPAN. Around 200 mg of silica supported nanoparticles (1wt%) previously calcined and reduced were introduced in the absorptions cells in a glove-box. The samples were then degassed at 623K for 3h under vacuum (10^{-6} mbar). The chemisorption measurements were performed at 298K, the pressures at equilibrium being recorded when the pressure variation was below 0.02% per minute. Platinum particle size estimations were based on truncated octahedron geometry, assuming complete reduction, and an H/Pt adsorption stoichiometry factor of 1.8.[125]

4.7.6. X-Ray photoelectron spectroscopy (XPS)

Spectra were recorded at the CEA-Grenoble, LITEN, on the SSI-SProbe XPS spectrometer with a Kα monochromated Al source. Samples are transferred from the glove-box to the spectrometer using a hermetic transfer box. Spectra are recorded with a collection angle of 35° and a pass energy of 25 eV for high resolution spectra. The pressure in the analysis chamber was bellow 10^{-9} Pa. Peaks are calibrated toward the C1s (adventitious contamination carbon) peak set at 284.8 eV. Synthetic components on Pt4f were analyzed with a Shirley background subtraction and the peaks shape were resolved with a combination of gaussians and lorentzians (30%).

4.7.7. Carbon supported nanoparticles preparation

4.7.7.1. Vulcan preparation

Prior to use Vulcan (1 g) was cleaned in a 100 mL 5M HCl solution. After 60 seconds of sonication, the solution was stirred and heated up to 50°C for 18 h. The solution was centrifugated (6000 rpm, 10°C, 20 minutes) and the supernatant eliminated. 20 mL of water were added, the solution was sonicated for 60 seconds and again centrifugated, finally the supernatant was eliminated. This procedure was repeated 6 times until a constant pH (7) of the supernatant was reached. A final procedure was performed with ethanol and the Vulcan was finally dried at 80°C under ambient pressure.

4.7.7.2. Nanoparticles loading

22 mg of Vulcan were introduced into a 10 mL THF solution of 22 mg colloidal platinum nanoparticles previously prepared. This solution was sonicated for 15 minutes in order to load the nanoparticles. THF was then evaporated under an air flow. A sticky solid was obtained.
This procedure was repeated for Pt, Pd and 3/1, 1/1, 1/3 Pt/Pd nanoparticles.

4.7.7.3. Preparation of the rotating electrodes

The carbon supported nanoparticles were dispersed by 5 minutes sonication in 22 mL of a water/isopropanol 80/20 solution, yielding a solution containing 1mg of metal per mL. Nafion (220 mg of a 5wt% Nafion solution in water - 11 mg of Nafion) was added and again the solution was sonicated for 5 min. A 25 µL drop of the solution was deposited onto a glassy carbon rotating electrode (0.25 cm^2) and dried under ambient pressure at 80°C for about 10 minutes.

4.7.8. Electrocatalysis

Rotating disk electrode (RDE) measurements were conducted in an interchangeable RDE holder (Pine Instruments, USA). A Pt-foil counter-electrode and a $Hg/HgSO_4$ reference electrode (separated by an electrolyte bridge) were used in a standard three-compartment electrochemical cell. Tests are performed into freshly prepared sulfuric acid solution (0.5 $mol.L^{-1}$). Voltammograms were recorded using the EC-Lab software.

Cyclic voltamperometry under N_2

The electrolyte solution was degassed under N_2 bubbling at least 20 minutes before use. The electrode rotating frequency was set to 100 rpm. Successive cycling were performed from -0.67 to 0.5, 0.6 and 0.7 mV *vs.* the $Hg/HgSO_4$ reference electrode at a scanning rate of 20 $mV.s^{-1}$. rate. For each maximum, two cycles were recorded. The maximum potential was then again set to 0.5 mV and two cycles are recorded. This procedure ensured the stabilization of the electroactive surface area and repeatable measurements.

Cyclic voltamperometry under O_2

The electrolyte solution was saturated with oxygen by bubbling at least 20 minutes before use. The electrode rotating frequency was set to 100 rpm. CVs were recorded from 0.5 to -0.67 mV at a scanning rate of 20 $mV.s^{-1}$. The Oxygen Reduction current were compared at 0.2 mV and measured by subtracting the CV under N_2 to the CV under O_2 (Appendix 27).

4.8. Appendix

Appendix 18. TEM picture of nanoparticles synthesized in Young NMR tube from $Pt(dba)_2$ with 1 equiv. octylsilane in THF-d_8

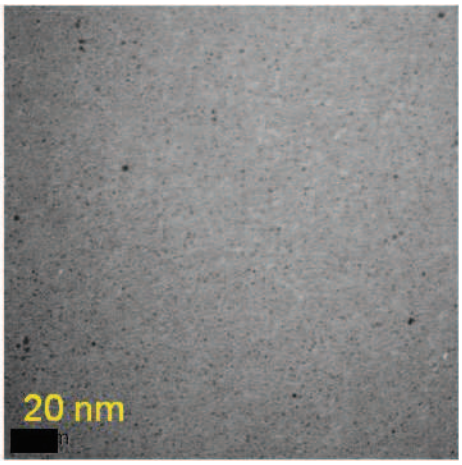

Appendix 19. DOSY spectrum of octylsilane in THF-d_8

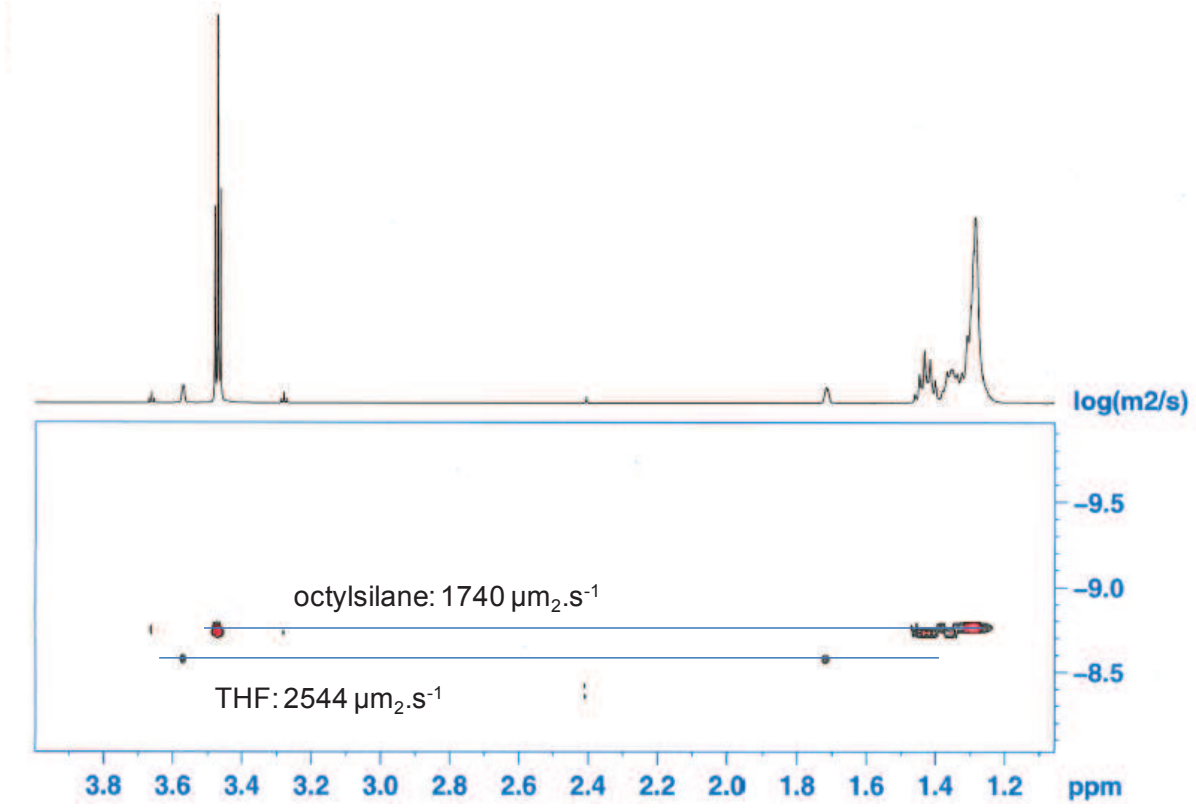

Appendix 20. Liquid state NMR in THF-d_8 (chemical shifts are referenced against the THF peak at 3.58 ppm):

a) Octylsilane

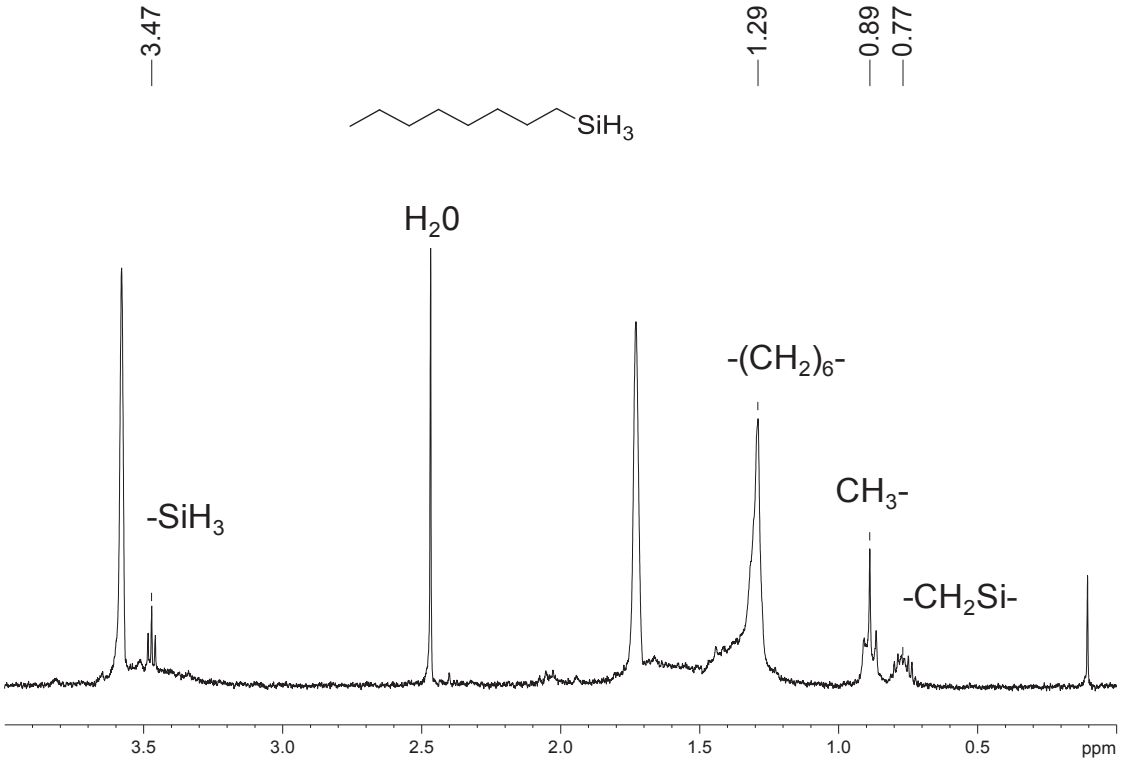

a) Octane

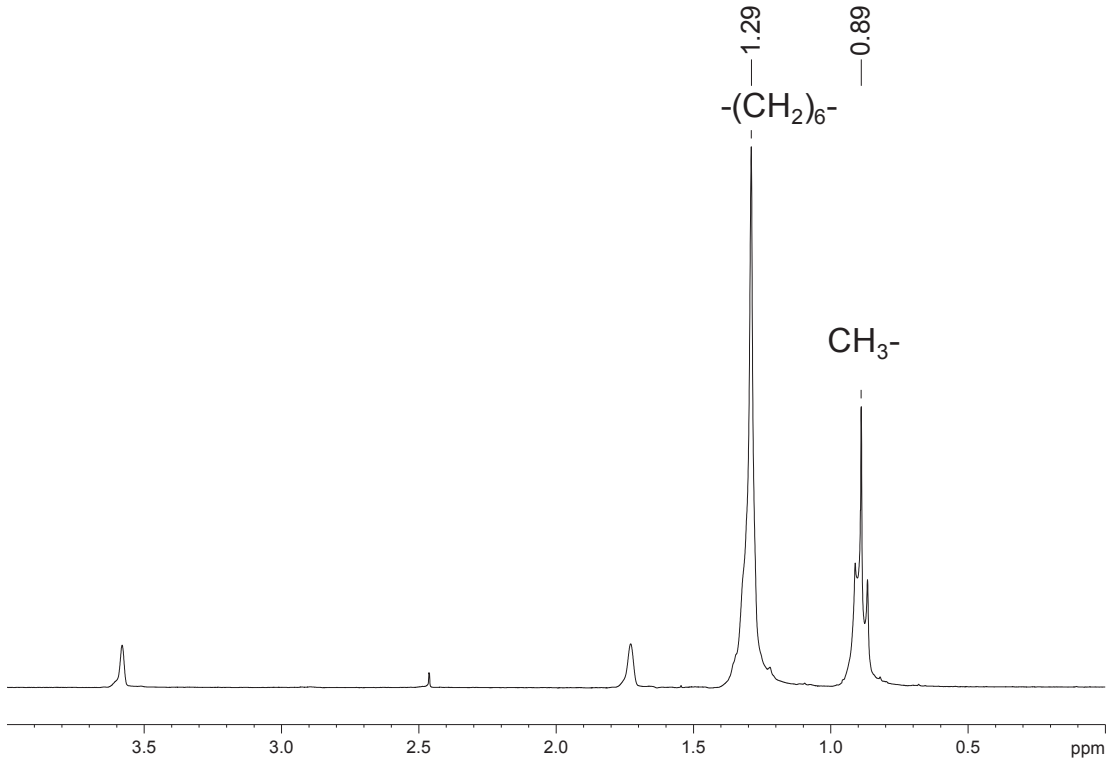

b) Cyclooctadiene

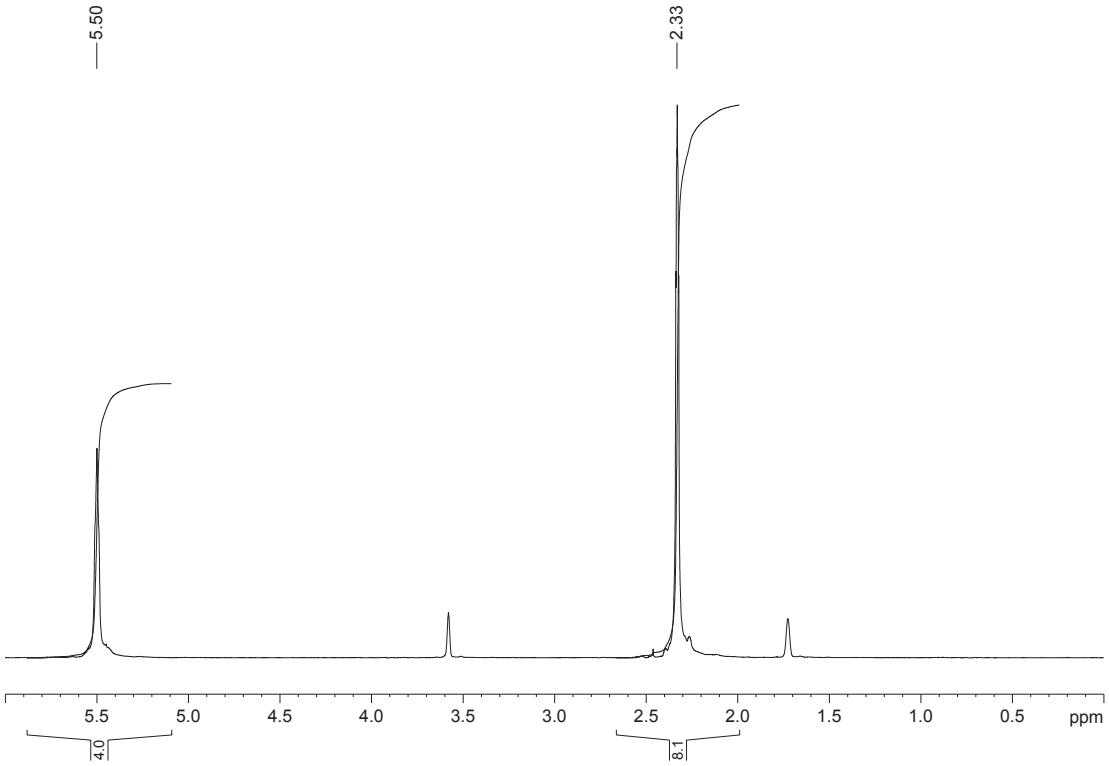

c) $HOSi(OtBu)_3$

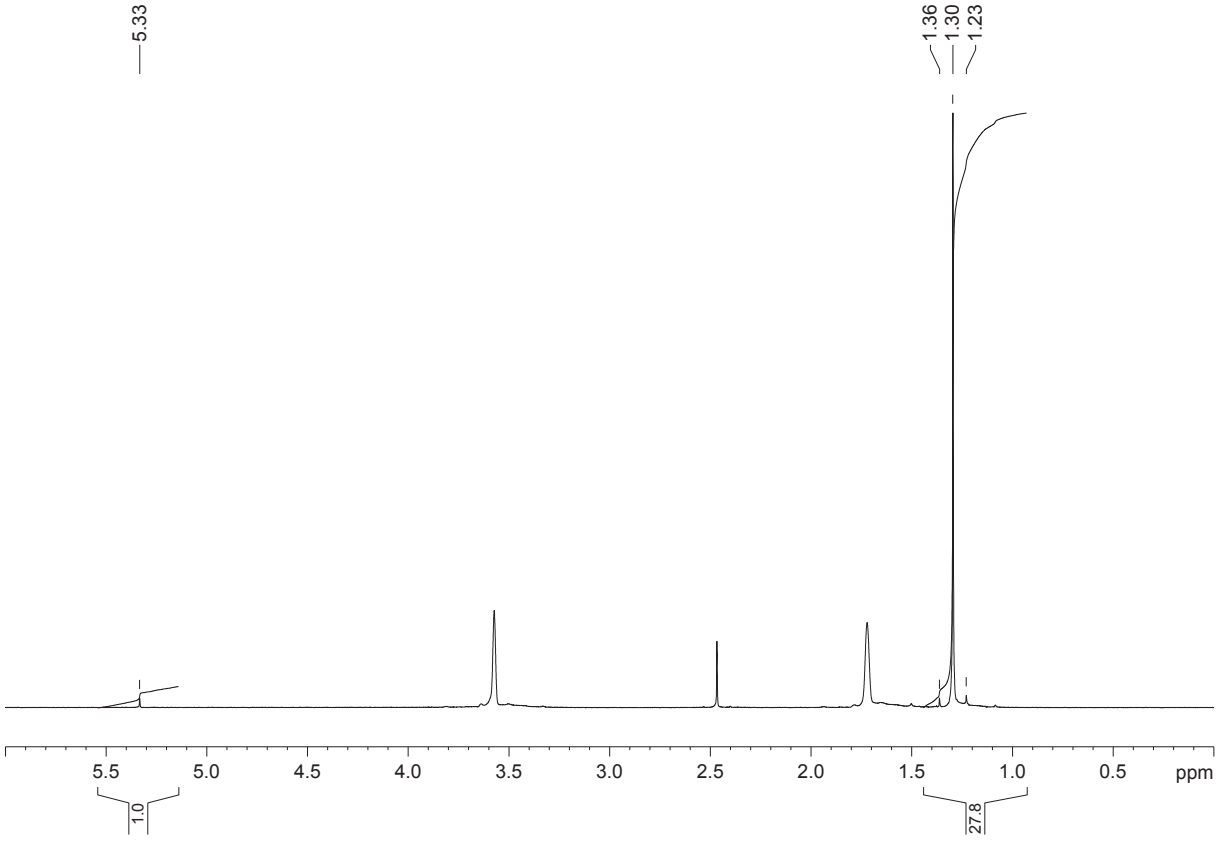

Appendix 21. Hydrodynamic radius calculation from diffusion coefficient

$$R_H = \frac{k_B T}{6\pi\eta D}$$

D is the diffusion coefficient in $m^2.s^{-1}$.

T is the temperature in Kelvin.

η is the solvent viscosity, at 298K the THF viscosity is $4.5.10^{-4}$ Pa.s.

k_B is the Boltzmann constant : $1.38.10^{-23}$ $J.K^{-1}$

R_H is the hydrodynamic radius of the molecule in m. It is defined as the radius of a sphere diffusing at the same rate of the studied molecule. In our case it mimics a spherical colloidal nanoparticle, R_H and the nanoparticle radius are thus expected to be very similar.

Appendix 22. Alkyl chain length

The SiC_8H_{17} chain at the surface of the nanoparticles is assimilated to octane with 1.54 Å C-C bond length and a (CCC) angle of 109.5°.

$$x = 1.54 \times \sin(54.75)$$

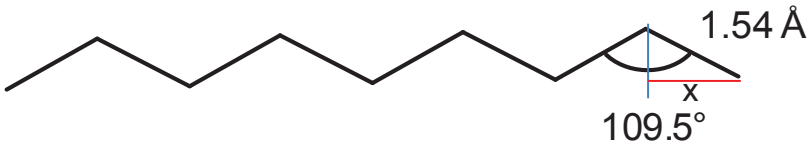

The total length is 8x =10 Å

Appendix 23. 1H-NMR - 1,1,3,3-tetramethyldisiloxane in $CDCl_3$

a: 4.69 ppm

b: 0.18 ppm

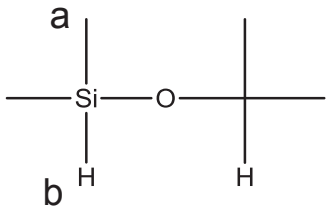

Reproduced from the Spectral Database for Organic Compounds, spectrum 22692, riodb01.ibase.aist.go.jp

Appendix 24. TEM picture of a 1/1 mix of separately synthesized platinum and palladium nanoparticles

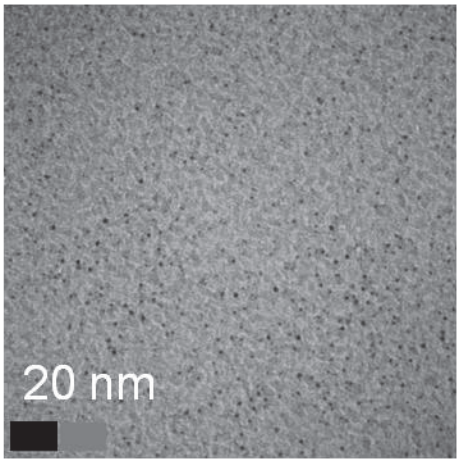

Appendix 25. d-spacing measurement on a large (4 nm) Pt/Pd 1:1 nanoparticles.

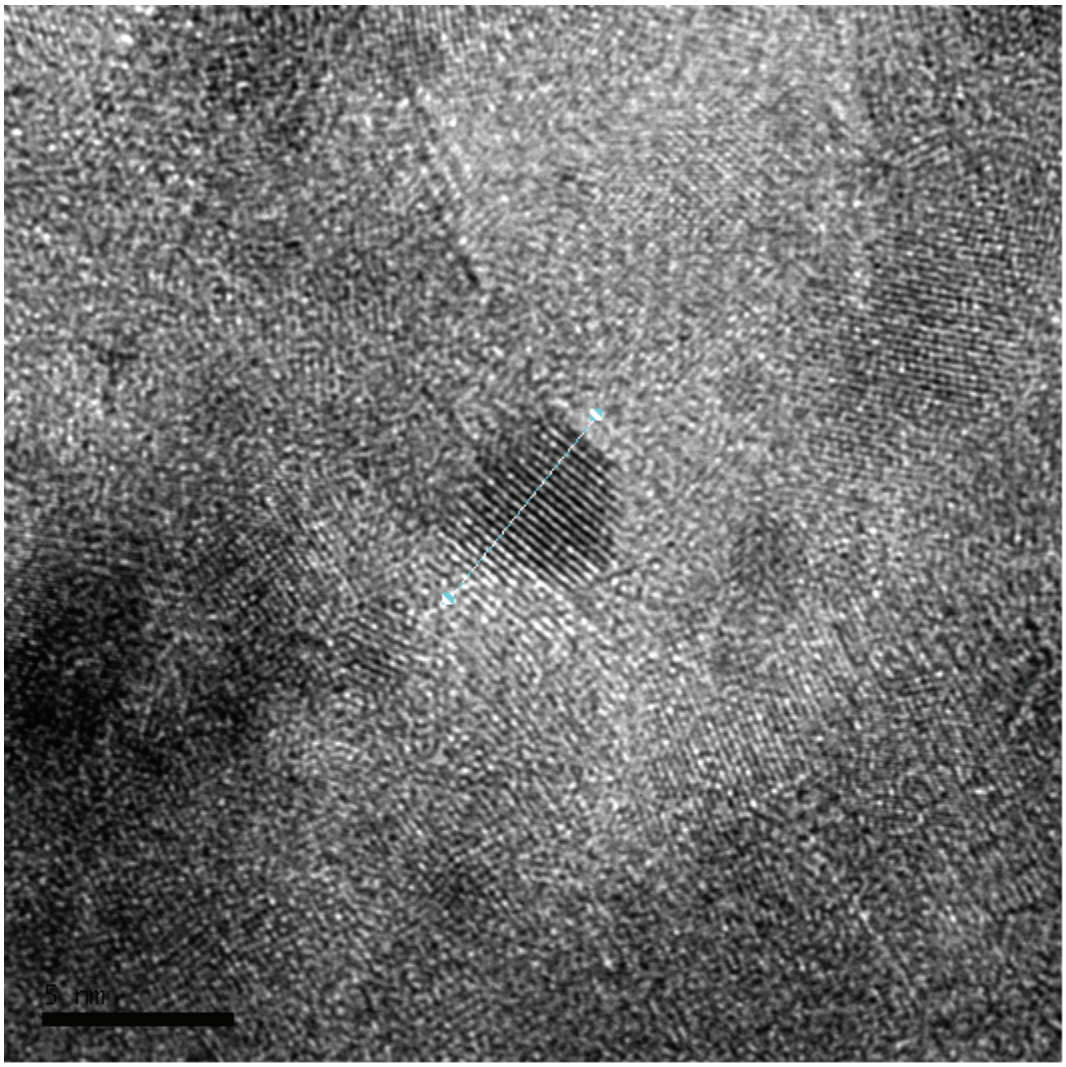

Voltage : 200 kV Indicated Magnification : X800000

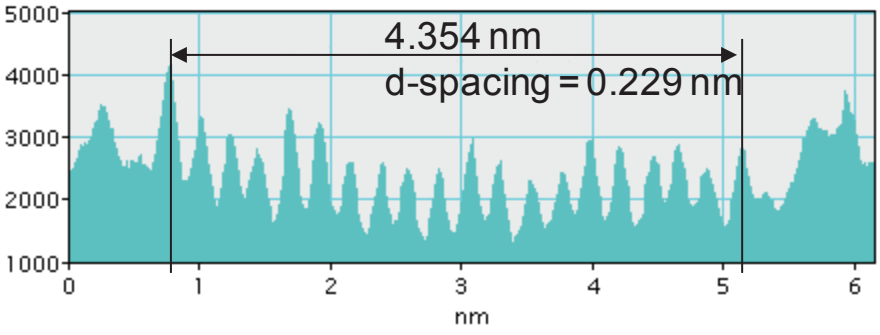

Appendix 26. N_2 absorption and desorption isotherms at -196°C onto cleaned Vulcan XC-72R.

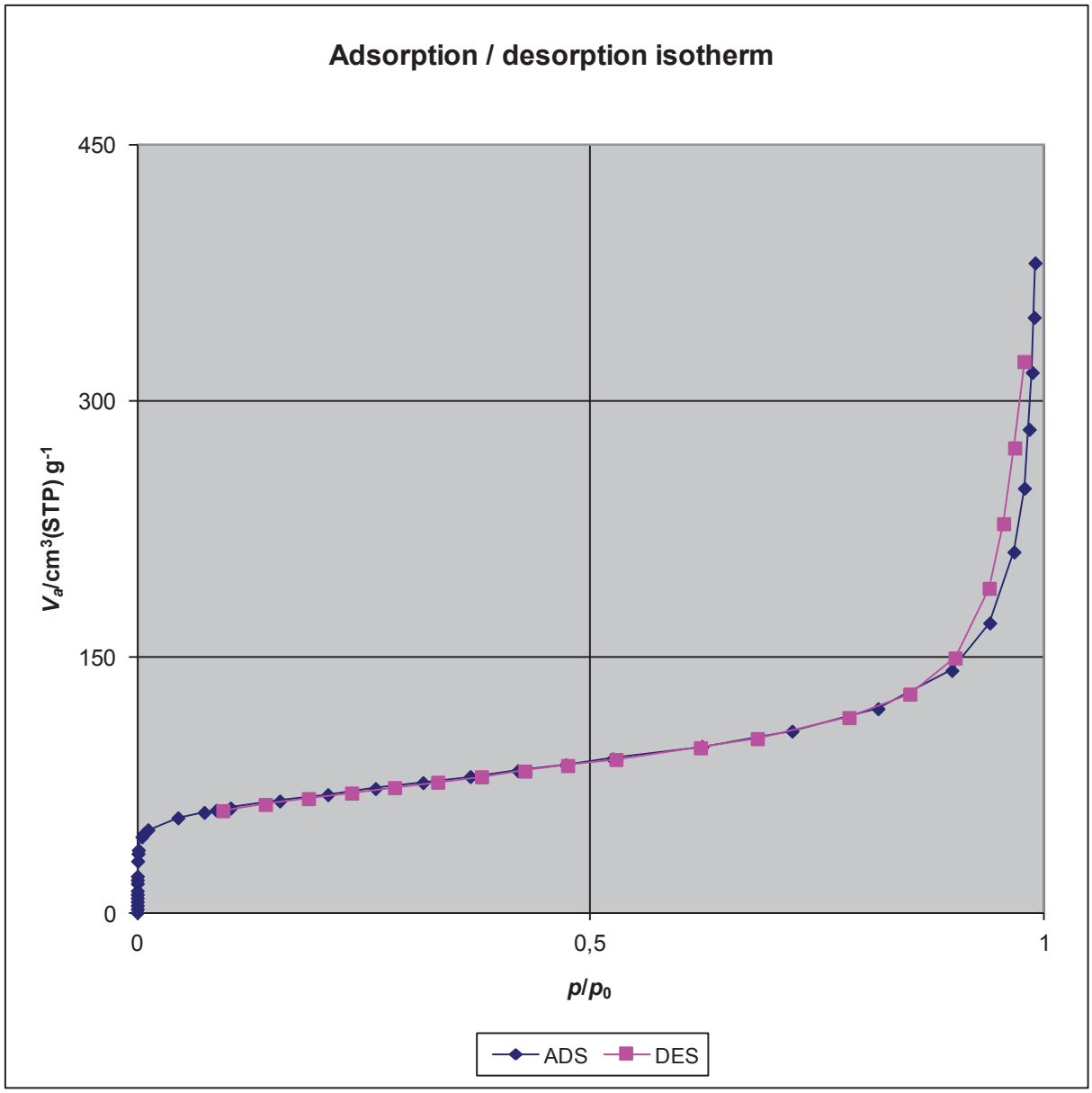

Appendix 27. ORR polarization curve of pure and alloyed nanoparticles in H_2SO_4 saturated with N_2 or O_2 and the difference O_2-N_2. Potential was sweep from 0.5 to 0 and back to 0.5 V at a 20 mV.s-1 scanning rate. The rotating electrode speed was set-up to 100 rpm.

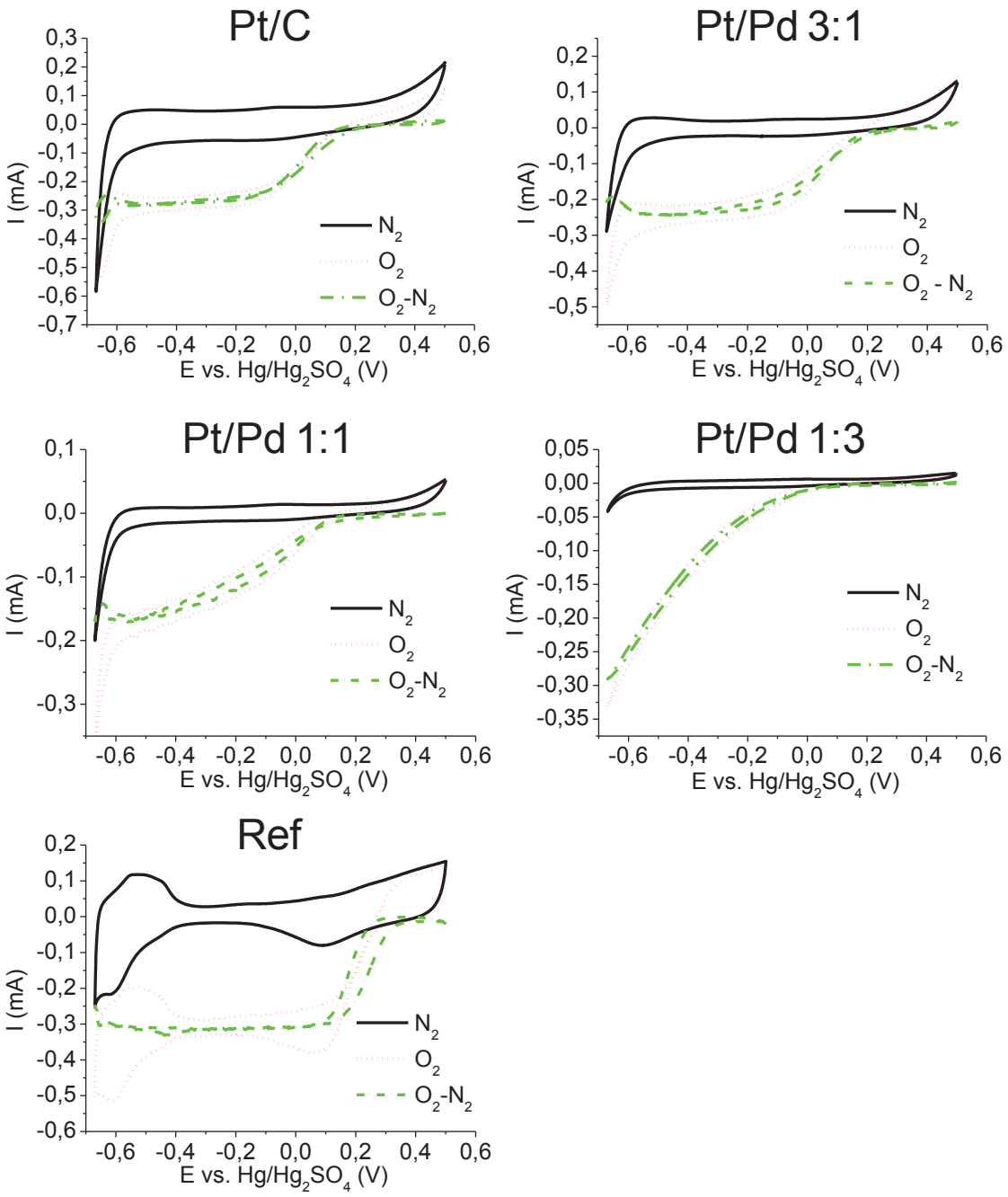

5. Conclusion and perspectives

In this PhD thesis, we have explored the preparation of supported Pt nanoparticles starting from well-defined organometallic compounds via Surface Organometallic Chemistry (SOMC), Metal Organic Chemical Vapor Deposition (MOCVD) and Colloidal chemistry in order to control the size, the distribution and the composition of the final systems. We also extended the colloidal approach to Pd and PdPt alloy to exploit the unique property of PtPd alloys for the Oxygen reduction Reaction.

First, we tuned the decomposition property of a Pt^{II} complex and introduced $(COD)Pt(OSi(O\mathit{t}Bu)_3)_2$ as efficient precursor to obtain small Pt nanoparticles via MOCVD. While successful, the thus-obtained Pt nanoparticles turned out to be inefficient catalysts for fuel cell applications, because of the formation of silica from the molecular precursor, which probably helped with the control of particle size, but also led to a loss of contact between the Pt particle and the conducting support.

Second, we have also prepared a series of well-defined $(COD)Pt^{II}(X)(Y)$ complexes in view of generating supported Pt nanoparticles *via* controlling the Pt-density/loading. This was done *via* the grafting of those Pt complexes and the growth through the tuning of the X/Y ligands. The study primarily focused on silica, but was also tested on ceria. On silica, it was shown that it was possible to exploit the controlled density of surface silanols, obtained through the dehydroxylation temperature, to control the Pt loading, the lower the OH density the smaller the Pt loading and the smaller the particle size (2-3 nm). We also showed that there was not a great impact of the nature of the X/Y ligand on the final Pt particle size unless a Cl-ligand was present (5-40 nm). This later effect could be partially circumvented when H_2 treatment was performed under flow conditions, which probably allowed HCl to be efficiently removed. When $N(SiMe_3)_2$ was used as a ligand, the grafting and the formation of Pt particles was accompanied with the formation of $\equiv SiOSiMe_3$ surface species, without a major impact on Pt particle size; this is in sharp contrast with what was found with gold.[69] Using the same approach, Pt nanoparticles were also obtained on ceria, but they display smaller sizes (below 1.5 nm); this is probably due to the so-called strong metal support interaction (SMSI). In fact, the effect of chlorine on the nanoparticle size was very limited on this support.

Third, we develop a colloidal approach, where nanoparticles are prepared at room temperature in the absence of dihydrogen from $(COD)Pt^{II}$ precursors through the use of octylsilane as a reducing agent and a stabilizer of the thus-formed Pt nanoparticles. This yielded Pt nanoparticles of very small sizes (1.2 nm), and this approach was extended to Pt^0 and Pd^0 dba

precursors, where particle sizes of 1.8 and 1.7 nm were obtained, respectively. This was then possible to extend this approach to the formation of PtPd alloys of various composition. Preliminary investigation by XPS of those nanoparticles show that $PtSi_x$ and $PdSi_x$, are probably formed either as alloys or solid solutions, and EXAFS analysis is currently under way to identify the structure of these nanoparticles. These colloids were deposited onto high surface area carbon and then tested for the Oxygen Reduction Reaction, providing encouraging results, The Pt/Pd 3:1 alloy demonstrating an enhancement of the catalytic properties by a factor of 1.4 *vs.* pure Pt. More work is certainly necessary on these systems; one key aspect to tackle being the clean removal of the organic ligands in ORR. Moreover, these nanoparticles were supported onto several supports (silica, alumina and ceria) and are currently tested for the preferential oxidation of CO.

Overall this work demonstrates the importance of understanding and controlling the chemistry at a molecular level, the metallic precursor having a strong influence for applications as different as surface organometallic chemistry, MOCVD or colloidal chemistry.

6. References

1. Curry, S. W. *Platinum metals review,* **1957**, *1*, 38-43.

2. Cong, H.; Porco, J. A. *ACS Catalysis,* **2012**, *2*, 65-70.

3. Liu, Y.; Li, D.; Sun, S. *Journal of Materials Chemistry,* **2011**, *21*, 12579-12587.

4. Shelef, M.; Graham, G. W. *Catalysis Reviews,* **1994**, *36*, 433-457.

5. Sanchez, M. G.; Gazquez, J. L. *Journal of Catalysis,* **1987**, *104*, 120-135.

6. Trovarelli, A. *Catalysis Reviews,* **1996**, *38*, 439-520.

7. Kim, G. *Industrial & Engineering Chemistry Product Research and Development,* **1982**, *21*, 267-274.

8. Yao, H. C.; Yao, Y. F. Y. *Journal of Catalysis,* **1984**, *86*, 254-265.

9. Bunluesin, T.; Gorte, R. J.; Graham, G. W. *Applied Catalysis B: Environmental,* **1998**, *15*, 107-114.

10. Morikawa, A.; Kikuta, K.; Suda, A.; Shinjo, H. *Applied Catalysis B: Environmental,* **2009**, *88*, 542-549.

11. Heck, R. M.; Farrauto, R. J. *Applied Catalysis A: General,* **2001**, *221*, 443-457.

12. Nagai, Y.; Dohmae, K.; Ikeda, Y.; Takagi, N.; Tanabe, T.; Hara, N.; Guilera, G.; Pascarelli, S.; Newton, M. A.; Kuno, O.; Jiang, H.; Shinjoh, H.; Matsumoto, S. i. *Angewandte Chemie International Edition,* **2008**, *47*, 9303-9306.

13. Olah, G. A.; Goeppert, A.; Prakash, G. K. S. In *Beyond Oil and Gas: The Methanol Economy*; Wiley-VCH Verlag GmbH & Co. KGaA: 2009, p 185-231.

14. Dillon, R.; Srinivasan, S.; Aricò, A. S.; Antonucci, V. *Journal of Power Sources,* **2004**, *127*, 112-126.

15. Services, E. G.; National Energy Technology, L. *Fuel cell handbook*; U.S. Dept. of Energy, Office of Fossil Energy, National Energy Technology Laboratory: Morgantown, WV :, 2004.

16. Sealy, C. *Materials Today,* **2008**, *11*, 65-68.

17. DOE, *Progress and Accomplishments in Hydrogen and Fuel Cells*; 2012, http://www1.eere.energy.gov/hydrogenandfuelcells/pdfs/accomplishments.pdf.

18. Gasteiger, H. A.; Panels, J. E.; Yan, S. G. *Journal of Power Sources,* **2004**, *127*, 162-171.

19. Nilekar, A. U.; Sasaki, K.; Farberow, C. A.; Adzic, R. R.; Mavrikakis, M. *Journal of the American Chemical Society,* **2011**, *133*, 18574-18576.

20. Gasteiger, H. A.; Kocha, S. S.; Sompalli, B.; Wagner, F. T. *Applied Catalysis B: Environmental,* **2005**, *56*, 9-35.

21. Wang, C.; Chi, M.; Li, D.; van der Vliet, D.; Wang, G.; Lin, Q.; F. Mitchell, J.; More, K. L.; Markovic, N. M.; Stamenkovic, V. R. *ACS Catalysis,* **2011**, *1*, 1355-1359.

22. Mott, D.; Luo, J.; Njoki, P. N.; Lin, Y.; Wang, L.; Zhong, C.-J. *Catalysis Today,* **2007**, *122*, 378-385.

23. Liu, Y.; Chi, M.; Mazumder, V.; More, K. L.; Soled, S.; Henao, J. D.; Sun, S. *Chemistry of Materials,* **2011**, *23*, 4199-4203.

24. Lee, Y.-W.; Ko, A. R.; Kim, D.-Y.; Han, S.-B.; Park, K.-W. *RSC Advances,* **2012**, *2*, 1119-1125.

25. Nesselberger, M.; Ashton, S.; Meier, J. C.; Katsounaros, I.; Mayrhofer, K. J. J.; Arenz, M. *Journal of the American Chemical Society,* **2011**, *133*, 17428-17433.

26. Perez-Alonso, F. J.; McCarthy, D. N.; Nierhoff, A.; Hernandez-Fernandez, P.; Strebel, C.; Stephens, I. E. L.; Nielsen, J. H.; Chorkendorff, I. *Angewandte Chemie International Edition,* **2012**, *51*, 4641-4643.

27. Markovic, N. M.; Gasteiger, H. A.; Ross, P. N. *The Journal of Physical Chemistry,* **1995**, *99*, 3411-3415.

28. Le Goff, A.; Artero, V.; Jousselme, B.; Tran, P. D.; Guillet, N.; Metaye, R.; Fihri, A.; Palacin, S.; Fontecave, M. *Science,* **2009**, *326*, 1384-1387.

29. Tang, Y.; Allen, B. L.; Kauffman, D. R.; Star, A. *Journal of the American Chemical Society,* **2009**, *131*, 13200-13201.

30. Bashyam, R.; Zelenay, P. *Nature,* **2006**, *443*, 63-66.

31. Ertl, G.; Knozinger, H.; Weitkamp, J.; Editors *Preparation of Solid Catalysts*, 1999.

32. Mond, L.; Langer, C.; Quincke, F. *Journal of the Chemical Society, Transactions,* **1890**, *57*, 749-753.

33. Levy, R. A.; Green, M. L. *Journal of The Electrochemical Society,* **1987**, *134*, 37C-49C.

34. Baum, T. H.; Jones, C. R. *Applied Physics Letters,* **1985**, *47*, 538-540.

35. Van Hemert, R. L.; Spendlove, L. B.; Sievers, R. E. *Journal of The Electrochemical Society,* **1965**, *112*, 1123-1126.

36. Liu, D. K.; Lai, A. L.; Chin, R. J. *Materials Letters,* **1991**, *10*, 318-322.

37. Serp, P.; Kalck, P.; Feurer, R. *Chemical Reviews,* **2002**, *102*, 3085-3128.

38. Thurier, C.; Doppelt, P. *Coordination Chemistry Reviews,* **2008**, *252*, 155-169.

39. Hierso, J.-C.; Feurer, R.; Kalck, P. *Chemistry of Materials,* **2000**, *12*, 390-399.

40. Serp, P.; Feurer, R.; Faria, J. L.; Figueiredo, J. L. *J. Phys. IV France,* **2002**, *12*, 29-36.

41. Valet, O.; Doppelt, P.; Baumann, P. K.; Schumacher, M.; Balnois, E.; Bonnet, F.; Guillon, H. *Microelectronic Engineering,* **2002**, *64*, 457-463.

42. Delmas, M.; Ucar, M.; Ressier, L.; Pons, M.; Vahlas, C. *Surface and Coatings Technology,* **2004**, *188-189*, 49-54.

43. Basset, J. M.; Choplin, A. *Journal of Molecular Catalysis,* **1983**, *21*, 95-108.

44. Copéret, C.; Chabanas, M.; Petroff Saint-Arroman, R.; Basset, J.-M. *Angewandte Chemie, International Edition,* **2003**, *42*, 156-181.

45. Jezequel, M.; Dufaud, V.; Ruiz-Garcia, M. J.; Carrillo-Hermosilla, F.; Neugebauer, U.; Niccolai, G. P.; Lefebvre, F.; Bayard, F.; Corker, J.; Fiddy, S.; Evans, J.; Broyer, J.-P.; Malinge, J.; Basset, J.-M. *Journal of the American Chemical Society,* **2001**, *123*, 3520-3540.

46. Millot, N.; Soignier, S.; Santini, C. C.; Baudouin, A.; Basset, J.-M. *Journal of the American Chemical Society,* **2006**, *128*, 9361-9370.

47. Copéret, C.; Thivolle-Cazat, J.; Basset, J. M. In *Fine chemical trough heterogeneous catalysis.*; Sheldon, R. A., Van Bekkum, H., Eds.; Wiley-VCH: Weinheim, 2001, p 553.

48. Chupin, C.; Candy, J. P.; Basset, J. M. *Catalysis Today,* **2003**, *79-80*, 15-19.

49. Meunier, D.; Piechaczyk, A.; De Mallmann, A.; Basset, J.-M. *Angewandte Chemie, International Edition,* **1999**, *38*, 3540-3542.

50. Saint-Arroman, R. P.; Basset, J.-M.; Lefebvre, F.; Didillon, B. *Applied Catalysis, A: General,* **2005**, *290*, 181-190.

51. Bini, F.; Rosier, C.; Saint-Arroman, R. P.; Neumann, E.; Dablemont, C.; de Mallmann, A.; Lefebvre, F.; Niccolai, G. P.; Basset, J.-M.; Crocker, M.; Buijink, J.-K. *Organometallics,* **2006**, *25*, 3743-3760.

52. Chabanas, M.; Baudouin, A.; Copéret, C.; Basset, J. M. *J. Am. Chem. Soc.,* **2001**, *123*, 2062-63.

53. Blanc, F.; Berthoud, R.; Coperet, C.; Lesage, A.; Emsley, L.; Singh, R.; Kreickmann, T.; Schrock, R. R. *Proceedings of the National Academy of Sciences of the United States of America,* **2008**, *105*, 12123-12127.

54. Rhers, B.; Salameh, A.; Baudouin, A.; Quadrelli, E. A.; Taoufik, M.; Copéret, C.; Lefebvre, F.; Basset, J.-M.; Solans-Monfort, X.; Eisenstein, O.; Lukens, W. W.; Lopez, L. P. H.; Sinha, A.; Schrock, R. R. *Organometallics,* **2006**, *25*, 3554-3557.

55. Herrmann, W. A.; Stumpt, A. W.; Priermeier, T.; Bogdanovic, S.; Dufaud, V.; Basset, J.-M. *Angewandte Chemie, International Edition in English,* **1997**, *35*, 2803-2805.

56. Gajan, D.; Rendon, N.; Wampler, K. M.; Jean-Marie, B.; Coperet, C.; Lesage, A.; Emsley, L.; Schrock, R. R. *Dalton Transactions,* **2010**, 8547 - 8551.

57. Zhuravlev, L. T. *Colloids and Surfaces A: Physicochemical and Engineering Aspects,* **2000**, *173*, 1-38.

58. Zhuravlev, L.; Potapov, V. *Russian Journal of Physical Chemistry A, Focus on Chemistry,* **2006**, *80*, 1119-1128.

59. Laachir, A.; Perrichon, V.; Badri, A.; Lamotte, J.; Catherine, E.; Lavalley, J. C.; El Fallah, J.; Hilaire, L.; Le Normand, F.; Quemere, E.; Sauvion, G. N.; Touret, O. *Journal of the Chemical Society, Faraday Transactions,* **1991**, *87*, 1601-1609.

60. Badri, A.; Binet, C.; Lavalley, J.-C. *Journal of the Chemical Society, Faraday Transactions,* **1996**, *92*, 4669-4673.

61. Li, C.; Sakata, Y.; Arai, T.; Domen, K.; Maruya, K.-i.; Onishi, T. *Journal of the Chemical Society, Faraday Transactions 1: Physical Chemistry in Condensed Phases,* **1989**, *85*, 1451-1461.

62. Binet, C.; Badri, A.; Boutonnet-Kizling, M.; Lavalley, J.-C. *Journal of the Chemical Society, Faraday Transactions,* **1994**, *90*, 1023-1028.

63. Ermakov, Y. I.; Kuznetsov, B. N.; Zakharov, V. A. *Catalysis by supported complexes*; Elsevier Scientific Pub. Co., 1981.

64. Mondloch, J. E.; Finke, R. G. *Journal of the American Chemical Society,* **2011**, *133*, 7744-7756.

65. Dufour, P.; Houtman, C.; Santini, C. C.; Basset, J. M. *Journal of Molecular Catalysis,* **1992**, *77*, 257-72.

66. Choi, Y. S.; Moschetta, E. G.; Miller, J. T.; Fasulo, M.; McMurdo, M. J.; Rioux, R. M.; Tilley, T. D. *ACS Catalysis,* **2011**, *1*, 1166-1177.

67. Mondloch, J. E.; Yan, X.; Finke, R. G. *Journal of the American Chemical Society,* **2009**, *131*, 6389-6396.

68. Bonati, M. L. M.; Douglas, T. M.; Gaemers, S.; Guo, N. *Organometallics,* **2012**, *31*, 5243-5251.

69. Gajan, D.; Guillois, K.; Delichère, P.; Basset, J.-M.; Candy, J.-P.; Caps, V.; Copéret, C.; Lesage, A.; Emsley, L. *Journal of the American Chemical Society,* **2009**, *131*, 14667-14669.

70. Gutel, T.; Garcia-Anton, J.; Pelzer, K.; Philippot, K.; Santini, C. C.; Chauvin, Y.; Chaudret, B.; Basset, J.-M. *Journal of Materials Chemistry,* **2007**, *17*, 3290-3292.

71. Chaudret, B. *Comptes Rendus Physique,* **2005**, *6*, 117-131.

72. Chaudret, B. *Actualite Chimique,* **2005**, *290-291*, 33-43.

73. Pan, C.; Pelzer, K.; Philippot, K.; Chaudret, B.; Dassenoy, F.; Lecante, P.; Casanove, M.-J. *Journal of the American Chemical Society,* **2001**, *123*, 7584-7593.

74. Lara, P.; Rivada-Wheelaghan, O.; Conejero, S.; Poteau, R.; Philippot, K.; Chaudret, B. *Angewandte Chemie International Edition,* **2011**, *50*, 12080-12084.

75. Bradley, J. S.; Millar, J. M.; Hill, E. W.; Behal, S.; Chaudret, B.; Duteil, A. *Faraday Discussions,* **1991**, *92*, 255-268.

76. Duteil, A.; Queau, R.; Chaudret, B.; Mazel, R.; Roucau, C.; Bradley, J. S. *Chemistry of Materials,* **1993**, *5*, 341-347.

77. Bradley, J. S.; Hill, E. W.; Chaudret, B.; Duteil, A. *Langmuir,* **1995**, *11*, 693-695.

78. Dassenoy, F.; Casanove, M. J.; Lecante, P.; Pan, C.; Philippot, K.; Amiens, C.; Chaudret, B. *Physical Review B,* **2001**, *63*, 235407.

79. Wang, C.; Daimon, H.; Lee, Y.; Kim, J.; Sun, S. *Journal of the American Chemical Society,* **2007**, *129*, 6974-6975.

80. Mazumder, V.; Sun, S. *Journal of the American Chemical Society,* **2009**, *131*, 4588-4589.

81. Pelzer, K.; Laleu, B.; Lefebvre, F.; Philippot, K.; Chaudret, B.; Candy, J. P.; Basset, J. M. *Chemistry of Materials,* **2004**, *16*, 4937-4941.

82. Pelzer, K.; Candy, J. P.; Bergeret, G.; Basset, J. M. *The European Physical Journal D - Atomic, Molecular, Optical and Plasma Physics,* **2007**, *43*, 197-200.

83. Boualleg, M.; Guillois, K.; Istria, B.; Burel, L.; Veyre, L.; Basset, J.-M.; Thieuleux, C.; Caps, V. *Chemical Communications,* **2010**, *46*, 5361-5363.

84. Boualleg, M.; Basset, J.-M.; Candy, J.-P.; Delichere, P.; Pelzer, K.; Veyre, L.; Thieuleux, C. *Chemistry of Materials,* **2009**, *21*, 775-777.

85. Boualleg, M.; Norsic, S.; Baudouin, D.; Sayah, R.; Quadrelli, E. A.; Basset, J. M.; Candy, J. P.; Delichere, P.; Pelzer, K.; Veyre, L.; Thieuleux, C. *Journal of Catalysis,* **2011**, *284*, 184-193.

86. Boualleg, M.; Baudouin, D.; Basset, J.-M.; Bayard, F.; Candy, J.-P.; Jumas, J.-C.; Veyre, L.; Thieuleux, C. *Chemical Communications,* **2010**, *46*, 4722-4724.

87. Liu, X.; Atwater, M.; Wang, J.; Dai, Q.; Zou, J.; Brennan, J. P.; Huo, Q. *Journal of Nanoscience and Nanotechnology,* **2007**, *7*, 3126-3133.

88. Xu, Z.; Shen, C.; Hou, Y.; Gao, H.; Sun, S. *Chemistry of Materials,* **2009**, *21*, 1778-1780.

89. Baker, M. V.; Brown, D. H.; Simpson, P. V.; Skelton, B. W.; White, A. H.; Williams, C. C. *Journal of Organometallic Chemistry,* **2006**, *691*, 5845-5855.

90. Bassan, R.; Bryars, K. H.; Judd, L.; Platt, A. W. G.; Pringle, P. G. In *Inorganica Chimica Acta* 1986; Vol. 121, p L41-L42.

91. Clark, H. C.; Manzer, L. E. *Journal of Organometallic Chemistry,* **1973**, *59*, 411-428.

92. Ruddy, D. A.; Jarupatrakorn, J.; Rioux, R. M.; Miller, J. T.; McMurdo, M. J.; McBee, J. L.; Tupper, K. A.; Tilley, T. D. *Chemistry of Materials,* **2008**, *20*, 6517-6527.

93. Arunachalampillai, A.; Johnson, M. T.; Wendt, O. F. *Organometallics,* **2008**, *27*, 4541-4543.

94. Klein, A.; Klinkhammer, K.-W.; Scheiring, T. *Journal of Organometallic Chemistry,* **1999**, *592*, 128-135.

95. Bonati, M. L. M.; Douglas, T. M.; Gaemers, S.; Guo, N. *Organometallics,* **2012**, *ASAP article*.

96. Anwander, R.; Roesky, R. *Dalton Transactions,* **1997**, 137-138.

97. Rhers, B.; Quadrelli, E. A.; Baudouin, A.; Taoufik, M.; Copéret, C.; Lefebvre, F.; Basset, J.-M.; Fenet, B.; Sinha, A.; Schrock, R. R. *Journal of Organometallic Chemistry,* **2006**, *691*, 5448-5455.

98. Lefort, L.; Chabanas, M.; Maury, O.; Meunier, D.; Copéret, C.; Thivolle-Cazat, J.; Basset, J.-M. *Journal of Organometallic Chemistry,* **2000**, *593-594*, 96-100.

99. Miller, J. B.; Schwartz, J. *Acta Chemica Scandinavica,* **1993**, *47*, 292-295.

100. Binet, C.; Daturi, M.; Lavalley, J.-C. *Catalysis Today,* **1999**, *50*, 207-225.

101. Binet, C.; Badri, A.; Lavalley, J.-C. *The Journal of Physical Chemistry,* **1994**, *98*, 6392-6398.

102. Nguefack, M.; Popa, A. F.; Rossignol, S.; Kappenstein, C. *Physical Chemistry Chemical Physics,* **2003**, *5*, 4279-4289.

103. Kohn, S. C.; Brooker, R. A.; Dupree, R. *Geochimica et Cosmochimica Acta,* **1991**, *55*, 3879-3884.

104. Lin, W.; Herzing, A. A.; Kiely, C. J.; Wachs, I. E. *The Journal of Physical Chemistry C,* **2008**, *112*, 5942-5951.

105. Bernal, S.; Calvino, J. J.; Cauqui, M. A.; Gatica, J. M.; Larese, C.; PÃ©rez Omil, J. A.; Pintado, J. M. *Catalysis Today,* **1999**, *50*, 175-206.

106. Rascon, F.; Wischert, R.; Coperet, C. *Chemical Science,* **2011**, *2*, 1449-1456.

107. Donet, S.; Laurent, P.; Guillet, N.; Copéret, C.; Thieuleux, C., France, App. number 1250458, 2012.

108. Mailley, S.; Capron, P.; Thollon, S.; Krebs, T., WO, 12179817, 2011.

109. Mailley, S.; Sanchette, F.; Thollon, S.; Emieux, F., WO, 12179793, 2009.

110. Giorgi, L.; Antolini, E.; Pozio, A.; Passalacqua, E. *Electrochimica Acta,* **1998**, *43*, 3675-3680.

111. Dobki, D.; Zuraw, M. *Principles of Chemical Vapor Deposition*; Kluwer Academic Publishers: Dordrecht, 2003.

112. Joint Committee on Powder Diffraction Standards, I. C. f. D. D., Newton Square, USA, Powder Diffraction File #00-004-0802.

113. Billy, E.; Maillard, F.; Morin, A.; Guetaz, L.; Emieux, F.; Thurier, C.; Doppelt, P.; Donet, S.; Mailley, S. *Journal of Power Sources,* **2010**, *195*, 2737-2746.

114. Goswami, J.; Wang, C. G.; Cao, W.; Dey, S. K. *Chemical Vapor Deposition,* **2003**, *9*, 213-220.

115. C. D. Wanger; W. M. Riggs; L. E. Davis; J. F. Moulder; G. E.Muilenberg *Handbook of X-ray Photoelectron Spectroscopy: a reference book of standard data for use in x-ray photoelectron spectroscopy*; Perkin-Elmer Corp.: Eden Prairie, Minnesota, USA, 1979.

116. Navessin, T.; Holdcroft, S.; Wang, Q.; Song, D.; Liu, Z.; Eikerling, M.; Horsfall, J.; Lovell, K. V. *Journal of Electroanalytical Chemistry,* **2004**, *567*, 111-122.

117. Vidakovic, T.; Christov, M.; Sundmacher, K. *Electrochimica Acta,* **2007**, *52*, 5606-5613.

118. Fuel-Cell_Technologies_Program *US Department of Energy,* **2011**.

119. Van Hardeveld, R.; Hartog, F. *Surface Science,* **1969**, *15*, 189-230.

120. Moseley, K.; Maitlis, P. M. *Journal of the Chemical Society D: Chemical Communications,* **1971**, 982-983.

121. Sakaki, S.; Ogawa, M.; Kinoshita, M. *The Journal of Physical Chemistry,* **1995**, *99*, 9933-9939.

122. Terrill, R. H.; Postlethwaite, T. A.; Chen, C.-h.; Poon, C.-D.; Terzis, A.; Chen, A.; Hutchison, J. E.; Clark, M. R.; Wignall, G. *Journal of the American Chemical Society,* **1995**, *117*, 12537-12548.

123. Badia, A.; Gao, W.; Singh, S.; Demers, L.; Cuccia, L.; Reven, L. *Langmuir,* **1996**, *12*, 1262-1269.

124. De Jong, K. P. *Synthesis of Solid Catalysts*; Wiley-VCH: Weinheim, 2009.

125. Candy, J. P.; Fouilloux, P.; Renouprez, A. J. *J. Chem. Soc., Faraday I,* **1980**, *76*, 616-629.

126. Coppel, Y.; Spataro, G.; Pagès, C.; Chaudret, B.; Maisonnat, A.; Kahn, M. L. *Chemistry – A European Journal,* **2012**, *18*, 5384-5393.

127. Rebaud, M. *IUT Internship report,* **2009**.

128. Györffy, N.; Tóth, L.; Bartók, M.; Ocskó, J.; Wild, U.; Schlögl, R.; Teschner, D.; Paàl, Z. *Journal of Molecular Catalysis A: Chemical,* **2005**, *238*, 102-110.

129. Tsen, S. C. Y.; Crozier, P. A.; Liu, J. *Ultramicroscopy,* **2003**, *98*, 63-72.

130. Mejias, N.; Serra-Muns, A.; Pleixats, R.; Shafir, A.; Tristany, M. *Dalton Transactions,* **2009**, 7748-7755.

131. Krumeich, F.; Marx, S.; Baiker, A.; Nesper, R. *Zeitschrift für anorganische und allgemeine Chemie,* **2011**, *637*, 875-881.

132. Bharadwaj, S. R.; Kerkar, A. S.; Tripathi, S. N.; Dharwadkar, S. R. *Journal of the Less Common Metals,* **1991**, *169*, 167-172.

133. Paulus, U. A.; Schmidt, T. J.; Gasteiger, H. A.; Behm, R. J. *Journal of Electroanalytical Chemistry,* **2001**, *495*, 134-145.

134. Fang, B.; Chaudhari, N. K.; Kim, M.-S.; Kim, J. H.; Yu, J.-S. *Journal of the American Chemical Society,* **2009**.

135. Antolini, E. *Applied Catalysis B: Environmental,* **2009**, *88*, 1-24.

136. Conway, B. E. *Progress in Surface Science,* **1995**, *49*, 331-452.

137. Mazumder, V.; Chi, M.; Mankin, M. N.; Liu, Y.; Metin, Ö.; Sun, D.; More, K. L.; Sun, S. *Nano Letters,* **2012**, *12*, 1102-1106.

138. Rand, D. A. J.; Woods, R. *Journal of Electroanalytical Chemistry and Interfacial Electrochemistry,* **1972**, *36*, 57-69.

139. Lukaszewski, M.; Czerwinski, A. *Journal of Alloys and Compounds,* **2009**, *473*, 220-226.

140. Baturina, O. A.; Aubuchon, S. R.; Wynne, K. J. *Chemistry of Materials,* **2006**, *18*, 1498-1504.

141. Boualleg, M.; Guillard, C.; Thieuleux, C.; Candy, J.-P.; Veyre, L.; Basset, J.-M., WO 153474

RESUME en français
Cette thèse a pour but la mise au point de méthode de synthèse de nanoparticules de métaux nobles pour la catalyse. Le projet s'est concentré sur la synthèse de nanoparticules composées de platine et de palladium. Trois voies de synthèses ont été explorées, i) par chimie organométallique de surface (COMS)), ii) par dépôt chimique en phase vapeur de composés organométalliques (MOCVD, Metal Organic Chemical Vapor Deposition et enfin iii) par voie colloïdale. La voie chimie organométallique de surface a permis la synthèse de nanoparticules supportées sur silice avec des tailles d'environ 2 nm. Le transfert de cette méthodologie vers l'oxyde de cérium a été effectué et permet d'obtenir des nanoparticules de moins de 1.5 nm de diamètre. Ces dernières recherches ont pour finalité l'obtention de catalyseurs d'oxydation supportés sur oxyde de cérium utilisé pour la dépollution automobile et ouvre la voie à la chimie organométallique de surface sur oxyde de cérium. Par MOCVD des nanoparticules de 4 à 6 nm ont été synthétisées sur couche de diffusion de gaz (GDL) pour des applications en pile à combustible. Des essais en électrocatalyse ont démontré la viabilité de la méthode de synthèse et l'activité catalytique des particules ainsi formées pour la réaction de réduction de l'oxygène (ORR), réaction clé des piles à combustible H_2/O_2.Enfin, pour cette même application, des nanoparticules de Pt, Pd et Pt/Pd dans différentes proportions ont été synthétisé par voie colloïdale. Ces nanoparticules, stabilisées par l'octylsilane ont une taille allant de 1.5 à 1.8 nm. Pour la platine, l'influence du précurseur organométallique et de la température ont été étudié, la synthèse sans apport de réducteur extérieur (H_2) et à partir de précurseur Pt^{II} a permis l'obtention de nanoparticules stables de 1.2 nm. Leur utilisation pour l'ORR a démontré l'intérêt de former des alliages Pt/Pd, la composition 3:1 démontrant une amélioration d'un facteur 1.4 par rapport au Pt.

TITRE en anglais
Molecular approach towards the design and the preparation of supported and non-supported Pt- and Pd-based nanoparticles

RESUME en anglais
The goal of this thesis is to develop synthesis methods for platinum and palladium based nanoparticles. We mainly focused on three synthesis pathways, i) Surface Organometallic Chemistry (SOMC), ii) metal organic chemical vapor deposition (MOCVD) and iii) a colloidal approach. Surface organometallic chemistry allowed the synthesis of silica supported nanoparticles with sizes of about 2 nm. The transfer of this methodology to cerium oxide has been carried out and allowed obtaining nanoparticles of less than 1.5 nm in diameter. Those researches had for purpose the synthesis of oxidation catalysts supported on ceria used for automotive pollution and paves the way for the surface organometallic chemistry on this oxide. By MOCVD, Pt nanoparticles from 4 to 6 nm were synthesized onto gas diffusion layers (GDL) for applications in fuel cell catalysis. Electrocatalysis results demonstrated the viability of this synthesis method and the efficiency of these catalysts for the Oxygen Reduction Reaction (ORR). For the same application, nanoparticles of Pt, Pd and Pt/Pd in various proportions were synthesized by the colloidal approach. These nanoparticles stabilized by octylsilane had a size ranging from 1.5 to 1.8 nm. For platinum, the influence of the organometallic precursor and temperature have been studied and synthesis without adding external reducing (H_2) and from Pt^{II} precursor allowed obtaining stable nanoparticles of 1.2 nm. Their use for the ORR has shown interest to form alloys, the Pt/Pd 3:1 composition demonstrating an improvement by a factor of 1.4 compared to pure Pt.

DISCIPLINE Chimie

MOTS-CLES
Chimie Organométallique de Surface, platine, paladium, allliages, particules, silice, cérine.

INTITULE ET ADRESSE DE L'U.F.R. OU DU LABORATOIRE :

C2P2, UMR 5265, CNRS–Université Lyon 1–ESCPE Lyon, ESCPE Lyon, 43 Bd du 11 Novembre 1918 F-69616 Villeurbanne, France.